

Fundamentals and Applications of Langmuir Probe Diagnostics in Complex Plasmas

Dissertation
zur Erlangung des Doktorgrades
der Mathematisch-Naturwissenschaftlichen Fakultät
der Christian-Albrechts-Universität zu Kiel

vorgelegt von
Markus Klindworth

Kiel
Dezember 2004

Referent: Prof. Dr. A. Piel
Koreferent:
Tag der mündlichen Prüfung: 28. Januar 2005
Zum Druck genehmigt: Kiel, den

Der Dekan

Abstract

This thesis explores the fundamentals and first applications of spatially-resolved Langmuir probe diagnostics in dusty plasmas with respect to laboratory and microgravity experiments. The basics of dusty plasmas and the subtleties of Langmuir probe theory in low density plasmas with weak collisionality are described. The investigations address the following topics:

- the design of an rf compensated miniature Langmuir probe with two-axis drive, which matches the constraints for experiments under microgravity
- the evaluation and adaption of available probe theories for the analysis of probe data under typical discharge conditions used for complex plasma experiments
- the quantification of possible feedback of the probe on the plasma and verification of the developed Langmuir probe system
- the investigation of effects of the probe on the surrounding particle distribution
- the demonstration of first probe diagnostics applications in dusty and dust-free plasmas

The major results can be summarized as follows: An automatic fitting algorithm for the Langmuir probe data based on the ABR-Model was developed that includes corrections for ion-neutral collisions. The competing OML-model was found to be not valid in given discharge regime. The random sampling technique to obtain probe characteristics was optimized to avoid dust contamination of the probe. An important discovery was the observation of “anti-voids” around probes and their explanation by quantitative modeling of the acting ion drag and electric field forces on dust particles in the presheath regime. From the understanding of this mechanism the formation of dust layering and its relationship to the gradients of exerted forces could be explained by direct comparison between model and experimental observations. The marking of the equilibrium point by dust tracers was introduced as a novel technique to visualize the sheath boundaries. The quantitative comparison of probe diagnostics with SIGLO plasma simulations shows now a reasonable agreement, which is an important prerequisite for future applications of the Langmuir probe in the IMPF experiments aboard the International Space Station.

Kurzfassung

Diese Dissertation untersucht die fundamentalen Eigenschaften und erste Anwendungen von orts aufgelöster Langmuir-Sondendiagnostik in staubigen Plasmen im Hinblick auf Experimente im Labor und in Schwerelosigkeit. Es werden die Grundlagen staubiger Plasmen und die Feinheiten von Langmuir-Sondentheorien in schwach stossbehafteten Plasmen geringer Dichte beschrieben. Die Untersuchungen zielen auf die folgenden Themen:

- Das Design einer HF-kompensierten Miniatur-Langmuir-Sonde mit Zweiachs Antrieb unter Berücksichtigung der Anforderungen für Experimente unter Schwerelosigkeit.
- Die Bewertung und Anpassung vorhandener Sondentheorien für die Auswertung von Sondendaten unter für Komplexe Plasmen typischen Entladungsbedingungen.
- Die Quantifizierung möglicher Rückwirkungen der Sonde auf die Entladung und die Verifikation des entwickelten SONDENSYSTEMS.
- Die Untersuchung des Einflusses der Sonde auf die umgebende Staubverteilung.
- Die Demonstration erster Anwendungen der Sondendiagnostik in staubigen und staubfreien Plasmen.

Die wesentlichen Ergebnisse lassen sich wie folgt zusammenfassen: Basierend auf einem ABR-Modell mit Korrektur für Ionen-Neutralatomstößen wurde ein automatischer Auswertungsalgorithmus für Sondenkennlinien entwickelt. Das konkurrierende OML-Modell erwies sich im gegebenen Entladungsregime als nicht gültig. Für die Aufnahme von Sondenkennlinien wurde die "Random-sampling"-Technik optimiert, um die Kontamination der Sonde durch Staub zu verhindern. Eine wichtige Entdeckung stellt die Beobachtung von "Anti-voids" um Sonden und ihre Erklärung durch die quantitative Modellierung der auf die Staubpartikel wirkenden Ionenwind- und elektrischen Feldkräfte im Vorschichtbereich dar. Mit dem Verständnis dieses Mechanismus konnte die Ausbildung von Partikelschichten und ihr Zusammenhang mit den Gradienten der wirkenden Kräfte durch Vergleich des Modells mit experimentellen Beobachtungen erklärt werden. Die Markierung des Kraftgleichgewichtsortes durch Tracer-Partikel wurde als neue Methode zur Visualisierung der Grenzen von Raumladungsschichten eingeführt. Als wichtige Voraussetzung für zukünftige Einsätze der Langmuir-Sonde im IMPF-Experiment an Bord der Internationalen Raumstation zeigt sich nun im quantitativen Vergleich von von Sondenmessungen und SIGLO-Plasmasimulationen eine ergänzende Übereinstimmung.

Contents

1	Introduction	1
2	Basics of complex plasmas	5
2.1	Capacitively coupled rf discharges	5
2.1.1	General Aspects of a Capacitive Discharge	5
2.1.2	Fundamentals of Plasmas	9
2.2	Dust particle charging	13
2.2.1	Probe theory for particle charging	13
2.2.2	Validity of the OML charging model	16
2.2.3	Charging time	18
2.2.4	Other charging mechanisms	19
2.2.5	Many-particle effects	20
2.2.6	Coulomb coupling	22
2.3	Forces on dust particles	23
2.3.1	Gravity	23
2.3.2	Neutral gas friction	23
2.3.3	Thermophoretic force	24
2.3.4	Electric field force	25
2.3.5	Ion drag force	26
2.3.6	Ordering of the forces	33
2.4	Force balance and “voids”	33
2.5	Ordering of particles under external forces	36
3	Experiment and diagnostics	39
3.1	Basic experimental setup	39
3.1.1	The PKE and IMPF plasma chambers	39
3.1.2	Dust particles	45
3.1.3	Particle injection	46
3.2	Microgravity experiments	47
3.2.1	Obtaining microgravity	47
3.2.2	Special experimental design issues	49
3.3	Video observation	50
3.4	Probe diagnostics	51
3.4.1	Probe design and rf compensation	52
3.4.2	Probe contamination	56

3.5	Modelling of plasmas	58
3.5.1	Simulation techniques	58
3.5.2	SIGLO-simulations	60
4	Langmuir probe models and analysis	62
4.1	Probe operation regimes	62
4.2	OML and radial motion	63
4.2.1	Orbital-Motion-Limit theory	64
4.2.2	Radial motion of ions	67
4.2.3	Comparison of theories for the ion current	68
4.3	Analysis with collisions	71
4.4	Finite length of a probe	74
4.5	Probe data processing	76
5	Characteristics of particle-free discharges	78
5.1	Effects by the probe	78
5.2	Probe model verification	81
5.3	Characterization of the discharges	85
5.3.1	PKE	85
5.3.2	IMPF	93
5.4	Summary of results	97
6	Probe induced secondary voids	98
6.1	Experimental observations	98
6.2	Interpretation: Secondary voids	101
6.3	Modeling the force balance	105
6.3.1	The force equilibrium position	105
6.3.2	Force induced particle layering	110
6.4	Discussion	111
7	Force balance in complex plasmas under microgravity	115
7.1	Experiment and observations	115
7.2	2D-equilibrium model	116
7.3	Comparison of results	121
7.4	Discussion	123
8	Discharges affected by dust	126
8.1	Experiment and results	126
8.2	Discussion	129
9	Summary and outlook	133

1 Introduction

“Complex plasma” or originally “dusty plasma” names a gas plasma, that consists of electrons, ions, neutral gas atoms and additional microscopic particles with sizes ranging from about 10 nm to several ten micrometers. While the old name addresses mainly the origin of such systems, that is related to dust clouds in space, the name “complex plasma” stands for the unusual properties of this kind of plasmas, e.g. the formation of crystalline phases due to the highly charged microparticles.

Two main reasons can be identified as motivation for the study of complex plasmas: As the plasma phase provides the major contribution to the cosmic matter, it often comes with embedded solid particles. This is the case for example in proto-planetary disks, planetary ring systems, comet tails and interstellar clouds [1]. Another origin of interest can be found in industrial applications. There, dusty plasmas are either a result of plasma etching of semi-conductors or a material reservoir and generator for deposition processes [2].

The interest of fundamental research is focused on the electrostatic phenomena of the strongly coupled particles in a complex plasma [3]. Previous work, for example, has been spent on the essential shielding and charging effects of dust grains (see Section 2.2), the propagation of waves and solitons [4, 5], formation of dust clusters and crystals [6] or the basic forces acting on the particles in the plasma environment (see Section 2.3) and on diagnostical aspects [7].

The advantage of complex plasmas experiments compared to other setups for investigation on strongly coupled particles, like laser cooled ions in particle traps [8], is that they yield easily observable physics of (screened) Coulomb systems at a relatively low rate of technical expense. Dusty plasmas are also in many respects preferable to colloidal suspensions, because suspensions include by definition a high damping rate, what makes them less suitable for e.g. wave investigations. Nevertheless, the convenient study of dynamical properties of particle systems consisting of micrometer sized grains in the laboratory is mostly restricted to two dimensions, since gravity is a dominant force and confines dust clouds in the lower boundary of the embedding plasma. Thus, only flat dust objects of significant particle size can be studied under laboratory conditions. To overcome these limitations and obtain three-dimensionally extended dust distributions, experiments have been performed under microgravity conditions on sounding rocket missions [9], parabolic flights [10], the MIR [11] and on the ISS* [12].

*International Space Station

These investigations yielded a wealth of data on new phenomena like dust-free regions (“voids”) [9], de-mixing of differently sized dust particle populations [13] and the repulsion of dust cloud boundaries [14], which can be observed only under microgravity conditions. The effects are theoretically assumed to result from the influence of dust on the discharge, shaping the plasma profile, which yields the amplification of inherent forces on the particles, like ion drag force and electric field force [15, 16, 17, 18, 19]. While various numerical simulations addressed these open questions [20, 21, 22, 23, 24], the experimental access to spatially resolved parameters of such complex plasmas is still missing. Thus, as a promising candidate, Langmuir probe diagnostics are highly desirable to overcome this limit.

Therefore, this study explores the fundamentals and the use of electrostatic probes in complex plasmas with respect to microgravity experiments and especially the envisaged application aboard the ISS as part of the IMPACT[†]-IMPF[‡] project. In detail, the main goals addressed are:

- the design of an rf compensated miniature Langmuir probe with two-axis drive, which matches the constraints for experiments under microgravity
- the evaluation and adaption of available probe theories for the analysis of probe data under typical discharge conditions used for complex plasma experiments
- the quantification of possible feedback of the probe on the plasma and verification of the developed Langmuir probe system
- the investigation of effects of the probe on the distribution of particles
- the demonstration of first probe diagnostics applications in dusty and dust-free plasmas

As one of the roots of complex plasmas is found in industrial processing, where capacitively and inductively coupled plasmas are used, these discharge types also dominate in scientific laboratories. The PKE[§] and IMPF devices, which were designed for microgravity experiments and have been used for this work, are members of the first type of reactors. Thus, the second chapter gives an introduction to complex plasmas in capacitive rf discharges starting with basics of plasmas under high frequency condition, the particle charging processes and the various forces, exerted on the dust grains in the ambient plasma. Based on these fundamentals, the mechanisms, which confine the third plasma species in the discharge volume, is treated and an introduction to the void-phenomenon and force-induced particle ordering is given.

In Chapter 3 the experimental setups are introduced in terms of plasma

[†]International Microgravity Plasma, Aerosol and Cosmic Dust Twin

[‡]International Microgravity Plasma Facility

[§]Plasma-Kristall-Experiment

chamber geometries, working conditions, dust particle properties and their video observation in the discharge. The aspects of experiments on parabolic flights, which have been used for the investigations, and other methods to obtain microgravity condition are also discussed. The description of the probe hardware includes the necessary compensation of fluctuations in the rf environment and avoidance of probe contamination by particles in dusty plasmas, which is strongly required for future long term experiments aboard ISS. Since no absolute parameters from plasma diagnostics are available for the PKE and IMPF devices, discharge simulations and especially the SIGLO code [25] are introduced as additional “experimental” method yielding necessary comparison data for the evaluation of probe measurements.

A method for the interpretation of measured probe data is worked out in Chapter 4. This is done by classifying the given plasma conditions and probe properties in comparison with the various existing probe theories as well as by empirical arguments regarding the reliability of the theoretical and the measured probe characteristics. The considerations require a decision between the applicability of the almost standard Laframboise theory [26] and the competing Allen-Boyd-Reynolds model [27].

The performance of the Langmuir probe design and analysis method as diagnostics in the experiments PKE and IMPF is characterized by measurements of quantitative plasma properties in dust-free discharges. First the influence of the probe on the discharge is addressed as non-negligible effect in feeble plasmas in order to estimate the validity of the method. Further on, the exploration of plasma properties as a function of discharge parameters is done by comparing systematic measurements with corresponding simulations in magnitude and two-dimensional spatial distribution. Besides the resulting information on the properties of the probe system, this data is required to improve and adjust plasma simulations and to characterize and rate plasma chamber designs for a future ISS-based experiment.

Investigations on the interaction of charged particles and Langmuir probes are a prerequisite for developing suitable diagnostic methods for complex plasmas. Taking into account the presence of dust in the plasma, Chapter 6 therefore focuses on the behavior of dust particles in the vicinity of an object, the probe, in the plasma. Since in the absence of gravity more subtle forces dominate the motion of particles, which also play a role in the dust’s behavior near the probe, the reported experiments had to be performed on parabolic flights.

To demonstrate the overall capabilities of the probe and concurrently go further into the understanding of complex plasmas, advanced probe applications are performed: Two-dimensional plasma parameter profiles from simulations and probe measurements in the IMPF chamber are used to calculate the forces on particles and obtain modeled equilibrium particle distribution. Recalling a

recent debate [28, 29], competing ion drag force theories are included in the model to promote a decision on the validity of models. The convenience of measurements and simulations is then evaluated by comparing the result to observed arrangements of tracer particles in the microgravity experiment. Finally, the influence of a large amount of dust on the plasma parameter profile of a discharge is explored by direct probe measurements in a laboratory investigation. Both experiments also contribute to the still not complete understanding of void formation in microgravity experiments [9, 10, 11, 30].

Besides the aim of this thesis to develop a diagnostic method, which opens a new access to the physics of complex plasmas, it serves as a prestudy on probe diagnostics in the IMPACT-IMPF project to establish an experiment infrastructure for dusty plasma aboard ISS.

2 Basics of complex plasmas

This chapter describes the properties of complex plasmas in capacitively coupled radio-frequency (rf) discharges, in which all presented experiments are performed and which generally dominate in scientific laboratories as dusty plasma experiments. Besides inductively coupled plasmas, this type of discharge is also favored in industrial processing, where it is used for anisotropic etching of semiconductors.

Therefore, starting with basics of plasmas under high frequency conditions, a survey of the processes that determine the charging of dust grains as well as the various forces, which are exerted on the dust in the ambient plasma, is given. Special emphasis is laid on competing ion drag force models. Based on these fundamentals, the mechanisms that trap the third plasma species, the particles, in the discharge volume and the effect of force induced particle ordering is discussed. Additionally, the void phenomenon is shortly described in terms of the present models.

For simplicity, all further considerations are limited to electropositive plasmas with only one gas component. Further, the ions are supposed to carry only one elementary charge. This assumption is valid for the later introduced noble gas discharges.

2.1 Capacitively coupled rf discharges

2.1.1 General Aspects of a Capacitive Discharge

In laboratory experiments, a plasma is produced in a vacuum chamber which is evacuated and filled at a low pressure of $(5 \cdots 150)$ Pa with a selected background gas. Often noble gases are chosen to provide the ions. An rf plasma chamber [31] is equipped with at least one powered electrode and a arbitrary number of grounded electrodes. In a simple setup the grounded electrode is represented by the chamber walls. Figure 2.1 shows the schematic drawing of a rf plasma chamber with two symmetrical plane electrodes. Typically the electrodes are in direct contact with the plasma and their radius ranges from $(2 \cdots 10)$ cm. They are separated by a gap $d \approx (1 \cdots 10)$ cm. The discharge is driven by an external rf source applied to the powered electrodes through a matching unit. To avoid the loss of all charged particles created in one half cycle of the rf, the frequency f_{rf} must be typically above 50 kHz. In laboratory experiments a standard frequency of $f_{RF} = 13.56$ MHz is commonly used. In contrast to the electrons, the ion

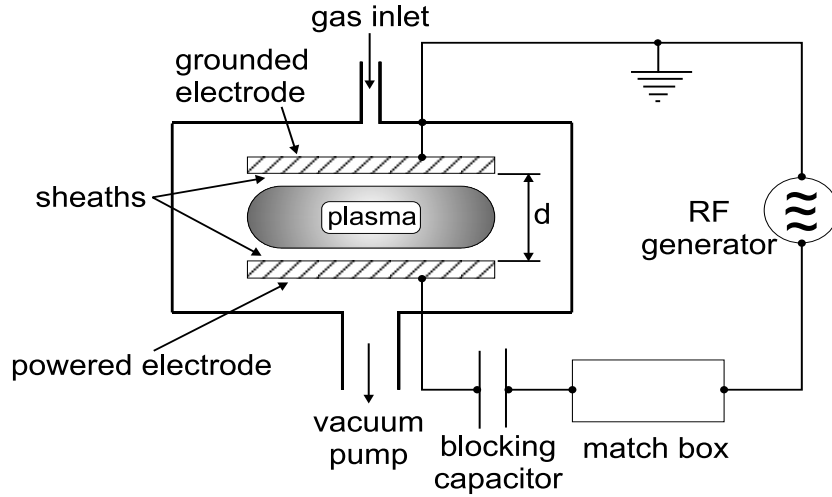


Figure 2.1: Scheme of a typical rf discharge setup with two symmetrical electrodes. One electrode is powered and the other one is grounded. Configurations with multiple powered electrodes are also possible (see Chapter 3).

inertia is so high, that they cannot follow the RF field and thus they gain energy only from the weak averaged fields generated by the plasma. The result is a plasma, that is far from equilibrium, with a hot electron and cold ion component. The differences in mobility implicate special properties of the plasma sheath, the interface from plasma to electrode.

The rf-sheath

To describe the structure of the space charge sheath that connects the plasma to an rf-driven electrode, we assume that a plane electrode, is in contact with a non-isothermal plasma of equal ion and electron densities $n_{i,e}$ (compare with Section 2.1.2). Then, the random electron flux to the plate is much high than the ion current, because of the higher electron mobility. This is analogous to the discussion of the potential of charged spherical bodies (Section 2.2.1) or the floating potential of cylindrical probes (Section 4.2.1) in a plasma. Thus, the electrode is charged up negatively and further electrons are repelled while ions are accelerated towards the electrode. The equality of charge-carrier densities (quasi-neutrality) is broken and the point, from whereon this universal property of a plasma is no longer valid, is known as the sheath edge. A positive space charge layer and an accompanying strong electric field that points towards the electrode establishes close to it. The potential of the electrode is maintained at a certain negative value, when the reduced electron current becomes equal to the ion current and if the electrode has no ground contact, which can be ensured by the blocking capacitor. The process of charging of an electrode to this floating potential is called self-biasing.

In an rf discharge the described process is superposed with a sinusoidal oscillating voltage $U_{rf}(t)$ fed to the electrode. It is shown in Section 2.1.2, that only

the electrons can follow the resulting oscillation of the electric field in the sheath. Keeping in mind Figure 2.2, the ion density n_i is unaffected, since the ions follow the average electric field, but the electrons are more repelled from the electrode during the negative half of the rf period and flood the former sheath during the other half. The sheath edge position $x_s(t)$ and the local electron density $n_e(z, t)$ is then time-dependent. Still, the time-averaged electron current has to compensate the ion flux to the electrode. Therefore, the averaged electron density \bar{n}_e at electrode surface $z = z_{electr.}$ is small, but non-zero. It is obvious, that an electron located in the bulk plasma, is able to reach an electrode, and thus can contribute to the discharge current when the electrode potential is more positive than the space potential ϕ_p in the plasma volume close to the sheath edge during a small fraction of the rf period. Therefore, considering only weak potential gradients in the bulk, the peak plasma potential ϕ_p of a discharge is expected to adjust itself at a value comparable to the rf amplitude or half of the peak-peak voltage $\frac{1}{2}U_{pp}^{rf}$ [31].

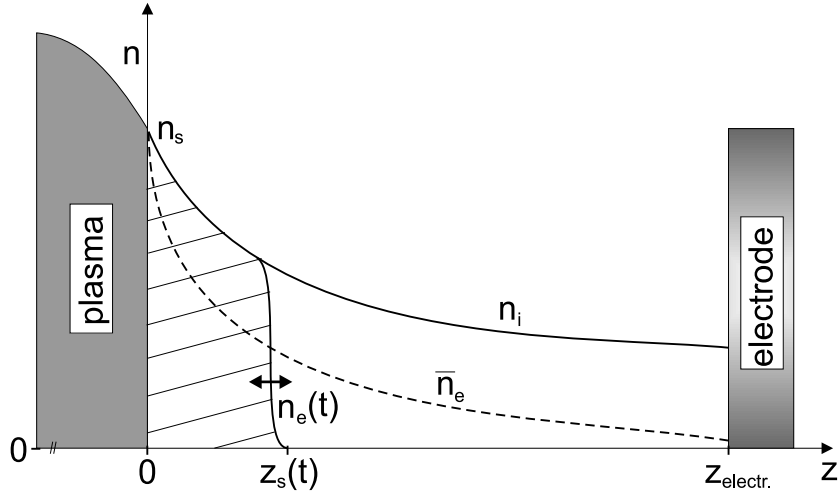


Figure 2.2: Charge carrier densities n_i and $n_e(t)$ in the sheath of a rf driven discharge. The sheath edge position is given by the break down of $n_e(t)$ and thus the invalidity of quasi-neutrality. The dashed line shows the averaged electron density over one rf cycle at the position z . After [32].

Often it is useful for the description of physics in the region of oscillating electron population, e.g. the determination of the charge of dust particles, to define a duty cycle

$$\alpha(z) = \frac{\bar{n}_e(z)}{n_i(z)} \quad (2.1)$$

for given quasi-neutrality at a point z . Assuming a time-averaged electric field $E(z)$ only dependent on the distance to the electrode z , Poisson's equation becomes

$$\epsilon_0 \frac{\partial E(z)}{\partial z} = \rho(z) = en_i(z)(1 - \alpha(z)) \quad (2.2)$$

Approximately, the charge density ρ from the averaged sheath edge \bar{z}_s to $z_{electr.}$ can be considered as constant. Solving Eq. (2.2), $E(z)$ linearly increases for $\bar{z}_s \leq z \leq z_{electr.}$, yielding

$$E(z) = E_0 \left(1 - \frac{z}{\bar{z}_s} \right) \quad , \quad (2.3)$$

with $E_0 = E(\bar{z}_s)$. The assumption of a linearly increasing electric field has been used previously [33] and proven by simulations [20] as a good approximation. Zafiu *et al.* [34] have experimentally studied the details of the sheath electric field in more detail. A sophisticated self-consistent model of a collisionless rf sheath is given by Lieberman and Lichtenberg [32]. In experimental setups the electric field in the space charge layer is found of the order of 10^4 V/m and is therefore very important for the confinement of negatively charged dust particle in the plasma (see Section 2.4). The width of the sheath ($\bar{z}_s - z_{electr.}$) can be estimated to extend over some electron Debye lengths (see Section 2.1.2) [35, 36].

As the potential distortion caused by the electrode cannot be completely screened by the space charge region, the field penetrates into a quasi-neutral transition region, the presheath. It can be shown [37], that the weak potential variation of the presheath accelerates the ions, so that the Bohm criterion [38]

$$v_{\perp} \geq v_B = \sqrt{\frac{k_B T_e}{m_i}} \quad (2.4)$$

is fulfilled for ions entering the sheath. Here, v_{\perp} is the ion velocity component perpendicular to the electrode surface, k_B the Boltzmann constant, T_e the electron temperature, m_i the ion mass and v_B is the ion acoustic speed, known as the Bohm velocity. Equation (2.4) is valid for a monoenergetic ion beam and is, as good approximation for most experimental conditions, satisfied with the equality sign. It should be noticed, that for a real ion velocity distribution $\langle v_{\perp}^{-2} \rangle \leq v_B^{-2}$ has been proposed as generalized Bohm criterion [39]. The brackets $\langle \rangle$ denote an average over the local distribution function. The Bohm criterion has direct applications in plasma diagnostics, because from the measured current of a Langmuir probe the plasma density at the sheath edge can be estimated (see Chapter 4). From here on, the position of the sheath edge z_s will be defined by $v_{\perp}(z_s) = v_B$. Further information on the physics of the plasma-wall transition, even under collisional conditions that have not been discussed here, is provided in [40] and the review [41].

Discharge modi

In order to produce a steady-state discharge, it is necessary to energize the electrons, so that enough ions are produced by electron-neutral collisions for the compensation of charge carrier losses to the plasma boundaries like chamber walls and electrodes. Two types of electron heating can be distinguished in a capacitive rf discharge.

Under moderate gas pressures $p_{gas} \gtrsim 15$ Pa, the electrons gain energy from the oscillating sheath edge. The expanding sheath accelerates the electrons in the plasma volume, where, after an electron mean free path, they perform elastic and inelastic collisions with neutral gas atoms. This type of heating is known as collisional or ohmic heating [32]. The energy loss in elastic collisions is very small due to the mass ratio of electrons and neutrals m_e/m_n , so that the electrons only experience a change in momentum. In inelastic collisions the energy is transferred to excitation and ionization of neutrals. As this process occurs close to the sheaths, the main light emission of the plasma is found here.

Under low pressure discharge conditions, the electron mean free path may become larger than the distance d of the two electrodes. Then a small fraction of the electrons can travel, accelerated at one sheath edge, through the plasma volume to the other sheath, where they “collide” with the sheath electric field. It depends on whether the sheath is contracting or expanding at the time of arrival, if the electrons lose or gain energy from these encounters. Statistically they are heated and become a high energy component of the plasma which is responsible for maintaining the plasma by ionization. On the other hand, the main electron component remains at a temperature even smaller than in the case of ohmic heating, which results from the lack of energy transfer from the “hot” to the “cold” electron population by electron-neutral collisions. Detailed work on this stochastic or collisionless heating was done by Gozadinos [42].

The transition from one heating regime to the other is performed erratic and yields a change in plasma brightness [43], density [44], and measured electron temperature [45] since the probe is more sensitive to the temperature of the major electron component. For the Langmuir probe measurements in complex plasmas studied here, the ohmic heating regime is preferred and as the transition from the ohmic to the stochastic mode is observed in the used PKE and IMPF experiments at higher rf power, when the neutral gas pressure is reduced below $p_{argon} \lesssim (10 \cdots 15)$ Pa, this pressure represents a lower limit for the experiments.

2.1.2 Fundamentals of Plasmas

The intention of the following section is to recall a few properties of plasmas and their extensions to dusty plasmas, that are of special importance for this work.

Quasi-neutrality

One of the most important features of plasmas is their quasi-neutrality,

$$\frac{n_e - n_i}{n_e} \ll 1 \quad . \quad (2.5)$$

n_i is the density of (singly charged) ions and n_e the electron density, respectively. But, as the quasi-neutrality after Eq. (2.5) is typically on the order of 10^{-6} , it is justified to use the known plasma approximation

$$n_e - n_i = 0 \quad (2.6)$$

and care for possible deviations from Eq. (2.6) by bearing in mind

$$\nabla\phi = E \neq 0 \quad . \quad (2.7)$$

Although a residual electric field \vec{E} in a plasma volume is weak and in many cases negligible, it does play a role, for example, in the acceleration of ions in small discharges from the central plasma to the chamber walls (see Section 2.4).

Taking into account a substantial number of charged dust particles as the third species of a complex plasma, the quasi-neutrality condition has to be extended to Eq. (2.40). The properties of a dusty many-particle plasma are discussed in section 2.2.5.

Shielding

Closely related to the tendency of the plasma to keep quasi-neutrality, is the shielding of disturbing charges. Assuming a point-like charge perturbation $Q\delta(r)$, Poisson's equation in spherical coordinates is given by

$$\begin{aligned} \Delta\phi &= -\frac{\rho}{\epsilon_0} \\ \Rightarrow \frac{1}{r^2} \frac{d}{dr} \left(r^2 \frac{d\phi}{dr} \right) &= -\frac{1}{\epsilon_0} [Q\delta(r) + e(n_e - n_i)] \quad , \end{aligned} \quad (2.8)$$

where ρ is the charge density and $n_{e,i}$ are the disturbed plasma densities. For clarity, the undisturbed densities far away from the test charge will be named $n_{e\infty} = n_{i\infty}$. Considering a Maxwellian energy distribution of ions and electrons in the plasma, $n_{e,i}$ affected by the field of the test charge ϕ is reduced by the Boltzmann factor and can be developed in a series to the first order,

$$n_e = n_{e\infty} \exp\left(\frac{e\phi}{k_B T_e}\right) \approx n_{e\infty} \left(1 + \frac{e\phi}{k_B T_e}\right) \quad (2.9)$$

$$n_i = n_{e\infty} \exp\left(-\frac{e\phi}{k_B T_i}\right) \approx n_{e\infty} \left(1 - \frac{e\phi}{k_B T_i}\right) \quad . \quad (2.10)$$

The latter approximation is valid, when the disturbance is small and thus the ratio of potential to kinetic energy $e\phi/(k_B T_{e,i})$ is small, too. $T_{e,i}$ are the ion and electron temperatures, k_B is the Boltzmann constant. Inserting Eqs. (2.9) and (2.10) in Eq. (2.8) yields

$$\frac{1}{r^2} \frac{d}{dr} \left(r^2 \frac{d\phi}{dr} \right) = -\frac{Q\delta(r)}{\epsilon_0} + \frac{1}{\lambda_D^2} \phi \quad . \quad (2.11)$$

It can be shown, that Poisson's equation can be solved with a Debye-Hückel (aka Yukawa or screened Coulomb) potential

$$\phi(r) = \frac{Q}{4\pi\epsilon_0 r} \exp\left(-\frac{r}{\lambda_D}\right) \quad . \quad (2.12)$$

The Debye-Hückel law describes the development of a potential that decays with the scale of the linearized Debye length

$$\lambda_D = \left[\frac{e^2 n_{e\infty}}{\epsilon_0} \left(\frac{1}{k_B T_e} + \frac{1}{k_B T_i} \right) \right]^{-1/2} = \left(\frac{1}{\lambda_{De}^2} + \frac{1}{\lambda_{Di}^2} \right)^{-1/2}, \quad (2.13)$$

with the individual electron and ions Debye lengths

$$\lambda_{De} = \sqrt{\frac{\epsilon_0 k_B T_e}{e^2 n_{e\infty}}}, \quad \lambda_{Di} = \sqrt{\frac{\epsilon_0 k_B T_i}{e^2 n_{i\infty}}}. \quad (2.14)$$

Typically $T_e \gg T_i$, so that $\lambda_D \approx \lambda_{Di}$. A result of the solution Eq. (2.12) is, that local deviations from quasi-neutrality of electrons and ions can exist only in sphere of radius λ_D , the Debye sphere, around the potential distortion.

As the charge of dust particles can comprise several thousand elementary charges, the assumption of $e\phi \ll k_B T_{e,i}$ is no longer tenable for the shielding problem of microspheres immersed in the plasma. Lampe *et al.* [46, 47] have solved Poisson's equation with electron and ion densities given by the OML-currents (see 2.2.1). They also included the influence of ions which can be trapped in orbits around the particle [48] and enhance the shielding of the particles electric field. The resulting potential distribution agreed within 25 % with Eq. (2.12) up to a maximum distance $r \approx 5\lambda_D$ from the particle. Far from the particle, the screened potential approximates a $1/r^2$ -dependence similar to an unscreened Coulomb potential.

Using the linearized Debye length as characteristic length for a Debye-Hückel potential, implies that ions and electrons contribute to the shielding in the same manner. In real discharges, ions are often accelerated in the residual electric fields of the finite plasma. These streaming ions are less affected by a potential distortion and thus they have a smaller contribution to the shielding process. The thermal energy $k_B T_i$ in the ion Debye length has to be substituted by the kinetic energy E_{kin} that accounts for the mean velocity of the ions v_s [49],

$$E_{kin} = \frac{1}{2} m_i v_s^2 = \frac{1}{2} m_i (v_{ti}^2 + v_i^2). \quad (2.15)$$

Here, m_i is the ion mass, v_{ti} the ion thermal velocity (see Eq. (2.21)) and v_i the ion beam velocity. The ion velocity dependent shielding length $\lambda_{Di}^v(v_i)$ is then given by

$$\lambda_{Di}^v(v_i) = \sqrt{\frac{\epsilon_0 k_B T_i}{e^2 n_{i\infty}} \left(1 + \frac{v_i^2}{v_{ti}^2} \right)}, \quad (2.16)$$

and yields the linearized Debye length as function of the ion speed,

$$\lambda_D^v(v_i) = \left[\frac{1}{\lambda_{D,e}^2} + \frac{1}{\lambda_{D,i}^2} \frac{1}{(1 + v_i^2/v_{ti}^2)} \right]^{-1/2}. \quad (2.17)$$

Equation (2.17) is a useful expression for $v_{ti} < v_i < v_B$ and can therefore be used for example for the shielding of particles located in the presheath of a plasma boundary. For $v_i \gtrsim v_B$, the contribution of ions to shielding can be neglected and $\lambda_D^v \approx \lambda_{De}$ [50]. A similar increase of the effective shielding length in the sheath region of a plasma was suggested in [51]. Thus, the electron Debye length can be considered as the characteristic length for the extent of sheaths around probes and other electrodes limiting the plasma.

Plasma frequencies

Up to now, the more or less static shielding has been considered. In the cases of dust particle motion or ion wave propagation the dynamic aspects have additionally to be taken into account. Due to their small mass, electrons are much more mobile than ions. The question is, up to which frequency they are able to screen deviations from quasi-neutrality, instantaneously. Considering the displacement of an electron in a fixed ion background of distance x , the force needed is eE and the approach can be formulated as the equation of a harmonic oscillator,

$$m_e \frac{d^2x}{dt^2} = -e \frac{dE}{dx} x = -\frac{e^2 n_e}{\epsilon_0} x \quad , \quad (2.18)$$

with the natural frequency

$$\omega_{pe} = \sqrt{\frac{e^2 n_e}{\epsilon_0 m_e}} \quad , \quad (2.19)$$

the electron plasma frequency. Dynamical phenomena taking place on a time scale smaller than $1/\omega_{pe}$ are not shielded, since the electrons cannot follow. An example is the transparency of the plasma for electromagnetic waves at a frequency $f > \omega_{pe}/(2\pi)$. Below the cut-off frequency $\omega_{pe}/(2\pi)$ the wave is reflected.

With $n_i = n_e$ the ion plasma frequency can be obtained from $\omega_{pi} = \sqrt{m_i/m_e} \cdot \omega_{pe}$. Here, another criterion for the use of the appropriate screening length is obvious. Accounting for processes with a characteristic frequency $\omega_{pe}/(2\pi) > f > \omega_{pi}/(2\pi)$, the electron Debye length has to be chosen, because the inertia of ions is too high. For $\omega_{pi}/(2\pi) < f$ it is justified to use the linearized length λ_D .

Of importance for e.g. Langmuir probe measurements in complex plasmas, is the response of charged dust particles to oscillating electric fields (see Section 3.4.2). The dynamic limit for particles is the dust plasma frequency, that writes, analogous to Eq. (2.19),

$$\omega_{pd} = \sqrt{\frac{e^2 n_d Z_d^2}{\epsilon_0 m_d}} \quad , \quad (2.20)$$

where n_d and m_d are the particle density and grain mass. Z_d is the absolute net number of elementary charges on the particle surface.

2.2 Dust particle charging

The complexity of a dusty plasma compared to an ordinary plasma is the presence of a third species of charged particles besides electrons and ions. The dust particles differ from the others by a large mass and a high charge. While the mass of a particle can be easily measured, the charge is strongly dependent on the properties of the ambient plasma in which the particle is immersed and can therefore only be estimated or measured with the same approximations, which are used to describe a plasma. In addition, the dust charge becomes a dynamic variable. But the magnitude of the charge is an essential parameter when the phenomena of dusty plasmas, e.g. forces on particles, dust waves and crystallization, are quantitatively described. Therefore, the most important aspects of the common understanding of particle charging are introduced in this section. While one of the first detailed contribution to this particular field has been provided by Whipple [52] for charging processes in space, the basic theory had already been worked out by Langmuir and Mott-Smith [53], who have developed the plasma diagnostic method of electrostatic probes.

2.2.1 Probe theory for particle charging

Charging currents

For the determination of the charge of a particle immersed in a plasma it is necessary to know the currents of electrons and ions that are collected by a body in the plasma with a surface potential ϕ_d . This problem is similar to the current collection by electrostatic probes (see Chapter 4). Langmuir and Mott-Smith calculated the currents to a probe of cylindrical and spherical geometry. The latter corresponds to the idealized shape of a dust particle, under the assumption of collisionless motion of the plasma species, that are additionally supposed to have isotropic velocity distributions. Considering the surface potential of a particle as negative with respect to the plasma potential ϕ_p , the *Orbital-Motion-Limit*-model (OML) assumes that the current contribution to this object in the plasma is limited to those positive ions that have an impact parameter $b < b_c$ (see Fig. 2.3). For simplicity the space potential is considered as $\phi_p = 0$. The assumption of a negatively charged particle is valid in non-equilibrium low temperature plasmas, since the ratio of electron and ion temperature $T_e/T_i \gg 1$ and therefore electron hit the particle more often than ions. Thus, the orbital motion of an ion ends either on the particle or, after a slight deflection in the central field of the charged particle, at infinity. Ions with $b = b_c$ will hit the particle at grazing incidence. The total energy E_0 of an ion starting at infinity with the average thermal velocity

$$v_{ti} = \sqrt{\frac{8}{\pi} \frac{k_B T_i}{m_i}} \quad , \quad (2.21)$$

is conserved in the electrostatic central field of the particle. Here, m_i is the mass of the ion and k_B is the Boltzmann constant. Thus, the maximum energy of a

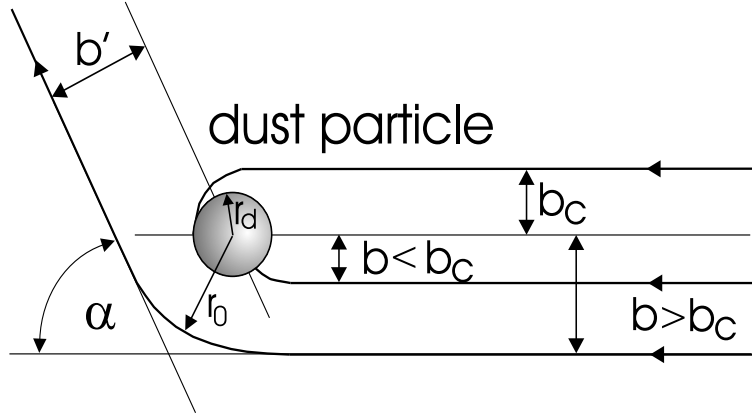


Figure 2.3: Assuming a particle with negative surface potential, only attracted ions, that have an impact parameter $b < b_c$, contribute to the particle charge. Ions with $b > b_c$ are deflected in the electrostatic field of the particle, but cannot reach it. α is the deflection angle and r_0 the distance of closest approach of the ion.

collected singly charged ion is

$$E_0 = \frac{1}{2}m_i v_{ti}^2 = e\phi_d + \frac{1}{2} \frac{L_0^2}{m_i r_d^2} \quad , \quad (2.22)$$

with the initial angular momentum $L_0 = m_i v_{ti} b_c$ and particle radius r_d . Transforming Eq. (2.22) gives

$$b_c = r_d \sqrt{1 - \frac{e\phi_d}{E_0}} = r_d \sqrt{1 - \frac{e\phi_d}{k_B T_i}} \quad . \quad (2.23)$$

The parameter b_c then represents the radius of an effective current collecting surface of the particle, which is larger than the real spherical area. If the current to a spherical particle is given by the charge flux $en_i v_{ti}$ through the effective surface area $A_{eff} = 4\pi b_c^2$ and including a geometry factor 1/4, I_i becomes

$$I_i = \frac{1}{4} A_{eff} n_i e v_{ti} = \pi r_d^2 n_i e \sqrt{\frac{8 k_B T_i}{\pi m_i}} \left(1 - \frac{e\phi_d}{k_B T_i} \right) \quad , \quad (2.24)$$

where n_i is the ion density of the ambient plasma.

The other plasma species which is in this case the electrons is repelled by the dust particle. Only those electrons which have an energy that is high enough to overcome the repulsive potential can contribute to the particle charge. Thus, the collection area for electrons is the real particle surface $A_d = 4\pi r_d^2$, but for a Maxwellian distribution the electron density

$$n_e(\phi_d) = n_{e\infty} \exp\left(\frac{e\phi_d}{k_B T_e}\right) \quad (2.25)$$

close to the surface is reduced by the Boltzmann factor. The electron current is then given by

$$I_e = -\frac{1}{4} A_d n_e e v_{te} = -\pi r_d^2 n_{e\infty} e \sqrt{\frac{8 k_B T_e}{\pi m_e}} \exp\left(\frac{e\phi_d}{k_B T_e}\right) \quad . \quad (2.26)$$

Figure 2.4 provides electron and ion currents to a particles with $r_d = 1.74 \mu\text{m}$ and $r_d = 3.4 \mu\text{m}$ as a function of the potential ϕ_d for selected values of T_e .

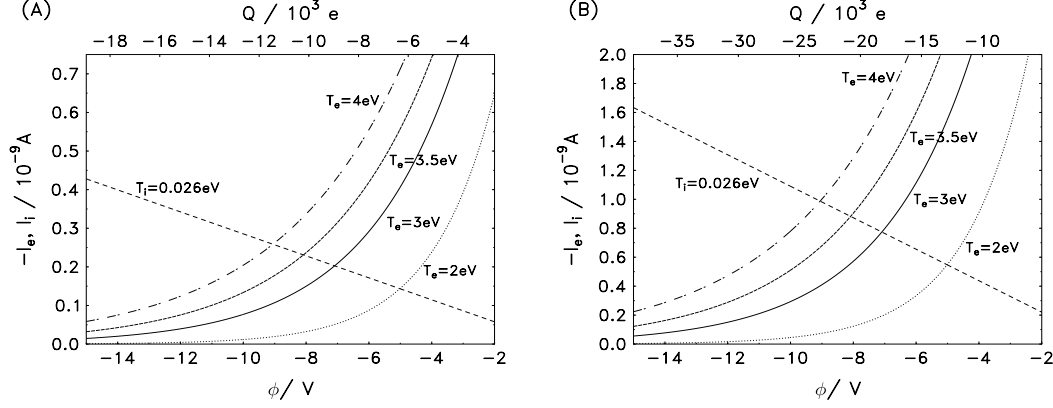


Figure 2.4: Charging currents to spherical dust particles of radius $r_d = 1.74 \mu\text{m}$ (A) and $r_d = 3.4 \mu\text{m}$ (B) in an argon plasma with $n_{i,e} = 1.2 \cdot 10^{15} \text{m}^{-3}$ for various T_e and $T_i = 0.026 \text{eV}$. The intersections of electron and ion currents indicate the magnitude of the floating potential, that is expected for the particle under the given conditions.

Determination of the charge

As the particle represents an isolated spherical probe in the plasma the net charge-carrier flux to the body must become $I_i(\phi_f) + I_e(\phi_f) = 0$ after the steady-state charge is reached. ϕ_f is the floating potential, at which the equality of ion and electron current is given. For a particle at steady state, $\phi_d = \phi_f$. Combining Eqs. (2.24) and (2.26) then gives the transcendent equation

$$1 - \frac{T_e}{T_i} \eta_f = \sqrt{\frac{m_i T_e}{m_e T_i} \frac{n_{e\infty}}{n_{i\infty}}} \exp(\eta_f) \quad , \quad (2.27)$$

with the normalized floating potential $\eta_f = e\phi_f/(k_B T_e)$. Equation (2.27) can be solved numerically and yields, for a quasi-neutral, non-isothermal plasma with $T_i \ll T_e$ (see Fig. 2.4),

$$\phi_f \approx (2 \dots 3) k_B T_e / e \quad . \quad (2.28)$$

At steady state the charge on the particle Q_d can be obtained from

$$Q_d = A_d \sigma = 4\pi r_d^2 \sigma \quad . \quad (2.29)$$

The surface charge density σ is determined by the electric field perpendicular to the surface and

$$\sigma = \epsilon_0 E(r_d) = -\epsilon_0 \left. \frac{\partial \phi}{\partial r} \right|_{r_d} = \epsilon_0 \left(\frac{1}{r_d} + \frac{1}{\lambda_D} \right) \phi(r_d) \quad . \quad (2.30)$$

Here, the Debye-Hückel potential (2.12) is used for $\phi(r)$. Then, the particle charge becomes

$$Q_d = C_s \phi_f = 4\pi\epsilon_0 r_d \left(1 + \frac{r_d}{\lambda_D}\right) \phi_f \quad . \quad (2.31)$$

C_s represents the capacity of the spherical capacitor under shielded conditions. In Fig. 2.4 the charge of the particle corresponding to its floating potential is shown under the assumption that $\lambda_D \approx \lambda_{Di}$, which is valid in drift-free low temperature plasmas.

2.2.2 Validity of the OML charging model

In laboratory plasmas, particles are often confined in the plasma sheath. Here, the OML requirement for Maxwellian distributed ions is no longer valid, due to the acceleration of the ions in the sheath. If the kinetic energy of the ions becomes $E_i \gg k_B T_i$ for high drift velocities v_{dr} , the charging current to the particle is [49]

$$I_i = \pi r_d^2 n_i e \sqrt{\frac{2E_i}{m_i}} \left(1 - \frac{e\phi_d}{E_i}\right) \quad , \quad (2.32)$$

with

$$E_i = \frac{1}{2} m_i v_s^2 \quad (2.33)$$

and an average ion velocity of

$$v_s = \sqrt{v_{ti}^2 + v_{dr}^2} \quad . \quad (2.34)$$

The development of the particle charge Q_d in an ion beam with a velocity up to v_B is shown in Fig. 2.5. For the determination of the charge with Eq. (2.31) both cases have been considered, namely a constant Debye length λ_D and a drift velocity-dependent Debye length λ_D^v (see Eq. (2.17)). The charging of particles under charge carrier drifts was also studied by Whipple [52]. Matsoukas and Russell presented an expression for arbitrary distribution functions [54]. Even for electrons the assumption of Maxwellian distribution is questionable, since in a rf plasma they are mainly energized in the sheath.

Furthermore, if the mean free path of the ions $\lambda_{mfp} = (n_n \sigma_t)^{-1}$ is significantly smaller than the electron debye length λ_{De} , collisions cannot be neglected. The total cross section σ_t for ion-neutral and charge exchange collisions in argon at “room temperature” is approximately 125 \AA^2 [55]. In Section 4.2.3 it is shown, that collisions destroy the orbital motion of ions and favor radial trajectories. Thus, even in the bulk plasma the OML theory for ions becomes questionable and a radial motion theory should be used. Using the ABR approach (see Section 4.2.2) in the case of $r_d \ll \lambda_D$, Nairn *et al.* [56] found the particle to carry

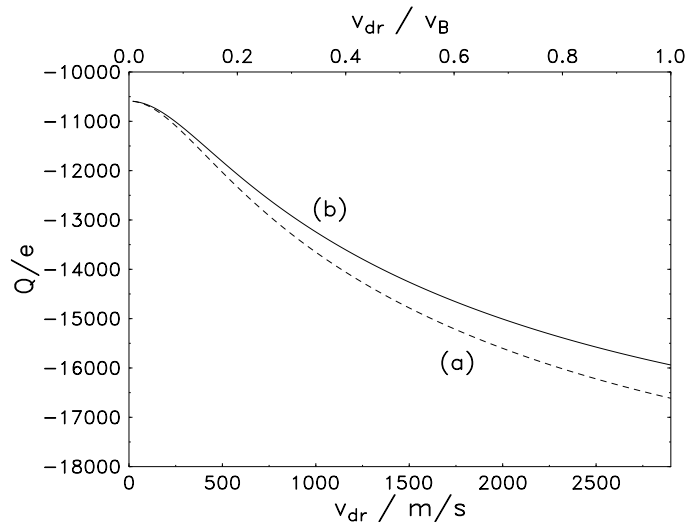


Figure 2.5: The particle charge Q_d vs. the ion drift velocity v_{dr} after [49]. The shielding length in Eq. (2.31) is assumed to be constant (a) or dependent on ion velocity (b). The particle radius is $r_d = 1.74 \mu\text{m}$, the argon plasma conditions are $T_e = 3.3 \text{ eV}$, $T_i = 0.026 \text{ eV}$ and $n_e = 1.2 \cdot 10^{15} \text{ m}^{-3}$.

a charge, which is approximately the same as if it were situated in a vacuum. Therefore, taking into account a Coulomb potential,

$$Q_d = C\phi_f = 4\pi\epsilon_0 r_d \phi_f \quad . \quad (2.35)$$

Bryant [57] investigated numerically the floating potential and the resulting charge of spherical dust grains with a more sophisticated ABR model which takes ion-neutral collisions into account. He finds the influence of collisions to be important for particles of several micrometers in diameter at 6 Pa or higher gas pressure in argon.

Nevertheless, the results of the OML model have been proven to be a valid approximation for small particles ($r_d \ll \lambda_D$) [58] and a good one up to $r_d \approx \lambda_{De}$ [59]. In the case of a particle radius of $r_d = 1.74 \mu\text{m}$ and a Debye length $\lambda_D \approx 40 \mu\text{m}$ the difference between particle charges obtained from Eqs. (2.31) and (2.35) is less than 10 %.

Experimentally, the particle charge can be measured indirectly via resonance methods [6, 33], the excitation of dust lattice waves [60, 61], the observation of dust particle collisions [62] or after extraction with a Faraday cup [63]. Another indirect method is the comparison of electron density measurements with and without the presence of a large number of dust particles [64]. In this case, the phenomenon of electron density depletion due to the binding of charge on the dust surfaces is employed. This effect is discussed in Section 2.2.5 in more detail.

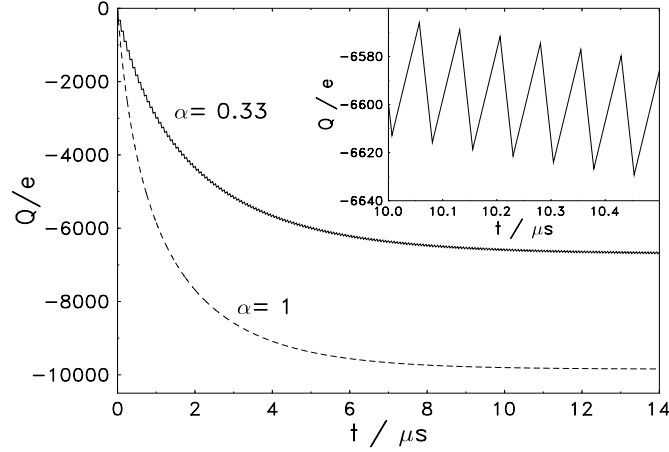


Figure 2.6: Charging of a dust particle ($r_d = 1.74 \mu\text{m}$) in an argon discharge under the alternating presence of electrons in the rf sheath ($\alpha = 0.33$) and in the undisturbed plasma ($\alpha = 1$). ($T_e = 3.3 \text{ eV}$, $T_i = 0.026 \text{ eV}$, $n_e = 1.2 \cdot 10^{15} \text{ m}^{-3}$).

2.2.3 Charging time

After the injection of a dust particle into the plasma, it will charge up according to the ordinary differential equation

$$t < \alpha T_{rf} : \quad \frac{dQ_d}{dt} = I_i + I_e \quad (2.36)$$

$$t > \alpha T_{rf} : \quad \frac{dQ_d}{dt} = I_i \quad . \quad (2.37)$$

Here, the generalized case of a particle trapped in the rf sheath of a plasma is considered where the presence of electrons and thus quasi-neutrality is only given during a time phase of α times the rf period T_{rf} . If the particle is charged up in the bulk plasma $\alpha = 1$ and assuming the validity of the OML model, so that the charge currents are given by Eq. 2.24 and 2.26, Eq. 2.36 transforms to

$$\begin{aligned} \frac{dQ}{dt} = & -\pi r_d^2 n_e e v_{te} \exp\left(\frac{eQ_d}{4\pi\epsilon_0 r_d (1 + r_d/\lambda_D) k_B T_e}\right) \\ & + \pi r_d^2 n_i e v_{ti} \left(1 - \frac{eQ_d}{4\pi\epsilon_0 r_d (1 + r_d/\lambda_D) k_B T_i}\right) \quad , \end{aligned} \quad (2.38)$$

where the particle potential is substituted using Eq. (2.31). The charging with time t of a particle with $r_d = 1.74 \mu\text{m}$ is shown in Figure 2.6. In the case $\alpha = 0.33$ the particle's negative charge increases during one third of the rf period, since $n_i = n_e$ in the ambient plasma. During the remaining two third of the period the electrons are displaced from the sheath and the ion current discharges the particle again until the next electron flood. If the particles are trapped in the bulk plasma under constant quasi-neutral conditions $\alpha = 1$ the equilibrium charge reaches a much higher absolute value.

Regarding electron and ion currents separately, time constants $\tau_{i,e}$ analog to the discharging of a capacitor $Q(t) = Q_0 \exp(-t/\tau)$ can be extracted from Eq. 2.38:

$$\tau_x = 4\pi\epsilon_0 r_d \left(1 + \frac{r_d}{\lambda_D}\right) \frac{k_B T_x}{e} \frac{1}{\pi r_d^2 e n_x v_{tx}}, \quad (x = e, i) \quad . \quad (2.39)$$

The formula given by [65] was extended, here, with respect to the shielding of the particle charge according to the Debye-Hückel potential. Under the conditions outlined in Fig. 2.6, $\tau_i = 8.7 \mu\text{s}$ and $\tau_e = 0.4 \mu\text{s}$. Obviously, the charging process is dominated by the longer time constant τ_i . Because of $\tau_{i,e} \gg T_{rf}$, the equilibrium charge of a dust particle can be considered as constant even in the sheath. Nevertheless, dust dynamical phenomena take place on a time scale, that is determined by $(\omega_{pd})^{-1} \gg \tau_{i,e}$. Therefore the charge is adjusted instantaneously to the changing plasma conditions during particle motion.

2.2.4 Other charging mechanisms

Besides the current collection from the ambient plasma as discussed in the previous sections, a number of other charging mechanisms exists. Even if their importance is mainly given for astrophysical plasmas [52], the most common ones will be mentioned for completeness in the following.

Secondary Emission

When energetic electrons of the ambient plasma collide with or, for example in space, cosmic rays hit a negatively charged dust particle, secondary electrons may be released from the particle surface [66, 67, 68, 69]. The loss of negative charge can be considered as a positive current towards the particle. The emission probability depends on the electron energy and on the particle material [70]. For the combination of electron energies less than 7 eV and the emission capability of the plastic particles, which are used in the presented laboratory experiments, the effect can be neglected. Ions require an energy in the range of keV before their contribution to the charge by secondary emission becomes substantial [70].

Impact Ionization

Complementary to the charged plasma species, the neutral gas atoms can collide with the particle at a high energy. Here too, electrons can be released from the particle surface or the atom itself ionizes and donates electrons to the dust particle. While in the first case the change in net charge is positive, it can be negative in the second case. Impact ionization becomes important at high neutral gas densities and temperatures.

Photo Emission

Electrons can also be removed from the particle by incoming photons. If the photon transfers its energy $h\nu$ to an electron in the particle surface, so that the electron can overcome the extraction work function, the particle is discharged due to electron losses. Typically, photons with an appropriate energy are emitted by ultra-violet light sources. Generally the intensity of the UV-component of the spectral emission in dusty plasma laboratory experiments is too weak to play a role in dust charging mechanisms, but in astrophysical plasmas under the effect of direct stellar radiation the photo effect even generates positively charged dust [71, 72].

Stochastic Fluctuations

For nanometer sized particles, stochastic fluctuations must be taken into account. It has been found that the charge of a particle has a Gaussian distribution around the average charge over the time [73, 74, 54]. These fluctuations are a stochastic result of the discreteness of electric charge. The standard deviation of the charge distribution is proportional to $Q_d^{1/2}$. Thus, small particles which carry only a few tens or hundreds of elementary charges can be positively charged for a short time. For micrometer sized dust as it is used for this work and on the time scale of dust dynamics, the described effect is negligible.

Several other mechanisms can be considered that play a role on dust charging under extreme conditions, e.g., emission of electrons resulting from very strong gradients of the electric field at the particle surface [52], or charge removal by radioactive α - and β -radiation. Dust particle charging in the experiments presented in Chapter 3 is assumed to be only affected by currents consisting of the plasma species, namely electrons and ions.

2.2.5 Many-particle effects

Up to now, dealing with the charging mechanisms the dust particles have been regarded as single or at least separated ($d \gg \lambda_D$) objects in the electron-ion plasma, consisting of electrons and ions, where d is the mean interparticle distance. When the dust particle density n_d is increased and d is of the order of the Debye length, more and more charge is accumulated on the third plasma species, the particles. The quasi-neutrality condition then becomes for a three component plasma

$$n_e e - n_d Z_d e - n_i e = 0 \quad , \quad (2.40)$$

where Z_d is the mean net number of elementary charges on the particle. The signs in Eq. (2.40) show, that the positive charge of the ions is compensated by free electrons and electrons bound to the dust grains. Due to typical conditions in laboratory plasmas, the particles are assumed to carry a negative charge. When

a high dust density concentrates a large amount of negative charge to a certain volume, the space charge potential in this volume increases negatively. Then, the free electron density is depleted, because a substantial part of electrons is bound on the particles. Thus, the negative charging current on the dust grains is affected and the particle potential ϕ_d is shifted to less negative values. This model has been proposed by Havnes *et al.* [15, 75] for astrophysical plasmas and was adopted to laboratory conditions by Goree [74]. If the undisturbed plasma potential outside the dust cloud is taken as $\phi_{p\infty} = 0$, then the charge-carrier density in the dusty plasma region with reduced (negative) space potential ψ is determined by the Boltzmann factor

$$n_e = n_{e\infty} \exp\left(\frac{e\psi}{k_B T_e}\right), \quad n_i = n_{i\infty} \exp\left(-\frac{e\psi}{k_B T_i}\right). \quad (2.41)$$

The charging of the particle shall be still given by OML currents. Substituting the densities in Eq. (2.27) with $n_{e,i}$ from Eq. (2.41) and keeping in mind $n_{e\infty} = n_{i\infty}$, gives

$$\exp\left(-\frac{e\psi}{k_B T_i}\right) \left(1 - \frac{T_e}{T_i} \frac{e\phi_d}{k_B T_e}\right) = \sqrt{\frac{m_i T_e}{m_e T_i}} \exp\left(\frac{e\psi}{k_B T_e}\right). \quad (2.42)$$

Using the vacuum solution $Z_d/e = Q_d = 4\pi\epsilon_0 r_d \phi_d$ which is valid for $r_d \ll \lambda_D$, the quasi-neutrality condition Eq. (2.40) can be written as

$$\exp\left(\frac{e\psi}{k_B T_e}\right) - \exp\left(\frac{e\psi}{k_B T_i}\right) - \frac{n_d}{n_{e\infty}} \frac{4\pi\epsilon_0 r_d}{e} \phi_d = 0. \quad (2.43)$$

The last coefficient on the left side is defined as

$$P \frac{e}{k_B T_e} \equiv \frac{n_d}{n_{e\infty}} \frac{4\pi\epsilon_0 r_d}{e}. \quad (2.44)$$

P is known as the Havnes reduction parameter and can be interpreted as a measure for the ratio of charge, that is bound on the particles, to the charge of free electrons.

Solving Eqs. (2.42) and (2.44) numerically yields the particle potential ϕ_d and the deviation from the dust-free plasma potential ψ from a given reduction parameter as plotted in Fig. 2.7. With increasing P the fraction of charges located on the dust surface is increased, while the space potential is supposed to decrease. The side effect of electron depletion results concurrently in a discharging of the particles.

A very high dust density in a low power rf discharge can cause a high value of P , so that even if only a few electrons are still found on the particles, the number of free electrons is so small that ionization and thus plasma production becomes insufficient. The plasma then collapses.

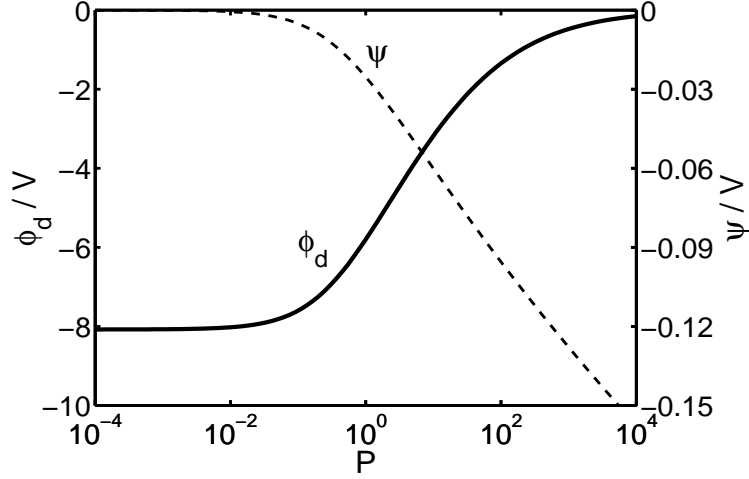


Figure 2.7: Particle potential ϕ_d and deviation ψ from the dust-free plasma potential as function of the reduction parameter P that characterizes the charge distribution in a complex plasma. Electron and ion temperatures are the same as in Fig. 2.6.

2.2.6 Coulomb coupling

The ability of a micrometer sized particle to carry typically 10^3 to 10^5 elementary charges in a laboratory plasma manifests in phenomena, that are related to particle-particle interaction. The electrostatic energy $E_{el}(d)$ between two similar grains separated by the distance d in a plasma is given by the Debye-Hückel law

$$E_{el}(d) = \frac{Q_d^2}{4\pi\epsilon_0 d} \exp\left(-\frac{d}{\lambda_D}\right) \quad . \quad (2.45)$$

To minimize the electrostatic energy the highly charged particles tend to generate ordered structures. This trend is opposed by the particles' kinetic energy, which can be approximated by the dust temperature T_d

$$E_{th} = \frac{1}{2} m_d \overline{v_d^2} = \frac{3}{2} k_B T_d \approx k_B T_d \quad . \quad (2.46)$$

The ratio of the Coulomb energy to the kinetic energy of a particle system is defined as the coupling parameter

$$\Gamma = \frac{E_{el}}{E_{th}} = \frac{Q_d^2}{4\pi\epsilon_0 d} \frac{1}{k_B T_d} \exp\left(-\frac{d}{\lambda_D}\right) \quad . \quad (2.47)$$

When $E_{el} \gg E_{th}$ the dust particle system is strongly coupled ($\Gamma \gg 1$) and it condenses in liquid or solid phases. The solid phase is known as dust crystal [76, 77, 78]. Critical values of Γ and the screening strength $\kappa = d/\lambda_D$ for crystallization in face-centered-cubic or body-centered-cubic structures have been provided for strongly coupled systems [79, 80, 81].

A weakly coupled complex plasma is indicated by $\Gamma \ll 1$ and a gaseous phase of the particle ensemble. Due to their small charge, weak coupling is also given for the plasma electrons and ions.

2.3 Forces on dust particles

Dust particles that are injected into a plasma obtain a high charge and can be trapped inside the discharge. Various forces acting on the particles are responsible for the motion of dust grains and the local equilibria, where they are balanced. Especially the electric force can overcome the gravity and prevents particles from leaving the plasma. This section gives an overview of the most important forces. In particular, the common models describing the ion drag force will be discussed. Further on, the final section will be focused on the force equilibria, that confine and arrange the particles under laboratory conditions and under microgravity.

More details on the variety of forces are given in [65, 82]. For the discussion of forces, separated spherical particles are assumed. Coagulation of two or more particles in the experiment is mostly suppressed by the method of particle injection (see Section 3.1.3).

2.3.1 Gravity

Without changing to an appropriate non-inertial reference system, in which the gravitational force does not appear, all experiments and thus the dust particles in the plasma underlie the acceleration $|\vec{g}| = 9.81 \text{ m/s}^2$ in the gravitational field of the Earth. With the material dependent mass density ρ_d a spherical particle of radius r_d is subject to the gravitational force

$$\vec{F}_g = m_d \vec{g} = \frac{4}{3} \pi r_d^3 \rho_d \vec{g} \quad . \quad (2.48)$$

For particles of the same material the force scales with the third power of the particle radius. As a result, the size distribution of the particles has a strong influence on equilibrium positions. For nanometer sized particles gravity plays a minor role, while it is the dominant force concerning micrometer sized particles. For the particles mostly utilized here (see Section 3.1.2) of $r_d = 1.74 \text{ } \mu\text{m}$, $|\vec{F}| = 3.3 \cdot 10^{-13} \text{ N}$. Methods to overcome the dominance of gravitational force are described in Section 3.2.1.

2.3.2 Neutral gas friction

Gas friction is based on the momentum transfer from neutral gas atoms to the dust particle. The gas drag is only present when the particle is moving with respect to gas background. The front side of the dust grain then, in average, experiences a higher momentum transfer from colliding gas atoms than the back side, due to the enhanced relative atom-grain velocity. Therefore the net momentum transfer is opposite to the relative particle velocity \vec{v}_d and the particle is slowed down.

Assuming the absorption of all neutral atoms colliding with the particle and $|\vec{v}_d| \ll v_{tn}$, yielding the gas atom's kinetic energy $E_{kin} \approx m_n v_{tn}^2 / 2$, the average transferred momentum per atom is

$$p_n = m_n \sqrt{\frac{2E_{kin}}{m_n}} = m_n v_{tn} \quad , \quad (2.49)$$

where m_n and v_{tn} are the mass and average thermal velocity of the neutral gas atoms. The product of the momentum and the flux on the particle cross section $\sigma_d = \pi r_d^2$ estimates the neutral gas friction (the neutral gas drag is written with the opposite sign),

$$\vec{F}_n = -p_n n_n \vec{v}_d \sigma_d = -\pi r_d^2 m_n n_n v_{tn} \vec{v}_d \quad . \quad (2.50)$$

n_n is the number density of neutral atoms.

Since the assumption of general absorption of the atoms is arbitrary, Epstein [83] has studied the statistics of collisions with the particle surface in dependence on the type of reflexion – radial, specular or diffusive – the colliding atom experiences with the grain. He obtained the neutral gas friction as

$$\vec{F}_n = -\delta \frac{4}{3} \pi r_d^2 m_n n_n v_{tn} \vec{v}_d \quad . \quad (2.51)$$

The Millikan coefficient δ includes the type of atom reflection and $1 \leq \delta \leq (1 + 4/9)$. Introducing the friction or Epstein coefficient

$$\beta_{fric} = -\delta \frac{8}{\pi} \frac{p_{gas}}{\rho_d r_d v_{tn}} \quad , \quad (2.52)$$

the friction force can be transformed to give

$$\vec{F}_n = -m_d \beta_{fric} \vec{v}_d \quad . \quad (2.53)$$

p_{gas} represents the neutral gas pressure. While the friction coefficient is reduced with increasing particle size, the resulting neutral gas friction is increases with r_d^2 .

The most important role of the gas friction can be found in the damping of dust dynamic phenomena, for example of stimulated particle oscillations in the sheaths or dust waves [5, 34, 61, 84].

Especially under microgravity conditions when the gravitational force as dominant effect is removed, the gas drag, produced by the gas flow from gas inlet to pumping port of an experiment, often appears as a undesired force that breaks the symmetry of a particle arrangement in the discharge. A way out to observe subtle forces is to seal the vacuum chamber at the targeted gas pressure for the duration of the measurement or to use a special chamber design that cares for symmetrical low gas flow (see Section 3.1.1).

2.3.3 Thermophoretic force

The thermophoretic force on a dust particle results, analogous to the friction force, from an asymmetry of momentum transfer to the particle due to neutral gas atom collisions. In this case the relative particle velocity to the background gas is assumed to be $\vec{v}_d = 0$ and a temperature gradient $\vec{\nabla}T$ is considered to exist in the gas. Because of the non-uniform temperature, the particle “sees” a hot and cold side. Atom impacts from the hot side transfer more momentum, since the kinetic energy is higher than on the cold side. Hence, a net force in

direction of the heat flux is exerted on the particle, that becomes important for micrometer sized grains, when $\vec{\nabla}T$ is of the order of a few Kelvin per meter [82, 85, 86, 87, 88, 89]. Rothmel *et al.* [90] have compared the expressions for the thermophoretic force \vec{F}_{th} , as they have been provided by several authors. With the thermophoretic levitation of particles, they proved the suitability of

$$\vec{F}_{th} = -\frac{8}{3} \frac{r_d^2}{v_{tn}} \Lambda \vec{\nabla}T \quad (2.54)$$

for the utilization under conditions similar to that in the experiments performed for this work. For argon gas, the translation heat conductivity at 293 K is $\Lambda = 0.016 \text{ WK}^{-1}\text{m}^{-1}$ [90].

In low pressure rf discharges ions are assumed to have approximately “room temperature” (see Section 2.1). Additionally, the ionization rate n_e/n_n at low rf power is of the order of 10^{-7} . Therefore, the energy transferred from the few ions to the neutral gas atoms is small. Plasma simulations for the PKE experiment [22] show, that under typical discharge conditions the deviation from the ambient temperature in the central plasma is $\approx 1 \text{ K}$. The resulting force is then negligible compared to the electric field force and the ion drag which will be discussed below.

An interesting application of the thermophoresis is the compensation of the gravitational force with an externally generated temperature gradient [90].

2.3.4 Electric field force

Due to the charge Q_d of a dust particle, a Coulomb force

$$\vec{F}_E = Q_d \vec{E} \quad (2.55)$$

is exerted on it in an external electric field \vec{E} . Since Q_d is approximately linear in the particle radius r_d (see Section 2.2), the field force increases with r_d . Although the electric fields in the quasi-neutral bulk plasma are small, \vec{F}_E becomes the dominant force in the plasma sheath, where strong electric fields exist (refer to Section 2.1.1). Considering a sheath electric field of $|\vec{E}| = 5000 \text{ V/m}$ and $|Q_d| = 6000e$, the Coulomb force $|\vec{F}_E| = 4.8 \cdot 10^{-12} \text{ N}$ and noticeably overcomes the gravitational force. The same particle in a quasi-neutral plasma region with $|Q_d| = 10000e$ and an estimated residual electric field $|\vec{E}| \approx 150 \text{ V/m}$, yields $|\vec{F}_E| = 2.4 \cdot 10^{-13} \text{ N}$. Thus, under gravity, micrometer sized particles can only be trapped in the sheath or presheath of a discharge.

Equation (2.55) has been used without taking care that the particle is not embedded in a vacuum, but in a plasma shielding the particle’s charge. In an external electric field, the charges on the particle surface and the shielding charges in the Debye sphere around the particle are polarized and form a dipole. Daugherty *et al.* [91] included the additional dipole force as a second term in the electric field force and obtained

$$\vec{F}_E = Q_d \vec{E} \left[1 + \frac{(r_d/\lambda_D)^2}{3(1 + r_d/\lambda_D)} \right] \quad (2.56)$$

Under the usually fulfilled condition $r_d \ll \lambda_D$, Eq. (2.56) approaches Eq. (2.55). The important result is that although the plasma ensures its quasi-neutrality by shielding the particle, it does not shield it from external electric fields. This result have been confirmed by Hamaguchi *et al.* [92]. Further on, Eq. (2.55) is used.

2.3.5 Ion drag force

In analogy to the neutral drag force, a relative velocity between ions and charged dust grains causes a force on a particle due to momentum transfer such that streaming ions can accelerate the particle, thus an ion drag is present, or a moving particle is slowed down as consequence of ion friction. The difference compared to the neutral drag manifests in two points:

- The cross section for ion impacts on the particle is larger than the geometric cross section, since the positive ions are attracted by the negatively charged dust grain.
- Due to the attractive Coulomb interaction, momentum transfer is also possible when passing ions do not collide with the particle.

In general, these two mechanisms are referred to as the collection force F_c and the orbit force F_o [49], the sum of which is the ion drag force $F_i = F_c + F_o$. In order to keep the scattering problem of F_o manageable, simplifications have to be made: An isolated dust particle is considered, i.e. the distance between two dust particles d is large compared to the Debye length, $d \gg \lambda_D$. Hence, no distortion of the grain charge and the surrounding Debye sphere has to be taken into account. Wake-field effects [93, 94] are neglected. The ion mean free path $\lambda_{mfp} \gg \lambda$, so that the ion motion is collisionless for the time of interaction with the particle and $r_d \ll \lambda_D$.

Despite the listed simplifications, additional approximations are necessary to derive an analytical expression for the ion drag force. The discussion concerning the orbit force [49, 59, 95, 88, 82] is still far from being settled [50, 28, 29]. Thus, to cover the broadness of contributions to this topic, the widely used standard approach of Barnes *et al.* [49] and a recent model of Khrapak *et al.* [50] will be introduced in the following.

The “Barnes formula”

Bearing in mind the effective collection radius b_c (Eq. 2.23) of ions from OML currents in Section 2.2.1, the enhanced cross section σ_c for the *collection force* is already known,

$$\sigma_c = \pi b_c^2 = \pi r_d^2 \left(1 - \frac{e\phi_d}{E_{kin}} \right) . \quad (2.57)$$

E_{kin} is the kinetic energy of the approaching ion with impact parameter b_c . With the averaged transferred momentum $p_i = m_i \sqrt{2E_{kin}/m_i}$ the collection force can

(analogously to Eq. (2.50)) be written as

$$\vec{F}_c = p_i n_i \vec{v}_i \sigma_c = \pi r_d^2 m_i n_i \sqrt{\frac{2E_{kin}}{m_i}} \vec{v}_i \left(1 - \frac{e\phi_d}{E_{kin}}\right) . \quad (2.58)$$

For a monoenergetic ion distribution, like an idealized ion beam, $E_{kin} = m_i v_i^2/2$, where v_i is the relative velocity to the dust particle. To give an approximate formula for a more general distribution function, Barnes *et al.* [49] identified E_{kin} as in Eq. (2.15), and obtained

$$\vec{F}_c = \pi r_d^2 m_i n_i v_s \vec{v}_i \left(1 - \frac{2e\phi_d}{m_i v_s^2}\right) . \quad (2.59)$$

It shall be mentioned that, to derive a more exact expression, the momentum transfer must be integrated over the real ion velocity distribution. This approach is followed in the discussion of Khrapak's model [50].

The momentum transfer by scattered ions in the electric field of the dust particle is the origin of the *orbit force*. Numerical methods are obligatory to calculate the momentum cross section of the orbit force [95, 96] for a screened Coulomb potential. For $r_d \ll \lambda$ it is a reasonable assumption to consider the potential $\phi(r)$ close to the particle $r < \lambda_D$ as approximated by the classical Coulomb potential and to cut off the potential curve at λ_D , hence $\phi(r > \lambda_D) = 0$. This is justified, since ions with impact parameter $b > \lambda_D$ experience only the mostly screened particle charge and their deflection in the residual field is weak. Thus, their contribution to the transferred momentum is small and can be neglected. This kind of potential is known as cut-off Coulomb potential with cut-off radius $b_{max} = \lambda_D$. The orbit cross section is then given by integration over the impact parameters, that do not result in a collection of the ion ($b > b_{min} = b_c$), but still contribute a substantial momentum exchange to the particle by deflection ($b < b_{max} = \lambda_D$) (see [55, 97]).

$$\sigma_o = 4\pi \int_{b_{min}}^{\lambda_D} \frac{b_{max}}{1 + (b/b_{\pi/2})} db . \quad (2.60)$$

The concept of a cut off-radius for the upper limit is essential, because the integral diverges for an infinite upper limit. $b_{\pi/2}$ is the Coulomb radius, which represents the impact parameter, that results in a $\alpha = \pi/2$ deflection angle (compare with Fig. 2.3) of the scattered ion trajectory. Estimating the interaction time $t = b_{\pi/2} v_i^{-1}$ during which the average Coulomb force F_E is exerted on an ion in the field of the dust particle and assuming that for large deflection angles α the momentum loss of the ion is total yielding $\Delta p_i = m_i v_i$,

$$m_i v_i = F_E t = -\frac{Qe^2}{4\pi\epsilon_0 b_{\pi/2}^2} \frac{b_{\pi/2}}{v_i} \Rightarrow b_{\pi/2} = -\frac{Q_d e}{4\pi\epsilon_0 m_i v_i^2} . \quad (2.61)$$

The type of the scattering interaction and the validity of the cut-off Coulomb approximation is often defined by the dimensionless parameter $\beta = b_{\pi/2} \lambda_D^{-1}$.

When $\beta \ll 1$, all large-angle deflections take place within the Debye sphere around the particle, where the ions can be considered to see the bare Coulomb potential. In this case the use of the cut-off Coulomb potential is additionally reasonable, since the neglected interaction of ions with $b > \lambda_D$ is weak. Thus, $\beta \ll 1$ is referred to as the “weak-interaction type”. The strong interaction case $\beta \gg 1$ is characterized by momentum transfer from ions from outside the Debye sphere. Here, the potential approximation with an unscreened Coulomb distribution and especially the use of the linearized Debye length as cut-off radius is extremely questionable.

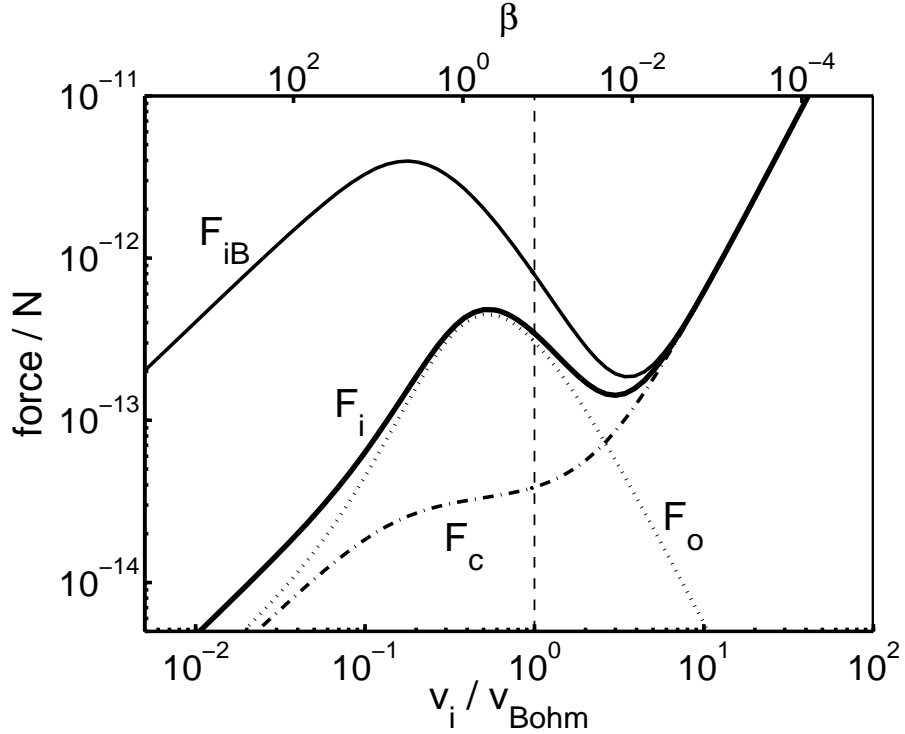


Figure 2.8: Orbit force F_o , collection force F_c , and the total ion drag force F_i vs. ion speed v_i and β after [49]. For F_{iB} the linearized Debye length as cut-off radius is substituted by the electron Debye length. The calculation is performed for a particle with $r_d = 1.74 \mu\text{m}$ and a fixed charge of $10500e$ at a plasma density of $n_i = 1.2 \cdot 10^{15} \text{m}^{-3}$.

Solving the integral in Eq. (2.60) for the unscreened potential yields

$$\sigma_o = 4\pi b_{\pi/2}^2 \Gamma \quad , \quad \Gamma = \frac{1}{2} \ln \left(\frac{b_{max}^2 + b_{\pi/2}^2}{b_{min}^2 + b_{\pi/2}^2} \right) \quad . \quad (2.62)$$

It should be noted that a different choice for the integral limits in Eq. (2.60) can be easily included by substitution of $b_{max,min}$ in the Coulomb logarithm Γ . In close resemblance to the collection force (Eqs. (2.58) and (2.59)), the orbit force

is written as

$$\begin{aligned}\vec{F}_o &= p_i n_i \vec{v}_i \sigma_o \\ &= 4\pi b_{\pi/2}^2 m_i n_i v_s \vec{v}_i \Gamma = 2\pi b_{\pi/2}^2 m_i n_i v_s \vec{v}_i \ln \left(\frac{\lambda_D^2 + b_{\pi/2}^2}{b_c^2 + b_{\pi/2}^2} \right) .\end{aligned}\quad (2.63)$$

Orbit force, collection force, and the total ion drag force after [49]

$$F_{iB} = F_c + F_o \quad , \quad (2.64)$$

are plotted vs. the relative ion velocity and β for a dust particle of $3.47 \mu\text{m}$ diameter in Fig. 2.8. Obviously, the orbit force is the dominant part of the ion drag at subsonic ion velocities. In typical rf plasmas, the ion speed reaches the sound velocity v_B only in the sheath, because the bulk plasma provides only weak acceleration fields combined with a limited ion mean free path. Therefore, the collection force plays a role exclusively at plasma boundaries.

In Figure 2.8 the drag force for a Coulomb cut-off radius of $b_{max} = \lambda_{De}$ is provided additionally to demonstrate the strong dependence of the calculated force on the inherent assumptions. The ‘‘Barnes formula’’ is also in use with $b_{max} = \lambda_{De}$ (see the discussion of the ion drag below).

The model of Khrapak *et al.* (2002)

It is obvious from Fig. 2.8, that for high ion speeds or small β , the ion drag force is dominated by the collection force. For $\beta > 10^{-2}$ the orbit force determines the ion friction force and is strongly influenced for example by the choice of the cut-off radius. In contrast to the idea of the cut-off radius, that ion Coulomb collisions with $b > \lambda_D$ need not to be taken into account, Fig. 2.9 shows, that for $\beta > 1$ the distance of closest approach r_0 (see Fig. 2.3) of the ion to the dust grain can be quite well smaller than the Debye length, even if the impact parameter is considerably larger. Thus, using the cut-off radius with $b_{max} = \lambda_D$ will neglect a significant fraction of the momentum transfer.

In the approach of Khrapak *et al.* [50] all ions, that come closer to the grain than λ_D during the collision are taken into account, yielding the cut-off radius condition $r_0(b_{max}) = \lambda_D$. With respect to the concept of the enhanced OML collection radius (Eq. (2.23)), b_{max} , matching the previous condition, can be easily obtained. Analogously, considering an ion grazing an imaginary sphere of radius λ_D with the surface potential $\phi(\lambda_D) = Q_d/(4\pi\epsilon_0\lambda_D)$, Eq. (2.23) can be rewritten,

$$b_{max} = \lambda_D \sqrt{1 - \frac{e\phi(\lambda_D)}{E_0}} = \lambda_D \sqrt{1 + \frac{2b_{\pi/2}}{\lambda_D}} = \lambda_D \sqrt{1 + 2\beta} \quad , \quad (2.65)$$

where $E_0 = m_i v_i^2/2$ has been used. For $\beta \ll 1$, Eq. (2.65) reduces to the standard cut-off radius λ_D . Using the same definitions, the collection radius b_c transforms

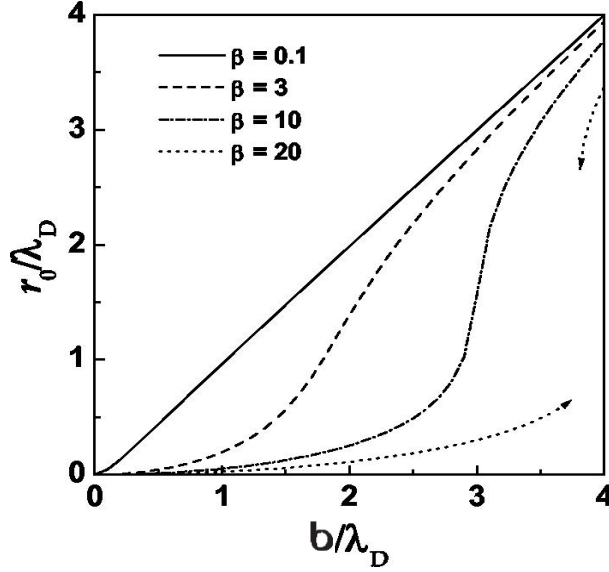


Figure 2.9: Numerical calculation of the ion distance of closest approach to the dust particle in dependence on the impact parameter b for a Debye-Hückel potential. For $\beta = b_{\pi/2}\lambda_D^{-1} = 13.2$ the effect of a potential barrier (see [96]) leads to a discontinuity in the curves. From [50].

to

$$b_{min} = b_c = r_d \sqrt{1 + 2 \frac{b_{\pi/2}}{r_d}} \quad . \quad (2.66)$$

Including the new b_{min} and b_{max} , the orbit force cross section (Eq. 2.62) becomes in Khrapak's model

$$\sigma_o = 4\pi b_{\pi/2}^2 \Gamma_K \quad , \quad \Gamma_K = \ln \left(\frac{\lambda_D + b_{\pi/2}}{r_d + b_{\pi/2}} \right) \quad . \quad (2.67)$$

Again, assuming the validity of the OML theory for ion motion, the cross section of the collection force has been chosen equal to that in Barnes' model [49].

Additionally refining the approach, the ion drag force F_{iK} is derived by integration over a given ion velocity distribution $f_i(\vec{v})$,

$$\vec{F}_{iK} = m_i \int_0^\infty \vec{v} v f_i(\vec{v}) (\sigma_c(v) + \sigma_o(v)) d\vec{v} \quad . \quad (2.68)$$

Gozadinos *et al.* [24] have simplified the general expression (2.68) given in [50] for the case of a shifted Maxwell-distribution,

$$f(\vec{v}) d\vec{v} = \left(\frac{m_i}{2\pi k_B T_i} \right)^{3/2} \exp \left(- \frac{m_i (\vec{v} - \vec{v}_i)^2}{2k_B T_i} \right) d\vec{v} \quad , \quad (2.69)$$

which is a reasonable assumption for subthermal ion flow – as well as disregarding the negligible contribution of the collection force, yielding $\sigma_c = 0$ in Eq. (2.68).

The integral then reduces to one dimension, providing the drag force in direction of the ion flow,

$$F_{iK} = \sqrt{\frac{2}{\pi}} \frac{n_i m_i}{v_T v_i} \int_0^\infty \sigma_o(v) v^3 \exp\left(-\frac{v^2 + v_i^2}{2v_T^2}\right) \left[\cosh\left(\frac{vv_i}{v_T^2}\right) - \frac{v_T^2}{vv_i} \sinh\left(\frac{vv_i}{v_T^2}\right) \right] dv, \quad (2.70)$$

where $v_T = \sqrt{k_B T_i / m_i}$.

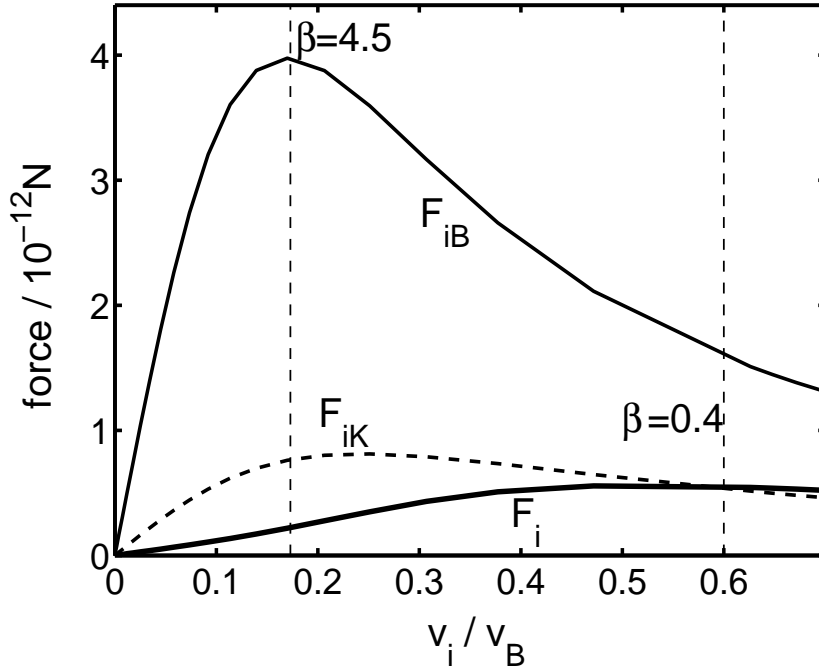


Figure 2.10: Comparison of the ion drag force after the Barnes model [49] for a cut-off radius $b_{max} = \lambda_D$ (F_i) and $b_{max} = \lambda_{De}$ (F_{iB}) and Khrapak's model [50] (F_{iK}) for subthermal ion velocities. In all three cases only the orbit force components are regarded. The conditions are similar to those given in Fig. 2.8.

Comparing the forces of Eqs. (2.70) and (2.63) in Fig. 2.10, F_{iK} overcomes F_i for very low ion speeds by a factor > 5 . For $v_i \approx v_B/2$, they are almost equal. F_{iK} is not approximately as large as the ion drag, using the ‘‘Barnes formula’’ with the electron Debye length as cut-off radius.

It should be noted that, for simplicity reasons, Khrapak *et al.* [50] still use a Coulomb potential to obtain their scattering cross section. Therefore and by comparison of their derived orbit cross sections with numerical data from [98] and [95], the authors limited the validity of the resulting ion drag formula to $\beta < 5$. In [96] a parameterization formula is given for slow ion drifts with $\beta > 13.2$. Here, potential barriers resulting from a high initial angular momentum of the ion and forcing it on orbits around the dust grain in a screened potential are taken into account. The model [96] has been compared with Barnes' model in [55].

Discussion

Both ion drag models, the “Barnes formula” [49] and the model of Khrapak *et al.* [50] are based on the approximation that the screened Coulomb potential surrounding a highly charged dust particle can be estimated by the standard Coulomb potential which is set equal to zero for distances to the grain larger than a cut-off radius b_{max} . The similarity of Coulomb and screened potential is reasonable for cut-off radii up to the screening length, namely the linearized Debye length λ_D [97]. Barnes *et al.* [49] have not specified, which (electron or linearized) Debye length they address. Since the screening length in a quasi-neutral plasma with ion drift velocities $v_i < v_{th,i}$ is given by λ_D , the Barnes’ approach fulfills the condition to use the Coulomb potential approximation, when using the linearized Debye length. Nevertheless, Kilgore *et al.* [95] had performed numerical simulations of the ion scattering cross section assuming a screened Debye-Hückel potential and found the results to be in a good agreement with the “Barnes formula” including the electron Debye length λ_{De} as cut-off radius. Since then, the model of Barnes is used with λ_{De} (e.g. [99]) – in contrast to the original idea of the cut-off Coulomb potential.

Additionally, experiments and simulations have demonstrated, that the Barnes model with λ_D does not explain the deflection of free falling particles in plasma column [100, 101] or the formation of a dust-free region (“void”) in the center of a discharge [22, 102], while the use of the electron Debye length does.

The model of Khrapak *et al.* [50] accounts for the possible large fraction of Coulomb collision with impact parameters $b > \lambda_D$, that are neglected in the Barnes force with $b_{max} = \lambda_D$, and therefore yields ion drag forces, that are, for low ion speed, a factor 5 to 10 higher than those of the Barnes model [49] and might be able to agree with the above mentioned experiments. Nevertheless, Khrapak’s model [50] is in conflict with the Coulomb potential approximation for $\beta \ll 1$ as well as the “Barnes formula” with $b_{max} = \lambda_{De}$.

The advantage to make allowance for a given real velocity distribution in Khrapak’s model, has the side effect of noticeable enlarged computation time. With respect to Fig. 2.11, where orbit force cross sections are plotted for different cut-off distances, it appears that the Barnes model can still serve as a fast approximation formula with results close to Khrapak’s expression, when used with the ion velocity dependent Debye length of Eq. (2.17) for a β of the order of unity. This will be shown to be the interesting β -range as it is found in the volume plasmas of the PKE and IMPF experiments in connection with the “void” formation (see Section 2.4).

Parameterization formulas obtained from numerically simulated scattering cross section have not been addressed here since the results of [95] are mostly covered by Eq. (2.67) or are not applicable [96] for the expected values of β .

In conclusion, it must be pointed out, that both discussed models suffer from the neglect of ion collisions and the influence of high dust densities which are evident in many complex plasma experiments. For example, Schweigert *et al.* [103] have shown in simulations that collisions can even lead to a negative ion

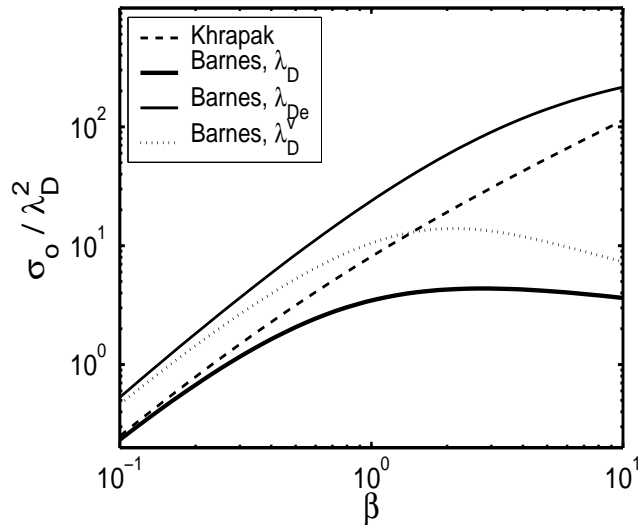


Figure 2.11: Orbit force scattering cross sections σ_o as used in the Barnes model [49] for cut-off radii $b_{max} = \lambda_D$, $b_{max} = \lambda_{De}$ and an ion drift velocity dependent cut-off distance $b_{max} = \lambda_D^v$ (see Eq. (2.17)) and from Khrapak’s model [50].

drag force. These features have not been included in any practicable ion drag expression up to now.

2.3.6 Ordering of the forces

The maximum neutral gas temperature and space potential in a typical capacitive rf discharge are reached in the center of the plasma. Therefore, all forces that depend on the gradients of these potentials act radially with respect to the geometry of the plasma. While the electric field exerts a force on the dust grains pulling them into the plasma, it accelerates the ions outwards, which on the other hand generates an ion drag in the same direction. The thermophoresis also drives the dust particles out of the plasma as it is shown in Fig. 2.12 (B). Only the gravitational force has a fixed direction for every particle in the discharge and can thus break the symmetry as long as its magnitude is comparable to F_i and F_E , and confine all grains in the bottom part of the plasma. It is obvious from Fig. 2.12 (A) that this feature is lost for $r_d \ll 1 \mu\text{m}$, since $F_g \propto r_d^3$. The dynamics of micrometer sized grains including the particles with $r_d = 1.74 \mu\text{m}$ that have been used in this work are determined by the dominant ion drag, electric field forces, and gravity (if present). The resulting equilibrium positions occupied by dust in the plasma is discussed in Section 2.4 in more detail. The thermophoretic force plays a minor role in a low temperature plasma.

2.4 Force balance and “voids”

Studies on forces on particles [101, 55] or on the influence of dust on the discharge [104] can be performed with particles falling through the plasma. But to observe

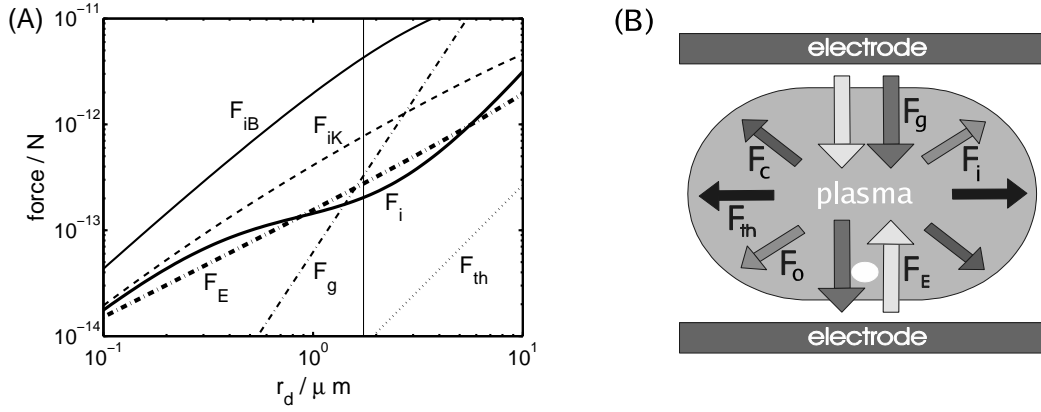


Figure 2.12: (A) Magnitude of forces on a dust particle inside an rf gas discharge versus particle radius. The vertical line marks the size of the grains ($r_d = 1.74 \mu\text{m}$) which have been mainly used in our experiments. The conditions $\nabla T = 25 \text{ K/m}$, $v_i = v_{ti}$, $n_e = 1.2 \cdot 10^{15} \text{ m}^{-3}$, $T_i = 0.026 \text{ eV}$, $|Q_d| = 10500e$ and $p_{\text{argon}} = 37.1 \text{ Pa}$ are possible values for the PKE experiment. (B) Directions of the forces (\vec{F}_E , \vec{F}_g , \vec{F}_{th} and $\vec{F}_{i,iB,iK} = \vec{F}_o + \vec{F}_c$) for the given conditions under gravity.

longer time scale dynamics like dust crystallization or oscillations of grains, a confinement of particles in the plasma is highly desirable. Certainly, large micrometer sized particles are easily observable, since the amount of scattered light is large and two particles are distinguishable due to their inter-grain distance. The problem is that their weight lets them sediment to the bottom of the experiment chamber. Nevertheless, because of $Q_d \propto r_d$ (see Eq. 2.35), large particles are more suitable to obtain a high Γ and thus, to yield dust crystallization (see 2.2.6). In a laboratory experiment with an electrode as lower boundary of the discharge like a typical capacitive rf discharge the gravitational force and the parallel ion drag force can be balanced by the electric field that reaches 10^4 V/m . In the lower sheath of an electro-positive plasma, the electric force on a negatively charged particle points upwards to the high potential region of the plasma (compare with Fig. 2.12). The opposing forces form a vertical potential well, which is to a good approximation parabolic [34, 78]. Minimizing their energy in the potential well, the trapped particles first fill up a single monolayer in a horizontal plane above the lower rf electrode. Depending on the chamber geometry, often an additional lateral confinement has to be applied in order to prevent the grains from being lost at the edge of the electrode. Increasing the number of particles, more layers appear but due to attractive wake-fields [94, 105] induced by the supersonic ion flow in the plasma sheath, the grains tend to line up in vertical chains. Thus the particle interaction in horizontal and vertical direction in the dust cloud is different and in the latter case asymmetric [93]. Plasma crystals are therefore known as flat, nearly two-dimensional systems.

To generate three dimensional particle arrangements, the particles have to be liberated from the narrow potential well in the non-equilibrium sheath region, which is possible by reducing the influence of gravity. For this purpose nanometric

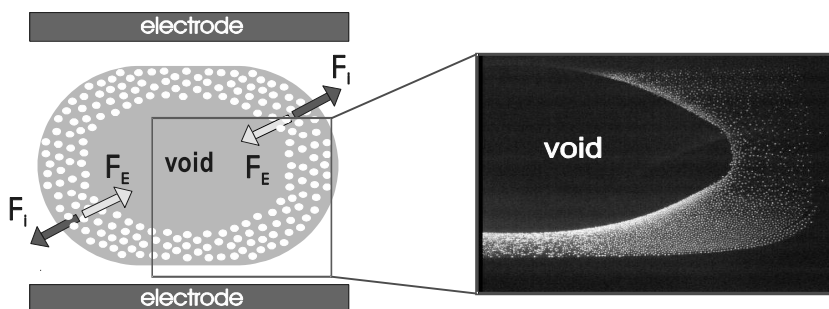


Figure 2.13: Scheme of the balance of electric field force and ion drag creating a dust-free region (“void”) in the central plasma. On the left side a video frame from the central meridional plane of the cylindrical PKE plasma chamber is shown.

particles have been used [30, 106, 107] for which gravity is negligible, or, keeping the advantages of large particles, experiments are performed under microgravity conditions [9, 10, 11, 12]. In both cases a “void” or void instability appears, when the dust can fill up the plasma volume. The void is a dust-free region with sharp boundaries, that is found mostly in the center of the discharge. The sharp boundary of the void comes along with a compression of the first dust particle layers, which yields particle stratifications [9] (see the following section). Goree [16] addressed the void phenomenon for collisionless ion motion, Tsytovich [108, 18] for the collisional case. The mechanism is so far understood that the electric field force pushing the particles towards the center of the plasma is position-dependent and weakest in the center of the plasma. The field force is then overcome by the ion drag force pointing in opposite direction radially outwards and creating a dust-free region (see Figure 2.13).

In a self consistent analysis of the process, the electron depletion as a result of charge bound to the particles in the dust cloud leads to an relatively enhanced ionization in the void and therefore amplifies the electric field at the void boundary. This may even result in the creation of double layers to match dust-free and dusty plasmas [13]. Some authors doubt the amplification process by enhanced ionization inside the void [16, 108].

Nevertheless, a quantitative description of the void phenomenon in real discharge geometries is only possible with numerical simulations [22, 24, 23], as they are introduced in Section 3.5. Akdim *et al.* [22, 23] demonstrated that the void creation cannot be explained with the standard Barnes model [49] for the ion drag but with the “Barnes formula” including the electron Debye length in the Coulomb logarithm. In the simulations of Gozadinos *et al.* [24], which neglect the dynamic process of void creation, it was shown that the void is stable with respect to the ion drag model of Khrapak *et al.* [50] and, in contrast to earlier findings that ionization must still occur inside the dust cloud.

Discharge conditions under which the void closes and dust structures can establish in the center of a plasma have been theoretically investigated in [17].

It is possibly a result of the few available experimental measurements of plasma parameters [109], or force gradients on test particles inside the void [110]

that the experimental proof of one of the theories is still pending. Therefore, the characterization of experimental, void developing complex plasmas with spatially resolved measurements is highly desirable.

2.5 Ordering of particles under external forces

The formation of ordered structures in a particle trap is one of the outstanding properties of complex plasmas. Thomson [111] already considered the behavior of charged particles in a confining potential with neutralizing background in his model of the classical atom. Similar strongly coupled Coulomb systems are known from various fields of physics. One well-known example are crystalline ionic systems in Paul [8] or Penning traps [112]. The advantage of complex plasmas in the study of Coulomb systems rests on the relatively simple experimental setups and observation methods. These systems range from small Coulomb clusters [113, 114] and linear chains [115] over large 2D [116] and 3D clusters [117] to crystalline arrangements with several thousand particles [76].

Being trapped in a potential well with a dissipative gas background, the kinetic or thermal energy of the charged particle ensemble is reduced. The potential energy due to Coulomb interaction then overcomes the kinetic energy and a coupling parameter $\Gamma > 1$ is obtained (see Section 2.2.6). For such a strongly coupled system further minimization of the total energy is preferably done by the optimization of inter-particle distances, yielding smaller Coulomb energy: the system becomes ordered. The type of the order is fundamentally affected by the geometry of the confining potential. Thus, for example, it has been experimentally [113, 116] and numerically [118, 119] demonstrated, that the radial confinement of 2D clusters induces the formation of outer circular particle rings to match the potential well. This behavior is also predicted by simulations [120] and observed in an experiment [117] in connection with 3D clusters, where the outer shell made of particles is spherical. The simplest configuration is represented by a one dimensional confining potential. Totsuji *et al.* [121, 122] assumed an infinite extension of a dust cloud in the x, y -plane, introducing periodic boundary conditions in their molecular dynamics simulations (see Section 3.5). The confinement of the Debye-Hückel system in the z -dimension is provided by an external parabolic potential well,

$$\phi_{ext} = \frac{1}{2}kz^2 \quad , \quad (2.71)$$

where k is the strength of the confining potential ϕ_{ext} .

At low dust temperatures T_d the authors found the arrangement of particles in parallel layers perpendicular to the external forces. This result is similar to that obtained for cooled ions in Paul traps [124]. The number of particle layers N was found to be only a function of two independent parameters ξ^* and η^* , as shown in Fig. 2.14. The first parameter is given by the ratio of mean inter-particle

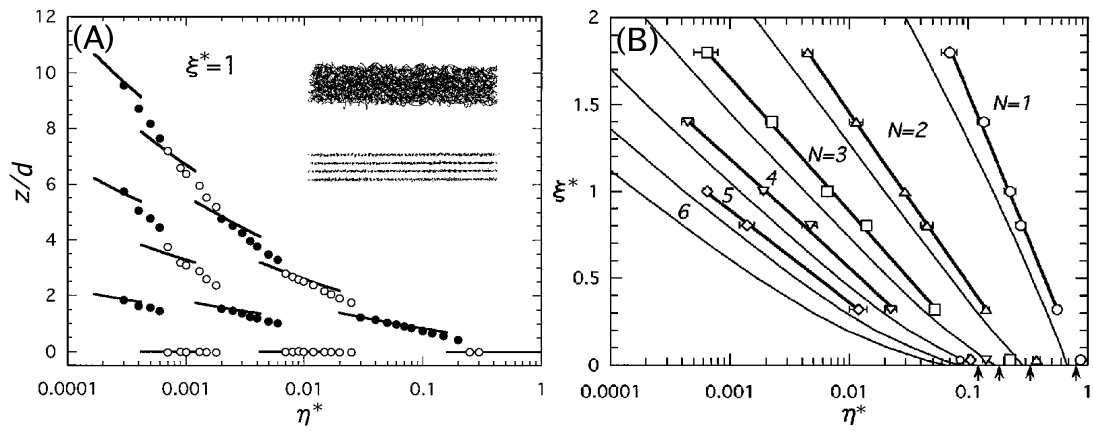


Figure 2.14: Position of particle layers in the z -dimension normalized to the mean particle distance d versus the confinement parameter η^* (A). Number of layers N as function of η^* and ξ^* (B). Symbols are results from simulations, thin lines are from the theory provided by Totsuji *et al.*. From [122]

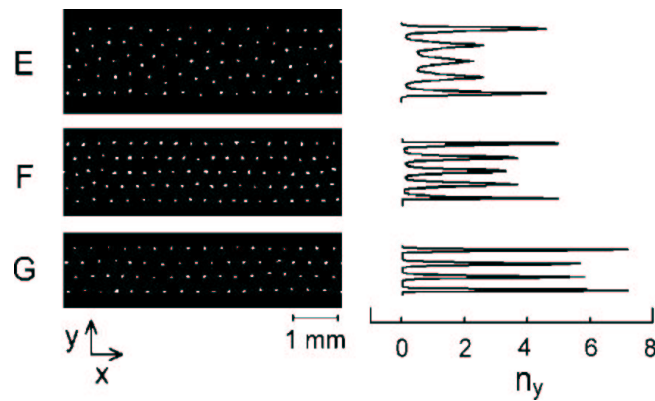


Figure 2.15: Experimental observation of a vertical confinement of a strongly coupled dusty plasma by wall of a narrow channel. The width between the walls has been reduced from the upper to the lower camera snapshot. The corresponding transverse particle density distributions (n_y) at the right side indicate the increasing formation of particle layers in the confinement. From [123].

distance d to the screening length,

$$\xi^* = \frac{d}{\lambda_D} = d\kappa \quad . \quad (2.72)$$

With respect to the confinement, another parameter is the ratio of potential energy related to the external particle trap kd^2 and the kinetic energy $k_B T_d$. As introduced in Section 2.2.6, the coupling parameter $\Gamma > 1$ defines a Coulomb system to be strongly coupled. Both parameters Γ and $kd^2/(k_B T_d)$ diverge at low temperatures – therefore, the second relevant parameter is defined as

$$\eta^* = \frac{\pi^{1/2}}{4} \frac{kd^2}{k_B T_d} \frac{1}{\Gamma^*} = \frac{\pi^{1/2}}{4} \frac{kd^2}{k_B T_d} \frac{4\pi\epsilon_0 dk_B T_d}{Q_d^2} = \frac{\epsilon_0 \pi^{3/2} d^3 k}{Q_d^2} \quad . \quad (2.73)$$

The arbitrary factor $\pi^{1/2}/4$ is inserted for consistency with previous work of the authors, $\Gamma^* = Q_d^2/(4\pi\epsilon_0 dk_B T_d)$ is similar to Γ , with removed dependency on ξ^* .

Teng *et al.* [123] have made the 1D confinement-induced layering visible by limiting the extent of a dusty plasma in a liquid state with a long and narrow mesoscopic channel. The increasing order of the confined particle cloud with reduced channel width is obvious from the transverse particle density distributions in Fig. 2.15.

The phenomenon of layer-like ordering under an external confinement is also known from colloidal suspensions [125] and on the nanometric scale from molecules in thin liquid films [126]. The latter, for example, plays a role in wear and lubrication processes on the atomic scale [127].

3 Experiment and diagnostics

3.1 Basic experimental setup

The experiments for this study have been performed in two different plasma discharge chambers, that represent different stages towards an optimized experimental setup on board the *International Space Station* (ISS). Both vacuum vessels, the PKE and the IMPF plasma chamber served as platform for experiments in our laboratory and under microgravity conditions on parabolic flights (2001 and 2003).

This chapter introduces the experimental setups and addresses some detailed issues concerning microgravity experiments. Special emphasis is given on the probe diagnostic systems. Besides the measurement methods, the discharge simulation is introduced as additional diagnostic method.

3.1.1 The PKE and IMPF plasma chambers

The PKE chamber

The *Plasma-Kristall-Experiment* (PKE) plasma chamber [9] has been originally developed by the *Max-Planck-Institut für extraterrestrische Physik* (MPE) in Garching and has since performed an impressive “career”. Starting with microgravity tests on several parabolic flights [10], it was operated by MPE on sounding rockets [9] and, in an cooperation of MPE and the *Institute for High Energy Densities* (IHED) in Moscow, became one of the first experiments aboard of ISS [12]. Studies on particle growth and dynamical dust behavior are described in [128] and simulations of physical processes in PKE geometry are reported for example in [22].

In a cooperation of MPE and our *Institut für Experimentelle and Angewandte Physik* (IEAP), the PKE experiment was flown on parabolic flights in November 2001 to test the first prototype of an optimized Langmuir probe system for low power dusty plasmas under microgravity conditions, that has been designed by our group and is described in Section 3.4.

PKE is a capacitively coupled rf discharge (see Section 2.1) with two identical size electrodes. The disk electrodes of $r = 20$ mm radius are mounted in the center with a gap of 30 mm. An active discharge is confined by a grounded guard ring, that is part of the base or top plate of the chamber. The walls are realized as a glass cuvette with square base area and a height of 54 mm, which allows the

illumination and observation of particles from all sides, as shown in Fig. 3.1. Due to the expected axial and vertical symmetry of dust arrangements in the plasma under microgravity the camera field of view is adjusted to cover at least one quarter of the inter-electrode space plus an overlap in center of the discharge. In order to scan the complex plasma in the y -dimension, camera and particle illumination laser are mounted on a motor driven translation stage (see Fig. 3.2). Details on the video observation system is provided in Section 3.3. Injection of

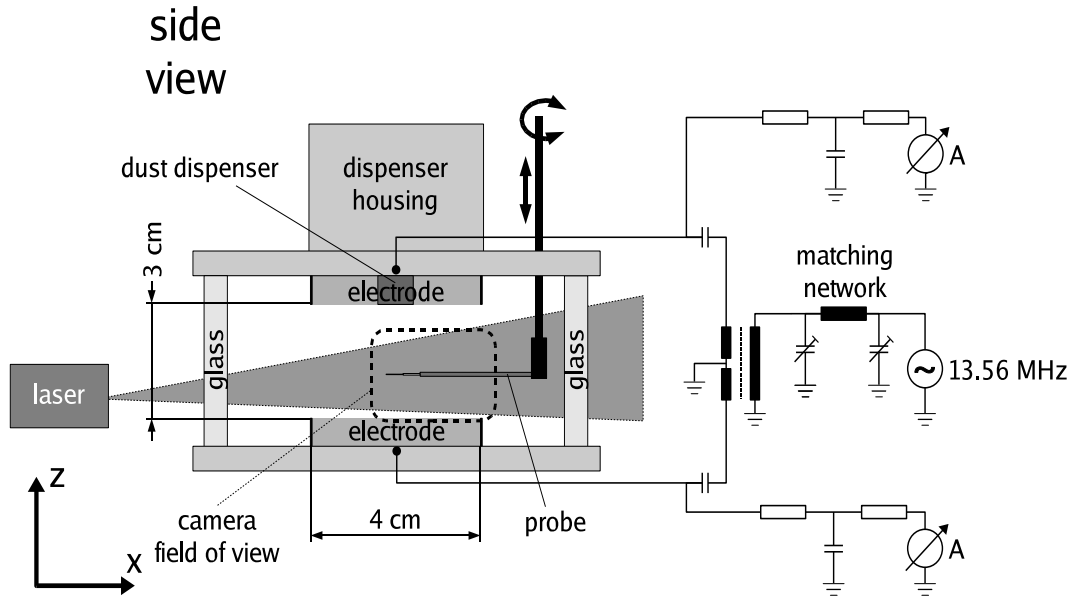


Figure 3.1: *Scheme of experimental PKE setup with Langmuir probe, illumination laser fan and generalized rf circuit.*

the dust particles (see Section 3.1.2) into the plasma is done by dust dispensers (see Section 3.1.3) through a sieve in the center of the electrodes. Since the lower dispenser has a small efficiency under gravity conditions in the laboratory, the chamber operated by the Kiel group includes only one dispenser in the upper electrode. Four flanges are integrated into the upper lid of the chamber, providing interfaces for the gas system, pressure gauges and diagnostics like the Langmuir probe. The rotatable and shiftable probe support is located in the front-right corner of the chamber, as can be seen in the side view (Fig. 3.1) and top view (Fig. 3.2) of the experimental setup. The probe itself is fixed with a miniature plug to a filter box, which is mounted at the end of a shaft, inserted into the chamber through a vacuum feed-through, forming a right angle with it. The probe-tip can be moved by stepper motors on circular arcs at different heights, that intersect the center of the discharge vessel, yielding a highly resolved 2D cross section of discharge parameters. The maximum speed of the probe-tip reaches 30 mm/s in vertical and 80 mm/s in the horizontal direction with sub-millimeter resolution. Therefore, in the limited measurement time of 20 s microgravity that is provided by parabolic flights, approximately 40 separate positions can be performed to acquire the local plasma parameters. During off-duty periods, the probe has a

parking position besides the upper electrode, where it does neither disturb the plasma nor the optical measurements.

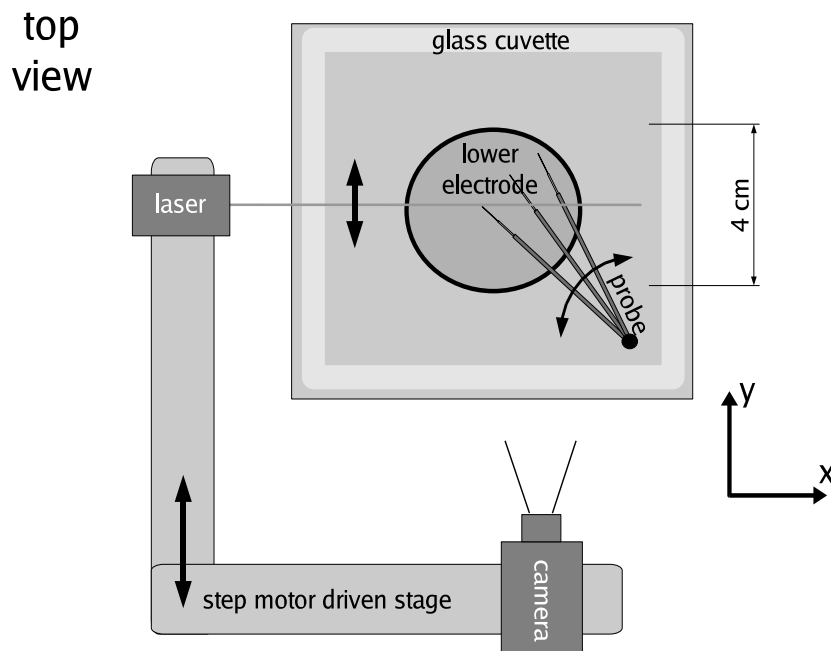


Figure 3.2: Top view into the open PKE chamber with visualized probe rotation. The illumination laser and the camera are fixed on a movable stage to allow scans in the y -direction through the discharge volume, in order to explore dust arrangements in three dimensions.

Argon has been chosen as the exclusively used working gas at pressures of (15...100) Pa. The discharge is driven by a 13.56 MHz rf signal in push-pull mode, with 180° phase-shift of the electrode voltages. This mode provides the highest electric fields between the electrodes and small time-averaged fields between plasma and grounded parts of the discharge vessel. The push-pull signals are supplied by a custom-made rf generator with tunable networks to match the generator impedance to the system of electrodes, plasma and additional shunting circuits. With applied rf voltages in the range of 50 V_{pp} to 120 V_{pp} the dissipated power in the plasma is typically a few hundred mW. The electrodes are connected to ground via a network that provides impedance termination for the rf generator as well as a DC path. Thus, self-biasing is avoided and the average electrode potential is then zero. The rf circuit is sketched in Fig. 3.1.

The IMPF chamber

The *International Microgravity Plasma Facility* (IMPF) is a planned experiment for studies on complex plasmas under microgravity conditions aboard ISS, in which several groups from a number of countries are involved. Due to its modular design several experimental inserts, based on rf and dc discharge vessels, will be

operated during the lifetime of the facility. IMPF will become part of a larger IMPACT (*International Microgravity Plasma, Aerosol and Cosmic Dust Twin*) facility, which shares part of the infrastructure with the ICAPS (*Interactions in Cosmic and Atmospheric Particle Systems*) experiments.

The plasma chamber, used on the second parabolic flight campaign for this work, is an early prototype of an rf chamber, which is intended to be used in the first experimental insert of IMPF. Therefore, this chamber will be referred to as “IMPF chamber”. This chamber was provided by *Kayser-Threde*, Munich, an industry contractor of the IMPF project. The IMPF chamber has been flown as part of experimental setup designed by our group on parabolic flights in June 2003.

Similar to PKE, the IMPF plasma chamber is a capacitively coupled discharge device with two opposing electrodes of circular symmetry at a separation of $d = 30$ mm. In more detail, each of the electrodes consists of a center disk and a ring electrode, which can be individually operated. The center disk has 55 mm diameter and the ring electrode 80 mm outer diameter (compare with Fig. 3.3 and 3.4). Each electrode pair, the rings and the disks, are operated by their own rf generator in push-pull mode. To ensure a fixed phase relationship of the rf signal of the disk or ring electrode, the two generators are synchronized. Due to the unavoidable capacitive coupling of the disk-ring arrangement, the maximum rf amplitude ratio of center to ring electrode is approximately 1 : 3 (or 3:1) at typically chosen signals of $U_{rf} = (30 \cdots 100) V_{pp}$. In analogy to PKE, self-biasing of the electrodes is suppressed by termination networks. The four electrode system allows the modification of the radial shape of plasma properties, as presented in Section 5.3.

The vacuum vessel itself is made of a stainless steel ring-shaped body-section and the upper and lower lids, in which the electrodes, the gas inlet, pressure gauge and pump flanges are integrated. Following a concept, that was introduced with the design of the Kiel experiment “Kleiner Topf” [129] in 1996, the four windows are flush mounted on the body section. The size of the windows matches the projected inter-electrode space and allows the illumination and observation of particles in the plasma for rectangular geometry. In order to visualize the global arrangement of the dust as well as to study the distance of only a few neighboring particles, two cameras with different fields of view have been installed. Again, the optical system, cameras, the particle illumination laser and further components, are mounted on a stepper motor driven translation stage to make scans in the y -dimension of the plasma volume, what allows the reconstruction of the three-dimensional dust arrangement in the plasma (see Fig. 3.4). Minimizing the laser reflections in the metal chamber and still illuminating the whole inter-electrode space, that is observed by the large-field-of-view camera, the laser fan has been parallelized by a cylindrical lens, thus providing a rectangular light curtain.

The body section of the vessel comprises also of four multi-purpose ports for mechanical access, that are arranged between the windows. During the measurement campaign, two of the ports hosted dust dispenser for two different particle sizes and a third carried the probe housing. The probe drive is again a special

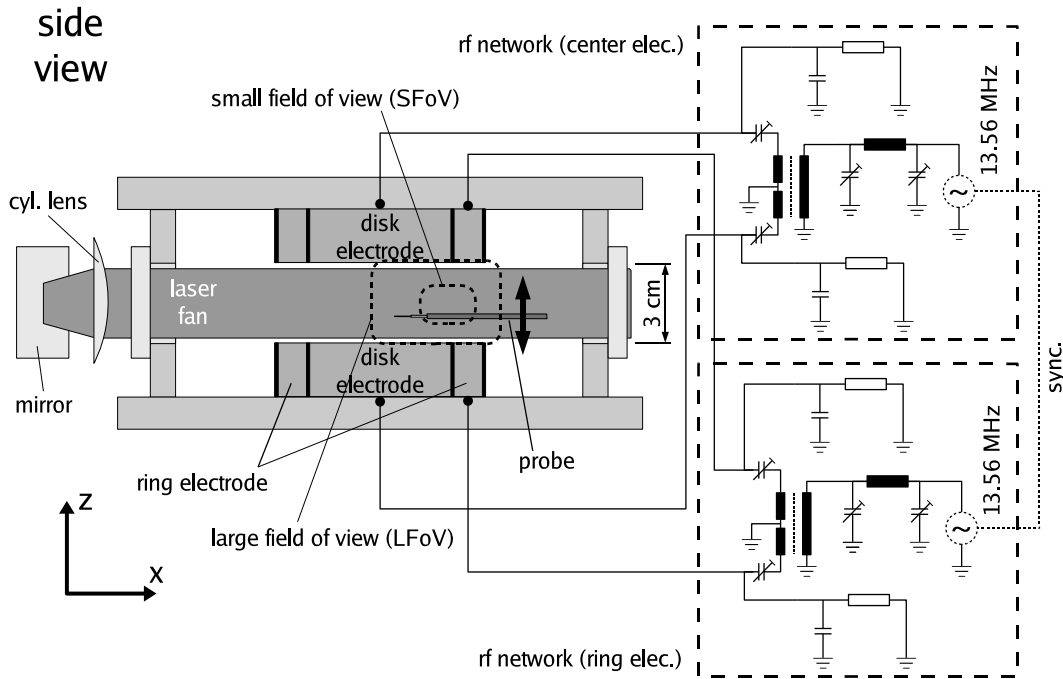


Figure 3.3: Side view of a cross section sketch of the IMPF chamber. Each pair of the disk-ring electrode system has its own rf network, allowing to supply ring and center electrodes with different rf voltages. Two viewing areas are recorded by the cameras.

design of the Kiel group to fit the constraints given in the restricted space conditions in a space station experiment. Unlike the design solution for PKE, the stepper motors and the 2D positioning stage are placed in a separated probe housing, which is attached to the IMPF chamber and therefore becomes part of the vacuum system. Therefore, no wearing parts, like a mechanical vacuum feed through, are needed. Being radially movable to the center of the chamber and 30 mm in z -direction, the probe can scan half of a two-dimensional cross section of the discharge, which, due to the axial symmetry, is representative for the whole plasma. Due to the different mechanical realization, the probe drive is slightly slower than the PKE system, but it still allows to record probe data on a 2D plane during parabolic flights maneuvers. The maximum speed of the probe is approximately 30 mm/s for both axis, again with sub-millimeter resolution. For optical measurements the probe is completely retractable into its housing.

Some of the special requirements which the experimental design has to fulfill to approve for parabolic flights, are listed in Section 3.2.2.

Gas system

The discharge in the IMPF microgravity experiment is an argon plasma with neutral gas pressures of $(15 \cdots 100)$ Pa. During the operation time of the experiment, an increasing amount of the plastic dust particles is deposited in the chamber and carbon and oxygen compounds are released into the working gas due to sputtering

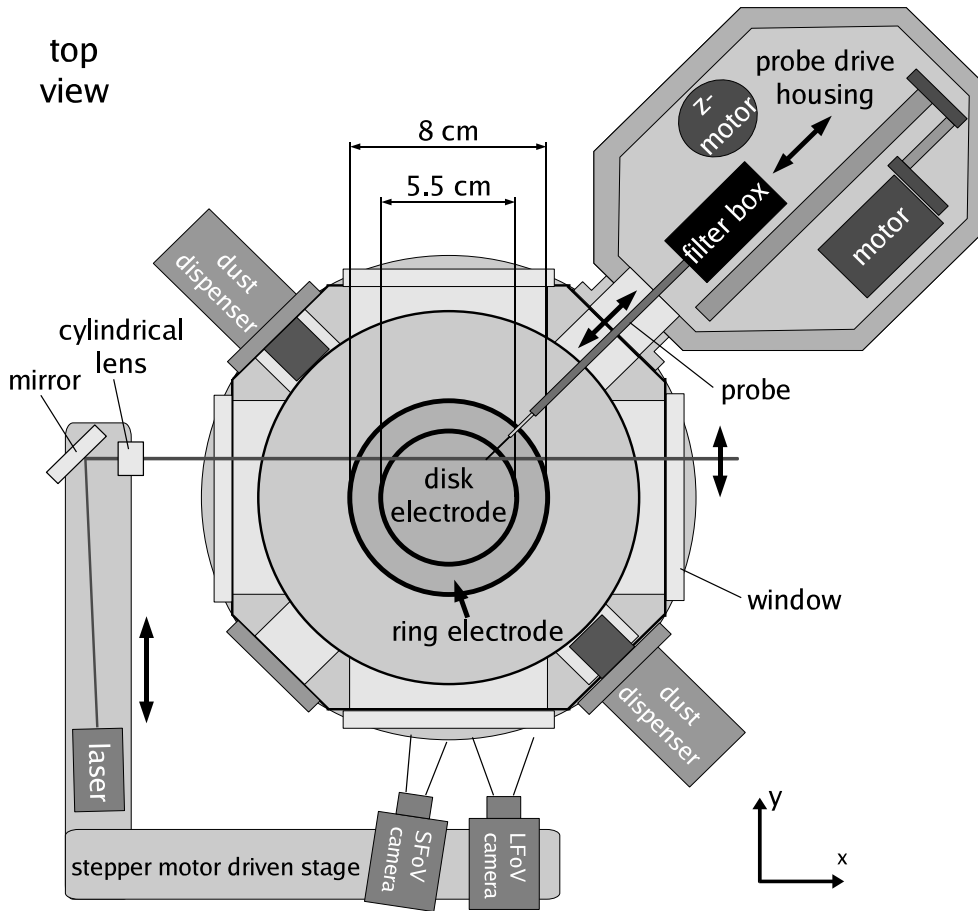


Figure 3.4: Sectional view into the IMPF plasma chamber with its ring electrode system. Cameras and laser are fixed on a motor driven stage. The probe drive is located in separated vacuum chamber being flanged to the IMPF vessel (the probe housing is only partly shown). For off-duty cycles the probe is fully retractable from the discharge chamber.

of the particles. To avoid the contamination of the argon atmosphere, the gas is refreshed at a low flow rate of approximately 0.25 sccm and a target pressure of 20 Pa. This gas flow is realized by pumping through an adapted bypass consisting of a thin tube (compare with Fig. 3.5). For pump down of the vessel the bypass valve can be opened.

When particles are trapped in the plasma, changes of the neutral gas pressure are possible with closed bypass valve only. Otherwise the neutral drag (see Section 2.3.2) of the gas flow removes all particles from the plasma. It turned out during microgravity experiments, that even a low gas flow has a severe influence on the particle arrangement. The dust cloud was still confined in the plasma, but shifted towards the gas outlet port. Therefore, the vacuum system has been completely sealed from the pump by a main valve during the measurement phase under microgravity – similar to the procedure used with the PKE chamber which does not allow any direct gas flow through the discharge vessel. The problem

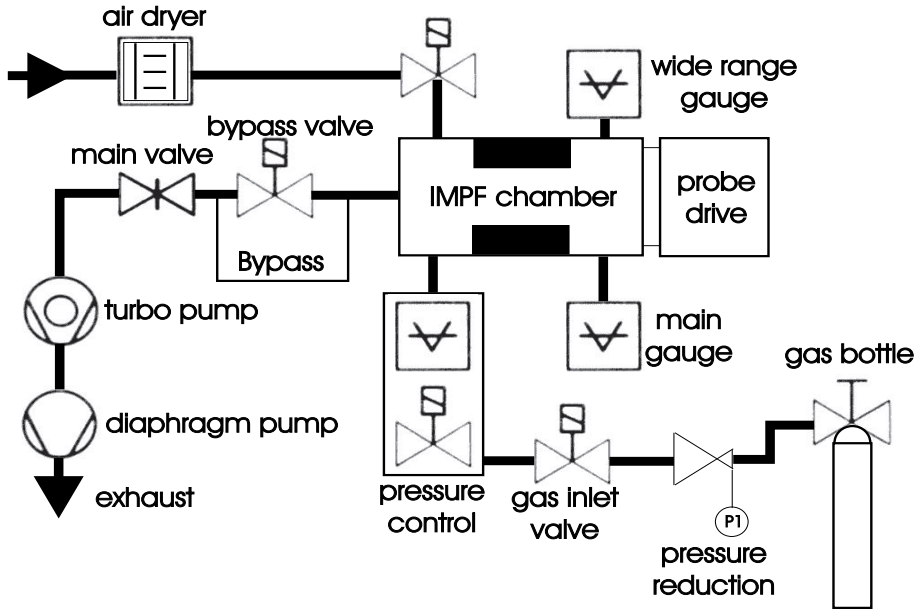


Figure 3.5: Schematic of the vacuum system in the IMPF parabolic flight experiment.

with the gas flow will be solved with a “shower head”-like symmetrical gas in- and outlet and further reduced flow rate in future experiments.

Since the IMPF chamber has to be opened for refilling of the particle dispensers, flooding of the vacuum is only done through an air dryer.

3.1.2 Dust particles

It is a basic requirement for the generation of regular structures, like plasma crystals, but also for general fundamental studies of complex plasmas it is desirable to reduce the number of unknown parameters in the experiment and thus to work with dust particles which all have an ideal shape and exactly the same mass and size. The identical shape, preferably spherical – to account for a simple approximation of the electric field around the charged particle and hence the validity of the OML charging model (see Section 2.2.1), together with the same size of two particles, guarantee an identical charge. Additionally, having particles of the same mass ensures identical dynamic properties in the plasma trap.

For the experiments spherical particles with a radius of $r_d = 1.74 \mu\text{m}$ have been mainly used. In the IMPF experiment a second dust dispenser has been equipped with $r_d = 3.4 \mu\text{m}$ particles to account for a size variation or to create binary mixtures. The dust grains are plastic particles, that are made of melamine formaldehyde condensation resin (MF) by MICROPARTICLES [130]. They excel by a highly uniform spherical shape with a smooth surface and a monodisperse size distribution with a coefficient of variance (CV) $< 3\%$. Their density is $\rho_d = 1514 \text{ kgm}^{-3}$, thus a small particle weights approximately $3.34 \cdot 10^{-14} \text{ kg}$. The temperature stability up to 573°K conserves the particles from degeneration under normal discharge conditions in the experiments, but allows a cleaning of the

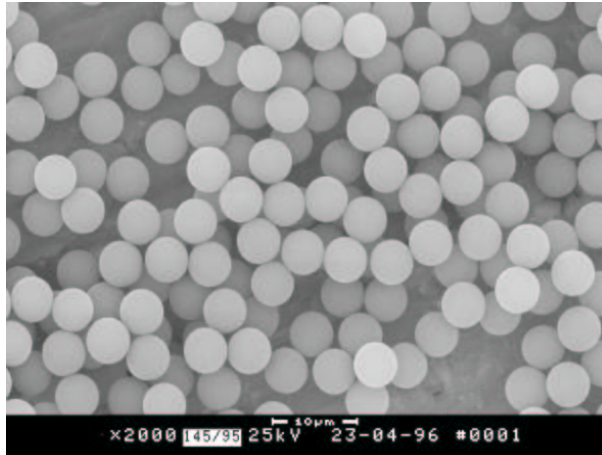


Figure 3.6: Scanning electron microscopy image of a sample of particles made of melamine formaldehyde condensation resin (MF) with an average radius of $r_d = 2.5 \mu\text{m}$. The size distribution is extremely narrow ($CV < 3 \%$). From [130].

Langmuir probe by heating via high drawn currents (compare with Section 3.4.2).

3.1.3 Particle injection

Injection of the particles into the plasma is done by dust dispensers, working on the principle of a salt shaker. A small container with a front sieve is filled with particles and releases them into the discharge under mechanical agitation. The dispenser of the PKE experiment is integrated into the upper electrode and driven by an electric motor driven crank shaft, while the two dispensers of the IMPF chamber are located at the chamber walls and are driven by ferromagnetic cores, that are attracted in the field of a pulsed electromagnet. To ensure that only single particles and no agglomerates are injected, but also to avoid a blocking of the sieve, the size of the holes in the sieve are selected to match approximately twice the particle size. The electro-formed sieve material, manufactured by [131], has square holes of $12 \mu\text{m}$ side length for the large and $8 \mu\text{m}$ side length for the small particles at a total transparency below 10 %. The small transparency reduces the particle consumption and allows long-term operation. It turned out, that the ratio of particles trapped in the plasma to particles injected into the vessel volume is notable higher in the PKE system, since the dispenser is located close to the plasma. In the IMPF geometry, the dust must have a higher initial kinetic energy to pass a long distance under neutral gas friction before entering the inter-electrode space, where it becomes charged and confined. Since the friction is dependent on gas pressure, the particle trapping efficiency is highest at low gas pressures.

3.2 Microgravity experiments

Even for micrometer sized particles, gravity plays a dominant role forcing confined particle to the lower sheath of a plasma and covering the effects of minor forces. Thus, if the advantages of large particles, like separate observation of single grains or a selectable size distribution, shall be kept as a necessity for the detailed study of the condensed state of complex plasmas, it is unavoidable to “switch off” the gravitational force. Hence the access to more subtle particle interactions is opened that control, on the other hand, the dynamics of nanometric grains that are relevant in industrial plasma processing. How microgravity can be obtained and how an experimental setup designed for parabolic flights looks like is described in the following.

3.2.1 Obtaining microgravity

Microgravity or “zero-g” names conditions, under which matter appears weightless. There are several ways to generate such conditions, although gravitational fields exist everywhere in the accessible universe. Since it is also hardly affordable to bring an experiment to a place, where the vector sum of gravitational forces on the experiment is zero, the practicable methods are all based on the change from the earth-bound laboratory into another non-inertial reference system, in which the gravitational force is balanced by an apparent force or which is moved synchronized with the trajectory of an attracted body in the present gravitational field.

The first category consists of the well known weightlessness on board of space crafts and satellites in the earth orbit. Here, the attraction of the earth is balanced by the centrifugal force resulting from the circular motion around the planet at an adjusted speed together with a matching altitude. The almost steady state microgravity conditions in orbit, for example on the International Space Station (ISS), allow long term experiments under a residual gravity of a magnitude of $10^{-6} g$, where g is the acceleration in the gravitational field of the Earth. This residual field is the origin of name microgravity. Recently, experiments with the PKE experiment have been carried out aboard the ISS [12].

Experiments of the second category have to perform a ballistic flight, then, in the moving reference system, the gravitational force is hidden. This method is less expensive than space flights but it has the fundamental disadvantage of a strongly limited experiment time. In a drop tower, the experiments, packed in a capsule, fall in an evacuated tube, providing typically $(4 \dots 5)$ s of microgravity with a quality of $10^{-5} g$. The drop tower located at the University of Bremen is a catapult system that will nearly double the time since the free fall of the capsule starts already at the bottom of the tower after the upwards shooting catapult is left.

Sounding rocket missions include strong limitations in volume and mass of the experimental setup, similar to the drop tower method, but the available time under “zero-g” lasts up to 6 or 7 minutes. The residual gravity is of the order of

$10^{-4}g$. The MPE has also used this opportunity for PKE experiments [9] with ESA's "TEXUS" rockets.

Due to the relatively low constraints, compared to the compact and automated designs that are necessary for rocket or drop tower experiments, parabolic flights have become very popular. Here, the ballistic flight is carried out with a modified commercial plane. In Europe, ESA offers flight opportunities with an AIRBUS A300. Therefore, up to 12 experiments with approximately 40 scientists, who observe and control their equipment, can join the flight. Typically three flights are performed in one measurement campaign, each consisting of 30 parabolas with approximately 20 s microgravity. Starting from a normal flight level at 6100 m, the plane is pulled up to an angle of 47° to the horizon. During this

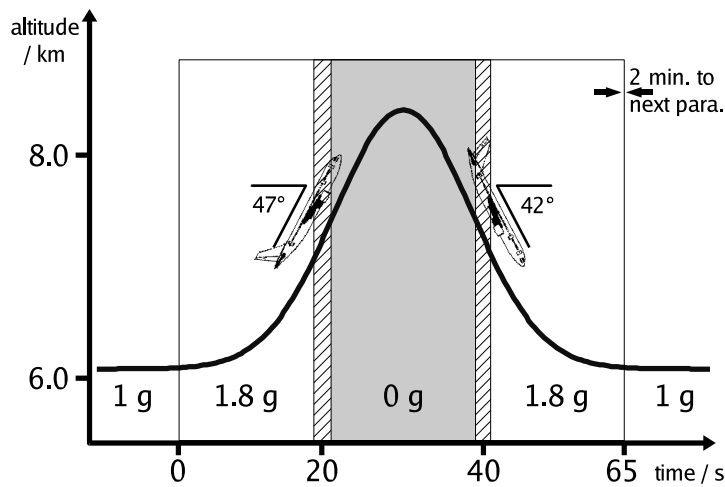


Figure 3.7: Profile of a parabolic flight maneuver. Thirty parabolas are performed following a narrow table table during on flight.

phase, the acceleration towards the floor of the plane sums up to $1.8g$. Then, in a short transition phase at 7600 m, the engines are throttled. During the following ballistic flight the pilots have to adjust the engine thrust and the tilt angle permanently to compensate the air drag and lift in order to obtain the parabolic flight curve. The apex of the parabola and thus the point of the lowest aircraft velocity is found at 8500 m height. Since this maneuver is very difficult, the resulting magnitude of microgravity is typically only $10^{-2}g$. The sequence of a parabolic flight procedure is sketched in Fig. 3.7.

Although the experiments are controlled by scientists, the experiment need to be automated as far as possible, since the microgravity phases are unusual to human beings and the time between two parabolas is very limited. A few notes concerning the design of the Kiel microgravity experiment are given in the next section.

A completely different approach to compensate the gravitational force on particles in a plasma in the laboratory has been made by Rothermel *et al.* [90]. They attached Peltier elements to the PKE experiment to heat the lower and cool the upper cover plate of the chamber. The temperature gradient has been adjusted to

the particle size and gas pressure in the chamber to generate an upward directed thermophoretic force (see Section 2.3.3) on the particles that balances gravity. Even if the method allows only the use of one size of particles, the authors were able to observe phenomena, that are known from the more costly microgravity experiments.

3.2.2 Special experimental design issues

The Kiel microgravity experiment for the study of complex plasmas was designed to take part in the 5th DLR (*Deutsches Zentrum für Luft- und Raumfahrt*) parabolic flight campaign in June 2003. The campaign has been organized by *NOVESPACÉ*, which is a subsidiary of CNES, the French space agency, which again is member of ESA. One of the first built AIRBUS A300's, after strengthening the wings, has been equipped for the flights – mainly, all seats are removed from the middle section of the plane, electric connection panels are installed and floor, walls and ceiling are covered with padding mats. Experiments are attached to the former seat mounting rails. This includes that the appropriate load specifications have to be fulfilled. Applied to the two racks, the Kiel experiment consists of, each rack is restricted to a maximum weight of 200 kg. Building up for mounting racks for the experimental setup, the resulting center of gravity of the fully equipped rack has to be taken into account in advance, since the selected upright material has to resist the bending forces, that occur at a horizontal acceleration of 9 *g*, which accounts for the stress during an emergency landing. Additionally, all custom-made pressure or vacuum vessels and moveable part have to be secured by a closed containment (see Fig. 3.9). The experiment must be also equipped with an emergency switch-off button, that disconnects it from the aircraft systems and brings it into a save fall-back modus. Each experiment is restricted to a maximum power consumption of 2 *kW*. Thus, a sequential start-up procedure has always to be kept, when the experiment is powered. All edges of the experiment racks have to be padded to avoid injuries of the experimenters during zero-*g* phases. The fully equipped experimental setup has to fulfill a security check by *NOVESPACÉ* before the flights.

Under microgravity, the experiment is computer-operated by predefined sequences that include, for example, camera scans, Langmuir probe scans or rf power ramps. Nevertheless an optimum number of three people is needed for the operation of the control computer, diagnostics computer, video recording and for coordination and documentation. Since the plasma chamber is located in a containment, the supervision of all functions is done on base of camera images and status indicators integrated into the computer control programs.

A schematic layout of the equipment mounted in the racks and a picture of the Kiel microgravity experiment is presented in Fig. 3.8.

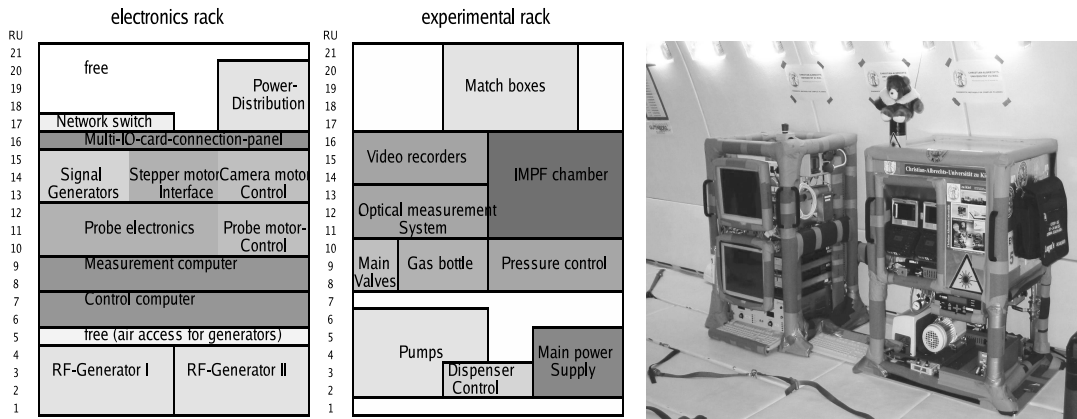


Figure 3.8: Schematic layout of the component arrangement in the two racks of the Kiel experiment for studies of complex plasmas under microgravity (left) and a picture of the complete experiment mounted in the plane (right).

3.3 Video observation

Besides the Langmuir probe measurements, the imaging and recording of particle positions or arrangements in the discharge is the main diagnostic method used with the experiments. The observed field of views of the one camera in the PKE setup and the two cameras of the IMPF experiment are marked in Fig. 3.1 and 3.3. The following description concerns the IMPF setup, but is largely valid for PKE, too. Due to the near field observation of the cameras the depth of focus is limited to record just one particle in the depth (y -dimension of the experiment), when a minimum inter-particle distance of approximately $100 \mu\text{m}$ is considered. In order not to receive scattered light from particles in front of or behind the focus plane, only the dust in the plane is illuminated by a vertical laser fan of an adjusted thickness of $\approx 100 \mu\text{m}$. To obtain an image of high contrast, the plasma light emission is suppressed by high transmission interference filter at the laser wavelength of 660 nm . The utilized monochrome CCD-cameras have an enhanced sensitivity in the infrared and hence their maximum spectral sensitivity is found close to the laser wavelength. To overcome the restrictions of observation time and the requirements for CPU power connected with direct recording of video material on computer disks, the cameras are generating a standard TV-compatible signal, that is recorded with digital video (DV) recorders. Any further transfer of movies or parts of them to a computer for analysis can be done without quality reduction. The large-field-of-view camera (LFoV) observes a field of $49 \times 37 \text{ mm}^2$ in the x, z -plane, representing approximately the half of the central meridional plane of the cylindrical discharge volume, while the small-field-of-view camera (SFoV) acquires only a $19 \times 14 \text{ mm}^2$ fraction of the LFoV, as it is sketched in Fig. 3.3. The resolution of the imaged area is finally given by $68 \times 64 \mu\text{m}^2/\text{pixel}$ for the large field of view and $27 \times 25 \mu\text{m}^2/\text{pixel}$ for the small field of view. In the PKE experiment the field of view is $29 \times 22 \text{ mm}^2$ at a resolution of $40 \times 40 \mu\text{m}^2/\text{pixel}$.

The arrangement of cameras and laser is mounted on a stepper motor driven

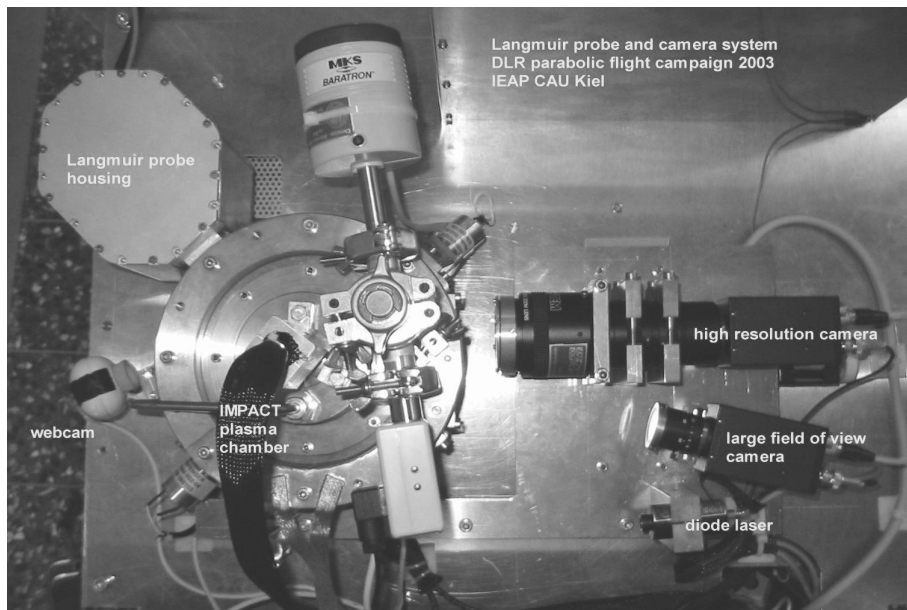


Figure 3.9: *Top view on the experimental setup inside the containment of the experiment rack. Main parts of the setup are the Langmuir probe housing (upper left corner of the picture), the IMPF vacuum chamber (central left hand side), cameras and the illumination laser (right hand side). The web-cam serves as survey camera for experiment control tasks.*

translation stage that allows to move the focus plane in the y -direction through the inter-electrode space, without re-adjusting the lenses (see Fig. 3.4). A scan over a distance of 75 mm, which covers the space, where particles are expected to be found between the electrodes, takes a minimum time of ≈ 3 s. To obtain a higher sampling rate per distance, the stage speed can be reduced. Thus, 3D particle arrangements are explorable in detail during one parabola. The spatial resolution of the scanning movement is of the order of a micrometer. Assuming the dust cloud in the plasma to have axial symmetry, as the plasma does, the dust arrangement is obtained from the recording of one half of a central two-dimensional cross section of the inter-electrode space. Therefore the standard position of the laser fan is in the center of the chamber.

3.4 Probe diagnostics

One of the main technical tasks of this work was the development of a tuned electrostatic probe system for measurements in the rf plasmas, that are used for complex plasma experiments under microgravity like the PKE experiment. This system has been further-on adapted to the IMPF plasma chamber in view of the development of an approved diagnostics for an international experimental platform for plasma physics (IMPF/IMPACT) on board of the ISS. The main challenges of the project are the small size of the plasma volume, compared to typical Langmuir probe dimensions, in the PKE and IMPF experiments, the rf plasma

generation, that requires special probe tuning, the development of probe positioning mechanics matching the spatial constraints of microgravity experiments, and the “dusty” operation environment. The scientific goal is an advanced understanding of the observed particle dynamics under microgravity and the influence of charged grains on the ambient plasma.

Since the mechanical aspects of the probe system have been introduced in connection with the PKE and IMPF chambers, this section will focus on the rf compensation of the probe and the issues that have to be taken into account, when highly charged dust particles are present in a plasma, that is scanned with an electrostatic probe.

Regarding the neutral gas pressure and ionization rate conditions in the dusty discharges, further effects must be considered during the analysis of measured probe data, which are explained in Chapter 4.

3.4.1 Probe design and rf compensation

The standard method of electrostatic probe measurements in a plasma, introduced by Mott-Smith and Langmuir [53], yields current-voltage characteristics, from which plasma parameters can be derived (see Chapter 4). To obtain the characteristics, a probe, consisting of a metal plate, sphere or mostly a simple wire, is inserted into the discharge and a dc voltage is applied. The resulting current is then dependent on the (known) geometry of the probe and the plasma density, potential and temperatures. To reduce effects of the inserted probe on

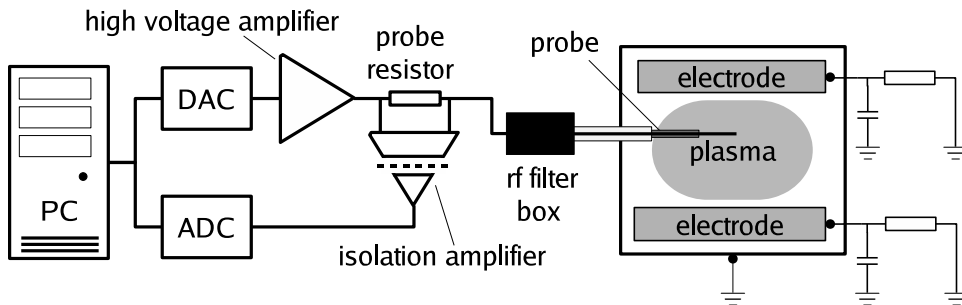


Figure 3.10: *General circuit diagram for Langmuir probe measurements in rf plasmas.*

the plasma, the dimensions of the probe-tip and its fixture have to be minimized to a point that still tolerates the mechanical stress due to the positioning and on parabolic flights. Minimizing the probe-tip, reduces the current, that is extracted from the plasma, while a small surface of the probe shaft minimizes the charge-carrier losses to this additional plasma boundary. The used probes are tungsten wires with a diameter of $r_p = 50 \mu\text{m}$, length of $l_p = (3 \dots 4) \text{ mm}$ and a maximum fixture shaft diameter with contact to the plasma of 0.9 mm (PKE) or 1.1 mm (IMPF) respectively. The PKE probe design is displayed in Fig. 3.12. A computer with digital-analog converter generates a voltage sequence, that is amplified and fed to the probe. To account for an expected plasma potential

of the order of the rf amplitude ($\approx (25 \cdots 60)$ V), the probe sweeps typically a range from -40 V to +70 V, so that the probe attracts a pure ion current at the lower limit and a pure electron current at the upper limit. Since the maximum electron current is usually an order of magnitude higher than the ion current (see Chapter 4) and hence may cause interferences with the plasma, the probe voltage sweep does only slightly overcome the plasma potential. An inserted probe resistor of $(20 \cdots 50)$ k Ω allows to measure the probe current with an isolation amplifier. The probe potential dependent current is then digitized and sampled with the computer. Hereby, the reduction of the potential applied to the probe-tip by the voltage drop over the probe resistor, is compensated by the computer program. Fig. 3.10 shows the schematic setup, that follows in general the detailed description in [132]. The function of the rf filter is described in the following.

Probe theories, which allow to derive plasma properties from the measured characteristic, mostly assume a plasma potential that is invariant in time as it is given in dc discharges. In rf plasmas, the potential is fluctuating, with respect to ground and the dc probe bias. These fluctuations are a composition of oscillations at the plasma excitation frequency f_{rf} and higher harmonics. In symmetrical discharge geometries, like the introduced parallel plate experiments, the largest amplitude is found at $2f_{rf}$. This is expected from the superposition of the sheath modulation of the two equal electrodes, while the fundamental frequency and its odd harmonics are fed by asymmetries of the excitation [133]. A spectrum obtained from a floating (isolated) probe in the PKE experiment is shown in Fig. 3.13. The voltage fluctuations across the probe-plasma sheath are rectified and lead to an additional unknown voltage between probe and plasma, distorting the sampling of the probe characteristic. It has been demonstrated, that these interferences result in a shifting of the floating potential (probe potential, at which the collected ion and electron currents are equal) towards more negative values and a flattening of the probe characteristic [134, 135, 136, 137]. Especially since the electron temperature is deduced from the slope of the exponential development of the electron retardation current close to the floating potential of the probe characteristics (compare with Section 4), such a flattening may lead to an error of factor two for the temperature determination. Thus, measured probe data cannot be used to infer plasma parameters.

To overcome these problems, two approaches can be distinguished: the active and the passive rf compensation. Both have in common that they try to superpose the bias at the probe-tip with an rf signal mostly identical to the space potential fluctuations. Then, the voltage difference over the plasma-probe sheath is constant and the characteristic can be treated in the same manner as for dc plasmas, when the probe current is averaged over several rf cycles.

In the *active rf compensation* method, the signal to overlay on the probe-tip is generated externally and matched in amplitude and phase to the local plasma potential, e.g. [138]. This technique implies the knowledge of the potential fluctuations at the probe positions or amplifier and phase shifter must be empirically tuned until the most positive floating potential is reached. Due to the increasing amount of external circuitry when more than one harmonic and non-sinusoidal

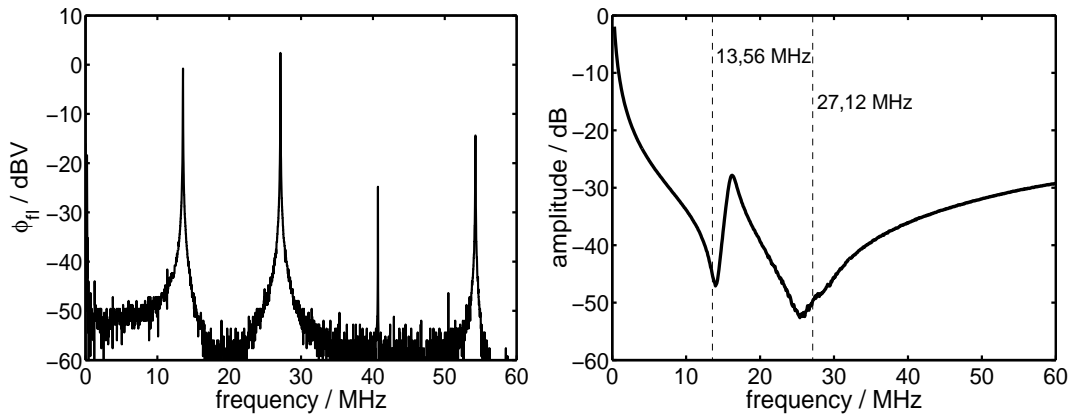


Figure 3.11: Floating potential spectrum in the center of a PKE plasma at $U_{rf} = 120 V_{pp}$ and an argon pressure of 50 Pa (left). Maximum voltage oscillations of $3 \text{ dBV} \approx 1.5 \text{ V}$ occur at twice the rf frequency of 13.56 MHz. Transmission spectrum of a four stage rf probe filter with inductors of (22, 15, 22 and 56) μH (right).

wave forms are taken into account, the method is often used with only the basic excitation frequency. Nevertheless a three harmonics system is presented by Dyson *et al.* [139].

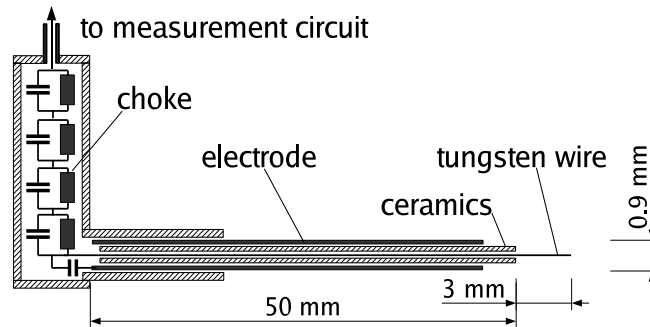


Figure 3.12: Schematic drawing of the PKE probe design with passive rf compensation by an reference electrode and the rf notch filter, that is shown here to consist of four oscillation circuits.

The *passive rf compensation* needs no extend signal conditioning. Following a probe design, suggested by Gagné and Cantin [140], the idea is, that the probe-tip “floats” with the plasma potential fluctuations, when the rf voltage drops mainly across an additional impedance in the measurement circuit and not across the probe-plasma sheath. Therefore, a series of inductors blocks the probe from the external measurement circuit for rf signals, while letting the dc and slowly varying signals pass. The inductors represent *LC* circuits with self-resonances selected to match the main harmonics of the plasma excitation frequency. The impedance at resonance must be larger than that of the sheath around the probe-tip. Since the capacity of the probe-plasma sheath is limited by the small area of the probe-tip,

the coupling of the rf signal onto the probe has to be enhanced by an additional large area reference electrode close to the measuring probe-tip to pick up the local space potential fluctuations. The electrically floating reference electrode then feeds the signal over a capacitor to the probe-tip. This method accounts for all spectral components of the time-variant space potential. The compensation network is housed in a small plexiglass cylinder to minimize the stray capacitance of the probe circuit.

Due to the substantially more compact components and the inherent adaptivity of the passive-filtered probe to changing plasma conditions, a rf filter box and a reference electrode have been included into the used PKE and IMPF probe system. This follows the results of an experimental comparison of the two methods by Annaratone and Braithwaite [141].

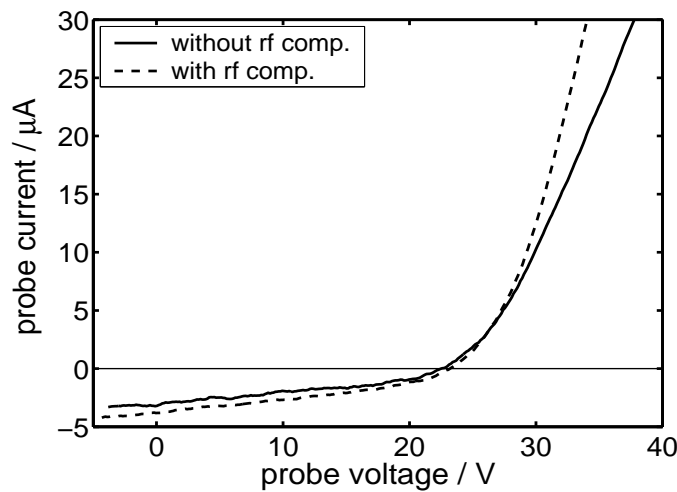


Figure 3.13: *Characteristic of a probe with fully equipped and with an empty (bridged) circuit board in the filter box.*

Derived from passive-filtered probe assemblies proposed in [45, 142, 143, 144] the notch filter, inserted into the probe circuit, is located in a dielectric box, supporting the probe shaft inside the vacuum. The box hosts four selected SMD-chokes with suitable self-resonances to block current components at $f_{rf} = 13.56$ MHz and $2f_{rf}$. The characteristic spectral transmission of such a filter is plotted in Fig 3.11. As pick-up or reference electrode a stainless steel tube has been put on the ceramics, that is supporting and isolating the tungsten wire as sketched in Fig. 3.12. The reference electrode is connected to the tungsten probe-tip via a capacitor, also integrated into the filter box. Probes and filter boxes are modular components, that can be replaced separately. The effect of the rf compensation on a probe characteristic is demonstrated by measurements in the PKE chamber in Fig. 3.13.

3.4.2 Probe contamination

It is a known problem, that in plasma discharges material is sputtered from the electrode and, in the case of complex plasmas, from the particles. This material is then deposited on the walls, windows and of course on probes which are in contact with the plasma. Such a contamination of the probe is often of low conductivity and thus distorts the measured characteristic.

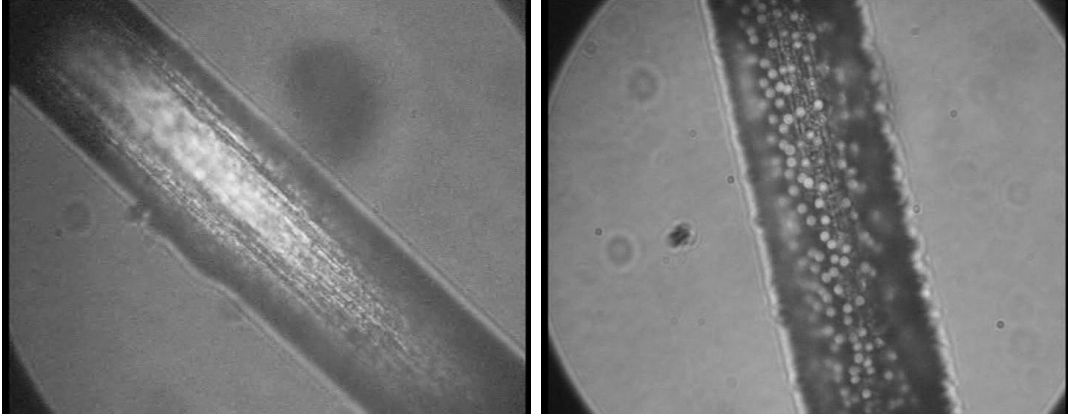


Figure 3.14: *Light microscopic image of the cylindrical tungsten probe-tip before the use (left) and after the use in a complex plasma with simple ramp-shaped voltage sweeps (right). Although the picture's depth of focus is narrow, single particles ($r_d = 1.74 \mu\text{m}$), that stick on the probe-tip, can be identified.*

Another type of probe contamination occurs, when the probe, positioned in a complex plasma with MF-plastic particles, is biased positive with respect to the space potential. Then, the highly negatively charged particles are attracted by the probe. They can approach the probe from the outmost tip, where the maximum electric field is found, and may stick on the surface of the tungsten wire, as shown in Fig. 3.14. The standard method to record a probe characteristic is to sweep the bias of the probe in a ramp-shaped time-voltage curve over the desired voltage range as plotted on the left hand side of Fig. 3.15. Even if the duration of the sweep is only a fraction of a second, particles are deposited on the probe, when the ramp voltage exceeds the plasma potential. In the laboratory the probe current reduction saturates already after a few voltage sweeps at approximately 60 % of the initial current value. In contrast, under microgravity conditions, a current reduction to 20% of the current drawn by a clean probe has been observed.

In order to prevent the particles from reaching the probe and sticking on it, several sweep functions have been tested. The combination of a randomized voltage scan together with sampling pauses of highly negative probe bias turned out to avoid the contamination most effectively (see Fig. 3.15). This sweep type increases the frequency ω of alternating positive and negative probe potentials, compared to the plasma potential, to overcome the dust plasma frequency ω_{pd} (see Eq. 2.20). Resulting in $\omega_{pd} < \omega \ll \omega_{pe,pi}$, the particles can hardly follow the transient attracting potential and “see” the averaged potential, that is

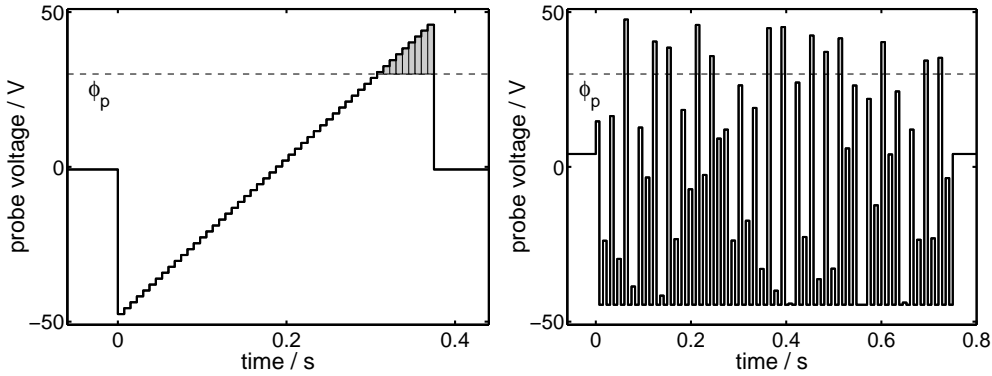


Figure 3.15: Schematic time-voltage plots of the probe bias to obtain a characteristic: The standard ramp sweep (left) and a randomized sampling(right), that alternates with negative potential pauses. When the bias exceeds the space potential ϕ_p , negatively charged particles are attracted.

dominated by the strongly repulsing sampling pauses. Due to their high plasma frequencies $\omega_{pe,pi}$, ions and electrons can react instantaneously on the bias fluctuations. Thus, the probe characteristic is not perturbed by the use of this special different sweep method.

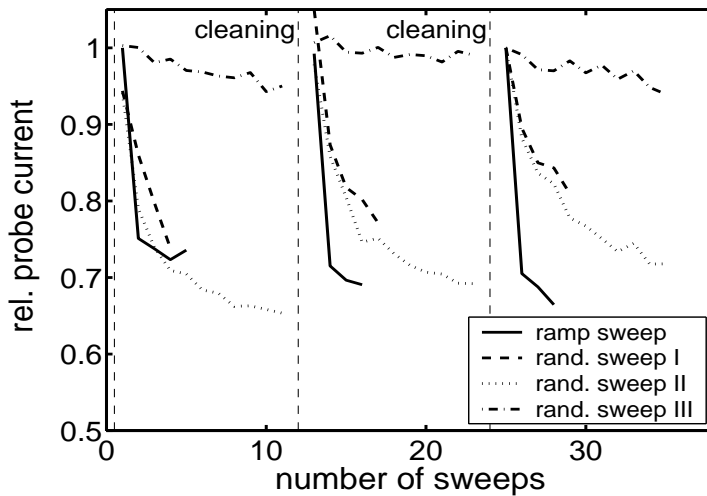


Figure 3.16: Probe current at a certain probe bias with respect to the initial value of a clean probe over the number of completed voltage sweep in a dense particle cloud. The randomized voltage sweep type III includes pauses of negative probe potential and has been used on the IMPF flight campaign.

Nevertheless, some particles can overcome the repulsive potential in a dense particle cloud. Therefore, like in particle-free discharges, the probe has to be cleaned from time to time. Probe cleaning is generally either done by ion bombardment, resulting from a high negative probe bias, or by electron heating, which allows to glow the probe-tip under the influence of high electron currents. The plastic particles used can be shrunk and then removed from the probe-tip by

electron heating. A sequence of cleaning procedures and measuring phases in a complex plasma with different sweep types is presented in Fig. 3.16. It is obvious that the probe contamination can be reversed and finally be reduced to a minimum. This finding is especially important for the future application of Langmuir probes aboard the ISS which requires long-term operation of the probe without contamination by the dust.

3.5 Modelling of plasmas

Whenever measurements with standard diagnostics tools in physical systems become a challenging task, numerical simulation are a convincing method to study hard to access experimental processes. This is also the case for the later on described rf plasmas which are characterized by a small discharge volume, low plasma densities and ionization rates. Therefore the use of interferometric or spectroscopic diagnostics is practically impossible, especially when spatial resolution is demanded. Even the use of a tuned Langmuir probe under the given conditions, must be considered as a new approach and thus the results need to be compared to an independent diagnostics. Due to the lack of measurements of absolute plasma parameter values for the PKE and IMPF chamber, the commercially available simulation code SIGLO-2D [25] will be used to provide two-dimensional plasma parameter sections, which are suitable for comparison with those obtained from probe measurements. A few additional data points are also available from a code similar to SIGLO, which has been extended to include microscopic dust particles in the discharge [145]. This section will briefly introduce the field of numerical simulations and describe the problem solved by the SIGLO code.

3.5.1 Simulation techniques

Besides the modeling of a gas discharge that makes use of equivalent circuits to describe only certain properties of the plasma and thus ignore the basic processes on the atomic scale, two main categories of simulations exist that imitate the system on base of fundamental physical equations, namely particle codes and fluid codes.

Particle simulation codes in plasma physics account for a full kinetic description of the charged particle transport, thus they are mainly used to describe a system on its microscopic scale. For instance, in molecular dynamics (MD) simulations, the trajectories of a sample of particles is followed in velocity-position space. The equations of motion are integrated on a time scale with respect to the collision frequency in a given electric field, and the field is then recalculated using Poisson's equation. Since the processing of typical possible particles numbers $10^2 < N < 10^6$ is very time consuming, particle codes are often focused only on selected parts of the whole discharge and need simplifying techniques. In particle-in-cell (PIC), codes the simulation space is divided by a grid, whose element size is adapted to the characteristic length of the process, e.g. the mean

free path, and the equations are only solved for the accumulated charges and masses of the cell on the grid points (see [146]). Other methods are the introduction of super-particles (one particle carrying mass and charge of many), and the appropriate choice of boundary conditions. Particle codes have been developed for one, two and three dimensional simulation space. Since no assumptions on the velocity distribution function have to be made, they are preferable for extreme non-equilibrium conditions like, for example, low neutral gas pressures where an additional high temperature electron population is present (compare with the collisionless heating in Section 2.1.1). Nevertheless, due to the number of involved particles and the different time scales the motion of electrons, ions and dust particles takes place, the application of MD simulations in dusty plasmas is mostly limited to the motion of dust particles. Their dynamics is then calculated in given model potentials or fields derived from fluid codes, that are described below. Examples can be found in [146, 147, 148, 149, 150].

Another distinguishable instance of particle codes is the Monte-Carlo technique (MC), where the fields are assumed to be a priori known and the next random step of particle motion is accepted when the Hamiltonian H of the system is decreased by the resulting system configuration. Steps with a positive change $\delta H > 0$ are also possible with a transition probability of $\exp(-\delta H/(k_B T))$, hence making allowance for a temperature T of the system. The MC method is often used to find the minimum energy states for particle-particle and particle-plasma interactions, for example [48, 94, 114].

Fluid codes have been developed to describe macroscopic systems and are thus dominant in the simulation of whole discharges. Here, each particle species is represented by fluid with its properties: momentum and energy density. Instead of solving the full Boltzmann equation, the first two or three moments are derived to describe the balance of the different densities. These moments are the continuity, momentum, and energy equation that are coupled to Poisson's equation for the electric field. Since every moment equation introduces a new unknown, additional simplifying assumptions have to be made to close the system of equations. Assuming high collision rates, the momentum transport equation is often replaced by an expression for the particle flux based on drift and diffusion coefficients. To derive the moments assumptions regarding the particle distribution function have to be made. This and the drift-diffusion approximation generally restrict applications of a fluid code to equilibrium systems. The main difficulty of the utilization of a predefined distribution function is the resulting ionization rate that can severely affect the simulation results. Therefore, special attention has to be paid also to the atomic cross sections used in the calculation. Nevertheless, fluid models have proved to be accurate enough to predict quantitatively the electrical behavior of a discharge under conditions comparable to those studied in this work, with a lower gas pressure limit of approximately 11 Pa [20, 151].

The SIGLO code [25, 151], introduced below, and the model used in [152, 153] are typical representatives of fluid simulation codes. Both have recently been extended to comprise dust particles as a third fluid [22, 24] to account for the large number of dust grains that are injected to microgravity void experiments

(see Section 2.4). Dealing with less particles, hybrid codes, deriving the plasma parameter profiles from a fluid code, calculating the dust motion from molecular dynamics and sometimes additionally determining plasma-dust interactions with a MC method, have been developed [154, 155, 156].

3.5.2 SIGLO-simulations

The SIGLO-2D code [25] is a commercially available computer program to simulate electrical properties of low-power rf or dc discharges in axial symmetry. It is based on the code used in [151, 21] and handles the electron and up to two ion species. As results two-dimensional profiles of charge carrier densities, plasma potential, electron temperature are obtained, as well as discharge currents on the electrodes. On the grid of a maximum of 50×50 cells, an unlimited number of electrodes, metal and dielectric walls and other elements can be defined. The electrodes can be directly (rf/dc) or capacitively (rf) coupled to the external power generator with different dc biases or rf amplitudes. Thus the program can be used to simulate the two electrode PKE plasma chamber as well as the four electrode IMPF chamber described in Section 3.1.1, which both have cylindrical geometry.

SIGLO is a fluid code, that includes a two-moment description of the ions and a two- or three-moment description of the electron. For the simulations in this work, the three-moment feature has been chosen, since the alternative drift-diffusion approximation is questionable for electrons in the small size and low pressure discharges, which are operated close to the transition to the collisionless heating regime (see Section 2.1.1), when the electron mean free path becomes comparable to the discharge dimensions.

SIGLO comes with a database of gas parameters for various gases, providing electron and ion mobilities, mean electron energy and ionization coefficients as function of reduced electric field strength E/n , where n is the neutral gas density. For argon gas, which is exclusively used for this study, two sets of parameters are available and have been employed for simulations to compare with probe measurements. Both sets contain ion mobilities taken from Ellis *et al.* [157] and while the other parameters have at first been calculated from cross sections discussed in [158] (later on referred to as first set of gas parameters), the newer data set is derived from cross sections from Phelps *et al.* [159, 160, 161] (referred to as second gas parameter set).

The conversion from the real plasma chamber geometry to the grid based simulation space setup is documented in the screen shots displayed in Fig. 3.17. A grid size of 50×50 cells for PKE and 50×45 for the IMPF chamber has been used. The electrodes are directly coupled, so that no self-bias establishes (see Section 3.1.1).

The time step of the simulation, which is automatically adjusted by the program to be always smaller than the dielectric relaxation time, is additionally reduced by a factor of 0.5 to obtain more accurate results. The listed control settings are the same for all simulations in the present work.

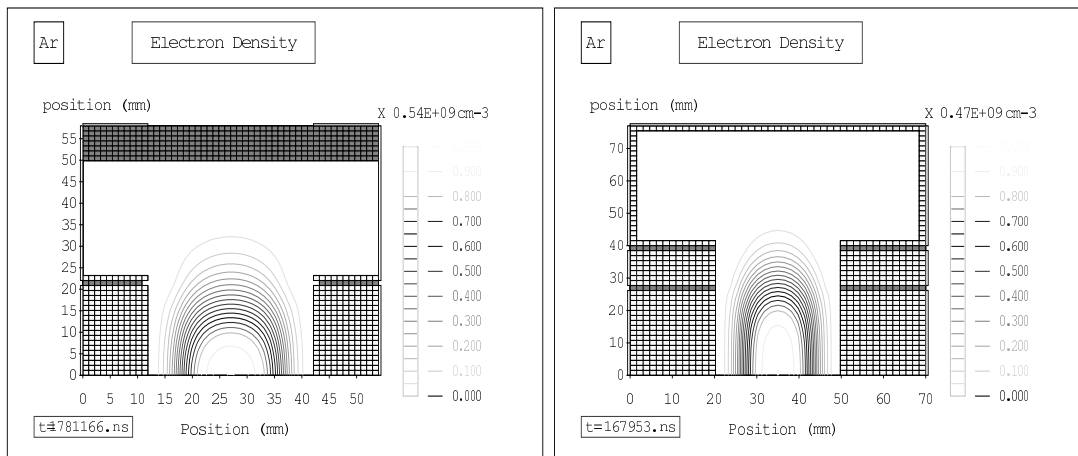


Figure 3.17: Screen shots from the SIGLO-2D program showing density profiles and the geometry definitions for the PKE chamber (left) and the IMPF chamber (right). The lower boundary of the simulation space represents the rotation axis of the cylindrical chamber geometry (compare with Fig. 3.1, 3.3). Light gray cells are metal, dark cells are dielectric parts.

4 Langmuir probe models and analysis

In Section 3.4 the cylindrical single-tip electrostatic probe was introduced to be capable to characterize spatially resolved the discharges used for this studies. The obtained probe data consist of a large set of probe characteristics taken at each position. Subsequently, a method for the interpretation of the data will be worked out in this chapter. This will be done by classifying the given plasma conditions and probe properties in comparison with the various existing probe theories as well as by empirical arguments regarding the reliability of the theoretical and the measured probe characteristics. The probe data analysis yields a two-dimensional cross section of discharge parameters, like electron density n_e and temperature T_e , ion density n_i and plasma potential ϕ_p . These parameters are crucial to determine the charging of dust particles immersed in the plasma and the forces acting on them, for example electric field and ion drag forces.

4.1 Probe operation regimes

As Langmuir probes are used in space, ionosphere, and in a wide variety of industrial or laboratory plasma devices, probe theories have been developed for very different operation regimes. In common usage, three parameters serve to distinguish the regimes: The probe radius r_p , the mean free path λ_{mfp} of charged species in the plasma and the Debye shielding length of the hotter species λ_{De} . It can be shown that the extent of the ion space charge sheath at a plasma boundary, for example around a Langmuir probe, can be estimated by equating the Child-Langmuir current [162] given in the sheath to the Bohm current (4.6) that is determined by the presheath to be a few λ_{De} [163]. Therefore, λ_{De} describes the matching of sheath and presheath and is a useful scaling length for boundary processes.

To distinguish between related theories in one of the operation domains, often the ion energy distribution function has to be taken into account. According to Fig. 4.1 thin sheath regimes are given by $r_p/\lambda_{De} \gg 1$ and thus the thick sheath is $r_p/\lambda_{De} \ll 1$. The probability of collisions in the sheath is described by the ratio $\lambda_{mfp}/\lambda_{De}$ and splits into the collisional ($\lambda_{mfp}/\lambda_{De} \ll 1$), the transitional ($\lambda_{mfp}/\lambda_{De} \approx 1$) and the collisionless ($\lambda_{mfp}/\lambda_{De} \gg 1$) sheath regimes. Overviews of the basic theories are given in [37, 136, 165].

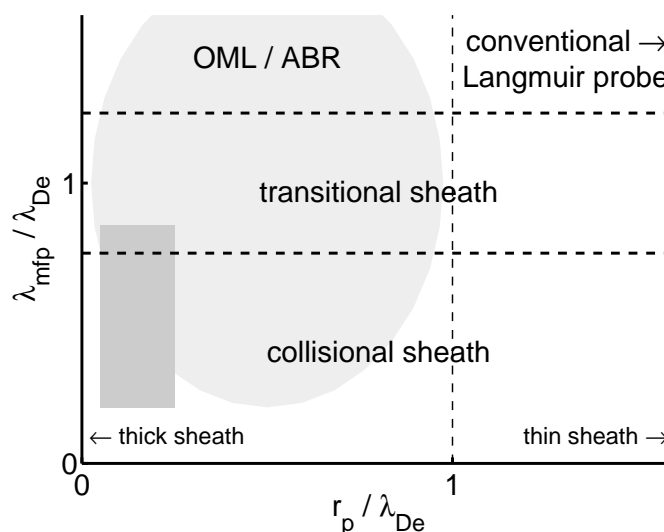


Figure 4.1: Probe radius r_p , ion mean free path λ_{mfp} and electron Debye length λ_{De} dependant representation of various probe operation domains. The rectangle marks the operation regime in the studied discharges. The light gray area indicates the approximate range of validity of the ABR model extension accounting for collisions (see Section 4.3 and [164]).

With a typical probe radius $r_p = 25 \mu\text{m}$ and, in anticipation of the following chapters, with electron Debye lengths of $\lambda_{De} \approx (150 \cdots 600) \mu\text{m}$ and ion mean free paths $\lambda_{mfp} \approx (50 \cdots 250) \mu\text{m}$ the region of interest for this work is found mainly in the thick sheath regime as indicated in Fig. 4.1. Since $\lambda_{De} \approx (2 \cdots 3)\lambda_{mfp}$, a few ion-neutral collisions are likely to occur in the sheath and presheath of the probe and their influence on the probe current becomes important. This regime can be characterized as weakly collisional. For complexity reasons exact theories are well established only in the cases of collision dominated ($\lambda_{mfp}/\lambda_{De} \rightarrow 0$) and collisionless ($\lambda_{mfp}/\lambda_{De} \gg 1$) plasma sheaths.

4.2 OML and radial motion

The *Orbital-Motion-Limited-* (OML) and the *Radial-Motion-*theory (ABR – after the authors **A**llen, **B**oyd and **R**eynolds) are two different approaches to describe the physics of Langmuir probes. While OML theory accounts for angular momentum effects which result from an initial tangential (thermal) velocity component of a probe attracted charge-carrier, ABR describes the limit of cold ions ($T_i \rightarrow 0$) yielding strict radial motion towards the probe. As both theories and their more sophisticated further developments are valid for the given ratio r_p/λ_{De} (see Fig. 4.1), they are introduced and discussed in the following.

4.2.1 Orbital-Motion-Limit theory

Starting in 1924, Langmuir has developed the method of electrostatic probes for measuring the properties of plasmas. Therefore, a single electrode probe, whose current-voltage characteristic is measured against a large reference electrode, is called a Langmuir probe. The wall of a plasma chamber often represents the reference electrode, while the probe itself is made of a small piece of metal wire, a sphere or a plate (compare with Section 3.4). A variable voltage V_p is applied to the probe-tip and the corresponding current I_p from the plasma is measured to obtain a characteristic as shown in Fig. 4.2. A strong negatively biased probe attracts only the positive ions and the ion current in this regime is only slightly dependent on the probe voltage. On account of their high thermal energy compared to the ions, the electrons can reach the probe even at a moderate negative bias with respect to the plasma potential ϕ_p . The electron retardation current part of the characteristic ends in an inflection point (“knee”) at the plasma potential. The electron saturation current is the regime with $V > \phi_p$. At the floating potential ϕ_f the absolute values of electron and ion current are equal. An isolated body in a plasma will charge up to ϕ_f as a result of the quite different charge-carrier fluxes of electrons and ions, e.g. the charging of dust particles (see Section 2.2).

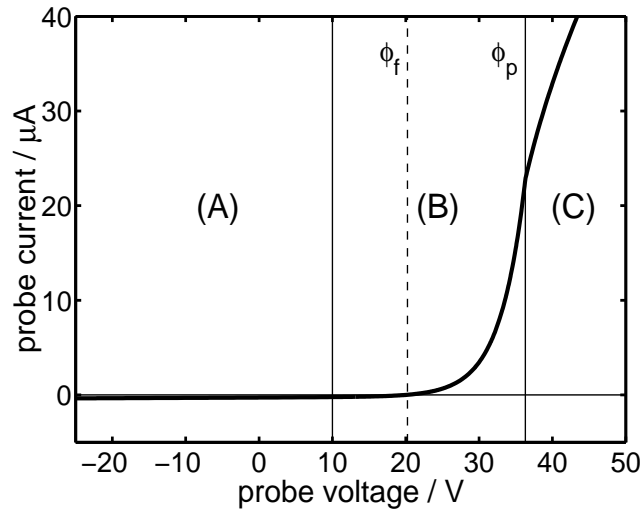


Figure 4.2: Schematic of a typical current-voltage characteristic of a single tip probe with (A) the ion saturation, (B) electron retardation, and (C) electron saturation part. The plasma potential ϕ_p is given by the inflection point, the floating potential ϕ_f by the zero of the characteristic. As a convention, the currents are plotted with negative sign.

Langmuir and Mott-Smith [53] started with the assumption that the space charge layer (sheath) around a probe is very thin compared to the probe ($\lambda_D \ll r_p$) and that the velocity distribution of the plasma species is undisturbed as far as to the edge of the sheath. Thus, the charged particle collecting (effective) surface A_s of the sheath of the probe is approximately equal to the real conducting

surface A_p . With an isotropic Maxwellian distribution with the temperatures $T_{i,e}$ the saturation currents then become

$$V_p \geq \phi_p : \quad I_e^{sat} = -\frac{1}{4}A_p n_e e v_{te} \quad (4.1)$$

$$I_i = 0 \quad (4.2)$$

$$V_p < \phi_p : \quad I_e = I_e^{sat} \exp\left(\frac{-e(\phi_p - V_p)}{k_B T_e}\right) \quad (4.3)$$

$$I_i^{sat} = \frac{1}{4}A_p n_i e v_{ti} \quad , \quad (4.4)$$

with the elementary charge e , the Boltzmann constant k_B , and the average thermal velocities

$$v_{tx} = \sqrt{\frac{8}{\pi} \frac{k_B T_x}{m_x}} \quad , \quad (x = e, i) \quad . \quad (4.5)$$

The saturation currents $I_{i,e}^{sat}$ thus represent the charge flux env_{tx} through the probe surface A_p . The factor $\frac{1}{4}$ is a result of the integration over the velocity distribution, in other words, if the direction of the velocity of plasma particles will make them enter the surface or not.

Equation 4.4 is untenable in low temperature discharges, where $T_i \ll T_e$ so that the ion energy distribution can be no longer considered to be Maxwellian, and with a sufficiently large negative probe bias yielding the formation of a space charge sheath. For this case, Bohm has shown that the ions are accelerated in a potential difference of $\phi_s = (-1/2)k_B T_e/e$, that occurs in a so-called presheath outside the space charge region. Hence, the ions then enter the sheath with the ion acoustic (or Bohm) velocity $v_B = \sqrt{k_B T_e/m_i}$ [38]. At the sheath edge, the deviation from the undisturbed electron density is given by the Boltzmann factor $n_e \exp(e\phi_{pre}/(k_B T_e))$ and, assuming quasi neutrality in the presheath, is equal to the ion density development. Then, with an ion density dilution at the sheath edge of $n_i \exp(-1/2)$ and all ions being directed to the probe, the ion saturation current is [166]

$$I_i^B = \exp\left(-\frac{1}{2}\right) A_s n_i e v_B \quad . \quad (4.6)$$

The effective ion collecting area then corresponds to the sheath surface A_s . Equation (4.6) is known as the Bohm current. The sheath edge is defined as the point where the quasi-neutral presheath solution becomes singular ($|E| \rightarrow \infty$). In fact, the transition from plasma to boundary is continuous. Therefore, the concept of a sheath edge is a feature of different physical approximations for the presheath and the sheath. Hence, using a model that features both, sheath and presheath, as in Section 6.3, the sheath boundary is taken at the point where $v_i = v_B$. For a discussion of the sheath edge definition and Bohm criterion in the collisional case see Riemann [35, 40] and Franklin [167, 168, 169].

For the thick sheath regime of a spherical or cylindrical probe when $r_p \ll \lambda_D$, the trajectory of plasma particles attracted by the probe may perform hyperbolic

orbits around the probe. The approach of Mott-Smith and Langmuir was the consideration of an infinite sheath, so that none of the plasma particles is prevented from reaching the probe by any effective potential barriers. Analogous to the outlined calculation in Section 2.2.1 for a cylindrical probe with length $l \gg r_p$ the OML electron current becomes

$$I_e = I_e^{sat} \left(\frac{2\sqrt{\eta}}{\sqrt{\pi}} + e^\eta \operatorname{erfc}(\sqrt{\eta}) \right) \quad (4.7)$$

$$\approx I_e^{sat} \left(\frac{2}{\sqrt{\pi}} \sqrt{1+\eta} \right) \quad , \eta > 1 \quad . \quad (4.8)$$

With the normalized probe bias

$$\eta = \frac{e(V_p - \phi_p)}{k_B T_e} \quad (4.9)$$

the saturation current is now voltage dependent. While for a cylindrical probe $I_{e,i} \propto \sqrt{\eta}$, the calculation for a sphere yields $I_{e,i} \propto \eta$ for $\eta > (3 \cdots 5)$. The corresponding equation for the ion saturation current to a cylindrical probe then is

$$I_i \approx I_i^{sat} \left(\frac{2}{\sqrt{\pi}} \sqrt{1 - \frac{e(V_p - \phi_p)}{k_B T_i}} \right) \quad . \quad (4.10)$$

Again, corresponding to the collection radius b_c in Section 2.2.1, an absorption radius

$$r_c = r_p \frac{2}{\sqrt{\pi}} \sqrt{1 - \frac{e(V_p - \phi_p)}{k_B T_i}} \approx r_p \sqrt{1 - \frac{e(V_p - \phi_p)}{k_B T_i}} \quad (4.11)$$

can be defined from Eq. (4.10) for a cylindrical geometry.

Comparing Eqs. (4.1) and (4.6), a recognizable feature of a probe characteristic in a low temperature plasma is the ratio of electron saturation current to the ion saturation (Bohm) current,

$$I_e^{sat}/I_i^B \approx 178 \frac{A_p}{A_s} \quad , \quad (4.12)$$

which can be typically 20–100 depending on the thickness of the space charge sheath.

Bohm, Burhop and Massey have substituted the artificial concept of an infinite sheath by an absorption radius [38]. In another extension, Bernstein and Rabinowitz have introduced the existence of potential barriers due to the angular momentum of incoming particles [170]. This effect has been picked up by Lampe in connection with the shielding of charged dust particles in a plasma [46, 47]. In the ambitious numerical works of Laframboise [26] and, parallel in time, in Hall and Fries [171], a Maxwellian distribution of attracted particles has been included in the OML model [170]. Several parameterizations of Laframboise's numerical results exist to make it more practicable in plasma diagnostics [172, 173, 174, 175, 176]. A review of the OML-theory can be found in [177].

4.2.2 Radial motion of ions

With respect to $T_i/T_e \ll 1$ in low plasma density discharges, Allen, Boyd and Reynolds studied the ion current to a spherical probe in the limit of cold ($T_i/T_e = 0$) ions [27]. Starting from rest at infinity towards an attracting probe, the ion motion is strictly radial. They obtained the following differential equation:

$$\frac{d}{d\xi} \left(\xi^2 \frac{d\eta}{d\xi} \right) - J_{sph} \eta^{-1/2} + \xi^2 e^{-\eta} = 0 \quad , \quad (4.13)$$

with $\xi = r_p/\lambda_{De}$. $J_{sph} = I_i/(2\sqrt{\pi}I_\lambda(A_\lambda^{sph}))$ is the normalized current to the probe,

$$I_\lambda(A_\lambda^{sph}) = \frac{1}{4} A_\lambda^{sph} n_i e \sqrt{\frac{8 k_B T_e}{\pi m_i}} \quad , \quad (4.14)$$

and $A_\lambda^{sph} = 4\pi\lambda_{De}^2$. Thus, Eq. (4.14) represents the random ion current through the surface of the Debye sphere λ_{De} if the ions had electron temperature. We assume only singly charged positive ions. Solving the equation numerically, ion current characteristics for a given ξ can be calculated. The ABR theory represents the correct limit for $T_i/T_e \rightarrow 0$ for the monoenergetic ion solution of Bernstein and Rabinowitz and the Maxwellian distribution of Laframboise for spherical probes. Chen [178] has proposed an analogous formulation for infinitely long cylindrical probes:

$$\frac{d}{d\xi} \left(\xi \frac{d\eta}{d\xi} \right) - J_{cyl} \eta^{-1/2} + \xi e^{-\eta} = 0 \quad , \quad (4.15)$$

with $J_{cyl} = I_i/(2\sqrt{\pi}I_\lambda(A_\lambda^{cyl}))$, I_λ given by Eq. (4.14) and $A_\lambda^{cyl} = 2\pi l_p \lambda_{De}$, where l_p is the length of the probe that collects the current I_i . Some results of ξ applicable in this work are given in Fig. 4.3. It is known as the ‘‘cold ion paradoxon’’,

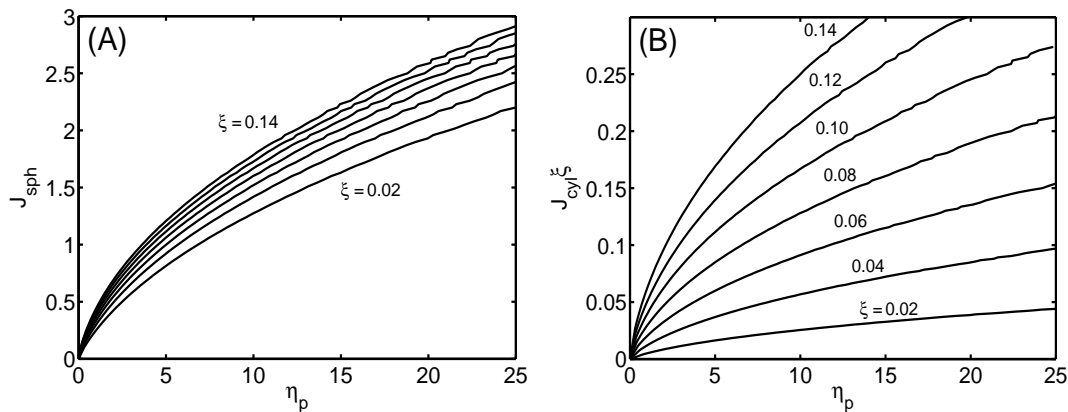


Figure 4.3: Radial motion ion currents J_{sph} , $J_{cyl}\xi$ versus probe potential $-\eta$ for spherical probes (A) and cylindrical probes (B) for various ratios of $\xi = r_p/\lambda_{De}$.

that the radial motion for cylindrical probes (Eq. (4.15)) does not fit the OML-theories [170, 26] in the limit $T_i/T_e \rightarrow 0$ [165].

4.2.3 Comparison of theories for the ion current

For the purpose of sampling densities in plasmas of small volumes, measurements in the ion collection regime are preferable over electron collection. Since the ion current is much smaller than the electron saturation current, the perturbation of the plasma by the probe is as well smaller. Often no inflection point can be found in the current-voltage curve at the plasma potential. This is an effect of potential shifting by the rf fluctuations and the non-negligible electron depletion created by the probe in very low density plasmas (see Section 5.1). In such cases it is hardly possible to derive information from the electron dominated part of the characteristic and the analysis has to concentrate on the ion current.

Two different approaches exist for the ion collection of cylindrical probes, OML and ABR. The detailed OML calculation of Laframboise [26] and Hall and Fries [171] cover essentially the entire range of r_p/λ_D , T_i/T_e and η for practical probe operation conditions in the collisionless limit. Sonin [179] confirmed the or-

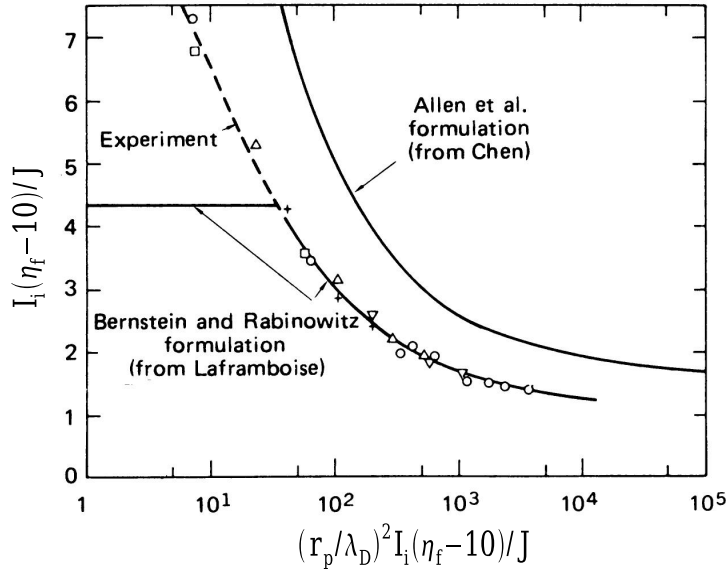


Figure 4.4: Sonin plot comparing OML (Bernstein and Rabinowitz formulation [26]) and ABR (Allen et al. formulation [178]) theory with experimental data for ion current collection of cylindrical probes. From [179].

bitual motion theory of Bernstein and Rabinowitz for large probe radii, but not for probe radii smaller than the sheath thickness. Under these conditions the OML probe current I_i is supposed to saturate for decreasing r_p as shown in Fig. 4.4. The figure provides a Sonin plot which is the usual way to compare experimental points with the theory curves of OML and ABR and determine whether the one or the other is applicable. But Sonin's experimental data exhibit an increasing behavior of the probe current with decreasing r_p as it is predicted by ABR. His measurements for $\xi = r_p/\lambda_{De} < 2.8$ fall between OML and ABR, as well as measurements by Sudit and Woods [180], Bryant *et al.* [164], and measurements performed for this study. More recent experiments have also shown, that

OML-theories often underestimate the ion currents or, as a result, overestimate the derived ion density by a factor up to ten compared to the electron density which is calculated from the saturation current at the “knee” of the characteristic [180, 181].

In contrast to Sonin’s findings [179], Annaratone *et al.* [182] observed better agreement of their experiments with the radial motion model than with OML over the whole range of ξ . Nevertheless, ignoring current reduction by potential barriers and trapped or orbiting ions, the cold-ion model overestimates the current under collisionless conditions [165]. Theoretical characteristics for OML and ABR in comparison with a measurement from one of the experiments treated in this work are shown in Fig. 4.5. The diagram provides synthetic probe characteristics with ion currents derived from OML-theory, ABR, and ABR with a correction for ion-neutral collisions (see Section 4.3) for a given set of plasma parameters. These parameters estimate the conditions in the discharge experiment from which a real characteristic is also shown in the plot. It is seen that, with all three electron saturation currents matching the measurement, only the collision corrected ABR model reproduces all experimental data points, while OML severely underestimates and simple ABR overestimates the ion saturation current. A Sonin plot corresponding to Fig. 4.4 based on experimental data of the present work is provided in Section 5.2.

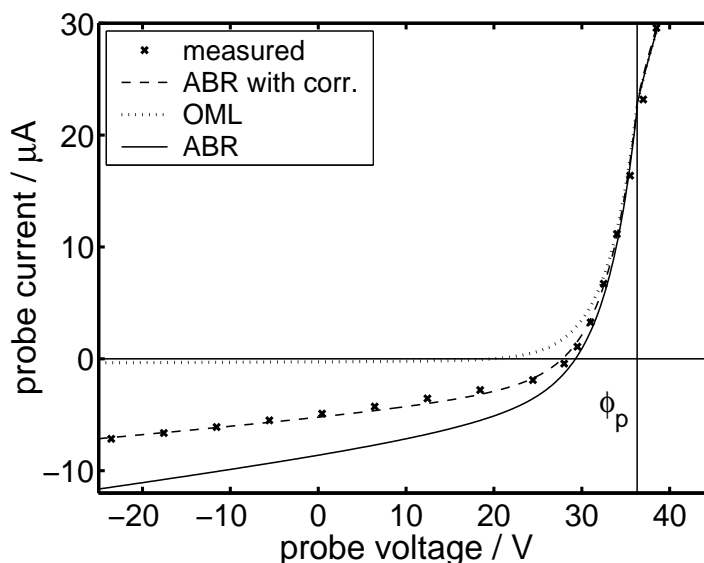


Figure 4.5: Three synthetic characteristics for a cylindrical probe ($r_p = 25 \mu\text{m}$, $l_p = 4 \text{ mm}$) and given plasma parameters of $T_e = 3.4$, $n_{e,i} = 6.5 \cdot 10^{14} \text{ m}^{-3}$ and $\phi_p = 36.3 \text{ V}$ are shown: (OML) is derived from Eqs. (4.8)–(4.10), (ABR) from Eq. (4.15) for the ion and Eq. (4.8) for the electron current. (ABR with corr.) takes into account the density correction for few collisions in the presheath of the probe (Section 4.3). Crosses mark a measurement in the PKE experiment at comparable conditions.

Summarizing the results of other authors and our own findings, experimental probe data for the ion current collection regime of a probe shows no saturation

for small probe radii as expected by the Orbital-Motion-Limit nor does it reach the current magnitude predicted by ABR. The influence of even a few ion-neutral and ion-ion collisions on the ion collection has been already stated by Schulz and Brown [183] in 1956, and has been made responsible for the above effect by several authors [164, 165, 180, 184, 185].

With a small but finite ion temperature T_i , orbital motion of ions should limit the current to the probe, which is surrounded by a thick sheath ($r_p/\lambda_{De} \ll 1$). When λ_{De} becomes comparable to λ_{mfp} , ions colliding with neutral gas atoms or other ions lose their angular momentum and will move radially towards the probe as it is claimed by ABR. As the cross section for ion-ion collisions increases rapidly with decreasing T_i , there should even be always enough ion-ion collisions to destroy OML effects [185]. Therefore the ion current is increased due to the reduction of orbital motion. In practice, a validity condition [178, 164, 182, 185] for the neglect of OM effects can be formulated: Following Annaratone *et al.* [182], the angular momentum of ions at least grazing the surface of a volume around the probe with the radius r_c (see Eq. (4.11)) and being collected is

$$L = r_c m_i \sqrt{\frac{2k_B T_i}{m_i}} . \quad (4.16)$$

Assuming that the mean free path λ_{mfp} is less than the linear dimensions of the plasma, the maximum allowed angular momentum is

$$L_{max} = \lambda_{mfp} m_i \sqrt{\frac{2k_B T_i}{m_i}} . \quad (4.17)$$

Thus, the OML theory will not be valid if $L > L_{max}$. This yields

$$\lambda_{mfp} < r_c = r_p \sqrt{1 - \frac{e(V_p - \phi_p)}{k_B T_i}} \approx r_p \sqrt{-\frac{e(V_p - \phi_p)}{k_B T_i}} . \quad (4.18)$$

Then, for parameters of $T_e = 3.5$ eV, $T_i = 0.026$ eV (a common assumption for low pressure discharges) and $r_p = 25$ μm , the mean free path must be less than 650 μm at a maximum probe voltage $\eta = -5$. This is fulfilled for all experiments in PKE and IMPF at a pressure of 15 Pa and higher.

When the number of collisions in the presheath of the probe is further increased, for example by increasing the background gas pressure, the ions experience a resistance, which yields again a current reduction. Thus, an ion current maximum is expected for weakly collisional conditions as it is the case in typical PKE and IMPF plasmas and the use of radial motion theory is justified. Fig. 4.6 plots the ratio n^{isat} , obtained from ABR theory, to n^{esat} derived from the electron saturation current with OML versus $\lambda_{mfp}/\lambda_{De}$. While in an undisturbed plasma $n_i = n_e$, the plasma densities obtained from real measurements often show $n^{isat} \neq n^{esat}$, although their magnitudes are similar. This is caused, since $n^{isat,esat}$ are determined from different parts of a probe characteristic where the plasma may be more or less perturbed by the current which is drawn by the

probe. A second reason is given by the different models the data analysis is based on. Therefore, the abbreviations for the measured densities $n^{i\text{sat},e\text{sat}}$ are chosen to be clearly distinguishable from $n_{i,e}$. Here, the current reaches a maximum

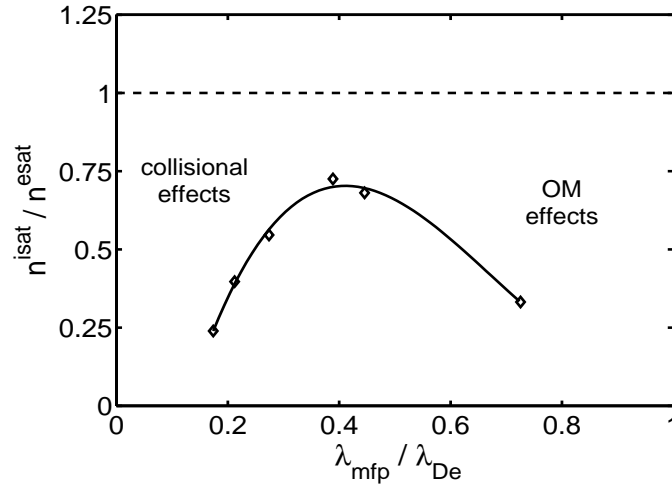


Figure 4.6: Ion density $n^{i\text{sat}}$, obtained by curve fitting of the ABR theory to the ion current characteristic, to electron density $n^{e\text{sat}}$ from saturation current at ϕ_p over $\lambda_{\text{mfp}}/\lambda_{\text{De}}$. The curve shows a peak, when weak collisionality is given ($\lambda_{\text{mfp}}/\lambda_{\text{De}} \approx 0.4$) and, thus, orbital motions are destroyed, but current reduction by collisions is still not dominant. The background gas is argon.

at $\lambda_{\text{mfp}}/\lambda_{\text{De}} \approx 0.4$ for argon gas. Left from the peak, towards the collisionless limit, orbital motion is possible and the ion current and therefore the derived ion density are reduced. On the other side, with collisions becoming dominant, the measured density is also reduced. Obviously even the peak density value is only about 70 % of the measured ion density, since the presence of collisions does not meet the assumption of the ABR theory for collisionlessness. For this special case, Shih and Levi have developed a theory that accounts for few collisions in the presheath and allows the correction of the ion density measured with ABR for this effect [185] (see Section 4.3).

4.3 Analysis with collisions

Based on previous numerical work of Self and Shih [186], Shih and Levi [185] presented an approximate formula for the correction of reduced density values due to weak collisionality. Their approach is essentially a modification of the radial motion concept. To account for collisions, they added a friction term to the ion equation of motion and calculated the additional ohmic potential drop $\phi_{\text{coll}} = \eta_{\text{coll}} k_B T_e / e$ in the presheath which allows the correction of densities obtained with the collisionless ABR theory. This presheath model for spherical probes is also utilized to calculate the local ion velocity and the resulting drag forces on charged dust particles in Section 6.3. Following on, the necessary results for

the analysis of cylindrical probe characteristics, are extracted from the work of Bryant *et al.* [164] who have consolidated the finding of Shih and Levi.

It was shown in Section 4.2.3, that it is adequate to use ABR theory to derive the plasma density from the ion part of a characteristic of a probe, because orbital motion of ions is destroyed by collisions. The theory of Shih and Levi [185] requires a few collisions to occur in the sheath to limit orbital motion, but not so many that the ABR current is significantly impeded (see Fig. 4.6). Under the experimental conditions treated in this work, this is a valid assumption for neutral gas pressure of $p_{argon} \approx (20 \cdots 50)$ Pa. It is then assumed that ion-neutral and ion-ion collisions occur mostly in the presheath of the probe as claimed by the model in [164, 185].

For describing the physics of the presheath surrounding a cylindrical probe, it is clever to use spheroidal coordinates ζ, μ [185] (see Fig. 4.7). The transformation relations to the cylindrical coordinates ρ, z are

$$\frac{\rho^2}{\zeta^2 - 1} + \frac{z^2}{\zeta^2} = L^2 \quad , \quad \frac{\rho^2}{\mu^2 - 1} + \frac{z^2}{\mu^2} = L^2 \quad (4.19)$$

Under the assumption, that the potential η varies only with the length coordinate ζ , the equi-potential surfaces are confocal prolate spheroids. With a focal distance of $L = 2l_p$, for $\zeta \ll 1$ such a surface fits to the cylindrical shape of the probe, while for $\zeta > 1$ it approximates a sphere. Hence, the finite length of the probe is properly taken into account. Another advantage derives from the alternative use of cylindrical coordinates yields a singularity in the electric field at infinity. Then ions are assumed to move with a velocity v_i perpendicular to $\zeta = const.$

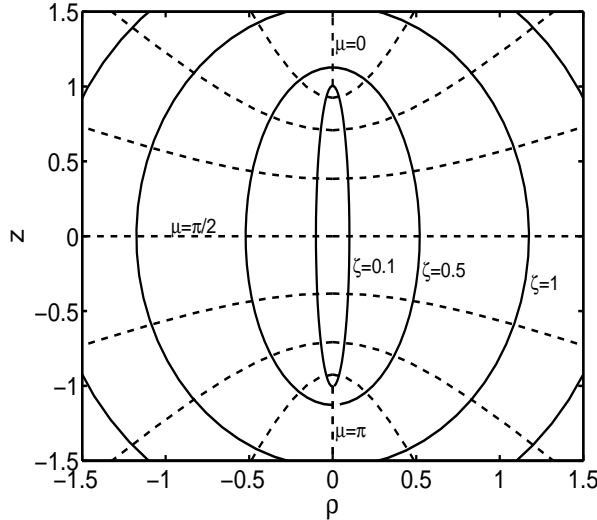


Figure 4.7: Spheroidal coordinates as function of the cylindrical coordinates ρ, z : length coordinate $\zeta \geq 0$ and angular coordinate $0 \leq \mu \leq \pi$. For $\zeta > 1$ the surfaces with $\zeta = const.$ approximate a sphere.

The set of ion continuity equation, ion equation of motion, and Poisson's

equation becomes, analogous the the spherical case in Section 6.3,

$$\frac{\partial}{\partial \zeta}(f_1 f_2 N V) = 0 \quad (4.20)$$

$$\frac{\partial}{\partial \zeta} \left(\frac{v^2}{2 + \eta} \right) = \frac{v L f_1}{\lambda_D f_2} V \quad (4.21)$$

$$\frac{\partial}{\partial \zeta} \left(f_2^2 \left[\frac{\partial \eta}{\partial \zeta} \right] \right) = \left(\frac{L}{\lambda_D} \right)^2 f_1^2 (\exp(\eta) - N) \quad , \quad (4.22)$$

with the normalized ion velocity $V = v_i/v_B$, local density $N = n_i/n_{e\infty}$ and $v = \nu_i/\omega_{pi}$, where $\nu_i = v_{ti}n_n\sigma$ is the ion collision frequency and $\omega_{pi} = (n_{i\infty}e^2/(\epsilon_0 m_i))^{1/2}$ is the ion plasma frequency. n_n stands for the neutral density. In the experiments, it is approximately 10^6 times higher than n_i . Therefore, only ion-neutral collisions are taken into account and σ is the sum of the gas kinetic and the charge exchange cross section. For clarity, the undisturbed plasma density far away from the probe is named $n_{e\infty}$. The current I_i drawn by the probe is normalized similar to the case of a spherical probe (see Eq. 4.14) with $J = I_i/(\sqrt{2\pi}I_\lambda(A_\lambda^{cyl}))$. (Note the lack of the factor $1/\sqrt{2}$.) Moreover $f_1 = (\zeta^2 - \mu^2)^{1/2}$ and $f_2 = (\zeta^2 - 1)^{1/2}$.

With approximations, which are using the spheroidal shape of the potential geometry far from the probe, the current continuity equation can be derived as

$$J = \frac{1}{2} \left(\frac{L}{\lambda_{D0}} \right)^2 f_2 \exp(\eta_0) (-2\eta_0)^{1/2} \left((\zeta^2 - 1)^{1/2} + \zeta^2 \sin^{-1} \left(\frac{1}{\zeta} \right) \right) \quad . \quad (4.23)$$

The subscripted “ $_0$ ” indicates a value as obtained from the collisionless case. A series expansion for the potential in Eq. (4.23) then reads

$$\eta_0 = -\frac{1}{2} \left(\frac{\lambda_{D0} \sqrt{J}}{L} \right)^4 (x^4 + \frac{4}{3}x^6 + \dots) \quad , \quad (4.24)$$

where $x = 1/\zeta$. Shih and Levi [185] and Bryant *et al.* [164] assume, that the Bohm criterion (Eq. (2.4)) is still valid in the presence of few collision. Thus, $\eta_{s0} = -1/2$ and the position of the sheath edge x_{s0} can be calculated. J is directly given by the actual normalized probe current. The normalized energy equation $V^2/2 = -\eta$ and Eq. (4.24) then yield

$$V_0 = \left(\frac{\lambda_{D0} \sqrt{J}}{L} \right)^2 (x^2 + \frac{2}{3}x^4 + \dots) \quad . \quad (4.25)$$

Equation (4.21) can be integrated to give the total potential drop in the presheath

$$\eta_s = -\frac{1}{2} - \eta_{coll} \quad , \quad (4.26)$$

with

$$\eta_{coll} = -\frac{vL}{\lambda_{D0}} \int_0^{x_{s0}} \frac{\sqrt{1 - \mu^2 x^2} V}{\sqrt{1 - x^2} x^2} dx \quad . \quad (4.27)$$

The additional ohmic drop η_{coll} becomes

$$\eta_{coll} = \frac{vJ\lambda_{D0}}{L} \left[x_{s0} + \left(\frac{7}{18} - \frac{\mu^2}{6} \right) x_{s0}^3 + \dots \right] , \quad (4.28)$$

when replacing V and λ_D in Eq. (4.27) by V_0 and λ_{D0} and expanding and integrating term by term. With $\mu^2 \approx 1$

$$\eta_{coll} \approx \frac{vJ\lambda_{D0}}{L} \left(x_{s0} + \frac{4}{18} x_{s0}^3 \right) . \quad (4.29)$$

Finally, with the presheath edge position x_{s0} calculated from the first zero of Eq. (4.24), the potential drop due to collisions can be approximated with Eq. (4.29). Remembering quasi neutrality in the presheath, the density n^{isat} obtained from the collisionless ABR model is then simply corrected for collisions by the Boltzmann factor for electron depletion. Therefore,

$$n^{icoll} = n^{isat} \exp(\eta_{coll}) . \quad (4.30)$$

Developing the perturbation method, Shih and Levi considered additional potential drops $\eta_{coll} \ll 0.5$. In [164] the applicability of the method up to $\eta_{coll} \approx 1$ was demonstrated. In the experiments presented here, for $0.25 < \lambda_{mfp}/\lambda_{De} < 0.4$ which corresponds to discharges with 20–50 Pa argon pressure, the corrected ion density n^{icoll} and the density n^{esat} obtained from the electron saturation current agree within 20 %. For lower gas pressures, Sudit and Woods [180] found the correction formula from [185] to be more successful than OML theory, but they still observed discrepancies to the derived electron density.

4.4 Finite length of a probe

Basic probe theories require a simple geometry of the probe, like spheres, cylinders of infinite length or planes without boundaries. The MF-microspheres immersed in a dusty plasma act like spherical probes, but a real probe needs a connector and a fixture, that both break the symmetry, and must be much smaller than the dimensions of the plasma. For a cylindrical probe the claim for infinite length is understood to be satisfied, when the aspect ratio $r_p/l_p \ll 1$. To allow spatially resolved measurements and not to disturb the central PKE plasma which has a maximum diameter of 4 cm, the length of the cylindrical probe cannot be larger than a few millimeters. With $r_p/l_p \approx 25 \mu\text{m}/3500 \mu\text{m}$ this requirement is fulfilled for the PKE and IMPF experiments. But if the effective current collecting area is not the probe surface itself, but an area given by the thickness of the sheath, the ratio is dramatically changed. Assuming the extent of the sheath around the probe to be of the order of a few $\lambda_{De} \approx 400 \mu\text{m}$, the effect of the ends on the sheath geometry surrounding the probe must be considered.

An obvious approach is to approximate the total current to a finite probe by the current to a theoretical cylindrical probe of length l_p and radius r_p plus the

current to a hemisphere of radius r_p at the end of the probe. Jaeger *et al.* [187] have modeled the trajectories of ions in the field of an infinite cylindrical probe and calculated the resulting current. The results have been compared with the current I_i obtained from OML theory for a cylinder $I_{i,cyl}$ and for a sphere $I_{i,sph}$ as

$$I_i = I_i^{cyl} + kI_i^{sph} \quad . \quad (4.31)$$

For the hemisphere representing the end cap of the probe, $k = 1/2$. The method was found to be a good approximation and has been discussed for instance in [176, 188]. Remembering the linear dependence of I_e^{sph} and the square-root dependence of I_i^{cyl} on the probe bias V_p , the slope of the development of the ion current with V_p is increased by the additional spherical part. This tendency is also valid for

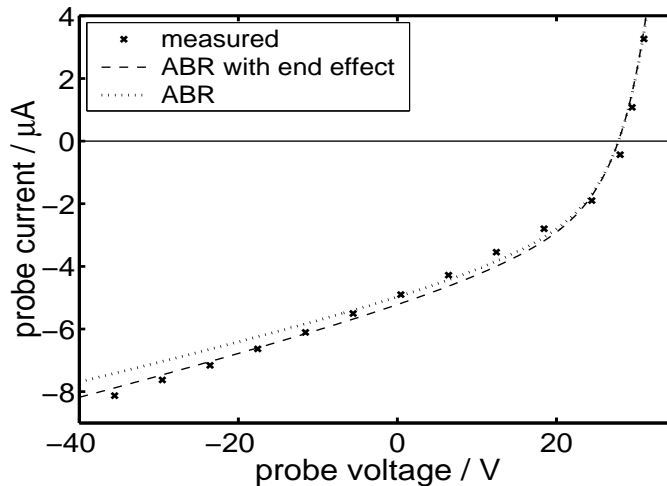


Figure 4.8: Ion saturation part of a cylindrical probe characteristic with modeled curves from ABR theory with and without an additional part of current from a spherical probe that represents the end effects of the probe.

ABR theory and the method will be used for probe characteristic analysis in this work. As the area of the cylindrical part is much larger than that of the spherical part of the probe, the total current is only slightly increased but a theoretically generated I - V -curve fits obviously better to a real characteristic as it is shown in Fig. 4.8 with $k = 0.75$.

While the probe has an end at one side, it has insulating parts of the fixture, carrying the probe, on the other. Nevertheless an “end effect” exists here, too. A ceramics tube with a diameter of $500 \mu m$ contains the tungsten wires of the IMPF and PKE probes on that side. As a result, a part of the probe is shadowed from plasma particles with a non-perpendicular trajectory to the probe axis and the current contribution from the second end of the probe is reduced. Thus, for further analysis, k was empirically adjusted to $k = 0.75$.

4.5 Probe data processing

Section 3.4 provides an overview of the efforts that have been spent on the hardware side to optimize the probe system for the measurements in the small and dusty RF-plasmas of the PKE and IMPF experiments with time-limit under microgravity conditions. In this section, the combination and adjustment of probe theory regarding the weak collisionality, low temperature, low density, and small size of the plasma will be summarized. This is done by explaining the structure of the algorithm for probe data analysis, which is sketched in Fig. 4.9.

In a first step, start values for the modeling of a theoretical characteristic are generated from the measured characteristic with the help of simple approximation formulae. Because of the possible disturbance of the plasma by high electron currents drawn by the probe, so that the “knee” of the curve disappears for these small-volume low-density discharges, the analysis will focus on the ion collection part of the probe data. This is done by weighting the ion current with a factor typically up to 200 for the later comparison of experimental data and modeled characteristic with a least-square method. With the help of the start values the parameter ξ is calculated in a next step and the appropriate ion current curve are chosen from a pre-computed set of ABR characteristics as they are shown in Fig. 4.3. ABR theory has been chosen since the low T_i and even weak collisionality favors the radial motion of the ions.

Bearing in mind the problem of the end effect of a finite cylindrical probe when the plasma density is low and thus the large shielding length changes the effective aspect ratio of the probe, this is done for the cylindrical as well as for the spherical geometry (see Section 4.4). For generation of the theoretical OML electron current curve, first n^{isat} has to be corrected for collisions in the presheath as described in Section 4.3. Then the OML curves for both basic probe geometries are derived from n^{icoll} and the start values T_e, ϕ_p . Combining the contributions of k times spherical probe current and cylindrical probe current of ion and electron collection parts, the modeled current-voltage-curve is completed.

Summing up the least-square-residuals of experimental and theoretical curves and their first derivatives decides whether the fit is successful or not. In the latter case the generation of a modeled curve restarts with slightly varied values for T_e, ϕ_p and n_i until the exit condition is fulfilled. In a last step, the electron density n^{esat} is then calculated from the electron saturation current at the fitted value of ϕ_p . The algorithm provides $T_e, \phi_p, n^{esat}, n^{isat}$, and n^{icoll} as results. Following on, n^{icoll} and n^{esat} are used to quantify the plasma density and, in comparison, to evaluate the consistency of the two different analysis methods, with which the values are derived.

Even if the presented algorithm is adjusted to various effects that are found in the PKE and IMPF discharges, it cannot account for all, since theories would be too complex or simply do not exist. One aspect, for example, is the anisotropic ion velocity distribution which is a result of the ion acceleration radially outwards from the center to the boundaries of the plasma. The strength of the responsible electric field is a consequence of the small-sized discharge volume in connection

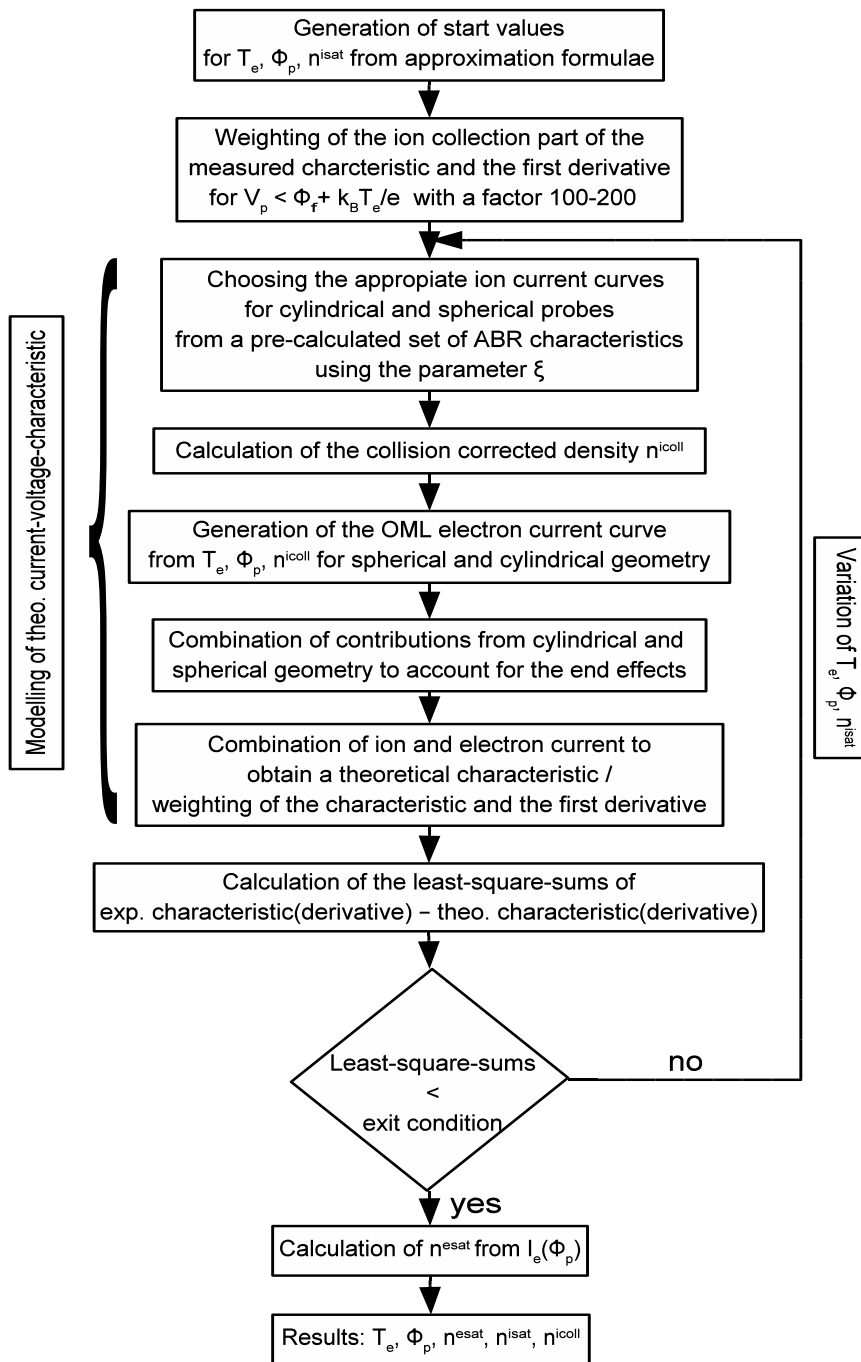


Figure 4.9: Scheme of the probe characteristic analysis algorithm.

with mean free path, that yields centrally peaked potential profiles (compare with Section 5.3). Another effect is the influence of the fixture parts of the probe on the effective geometry of the current collecting probe-tip which is discussed in Section 6. It should also be kept in mind that the above considerations require the presence of only one species of singly charged positive ions.

5 Characteristics of particle-free discharges

This chapter addresses the determination of the performance of the Langmuir probe hardware design and analysis method as diagnostics in the experiments PKE and IMPF and their characterization by quantitative plasma properties. The first section is concerned with the influence of the probe on the discharge, which have to be considered in finite plasmas to estimate the validity of the method. Further on, the exploration of plasma properties as a function of the discharge parameters is done by comparing measurements with corresponding simulations in magnitude and spatial distribution. Since only particle-free plasma simulation codes have proved their suitability to make quantitative predictions and complex plasmas can potentially adversely affect probe measurements (see Section 3.4.2), this section is focused on dust-free discharges.

5.1 Effects by the probe

Probe theories assume that the dimensions of a probe inserted into a plasma are negligible compared to the size of the plasma. The plasma can then be considered as infinite and the influence of the probe on the discharge is negligible as well. For a small discharge chamber like the PKE experiment with its inter-electrode distance of 30 mm and an expected electron shielding length λ_{De} of the order of 0.4 mm, it is impossible to build a “small” probe, because even a fine wire inserted in the discharge will develop a sheath around it. As mentioned, this sheath extends up to a few λ_{De} and therefore even the smallest probe may affect the plasmas.

Since the properties of a discharge are a priori unknown, but the measured values may be influenced by the presence of the probe, the idea of studying these influences is to insert a second probe. The second probe can be inserted into and retracted from the plasma, while the first one scans possible changes in the plasma parameters, that are related to the action of the second probe. It is assumed, that the first probe in a plasma causes comparable effects as the additional second probe.

Besides the plasma parameters obtained from the probe, the discharge current to the electrodes has been studied in dependence of probe operation (see ampere meters in Fig. 3.1). Since the (negative) self-biasing of the PKE and IMPF

electrodes is suppressed by dc paths to ground, the electron confinement in the plasma is less effective and negative currents to ground establish to compensate the enhanced plasma losses on the electrodes. Due to the complex self-adjusting processes and the resulting current balance of the discharge, it is hardly possible to derive probe induced changes of plasma properties from the electrode current. This is especially true, when the current collecting (effective) area of the probe is unknown, since it depends on the local plasma parameters. Nevertheless the discharge currents are a measure for the current densities in the electrode-plasma interface, the sheaths, and can therefore serve as a qualitative indicator of plasma disturbances.

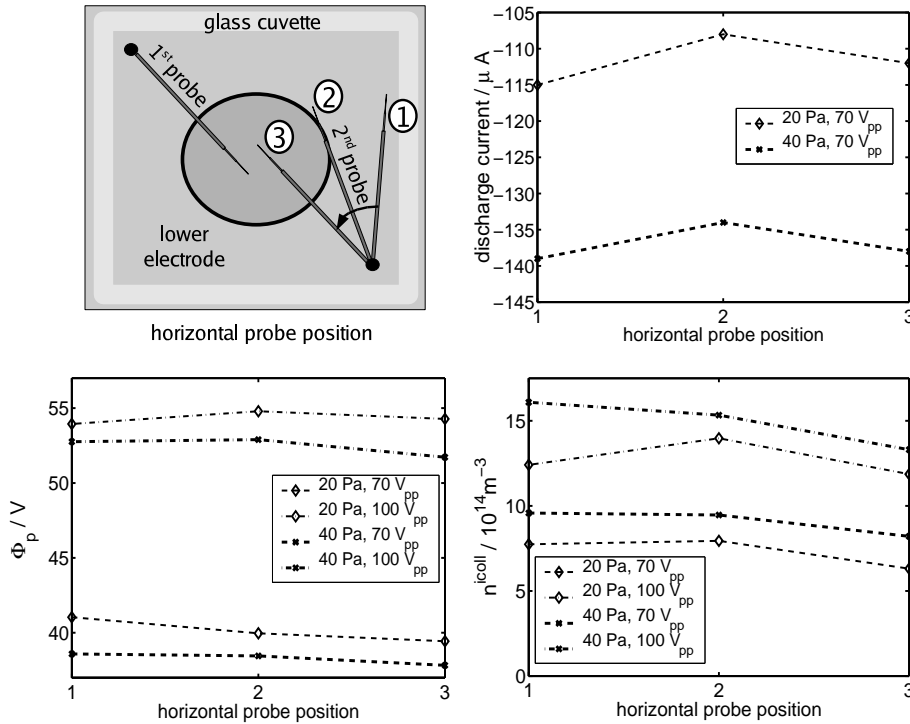


Figure 5.1: Discharge current, central plasma potential ϕ_p , and plasma density n^{coll} in dependence on the horizontal position of a second floating probe for various discharge conditions. The vertical position of the probe is in the mid-plane between the electrodes. The measuring first probe is located at 10 mm distance to position (3).

Figure 5.1 shows the development of the total electrode current and plasma parameters, measured by a second probe, in dependence on the position of a floating probe with respect to the plasma. Rotating the probe from the “neutral” position close to wall and far from the plasma to the border of the plasma glow, the central space potential and plasma density are mostly unaffected, although the absolute discharge current is reduced by approximately 5 %. When the probe is rotated further into the central plasma, but still with a closest distance of 1 cm from tip to the tip of the reference probe, the discharge current is again increasing, while the space potential is lowered by a maximum of 5 % with respect to the fully retracted probe. Due to the shielding effect of the plasma, the minimum

distance is large enough to exclude any interferences between the two probes. Noticeable are the plasma density measurements, that yield a reduction of up to 20 % for lower rf powers and thus lower absolute densities. A density reduction by the proximity of the probe has been expected, because the effective plasma boundary area and, as a result, the plasma particle losses are increased. In detail, we consider the charging currents of the floating support structures (ceramic tube and reference electrode) of the probe as the most perturbing parts. When biased close to the floating potential, the probe-tip itself contributes with less than 1 % to this current. Only with a positive bias $V_p > \phi_p$ the current drawn by the tip reaches the magnitude of the charging currents to the probe shaft.

The influence of a probe voltage sweep, which is used for measurements, on the floating potential ϕ_f in the central plasma and the discharge currents is shown in Fig. 5.2. In the range from minimum probe voltage $V_p = -2.5$ to $V_p = \phi_p$, which

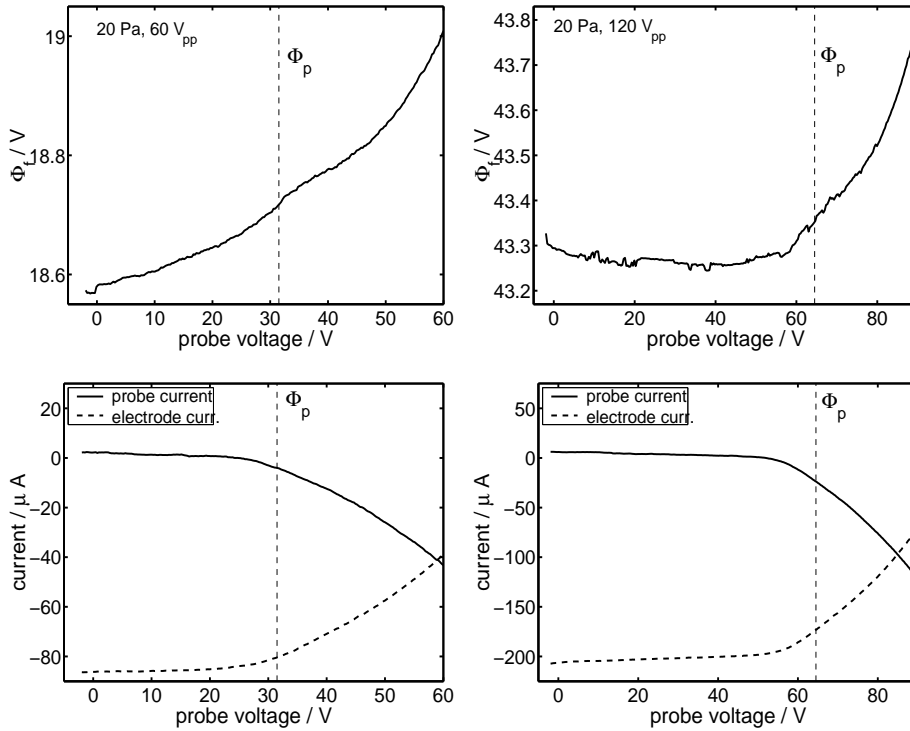


Figure 5.2: Floating potential ϕ_p and discharge currents to the electrodes vs. probe bias voltage for low (left) and high (right) rf power. Together with the electrode currents, the probe characteristic is given – contrary to the convention – with the correct sign.

is used to analyze a characteristic, the floating potential only changes within 1 % or less than 0.15 V, respectively. Since ϕ_f is closely related to ϕ_p (see Eq. (2.28)), these shifts are transferable to the behavior of the plasma potential. In the same bias interval the absolute electrode currents are typically lowered by 10 % in the low rf power regime and 16 % at high rf power. It is obvious from the measured probe characteristics, being also plotted in Fig. 5.2, that this corresponds exactly to the current drawn by the probe. This effect shows that the contact of the

plasma to other grounded parts of the chamber, like the top and base plates can be neglected and that the probe measurement circuit is closed to ground via the electrodes. Identifying the main loss region for the plasma at the electrodes, the current drain caused by the probe sampling is found to be still much smaller than the total loss of charged particles by other mechanisms.

Summarizing, the presence of a probe or any other floating body of a corresponding size, in the small-volume PKE plasma affects the discharge detectably. Nevertheless, the resulting errors in potential measurements are expected to be of the order of a few percent. Performing density measurements, a systematic error of approximately 20 % reduced values has to be taken into account. Data obtained at an applied probe bias, that exceeds the plasma potential substantially, should not be regarded in the data analysis.

Since the discharge volume of the IMPF vessel is four times larger than of PKE, corresponding effects lead to smaller errors in the derived plasma parameters.

5.2 Probe model verification

Probe data obtained from measurements under various discharge conditions are processed by fitting theoretical characteristics to the data. The quality of the fit is a first indicator if the used theoretical probe model is valid. The first evaluations of probe characteristics have been performed with the most commonly used OML theory for cylindrical probes. In Fig. 5.3 (A) a typical probe characteristic from the center of the PKE plasma and the best fit of this model, including Laframboise extensions [26] in the parameterized form suggested by [174], to the experimental data is shown. Although the model nearly matches the ion current part of the measured characteristic, the theoretical electron retardation current strongly exceeds the experimental data and does not saturate until $I_e^{sat} \approx 470 \mu\text{A}$ at $\phi_p = 51.9 \text{ V}$. This mismatch of the theoretical curve and the measured electron current becomes visible from Fig. 5.3 (B) which contains the same diagram as Fig. 5.3 (A) at a larger axis scaling.

Figure 5.4 provides a fit of the ABR model with correction for ion-neutral collisions [164] which is discussed in Section 4.5. The model data agrees very well with the experimental data, except for the missing “knee” in the measured characteristic and the non-saturating electron current. The ABR model gives a much closer representation of the ion current and the transition to the electron retardation regime. The OML model especially extrapolates the electron current for $V_p > \phi_f$ towards extremely high magnitudes which are inconsistent with the measured probe characteristics.

Plasma parameters derived from both model fits are presented in Tab. 5.2 in comparison with results from an appropriate SIGLO simulation. The plasma density $n_{e,i}$ following the OML model exceeds the density derived from the ABR model and the simulation by a factor of 15 which obviously results from the overestimation of the electron current by OML theory. A fit of the OML model to

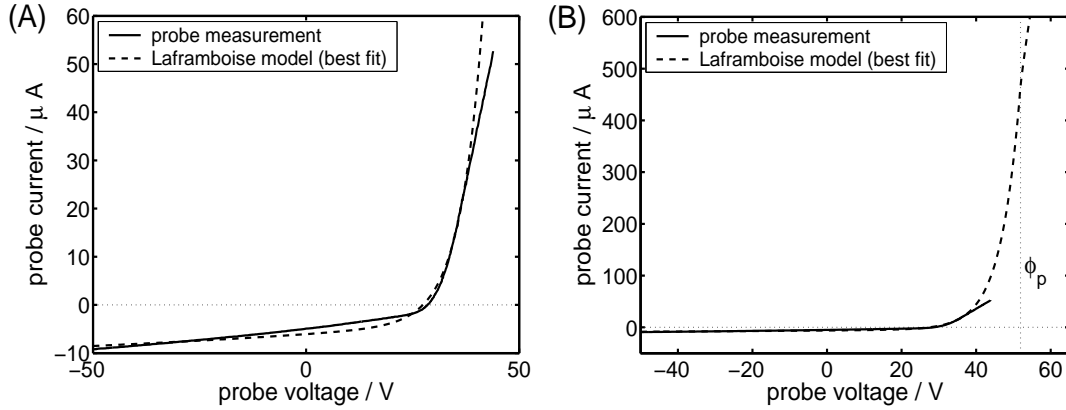


Figure 5.3: Probe characteristic and best fit of the standard OML probe model of Laframboise [26]. The model has been implemented after [174]. Both diagrams show the same data, but at different scale ranges. The vertical line marks the plasma potential ϕ_p as derived from the applied model. For the resulting plasma parameters see Tab. 5.2. The probe data is obtained from the center of a PKE plasma with $p = 40$ Pa and $U_{rf} = 60 V_{pp}$.

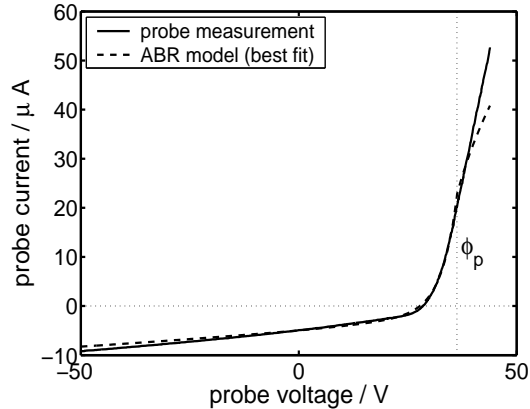


Figure 5.4: Probe characteristic and best fit of the model discussed in Section 4.5. The vertical line marks the plasma potential ϕ_p as derived from the applied model. For the resulting plasma parameters see Tab. 5.2. The probe data is obtained from the center of a PKE plasma with $p = 40$ Pa and $U_{rf} = 60 V_{pp}$.

only the measured electron current, would yield a theoretical ion saturation current, which is an order of magnitude too small to match the ion current regime of the probe characteristic. This discrepancy has been reported earlier, for example in [180], for low temperature plasmas. The OML model also yields a plasma potential of $\phi_p = 51.9$ V, which is noticeably larger than the expected value of $\phi_p \gtrsim U_{rf}/2$ [31]. In comparison, under the given experimental conditions, the extended ABR probe model provides plasma parameter values which are distinctly better supported by simulation and theory than by the OML model. Residual differences to the simulation results will be discussed in detail in Section 5.3.

Since the probe is an invasive device, that acts as a sink for plasma particles,

it is important to minimize the current, drawn by the probe, in order not to alter the nature of the plasma significantly. The analysis algorithm has thus been focused on the ion saturation and the electron retardation current. It has been shown above that, as a result, the OML probe model yields substantially too high measured plasma densities and, therefore, should not be used.

probe model	ϕ_p (V)	T_e (eV)	$n_{e,i}$ (10^{15}m^{-3})
(Ion-) OML/Laframboise	51.9	5.3	12.0
(Ion-) ABR/coll.	36.3	3.4	0.65
SIGLO	44	3.9	0.86

Table 5.2: Plasma parameters derived from a probe characteristic ($p_{gas} = 40$ Pa, $U_{rf} = 60$ V_{pp}) following an OML probe model, described in [174] and the collision corrected ABR model, discussed in Section 4.5, in comparison with results from the SIGLO code (new set of collision coefficients).

It is also known that the OML theory for cylindrical probe geometry does not approach the ABR theory in the limit of vanishing initial ion energy [177, 165], although ABR is valid under such an assumption. In the plasmas studied here, the gas temperature is equal to room temperature [22] and since the ions cannot follow the driving rf fields, effective ion thermalizing mechanisms do not exist, yielding $T_i \approx 0.026$ eV. Thus, the ions can be considered as “cold”. Regarding the measured electron densities from the example above, the deduced electron Debye length is $\lambda_{De} \approx 500$ μm , while the ion mean free path $\lambda_{mfp} = 123$ μm for 40 Pa and a total ion-neutral scattering cross section of $\sigma_t = 85$ \AA^2 [32]*. Since attracted ions then experience collisions, their initial angular momentum with respect to the probe is destroyed and radial motion towards the probe is favored. Further on, radial ion trajectories are expected also from attracted ions with zero initial energy. Therefore, an ABR theory based model is preferable for the studied low temperature discharges, as it has been generally discussed in Section 4.2.3.

The ion current predicted by Chen’s (collisionless) formulation [178] of the radial motion theory for cylindrical probes is slightly too large and exceeds the measured ion current by approximately 50 % under the given discharge conditions, as it has already been shown in Fig. 4.5. This current reduction is due to the resistive effect of ion-neutral collisions on the ion flux to the probe at relatively high gas pressures.

The influence of increasing gas pressure, yielding an increased collision frequency, on the deviation of measured currents from the ABR theory is demon-

*Recently, Hirt [55] performed ion beam experiments in a dc discharge at argon gas pressures of $0.1 \dots 10$ Pa and found the results to be in a good agreement with a total ion-neutral cross section of $\sigma_t = 125$ \AA^2 .

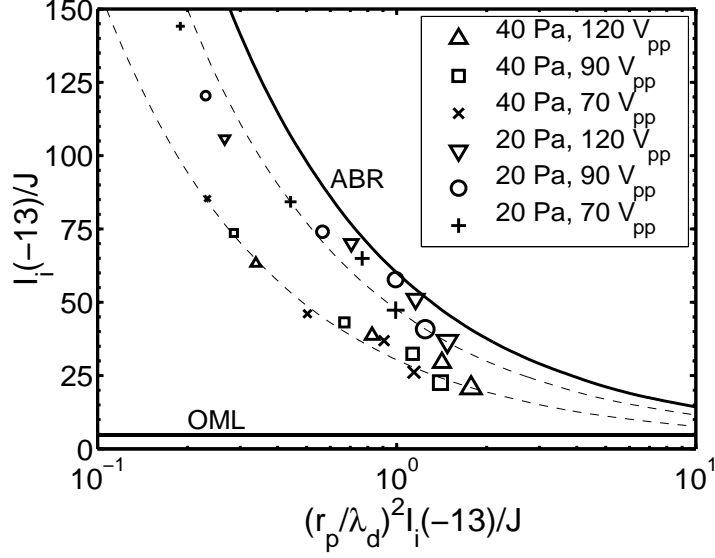


Figure 5.5: Sonin plot for probe data taken from the PKE experiment for 20 Pa and 40 Pa neutral gas pressure and various rf voltages. Solid lines represent ABR and OML curves. The dependence on the gas pressure is emphasized by the dashed lines. The size of the data point markers indicates the size of the probe: (\circ) $r_p = 25 \mu\text{m}$, (\circ) $r_p = 50 \mu\text{m}$, (\circ) $r_p = 75 \mu\text{m}$, (\circ) $r_p = 100 \mu\text{m}$.

p_{gas} (Pa)	U_{rf} (V _{pp})	T_e (eV)	n^{esat} (10^{15}m^{-3})	n^{isat} (10^{15}m^{-3})	$I_i(-15)$ (μA)	\sqrt{J}	η_{coll}	n^{icoll} (10^{15}m^{-3})
100	120	3.0	6.80	1.30	13.0	3.8	2.19	11.57
100	60	3.2	2.32	0.43	7.0	2.7	2.19	3.81
60	80	3.2	1.65	0.61	8.1	2.9	1.20	2.01
60	60	3.3	0.90	0.35	6.1	2.4	1.20	1.16
40	80	3.4	1.14	0.50	8.2	2.8	0.86	1.16
40	60	3.2	0.58	0.24	5.9	2.4	0.88	0.58
20	120	3.0	1.03	0.68	9.2	3.2	0.46	1.09
20	60	3.1	0.43	0.26	5.2	2.4	0.46	0.41

Table 5.4: Plasma densities n^{esat} , derived from the electron saturation current, n^{isat} from the ion saturation region and ion current $I_i(\eta_p = -15)$ obtained from central probe measurements in the PKE chamber under various discharge conditions. The collision correction (see Section 4.3) yields the additional ohmic drop η_{coll} and further on the corrected plasma density n^{icoll} .

strated in the Sonin plot in Fig. 5.5. Data points of ion saturation currents, obtained at equal neutral gas densities, are found on a single curve, even if they differ in the corresponding rf powers or probe dimensions. Such a curve can be simply derived from the curve representing the radial motion theory in the Sonin plot. Therefore, the use of the collision correction method for the ABR theory, presented in Section 4.3, is obvious. Figure 5.5 can be considered as the continuation of Fig. 4.4 for small ξ_p .

Bryant *et al.* [164] proved their extension of Shih and Levi's correction method [185] to be valid for neutral gas densities and resulting collision frequencies which yield an additional ohmic voltage drop in the presheath of the probe of up to $\eta_{coll} \approx 1$. It can be seen from Tab. 5.4 which lists analysis results of the corrected ABR model, that this condition is fulfilled for gas pressures up to about 60 Pa. To evaluate the results of density correction for ion-neutral collisions, yielding n^{icoll} , Tab. 5.4 also list n^{esat} , which is derived directly from the electron saturation current at ϕ_p using Eq. (4.1). The plasma potential ϕ_p itself is a result of the fit algorithm (see Section 4.5). With $p_{argon} < 60$ Pa, n^{esat} and n^{icoll} are in a good agreement. For higher gas pressures n^{icoll} is overestimated compared to n^{esat} . Nevertheless, the relative deviation of the uncorrected ion density value n^{isat} from n^{esat} is much higher than of n^{icoll} . Due to the lack of other suitable methods for this parameter range, the proposed method still remains the one to choose. The rf power, as second important discharge parameter, has no relevant effect on the analysis in the interval, which is appropriate for the experiments.

5.3 Characterization of the discharges

The previous section addressed the general suitability of the probe model to hold under the conditions of PKE and IMPF discharges. This was done by a detailed view on probe data from single measurements in the central bulk plasma. In the following, the experimental results are compared to parameters obtained from simulations, covering the whole range of experimental pressure and power constellations. Additionally, the comparison of two-dimensional plasma property profiles cares for the spatial resolution of probe measurements.

To do so, SIGLO simulations have been performed with both sets of scattering coefficients (see Section 3.5). A few data points have also been included from the simulation code used by Goedheer and Akdim [22, 189].

5.3.1 PKE

For a general characterization of the dust-free plasmas in the PKE chamber in dependence on the two discharge parameters (neutral gas pressure and rf voltage amplitude, representing a measure for the applied power) probe data and simulation results from the center of the plasma have been plotted in Fig. 5.6. Due to the geometry of the discharge setup, these parameters are the peak-values of the profiles.

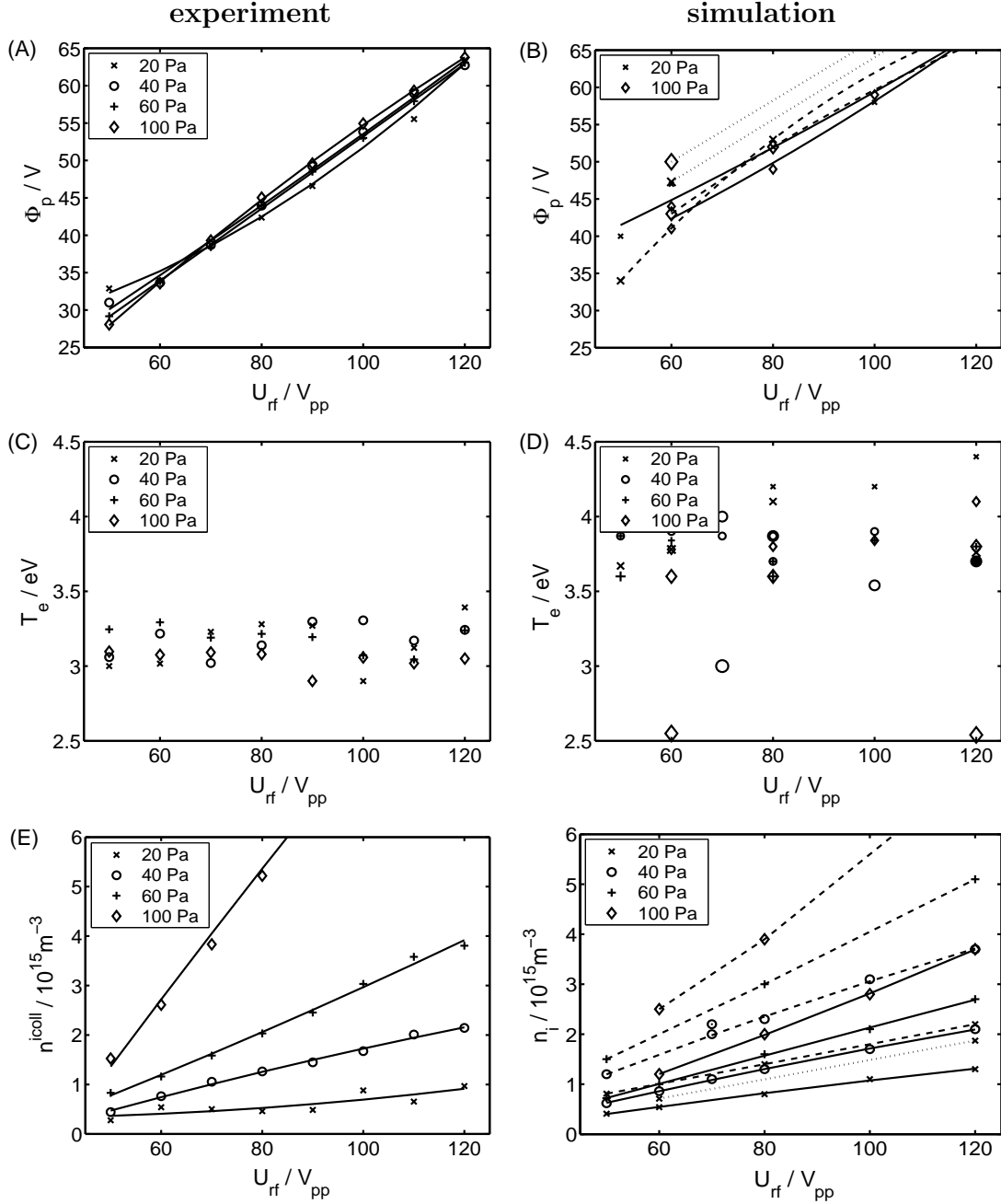


Figure 5.6: Central plasma potential ϕ_p , electron temperature T_e and plasma density vs. the peak-to-peak rf electrode voltage U_{rf} for various neutral gas pressures. (A), (C), (E) are experimental results, while (B), (D), (F) are obtained from simulations. The simulation data is distinguished as follows: small symbols (\circ) and a solid interpolation curve are derived from the SIGLO code using the second gas parameter set, medium sized symbols (\circ) and dashed lines is from SIGLO with the first parameter set and large symbols (\circ) with dotted lines are from the simulation code used in [22, 189]. Interpolation lines have been intentionally left out for the electron temperatures.

Plasma potential

It is seen from the diagrams, that the time-averaged plasma potential derived from measurements as well as from simulations increases almost linearly with the rf electrode voltage (Fig. 5.6 (A/B)) as expected from [133]. A clear dependence on the neutral gas pressure has not been observed. All data points for various pressures but equal rf voltage are found within an interval of $(3 \cdots 5)$ V. The average slope of the experimental curves is 0.47, while the simulation results yield a slope of 0.41. Then, in dependence on the driving voltage U_{rf} the obtained central plasma potential can be approximated by $\phi_p \approx 0.47 \cdot U_{rf} + 5$ V for the experimental case or $\phi_p \approx 0.41 \cdot U_{rf} + 20$ V for the SIGLO simulations, respectively. The potential values from [189] still exceed the SIGLO results by ≈ 8 V.

It has been shown (see Section 2.1.1) that the time averaged potential drop V_s over the electrode sheath must be slightly smaller than $1/2 \cdot U_{rf}$ with respect to a dc grounded electrode bias, so that the plasma electron population can reach the electrode during a small fraction of the rf cycle. This process can be considered as rectification of the rf voltage peaks. In previous experimental [133, 190] and theoretical [191] studies the $\phi_p(U_{rf})$ -function has been reported to be linear for $U_{rf} \gtrsim 50$ V with a slope of 0.39 to 0.42. Following Godyak and Piejak [133], the voltage drop ΔV_{vol} in the bulk plasma between the center and the axial plasma boundary close to the electrodes is given by

$$e\Delta V_{vol} = k_B T_e \ln \left(\frac{n_c}{n_b} \right) \approx (1 \cdots 2) k_B T_e \quad , \quad (5.1)$$

where $n_{c,b}$ are the plasma densities in the center and at the axial boundary. Thus, with respect to electron temperatures of $(3 \cdots 4)$ eV (see Fig. 5.6 (C/D)), ϕ_p is expected to be $V_s + V_{vol} \lesssim 0.42 \cdot U_{rf} + 8$ V, which is in a better agreement with the probe measurements than with the simulations. This might be caused by the gridded simulation space of fixed low resolution, where the strong electric fields in the sheath occur within a few grid cells overestimating the potential gradients. Distortions by the probe that result in too small measured potentials, such as short circuiting of inner and outer plasma regions due to the conducting surface of the reference electrode seem to have minor influence, since the measurements are in accordance with the work of other authors. Additionally, the cross-check with a second probe proved an almost indifferent behavior of the space potential in the presence of a probe (Section 5.1). But the averaging effect of the finite spatial resolution, caused by the total size of probe-tip diameter plus two times the sheath thickness, might yield a slight flattening of the potential profile. Nevertheless, experimental and simulated plasma potentials show comparable trends with the discharge parameters.

Electron temperature

For determining the most important properties of complex plasmas, for example the electron Debye length, as general scaling length for boundary processes in the plasma, or the charge of microparticles, the electron temperature is a crucial

input parameter (see Chapter 2). Nevertheless, the determination of T_e comes with an empirically estimated error of ± 0.3 eV, since the electron retardation region of the probe characteristic is perturbed by rf fluctuations in the plasma that lead to a flattening of the measured characteristic.

Figure 5.6 (C/D) presents the central electron temperature derived from probe data and simulations. The measured data points are scattered around an average temperature value of approximately 3.2 eV, the averaged electron temperature of the simulations is found at ≈ 3.8 eV. Obviously, the experimental and numerical results shown neither a clear dependence on the rf voltage nor on the neutral gas pressure. Only the temperatures from Goedheer's code [189] decrease with increasing gas pressure.

Comparing the results with other experimental work, one has to distinguish clearly if the compared discharge is maintained by stochastic or ohmic heating (refer to Section 2.1.1), since the transition is connected with a sudden increase of T_e . All experiments have been performed in the ohmic heating regime that turns to the stochastic mode for gas pressures $p_{argon} \lesssim 15$ Pa. Keeping in mind, that, within a discharge mode, the electron temperature is expected to decrease slightly with increasing neutral density [45, 192, 193, 194], comparative values for the appropriate experimental pressure range of $p_{argon} = (15 \cdots 100)$ Pa are $T_e \approx (3.2 \cdots 2.8)$ eV [45], $T_e \approx (3.8 \cdots 2.3)$ eV [194] and $T_e < 3.8$ eV [195]. Thus, the magnitudes of the simulated and especially the measured temperature are in a good agreement with literature, but the pressure dependence is resolved only by the code from [189]. Probably a variation of $\Delta T_e \approx 0.4$ eV reported in [45] is hidden by the observed methodical error in determining the electron temperature from probe characteristics under rf influences. Supporting the present results, Lai [193] and Wüst [194] also did not observe any dependence of T_e on the rf power.

Plasma density

The central PKE plasma (ion) densities n^{icoll} , obtained from probe measurements, are shown in Fig. 5.6 (E). As for the plasma potential, n^{icoll} is increasing almost linearly with the applied rf voltage, but also with the neutral gas pressure. The linear scaling of the measured function $n^{icoll}(U_{rf})$ has also been reported from other experiments [196, 193, 133, 197] and simulations [20, 198]. Depending on the neutral gas pressure with constant rf voltage, the measured density increases almost proportional to p_{argon}^2 . This scaling behavior is in accordance with available simulation results from Goedheer's code [189] in the geometry of the PKE chamber, which agree essentially with the present experiments and SIGLO simulation for 20 Pa and 40 Pa, but both exceed other methods by a factor of ≈ 3 at $p_{argon} = 100$ Pa. Therefore, these data points are not included in Fig. 5.6 (F). Nevertheless, models of Misium *et al.* [192] and probe measurements in other argon rf discharges [194, 197] show a plasma density scaling with approximately the square root of the neutral gas pressure. It has been noticed in Section 5.2 that the compensation of the ion current reduction, which is caused by collisions, by the

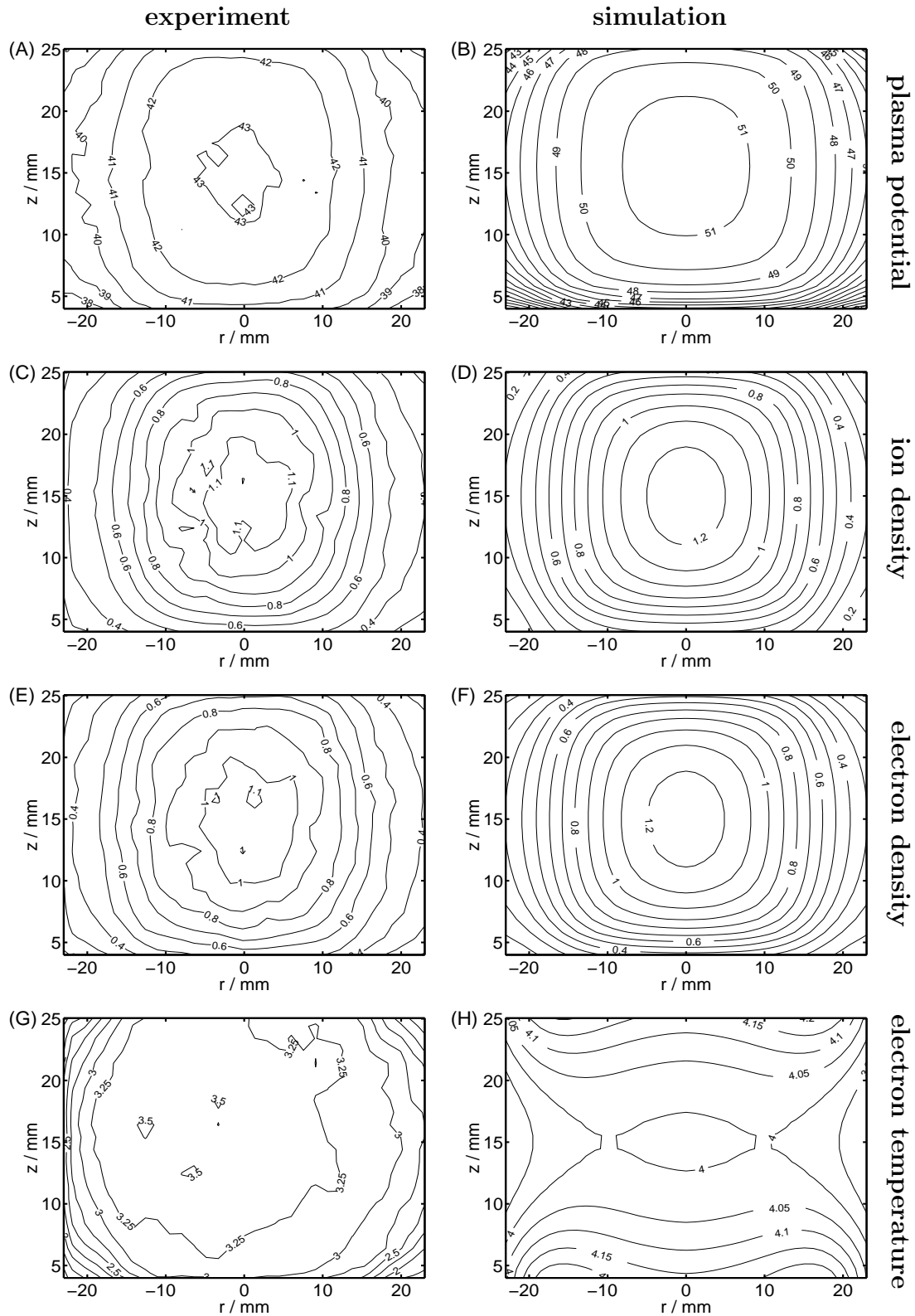


Figure 5.7: Example 1: Contour plots of parameter profiles from a meridional cross section of the inter-electrode space of a PKE discharge at 40 Pa and 80 V_{pp}. The left column of plots is derived from probe measurements, the right column from SIGLO simulation. Shown are the plasma potential in Volt (A/B), the ion density ((C) with the measured n^{icoll} and (D) with the simulated value n_i), the electron density ((E): n^{isat} , (F): n_e), all normalized with a factor of $10^{15} m^{-3}$, and the electron temperature in eV (G/H). The coordinate's origin is the center of the lower electrode surface.

applied probe analysis method at high neutral densities yields plasma densities which are, at 100 Pa, a factor 1.6 higher than the density values n^{esat} which are derived from the electron current to the probe. But still, taking this effect into account, $n^{esat} \propto p_{argon}^{1.5}$.

Trends found in the simulated ion densities are plotted in Fig. 5.6 (F). In contrast to the measurements, the dynamic behavior with the neutral gas density is less pronounced. The slope of the $n^{icoll}(p_{argon})$ -function flattens with increasing gas pressure yielding approximately $n^{icoll} \propto p_{argon}^{0.5}$ as also reported in [192, 194, 197]. Additionally, the two sets of gas parameters for argon, the SIGLO code comes with (see Section 3.5.2), yield quite different peak densities. As a combined effect, results from the first set of collision coefficients, match closer to the measured values for $p_{argon} \approx (50 \cdots 100)$ Pa, while calculations with the second gas parameter set match experiments better at lower gas pressure.

With respect to the magnitude of the derived density values, experiments and simulations support each other, since, for the most interesting pressure range of $p_{argon} = (20 \cdots 60)$ Pa, the results agree within a factor less than two and are of the order of values reported from other experiments [45, 197].

The remaining effect of closer agreement with simulations using either the first or the second set of argon collision coefficients suggests that an unknown parameter affects the experiment, but is not included in the numerical model. Classical candidates affecting the plasma density are impurities in the working gas. Typically, residual water vapor in the vacuum vessel is changing the ion diffusion coefficient related to the neutral gas background and thus takes control of plasma losses to the walls. But since the mass ratio of argon atoms to water molecules is only ≈ 2 , this effect should be small. In general, the diffusion coefficient is lowered in the presence of atoms which are lighter than the working gas, for example hydrogen from dissociated water. Thus, the effect can not be responsible for a strong increase of plasma density with increased neutral gas pressure.

A more dominant influence may be caused by negative ions [199], such as O^- , which can penetrate the discharge from the ambient air if the air tightness of the chamber is broken or can be generated from sputtering of, for example, residual dust particle material in the chamber. Even a small fraction of oxygen found in the argon gas background can substantially replace the electron population [200] and reduce the negative charge flux to the probe while the positive ion current is slightly increased. On the other hand, Amemiya [201] has shown numerically that the presence of negative ions leads to a reduced probe current and thus a decreased measured plasma density. The order of magnitude of both effects could be sufficient to explain the remaining differences between experiment and simulation if oxygen is present in the discharge. Nevertheless, performing the experiments, no possible leaks in the vacuum system as source of undesired gas components have been proved.

It should be mentioned here that negative ions can also severely affect the properties of complex plasmas [156, 200, 202].

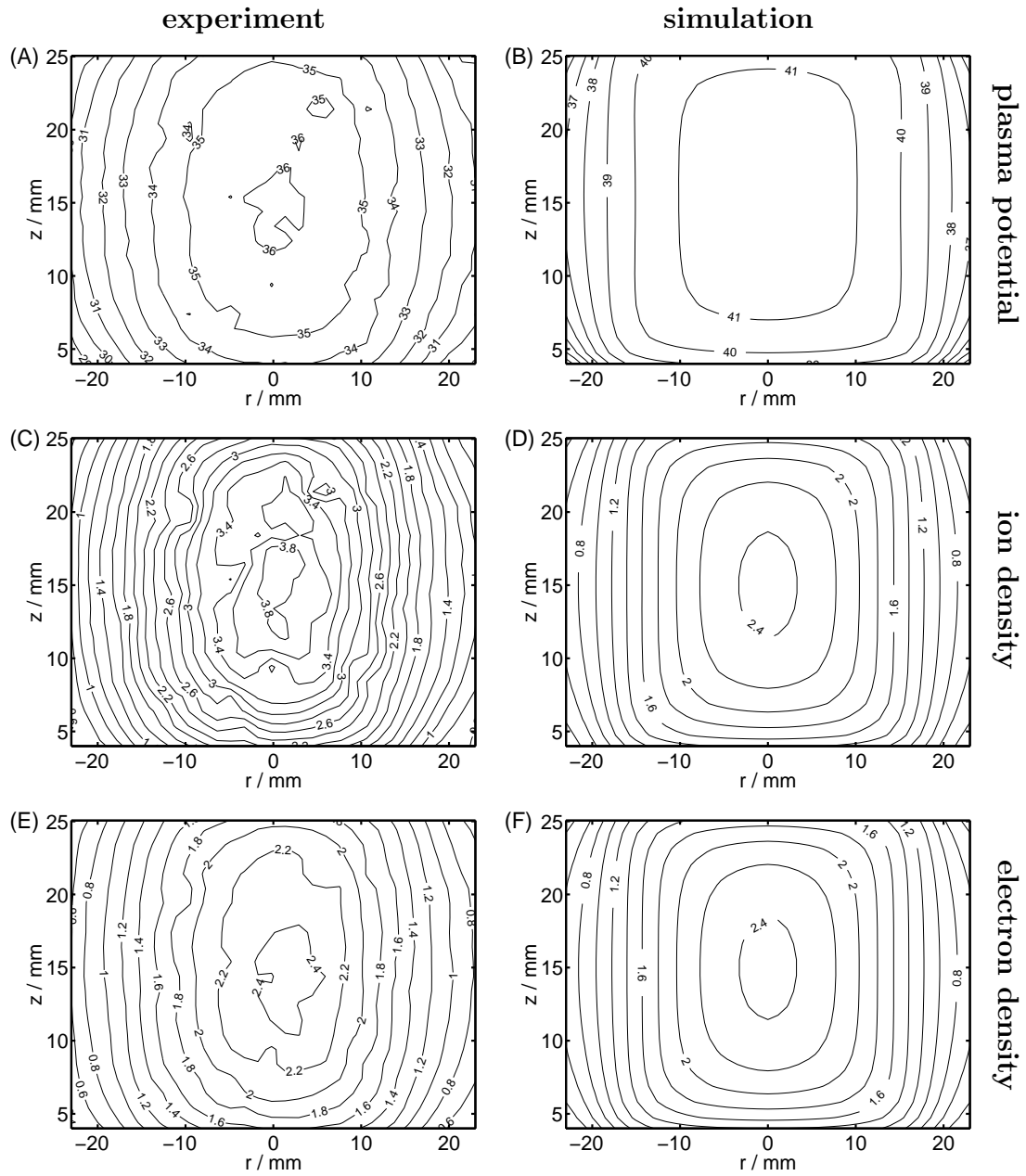


Figure 5.8: Example 2: Contour plots of plasma parameter profiles from a meridional cross section of the inter-electrode space of a PKE discharge at 100 Pa and $60 V_{pp}$. The left column of plots is derived from probe measurements, the right column from SIGLO simulation. Shown are the plasma potential in Volt (A/B), the ion density ((C) with the measured n^{icoll} and (D) with the simulated value n_i) and the electron density ((E): n^{isat} , (F): n_e), all normalized with a factor of $10^{15} m^{-3}$.

2D-parameter profiles

In the previous section, single probe measurements in the center of the discharge have been used to give an overview on the general trends of the plasma parameters with a variation of gas pressure and applied rf voltage. For the later understanding of dust particles arrangements as result of local plasma properties, it is necessary to study the spatial development of ϕ_p , $n_{i,e}$ and T_e . With the axial symmetry of the PKE (and IMPF) experiments, a two-dimensional profile of plasma parameters on a meridional plane intersecting the discharge axis is sufficient to characterize the whole volume plasma. Figures 5.7 and 5.8 provide examples for the such 2D-profiles of the bulk plasma for the two condition sets $p_{argon} = 40 \text{ Pa} / U_{rf} = 80 \text{ V}_{pp}$ and $p_{argon} = 100 \text{ Pa} / U_{rf} = 60 \text{ V}_{pp}$. Again, the measurements are presented in combination with suitable results from SIGLO simulations (calculated with the second set of gas parameters). The measured profiles consist of (32×27) individual probe characteristics. The spatial coordinates origin is located in the center of the lower electrode's surface. Thus, only the electrode plasma sheaths are excluded from the explored inter-electrode space.

Regarding Fig. 5.7 (A/B), it is again seen, that the measured plasma potentials are about $2T_e/e$ smaller than the modeled values. The gradients of the electric potential which are indicated by the density of the equi-potential lines appear almost similar in the more central region of experiment and simulation. At the plasma boundaries, $r > 18 \text{ mm}$, and close to the electrodes, the SIGLO code provides steeper gradients than the measured profile, which shows a more homogenous bulk plasma. Comparing the shape of the plotted contour lines, the experimentally obtained profile is slightly more elongated (or stretched) along the discharge axis than the simulation result. Except for the magnitude of ϕ_p , the two obtained profiles are quite similar.

The above mentioned elongation in comparison with the simulations reappears in the density profiles, as it is visible from the ion density in Fig. 5.7 (C/D). Comparing the absolute density values and distances of the equi-density lines (for example looking at the $0.4 \cdot 10^{15} \text{ m}^{-3}$ -contours), measurements and simulations are nearly equal.

Figure 5.7 (E) shows the electron density deduced from the probe current at the plasma potential, Fig. 5.7 (F) the appropriate numerical results. Both profiles coincide with the corresponding ion density plots, as it is demanded by quasi-neutrality. The similarity of the measured plasma density calculated from the ion current (n^{icoll}) and from the electron current (n^{esat}) demonstrates also the accuracy of the probe current correction method for collisions at moderate gas pressures. Regarding the corners of Fig. 5.7 (D) and (F), one can see that the contour lines of n^{esat} and n^{icoll} at the very edge of the volume plasma do not correspond to each other, any longer. Here, the beginning of the sheath at the plasma boundary near the edge of the electrodes evolves. Thus, the more effective electrons diffusion to the walls results in $n^{esat}/n^{icoll} > 1$, breaking the quasi-neutrality.

The discrepancy of electron temperatures, determined by the probe and

SIGLO simulations has been discussed in the previous section and is found again in the diagrams of Fig. 5.7 (G/H). More noticeable are the differences in the shape of the temperature profiles. While the measurements yield a central plateau at maximum value that fills almost the whole area of the plasma glow, the simulations predict a spatial temperature distribution with local maxima close to the electrodes. In more detail, the residual variation of the temperature plateau is $\Delta T_e \approx 0.5$ eV. The variation found in the simulation of the whole inter-electrode space is only $\Delta T_e \approx 0.2$ eV. Thus the simulated plasma can be considered as homogenous in electron temperature. With respect to the estimated error of the temperature determination from probe characteristics of ± 0.3 eV, the measured T_e -profile also suggests to be approximated by a uniform electron temperature for the volume plasma where injected particles are later confined and observed.

The second example of 2D-plasma parameter profiles shown in Fig. 5.8 has been scanned at a high pressure of 100 Pa and reduced rf power. Obviously, the profile's shape is further elongated to the electrodes, extending the homogeneity of the bulk plasma along the discharge axis. Especially in the simulation, the contour lines approximate a rectangular shape (or cylindrical shape in the 3D-plasma volume). Again, the measured electron density n^{isat} is in a very good agreement with the simulation and is found to be twice of the magnitude, that has been measured in the case of 40 Pa/80 V_{pp}. On the other hand, n^{icoll} exceeds n^{esat} by a factor of ≈ 1.5 , as it has been already observed in the limit of high gas pressure (see Section 5.2).

5.3.2 IMPF

Analogous to the parameterization of the central peak plasma properties in the PKE experiment on argon pressure and rf voltage, measurements have been carried out in the IMPF chamber. Since the parameter space has substantially grown with the possibility to apply different driving voltages at the center and ring electrodes, for this overview the same voltage is fed to both electrodes. This procedure ensures also that the maximum potential or density values are still located in the center of the inter-electrode space. It can be seen later from the 2D-profiles, that the global shape of the plasma can be transformed from a convex to a concave shape, with a high density region of toroidal shape located between the ring electrodes.

Comparing the simulation results and probe measurements in Fig. 5.9 most of the differences and similarities found for PKE in Section 5.3.1 are rediscovered. It is noticeable that, besides the identity of the central plasma potential in the PKE and IMPF chamber, the plasma density is almost similar, although the electrode area is nearly four times enlarged in the IMPF experiment. This can be understood, since the displayed discharge parameter is the rf voltage and not the often used "forward" rf power. Therefore, the power density per electrode area is the same as in the PKE experiment and leads to similar plasma densities, because of the same electrode gap of 30 mm in both chambers. Nevertheless, n^{icoll} is for all parameters slightly smaller than measured in corresponding PKE

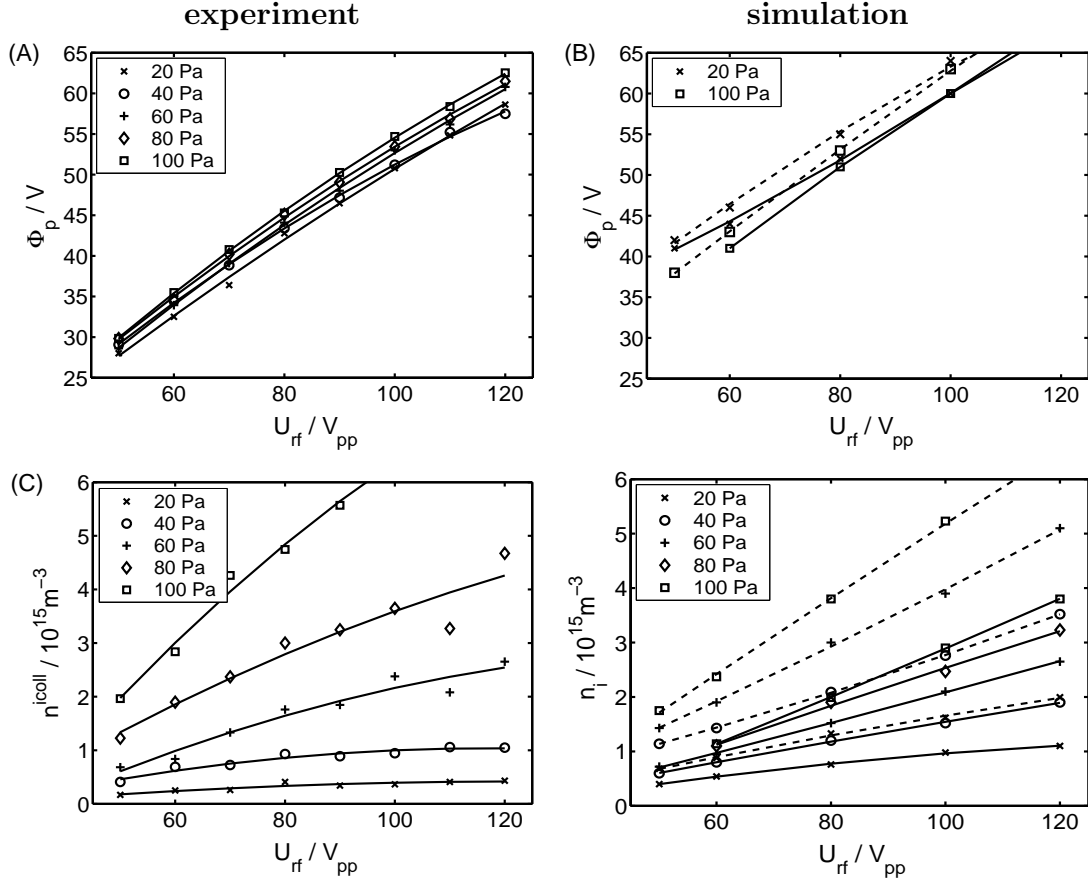


Figure 5.9: Central plasma potential ϕ_p and plasma density vs. the peak-to-peak rf electrode voltage U_{rf} for various neutral gas pressures. (A/C) are experimental results, while (B/D) are obtained from simulations. The simulation data is distinguished as follows: solid interpolation curves are derived from the SIGLO code using the second gas parameter set, dashed lines are from SIGLO with the first parameter set.

plasmas. Increased plasma particle losses to the grounded metal walls of IMPF, in comparison to PKE's dielectric glass walls, and the gaps between ring and disk electrodes, that yield a discrepancy in the ratio of inter-electrode volume to the electrode surface, when scaling from PKE to IMPF sizes, can be made responsible for this small effect. The decreasing slope of the $\phi_p(U_{rf})$ - and $n_i^{icoll}(U_{rf})$ -plot with increasing U_{rf} , which is not visible in the simulation and in PKE results, is probably a result of a systematic error in the measurement of the electrode voltage due to unintended rf coupling in the more complex circuit of the IMPF experiment.

Figures 5.10 and 5.11 provide examples for the 2D-profiles of the bulk plasma for two different combinations of ring and center electrode voltages, both at 15 Pa. For comparison, the measurements are presented in combination with suitable results from SIGLO simulations. The measured profiles consist of 41×24 single probe characteristics. As the IMPF probe, in radial direction, can only reach the

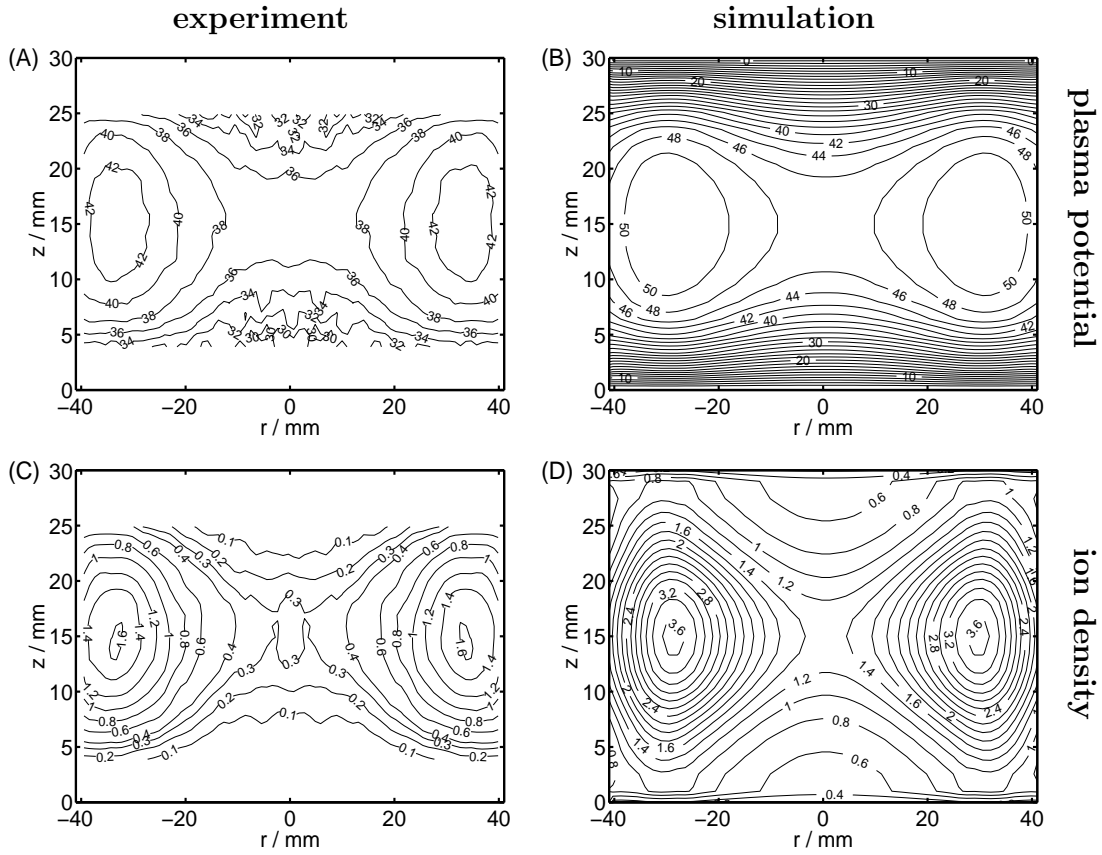


Figure 5.10: *Example 3: Contour plots of plasma parameter profiles of the inter-electrode space in the IMPF experiment chamber. The neutral gas pressure is 15 Pa. The ring electrodes are supplied with $U_{rf}^r = 88 V_{pp}$ and the disk electrodes with $U_{rf}^d = 41 V_{pp}$, respectively. The left column of plots is derived from probe measurements, the right column from SIGLO simulation. Shown are the plasma potential in Volt (A/B) and the ion density ((C) with the measured n^{icoll} and (D) with the simulated value n_i), both normalized with a factor of $10^{14} m^{-3}$.*

center of the chamber, the data array has been mirrored at the chamber axis to display a profile of the whole inter-electrode space. This has also been done with the simulation data.

It is seen from Fig. 5.10, with $U_{rf}^d = 41 V_{pp}$ rf voltage applied to the disk and $U_{rf}^r = 88 V_{pp}$ fed to the ring electrodes, that the IMPF plasma profile can be fundamentally changed by the newer concept of divided electrodes. The peak values of ϕ_p and n^{icoll} are now located in between the ring electrodes, that cover the radial range of $|r| = (23.5 \cdots 40)$ mm, forming a concave plasma distribution. In comparison, in the center of the discharge, plasma potential and density are substantially reduced. This constellation allows to invert the radial electric field, and, as a result, the ion drag, that are both understood to be responsible from the generation of central dust-free regions (“voids”) in complex plasmas.

Similar rf voltages ($U_{rf}^r \approx U_{rf}^d$) have been selected for the probe scan and simulation presented in Fig. 5.11, to obtain a PKE-like shape of plasma property

profiles. Although the simulation results show convex elliptical contour lines, the probe measurements already detected a central constriction in the high density region.

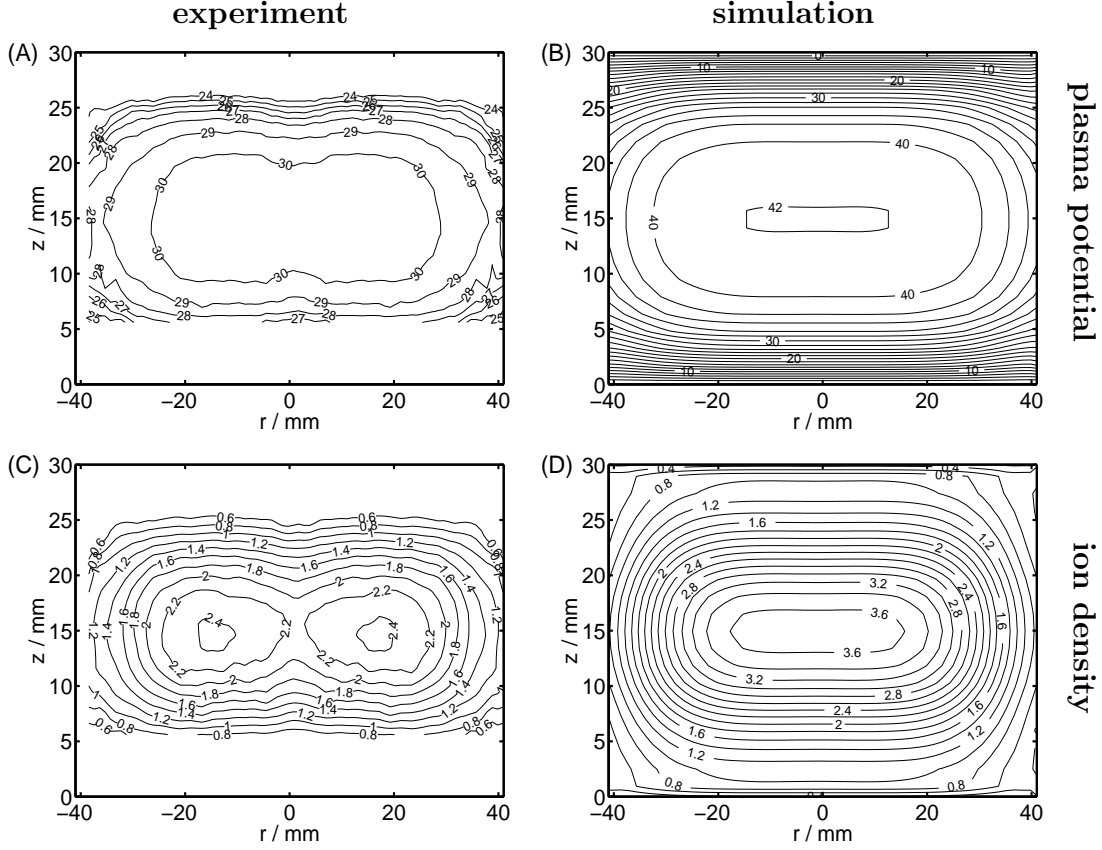


Figure 5.11: Example 4: Contour plots of plasma parameter profiles of the inter-electrode space in the IMPF experiment chamber. The neutral gas pressure is 15 Pa. The ring electrodes are supplied with $U_{rf}^d = 55 V_{pp}$ and the center electrodes with $U_{rf}^r = 54 V_{pp}$, respectively. The left column of plots is derived from probe measurements, the right column from SIGLO simulation. Shown are the plasma potential in Volt (A/B) and the ion density ((C) with the measured n^{icoll} and (D) with the simulated value n_i), both normalized with a factor of $10^{14} m^{-3}$.

It is also visible from both 2D-IMPF profiles, that, contrary to the PKE experiments, the simulated plasma density is higher than the measured. This trend is continued with a more extended plasma volume, as the toroidal plasma distribution of Fig. 5.10, that yields a larger plasma boundary and more fragile profile structures. The apparent deviations cannot be explained by influences of the scanning probe, since the probe is able to detect even weak density inhomogeneities (as shown in Fig. 5.11) which are not included in the modeling results.

5.4 Summary of results

The rf-compensated Langmuir probe hardware developed here (see Section 3.4) and the adapted probe data analysis method, described in Section 4.5, have been applied to characterize dust-free argon discharges in the PKE and IMPF (see Section 3.1.1) plasma chambers at gas pressures $p_{argon} = (15 \cdots 20)$ Pa and rf electrode voltages $U_{rf} = (50 \cdots 120)$ V_{pp}.

Studies of the influence of a probe, introduced into the discharge, on the plasma properties demonstrated that the potential distortions are negligible, while the density measurements may suffer a systematical reduction of up to 20 %.

It has been shown that the standard method for analyzing Langmuir probe characteristics, namely the Laframboise model (for example [174]), leads to completely inconsistent measurements of electron and ion densities under the given discharge parameters. Especially the desired determination of the plasma density from the ion saturation current of the probe yields values that are more than one order of magnitude too high. This disagreement has been solved by the use of a radial-motion probe model with correction for weak ion-neutral collisionality [164].

Summarizing, the following constraints should be fulfilled to obtain processable probe data: The measured plasma density must be at least on the order of $1 \cdot 10^{14} \text{m}^{-3}$. This is generally not fulfilled outside the inter-electrode space of the PKE and IMPF chambers or close to the electrodes, where probe measurements fail. The neutral gas pressure (for argon) should be smaller than 60 Pa, to work in the validity range of the collision correction procedure of the data analysis. For $p_{argon} > 60$ Pa the deviation of the density obtained from the ion current from the determined electron density can be approximately estimated. On the other hand, for $p_{argon} < 15$ Pa, the discharge is likely to perform a transition into the stochastic electron heating regime which has been excluded from the present study.

Comparing plasma properties derived from probe measurements and fluid simulations, it can now be stated that both methods yield agreeing results. The residual differences in experimental and simulated plasma potential, density and electron temperature can be attributed to non-idealities of the probe method and the simulation code: The finite size of the probe-tip and surrounding sheaths limits the resolution of probe measurements and blurs especially small structures in the measured 2D-profile. Impurities in the PKE and IMPF plasmas, which distort the probe measurements, have not been evident, but may play a role in dusty discharges as plasma sputtering products of plastic particles.

Nevertheless, probe and simulation data are widely consistent with theoretical and experimental work of other authors.

The developed probe system is able to scan the bulk plasma and provides reasonable parameter profiles, which can serve, for example, as the base for calculation of resulting forces on microparticles immersed in the discharge.

6 Probe induced secondary voids

The preceding chapter examined the properties of the Langmuir probe in a dust-free environment. Now, the presence of dust in the plasma is taken into account. The investigations on the interaction of charged particles and Langmuir probes are a prerequisite for developing suitable diagnostic methods for complex plasmas. This section is therefore focussed on the behavior of dust particles in the vicinity of an object, the probe, in the plasma. In previous investigations, Law *et al.* [51] studied probe-induced particle streaming. Thompson *et al.* [203] reported on dust-free cavities around a floating rod moved across a large dust cloud. The interplay of electrostatic repulsion and ion drag on particles close to a biased wire has been investigated by Samsonov *et al.* [204]. These observations suffer from the presence of the dominant gravity force, that breaks the expected symmetry around a probe-like object, or use small, non-distinguishable particles which are possibly hiding details of the effects. Here, experiments under microgravity conditions will be presented that allow a detailed modeling of the probe-dust system and have direct implications on the study of the void phenomenon (see Section 2.4). The proposed force interaction model will suggest to name the observations as “secondary voids” or “anti-voids”.

6.1 Experimental observations

The experimental arrangement consists of the PKE-setup (see Section 3.1.1), which has been flown on the 3rd DLR* parabolic flight campaign (2001) to obtain microgravity conditions. With discharge parameters of 40 Pa argon pressure and an rf voltage of approximately 80 V_{pp} a large dust-free region is formed in the plasma. The immersed particles have a diameter of 3.4 μm. Nearly half of this void that is surrounded by a thick dust layer can be observed by the LFoV-camera as it is seen in Fig. 2.13. The field of view, illuminated by the laser fan, is in many cases intersected by the probe (see Section 3.2), which allows to study the particle distribution around it. For example, corresponding to the findings in [203] a dust-free cavity around the shaft of the probe is established instantaneously, when it enters a particle cloud.

A more interesting phenomenon was observed when probe measurements have been performed inside the central void of a dusty plasma. When the Langmuir

*Deutsches Zentrum für Luft und Raumfahrt

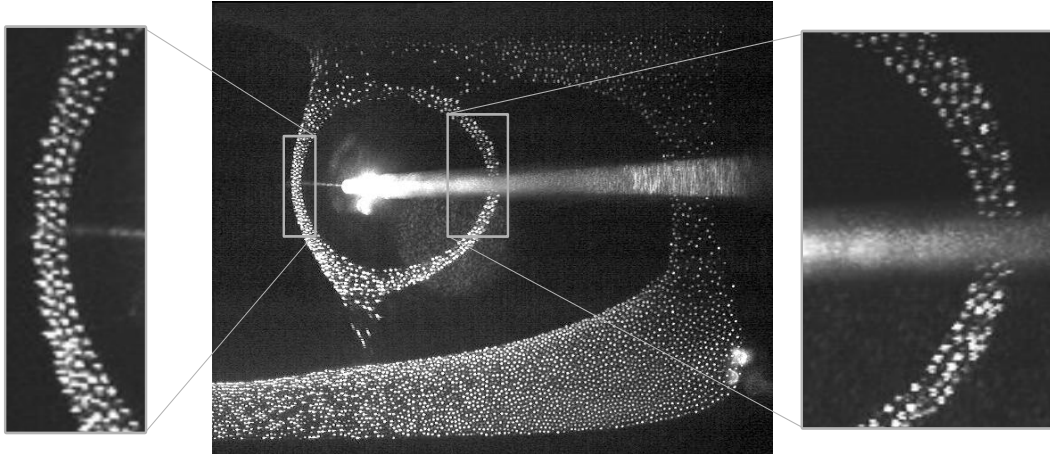


Figure 6.1: Video frame from the LFoV-camera. Most of the particles are arranged around a dust-free area (“void”) in the center of the PKE plasma. The probe, mounted at the front right, is positioned inside the void where it is intersected by the illumination laser which is noticeable by the bright reflections. A ring of particles is formed around the probe. In a detailed view of the ring the layer structure of the particle arrangement becomes visible. (A schematic view from the top on the present observation geometry is shown in Fig. 6.2 (a).)

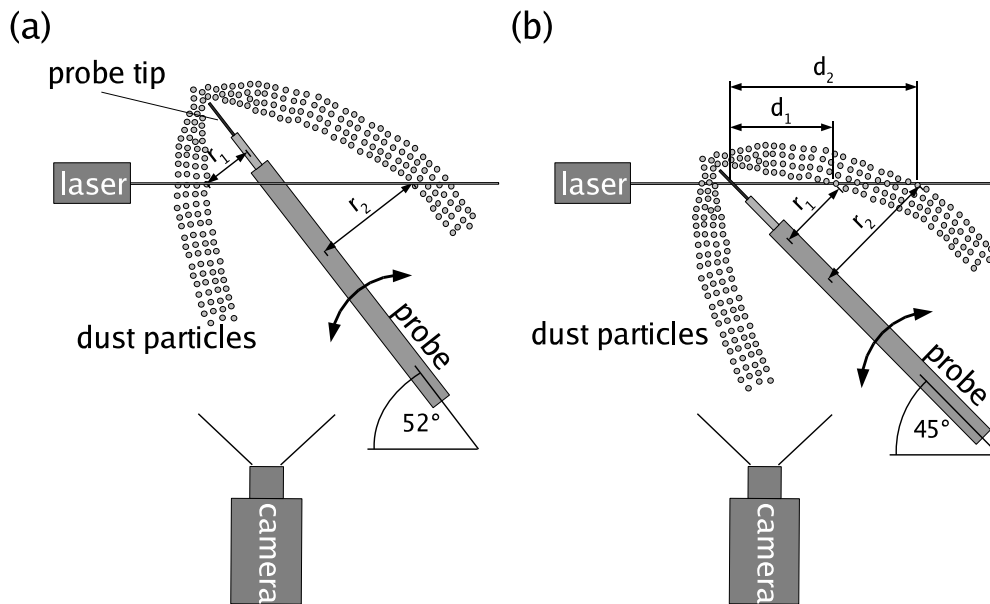


Figure 6.2: Observation geometry of the particle cloud around the probe from the top. The rotational movement of the probe leads to an intersection of the probe shaft by the laser beam that can, for example, be located at the shaft (a) or the very tip of the probe (b). Thus the size (radius r) of the dust formation can be determined as function of the probe length.

probe rotates from its parking position beside the upper electrode of the plasma chamber into the center of the void, it traverses the outer particle population at a high speed. Entering the void region, a large amount of dust is found trapped in a shell surrounding the probe. The space around the tip and shaft of the probe is dust-free and appears as a “secondary” void inside the large void (see Fig. 6.1). In a closer view, it becomes visible that the internal structure of the dust ring is not random, but consists of 3 to 4 distinct particle layers. Even close to the thin tip of the probe where the diameter of the dust ring is substantially smaller, four layers can be clearly identified (Fig. 6.4). It is also seen from Fig. 6.1 that the particle formation around the probe shaft widens at the top and bottom. Here, the distance to the boundary of the main void is smallest, the strict internal structure of the ring vanishes and a few particles flow from the dust ring towards the outer particle cloud. This region apparently forms a saddle point in the confinement. The mean interparticle distance in the areas with pronounced stratifications is only about $a \approx 100 \mu\text{m}$, increasing at the top and bottom of the ring.

While a single camera image provides only the two dimensional cross sectional information of the particle-probe interface, the geometry along the third dimension can be derived from the movement of the probe under the assumption of a particle arrangement which is independent on the probe position. Because of the varying probe inclination with its rotation, the laser intersection plane moves along the probe shaft and allows to determine the radius of the dust ring as a function of probe length. Additionally a single video frame at fixed probe position provides already two radii of the dust shell as it is sketched in Fig. 6.2.

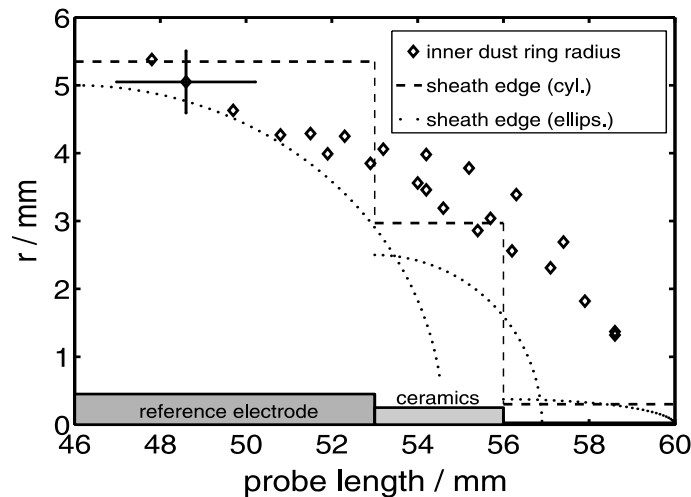


Figure 6.3: Inner dust ring radius around the probe’s tip and shaft. The dashed and dotted lines indicate the theoretical sheath edge with respect to the radius of the different cylindrical probe parts under the assumption of a strict ion flow perpendicular to the probe axis (cyl.) and with consideration of the finite length of the probe (ellip.). The probe-tip covers range (56 · · · 60) mm.

The measured radius of the secondary void along the shaft of probe is plotted

in Fig. 6.3 and varies from 1 mm at the probe-tip up to 6 mm. Obviously, the size of the dust shell increases with the diameter of the cylindrical parts of the probe, which are explained in Section 3.4.1. It follows, that the overall shape of the dust distribution is a hollow conical sleeve with the probe shaft on its axis. Since the laser sheet crosses the cone geometry obliquely to its axis, the ring that is observed on the video image appears egg-shaped. It is presumed, that the dust sleeve connects to the outer (large) particle cloud, where the probe penetrates the cloud.

Although the probe-tip is biased with a voltage ramp from $U_p = -40$ V to $U_p = 80$ V to analyze the plasma, the particle formation remains mostly undisturbed, since the shaft, comprising of reference electrode and ceramics, is insulated and thus expected to float at the constant potential of ϕ_f . Only close to the probe-tip the dust ring is observed to collapse in size for a short interval, when U_p exceeds the plasma potential ϕ_p . Figure 6.5 shows a sequence of eight probe voltage sweeps at a probe position in the center of the discharge. This position allows to study the arrangement of trapped particles near the probe-tip as it can be seen from Fig. 6.2 (b). During the sequence, the rf power has been intentionally reduced with time t . Thus, ϕ_p varies from +57 V at $t = 1$ s to +40 V at $t = 7$ s, as indicated by the dashed line in the plot. The dust distribution has settled after injection at 2 s. As long as the probe's tip potential is negative with respect to ϕ_p and thus repulsive for the negatively charged particles, the void size shows a gradual decay with the decreasing rf power. For $\phi_p < U_p$, which is emphasized by the shaded areas in Fig. 6.5, the dust is attracted by the probe and the local void size shows a sudden reduction. The minimum size of the void occurs exactly at the highest probe potential. At $t = 5$ s and $t = 7$ s the relative reduction becomes more pronounced because of the reduced plasma potential which expands the interval with $\phi_p < U_p$. Close inspection of the video data shows that during the collapse of the void the dust particles approach the probe at its very tip. The contact between dust cloud and probe leads to a gradual contamination of the probe surface as it has been described in Section 3.4.2. The thickness of the dust formation around the probe, which is estimated from the inner and outer radius of the ring, shows no dependence on the probe bias and is almost constant during the sequence.

It should be noted that the observed “breathing” of the small void with the voltage applied to the probe is localized to the vicinity of the probe-tip. The smallness of the effect can be understood in terms of the dominance of probe parts with a fixed potential ϕ_f , that maintain the size of their surrounding void irrespectively of the bias on the probe-tip.

6.2 Interpretation: Secondary voids

Trying to explain the phenomenon of the dust shell around a floating object in the central void of a complex plasma, the most important open question is which mechanism confines the particles at a defined distance from the object,

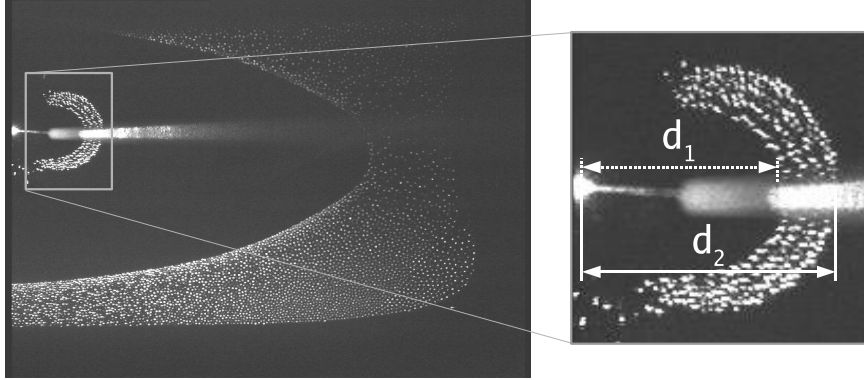


Figure 6.4: Image from the LFoV-observation camera at a probe position, where the laser beam crosses the tip of the probe and illuminates a part of the trapped particle cloud close to the thin end of the probe. Here, the response of the visible fraction of the dust shell around the probe can be studied by calculating the probe bias dependent shell radius from the distances d which range from the laser reflection point to the dust cloud boundaries. The observation geometry corresponds to Fig. 6.2 (b).

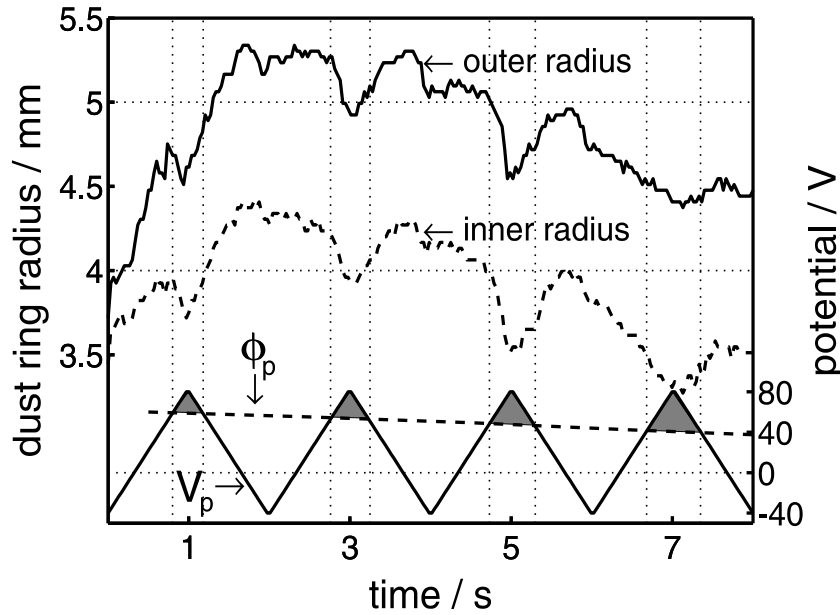


Figure 6.5: Outer and inner radius of the dust ring close to the probe-tip (as indicated in Fig. 6.4) plotted versus time together with the applied probe bias voltage U_p (ramp voltage sweeps) and the measured plasma potential ϕ_p . Intervals with $U_p > \phi_p$ are marked by the shaded areas.

although the objects surface potential and particle potential are negative with respect to the space potential and thus repel each other. Moreover, the trapped particles are located in an area, from which, in general, the ion drag force removes all dust grains towards the plasma boundaries and forms the central dust-free void region. Thus two opposite forces, directed from and towards the probe, must act on the particles, generating a trapping potential well. The observed stratifications of single particle dust layers inside the cloud surrounding the probe also hints at strong confining forces as discussed in Section 2.5. It is obvious to attribute the repulsive force to the electrostatic force resulting from the negative surface charges of the floating probe shaft and dust grains. According to [204] the attractive force is supposed to be the ion drag force, mediated by positive argon ions streaming on the probe's shaft. The interplay of these two forces is also

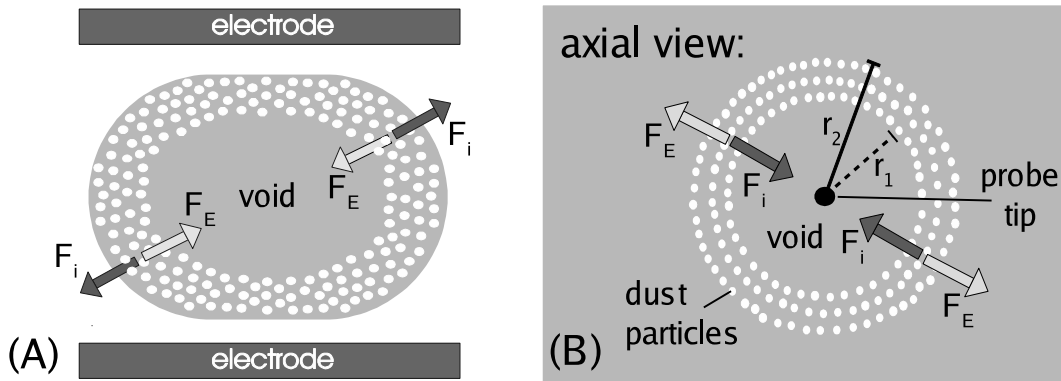


Figure 6.6: *Opposite to the supposed forming mechanism of the void phenomenon (A), the dust-free area around the probe (B) is generated by an outward acting electrostatic force \vec{F}_E and an inward pointing ion drag force \vec{F}_i . The number of induced particle layers between outer and inner cloud radius r_1, r_2 hints the confining strength of the resulting particle trap.*

suggested to drive the dust removal from the central bulk plasma, the “primary” void phenomenon (see Section 2.4). In that case, the ion drag \vec{F}_i exerted on the particles overcomes the oppositely directed electrostatic force \vec{F}_E in the high space potential region of the central plasma and pushes the particles towards the plasma boundaries, where \vec{F}_E increases strongly and (over-)compensates \vec{F}_i as it is indicated in Fig. 6.6 (A). Trapped dust grains around the probe are balanced by the same but inverted forces, as sketched in Fig. 6.6 (B), thus the probe induced void is named “secondary void” or “anti-void”.

Since the particles are trapped in the generally dust-free main void, there is a region where the drag force changes sign. Considering the confinement potentials of the outer dust cloud and the ring around the probe, the height of their separating potential barrier shrinks with reduced distance of the dust clouds. With respect to the main cloud confinement potential, the secondary trapping potential is a local minimum only. For this reasoning the high force gradients, which induce the particle layering, and thus the sharp boundaries of the dust ring vanish close to the outer dust cloud and particles are leaking from the ring to the main dust

accumulation.

The assumption on the role of ion drag and electrostatic field force is supported by comparison of the secondary void radius, representing the particle equilibrium position measured from the axis of the probe, and the location of the space charge sheath around the probe. For calculating the sheath radius r_s it is assumed, that the probe-tip, as the insulated parts of the probe, is floating at ϕ_f . Therefore, ion and electron current $I_{i,e}$ to the probe are equal, $I_i = -I_e$. With respect to the cold ions and the destruction of angular momentum by weak ion-neutral collisionality, the ion current is described by the Bohm formula (Eq. (4.6)). Note, that the Bohm criterion is generally deduced under the assumption of a plane sheath geometry (e.g. [37, 166]). Thus, dealing with the problem of spherical and cylindrical probes, a thin sheath, $r_s - r_p \ll r_p$, where r_s is the radius of the sheath-plasma boundary and r_p the radius of the considered part of the probe, is required to approximate the sheath with the idea of the plane sheath [166]. In the the present case, we expect $r_s - r_p > r_p$, and the existence of a sheath edge, where the ions reach Bohm velocity and which is defined by the breakdown of the quasi-neutrality condition (see Section 2.1.1), appears unclear. Nevertheless, Chen [37] stated that also for spherical and cylindrical probes the basic predictions of the plane sheath criterion are valid and a sheath does exist even for negative probe biases. With respect to spherical probes, Braithwaite and Allen [205] have shown that, for ABR theory, the initial restriction to thin sheaths can be replaced by the condition $(\lambda_{De}/r_s)^2 \ll 1$. This condition is fulfilled for the supporting parts of the probe in the present experiments. Additionally, following Bryant *et al.* [164], we assume that the Bohm criterion still holds for a weakly collisional plasma. For details on the influence of collisions on the Bohm criterion see [40, 41]. Further on, we will use the kinetic sheath criterion defining the sheath edge as the point, where the ion velocity towards the plasma boundary becomes sonic ($v_i = v_B$). Thus, assuming that the ions are accelerated from thermal velocity and to Bohm velocity at the sheath edge, the Bohm formula gives the current through the sheath surface, which is, by flux conservation, the same at the probe surface. Because for velocities between the ion thermal and ion-acoustic velocity, the ion drag force has a falling characteristic (see Figs. 2.8 and 2.10) and the electric field force increases towards the probe, an equilibrium position somewhere outside the sheath edge is expected. The electron current I_e is determined by the electron random motion and reduced by a Boltzmann factor (Eq. (2.10)). Equating (4.6) and (4.1), the sheath surface area A_s becomes a function of the probe surface area A_p , electron thermal velocity, and Bohm velocity,

$$A_s = \frac{1}{4} \frac{v_{te}}{v_B} A_p \exp\left(\frac{1}{2}\right) \quad , \quad (6.1)$$

with given quasi-neutrality far from the probe, $n_i = n_e$.

In a first approximation, we consider strictly perpendicular motion of the ions to the probe axis, which gives a cylindrical shape of the sheath edge as indicated by the dashed lines in Fig. 6.3. All calculations have been carried out separately for each component of the probe design with its stepwise increasing diameter,

thus the steps also appear in the simplified sheath edge geometry. The sheath surface area of the cylinder model is then $A_s = 2\pi r_s l$, where l is the length of the respective part of the probe. This approximation already matches the void radius around the shaft pretty well.

In a second step, the idea to identify the equi-potential surfaces and thus the sheath edge geometry around a finite cylindrical body as prolate spheroids as suggested in [164, 185] is applied (see also Fig. 4.7). The surface area of a prolate spheroid is

$$A_s = \frac{2s^2 r_s \pi \arcsin(l/s)}{l} + 2r_s^2 \pi \quad , \quad s = \sqrt{l^2 + r_s^2} \quad , \quad (6.2)$$

with the maximum radial extension r_s . Regarding only the front part of the probe, the cylindrical parts of the probe appear to be single-ended. This is taken into account by considering the focal distance of the spheroid as $2l$ and thus considering the probe as a symmetrical object with two ends. The above model gives the dotted contours in Fig. 6.3. Obviously, the approximation confirms the expected equilibrium particle position outside the sheath, but close to its edge. Here, in the vicinity of the sheath edge, the ion drag force is decreasing with increasing ion velocity and the repulsive floating potential of the probe shaft becomes dominant for the negatively charged particles due to reduced shielding at the space charge layer. Hence, the assumption of the interplay of electric field force and ion drag force as main driving mechanism of the secondary void phenomenon turns out to be valid and will be investigated quantitatively in the following section.

6.3 Modeling the force balance

For a quantitative understanding of the dust shell around a floating body in the plasma, it is desirable to model the system. With such a model the remaining question, at which distance from the central body and its surrounding sheath an equilibrium of ion drag force and electric field force establishes, can be answered. Additionally, the results will open access to the shape of the particle trapping potential from which the expected number of confinement-induced particle layers can be derived (see Section 2.5). The obtained results, the quantified stratification as well as the equilibrium particle position in the calculated potential well, will then allow to test the model directly against the experimental observations. The comparison will also allow to evaluate the suitability of different ion drag models (Section 2.3.5) that will be used in the calculations.

6.3.1 The force equilibrium position

Modeling the plasma density and potential structure around an object with a geometry of the present probe is a difficult problem, since each floating part of the probe affects the sheath geometry of its neighboring probe component. This

is visible from the contour of the approximated sheath edges in Fig. 6.3. It is also known, that the obvious description of the problem in cylindrical coordinates gives a singularity in the electric field at infinity [178] and spheroidal coordinates should be used instead [164, 185]. Bryant *et al.* [164] argue that the spheroidal potential contours in the presheath of a cylindrical probe become nearly spherical as soon as the radius is larger than the probe length ($r_s \gtrsim l$). Following this reasoning, it is valid to discuss the force equilibrium in a presheath model for a spherical probe when focussing exemplarily on the current fluxes to the ceramics cylinder which insulates the probe's tungsten wire from the reference electrode (see Section 3.4.1).

The used model of Shih and Levi [164, 185] requires radial motion of the ions which is a good assumption under the current experimental conditions and has been proven by the analysis of probe characteristics in Section 5.2. Weak ion-neutral collisionality, that must also be accounted for, is included in the perturbation ansatz by introducing a friction term in the ion equation of motion. The presheath problem is then formulated in analogy to Eqs. (4.20)–(4.22) for spherical geometry. The set consists of ion continuity equation, ion equation of motion, and Poisson's equation:

$$NV = x^2 \quad (6.3)$$

$$\frac{dV}{dx} = \frac{1}{x^2 V} \left(-x^2 \frac{d\eta}{dx} - v\sqrt{JV} \right) \quad (6.4)$$

$$\frac{d^2\eta}{dx^2} = \frac{-a^2(N - \exp(\eta))}{x^4} \quad (6.5)$$

Normalizations and definitions are the same as for Eqs. (4.20)–(4.22). The ion-neutral scattering cross section $\sigma = 85 \text{ \AA}^2$ which enters the ion collision frequency ν_i in $v = \nu_i/\omega_{pi}$ is taken from [32]. Under the assumption of a quasi-neutral presheath Eqs. (6.3)–(6.5) reduce to the simple form

$$\frac{d\eta}{dx} = \frac{2x^3 \exp(-\eta) + v\sqrt{J}}{x^4 \exp(-\eta) - \exp(\eta)} \quad (6.6)$$

The numerical solutions of Eqs. (6.3)–(6.5) and (6.6) yield the normalized potential distribution $\eta(x) = e\phi(x)/(k_B T_e)$ as function of the reciprocal radial coordinate $x = \lambda_{De} \sqrt{J}/r$ and the normalized ion velocity $V(x) = v(x)/v_B$. The model has been solved with and without the assumption of a quasi-neutral presheath for the experimental parameters: an ion mean free path $\lambda_{mfp} \approx 130 \text{ \mu m}$, an electron Debye length $\lambda_{De} = 390 \text{ \mu m}$ and an ion current $I_i = 18 \text{ \mu A}$, which corresponds to the electron random current to the floating probe ceramics with its size of 3 mm length and 0.25 mm radius. Referring to the estimated sheath geometry in Fig. 6.3, the ion flux to the ceramics is anisotropic and is collected only, when coming from the front (tip sided) half of the surrounding plasma. Thus, considering a spherical probe, the current value represents the ion current into a hemisphere of 3 mm radius at a plasma density $n_e = 1.2 \times 10^{15} \text{ m}^{-3}$ and a Bohm velocity $v_B = 2800 \text{ m/s}$ that corresponds to $T_e = 3.3 \text{ eV}$. The plasma potential

$\phi_p = 38$ V and floating potential $\phi_f = 29$ V is, as well as n_e and T_e , known from probe measurements. The resulting radial distributions for the poten-

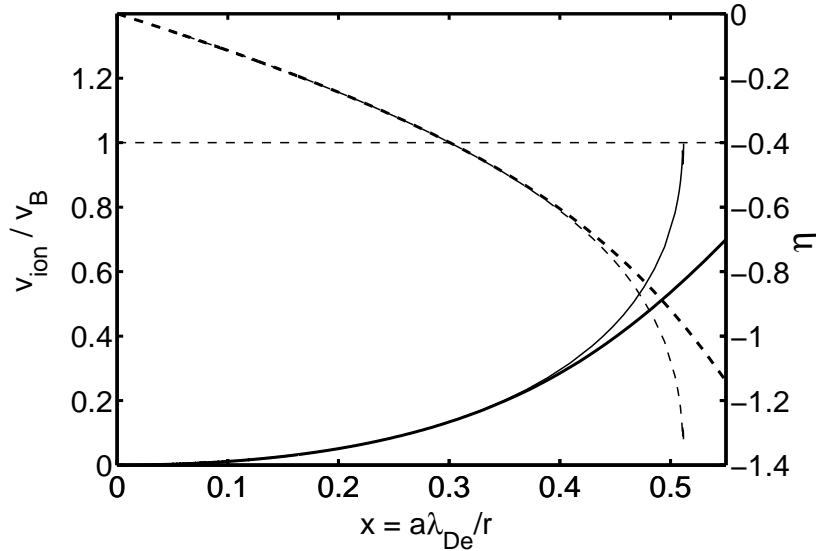


Figure 6.7: Numerical solution for the normalized ion velocity $v_i(x)/v_B$ (solid lines) and potential $\eta(x)$ (dashed lines) of the spherical presheath model from Bryant *et al.* [164]. The underlying parameters are described in the text. Thick lines represent the solution of the full set of Eqs. (6.3)–(6.5), while the thin lines are calculated from Eq. (6.6).

tial and ion velocity for the full model and the presheath solution are plotted in Fig. 6.7. The two solutions diverge only close to the sheath edge position $x_s = 0.51$ ($\Rightarrow r_s = 3.1$ mm) which is visible by the breakdown of the presheath solution. Therefore, later results on the force equilibrium are almost the same for both approximations. Nevertheless, defining a criterion for the sheath edge as $v_i(r_s) = v_B$ yields $r_s = 2.4$ mm for the full solution which is used for further comparisons of the different ion drag force expressions. The necessity to use the model described by Eqs. (6.3)–(6.5) which carefully accounts for the ohmic drop in the presheath, becomes evident from a comparison with a collisionless presheath model where the sheath edge would shift to $r'_s = 1.7$ mm (full solution).

Evaluating the forces on a particle of radius $r_d = 1.74$ μm in the presheath of the considered part of the probe the charge of the particle Q_d has been determined by OML-theory with respect to the drift of the accelerated ions in the presheath (see Fig. 2.5). The number of elementary charges on a grain increases from approximately 10500 in the undisturbed plasma up to 16000 at the sheath edge. With respect to the small particle size and large electron Debye length, Bryant [57] has shown that the influence of collisions on the floating potential of a dust grain and thus on the particle charge is negligible. Then, the electric field force on the particle is obtained with $F_E(x) = Q_d E(x)$ where the electric field strength $E(x)$ is derived from $\eta(x)$.

As counteracting force, the ion drag has been calculated according to the

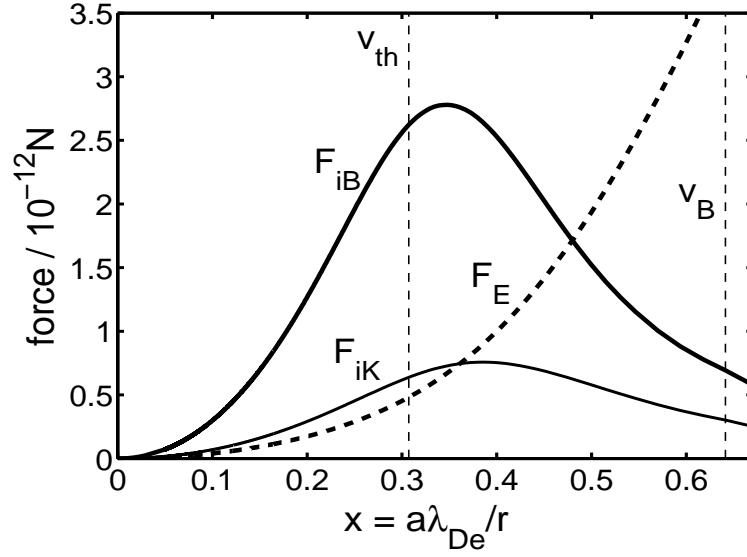


Figure 6.8: Comparison of the ion drag force F_{iB} by Barnes *et al.* [49] (at a fixed shielding length $\lambda_{De}/\sqrt{2}$) and F_{iK} by Khrapak *et al.* [50] (using λ_{Di}) with the electric field force F_E on a charged particle in the presheath of a spherical probe as function of the normalized (reciprocal) radius x . Vertical lines indicate, where the accelerated ions reach the average ion thermal velocity v_{ti} and Bohm velocity v_B .

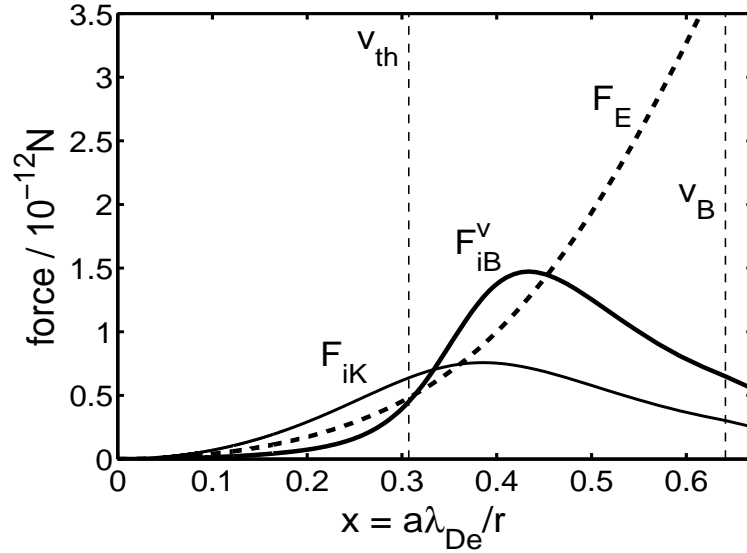


Figure 6.9: Same diagram as in Fig. 6.8, except for the ion drag after Barnes *et al.* (F_{iB}^v), that has been calculated under the assumption of an ion drift velocity dependent shielding length λ_D^v as cut-off radius entering the orbit force component.

models of Barnes *et al.* [49] and Khrapak *et al.* [50] in three different ways:

1. The Barnes model has been used following Eq. (2.64). As fixed cut-off radius in the Coulomb logarithm of the orbit force component, $b_{max} = \lambda_{De}/\sqrt{2}$ was chosen. This value accounts for the effective ion shielding length at the sheath edge, that is determined by ion energy rather than ion temperature [50]. Hence, drifting ions at Bohm velocity yield $\lambda_{Di}(v_B) \approx \lambda_{De}$ (compare with Eq. (2.16)). A similar increase of the effective shielding length was suggested in [51]. The combined action of thermal electrons and Bohm ions thus yields $\lambda_D = \lambda_{De}/\sqrt{2}$. Remembering the discussion on the influence of the cut-off radius on the ion drag force in Section 2.3.5, this ion drag expression can be considered as an upper limit for the force and is hereafter named F_{iB} .
2. To take into account the development of the shielding length from $\lambda_D \approx \lambda_{Di}$ in the undisturbed plasma to $\lambda_D \approx \lambda_{De}/\sqrt{2}$ near the space charge layer of a plasma boundary (see above), the Barnes formula has also been evaluated with the ion drift velocity dependent shielding length given by Eq. (2.17) as cut-off radius. This yields the drag force F_{iB}^v .
3. Setting a lower limit to the magnitude of the ion drag, Khrapak's model has been used with the linearized Debye length in the undisturbed plasma $\lambda_D = (1/\lambda_{De}^2 + 1/\lambda_{Di}^2)^{-1/2} \approx \lambda_{Di}$. It should be noticed, that the resulting force F_{iK} is still larger than using Barnes formula with $b_{max} = \lambda_{Di}$ (compare with Fig. 2.10), since Khrapak *et al.* have introduced a modified Coulomb logarithm in their orbit force term. This orbit force accounts for the closest approach r_0 of a scattered ion to the dust grain and not for its impact parameter (see Section 2.3.5).

All expressions include the locally varying particle charge and plasma density that can be easily obtained from $V(x)$ and Eq. (6.3).

Figure 6.8 presents the force magnitude distribution in the presheath of the spherically approximated part of the probe for F_E , F_{iB} and F_{iK} . The ion drag forces take a maximum close to the average ion thermal velocity and decrease again, while F_{iB} is a factor of up to four larger than F_{iK} . In this range of v_i , the ion drag is determined by Coulomb scattering (orbit force), while the collection force component becomes dominant at about $v_i/v_B \approx 3$ (see Fig. 2.8). This explains the big difference in the force magnitudes between Barnes' and Khrapak's model. Both ion friction forces exceed the electric field force for sub-thermal ion drift velocities. Nevertheless, F_E intersects the ion drag at subsonic ion speeds. The point of intersection represents the equilibrium positions for dust grains surrounding the probe, which are listed in Table 6.2. The results confirm our expectation that the dust will be trapped outside the space charge layer.

Now we consider a model in which the shielding length λ_D^v is considered as a function of position. Figure 6.9 shows the ion drag force after the Barnes formula including λ_D^v which is depending on the local ion velocity (F_{iB}^v). In contrast to

the previously discussed models, here, the electric field force exceeds the ion drag for $v_i < v_{ti}$. Closer to the probe, with increasing ion speed, the effective shielding length increases and F_{iB}^v overcomes F_E before it decreases again. Thus, also in this case an equilibrium position establishes. It is found close to the force balance point of F_{iB} and F_E .

ion drag model	x_{eq}	r_{eq} (mm)	k (N/m)	ξ^*	η^*	N_l	β
1. Barnes ($\lambda_{De}/\sqrt{2}$)	0.48	3.4	$2.9 \cdot 10^{-9}$	0.24	0.022	4	0.8
2. Barnes (λ_D^v)	0.45	3.5	$1.6 \cdot 10^{-9}$	0.42	0.013	4–5	1.0
3. Khrapak (λ_D)	0.37	4.4	$0.65 \cdot 10^{-9}$	2.1	0.006	4–5	2.3

Table 6.2: The positions of the force equilibrium point x_{eq}, r_{eq} as radial distance from the probe, the local confining strength k of the formed potential well and the resulting ordering parameters ξ^*, η^* , which are described in Sect. 2.5, for the three ion drag models. According to ξ^* and η^* the number of induced particle layers N_l in the trap is derived from Fig. 2.14. Additionally, the corresponding scattering parameter β is given.

6.3.2 Force induced particle layering

The point of balanced forces F_i and F_E marks the position of the minimum of a confining potential well the particles are trapped in. In the real experimental system more than a single dust grain have to arrange in the well, yielding a competition of repulsive inter-particle forces and confining forces according to the shape of the potential trap. The resulting ordering of particles is addressed in the following:

The net restoring force ($\vec{F}_E + \vec{F}_{iB}$) on a particle in the vicinity of the force equilibrium point increases approximately linearly, which makes the force balance stable. Although the ion friction force is non-conservative, the dust can be considered as being confined in a nearly parabolic potential well of the form $\phi = kr^2/2$. The confining strength k can be estimated from the gradients of the forces at the equilibrium points for the different ion friction force models (see Table 6.2).

The experimental observations show that the particles which are trapped in the generated potential well arrange in distinct layers, forming the probe surrounding dust shell with a sharp inner and outer boundary. In a first approximation the dust shell can be considered as a particle cloud in a one-dimensional confining potential. The particles can move freely along the two dimensions of the shell surface, but underly the ion drag force and electric field force which are acting perpendicular to the surface. This approach corresponds to the system that was theoretically investigated by Totsuji *et al.* [121]. These studies have been introduced in Section 2.5. In their simulations, Totsuji *et al.* found the number

of induced particle layers in a parabolic 1D-potential well to be only dependent on two ordering parameters ξ^* and η^* which are a measure for the shielding inside the dust cloud and for the ratio of external (force generated) potential to thermal energy of the particles.

Hence, the number of expected particle layers N_l , according to the present model, is derived from Fig. 2.14 (B) by calculating the local ordering parameters at the equilibrium positions. The results are presented in Table 6.2, where λ_d^v has been used as local shielding length, which enters ξ^* , for all three ion drag models. Typically four to five layers should establish in the modeled particle trap around the probe ceramics. This is in a good agreement with the observed four layers. It should be noticed, that N_l is the same for ion drag models two and three, although the resulting confining strengths are quite different. This is caused by the dependence of ξ^* on the locally varying shielding length.

6.4 Discussion

The ring of dust particles around a probe inside the (normally) dust-free void region of a complex plasma under microgravity conditions can be understood as a cross section through a conical sleeve of dust particles that are confined by repulsive forces from the probe and compression forces from the inflowing ions. This is quantitatively confirmed by the force equilibrium positions of electrostatic field force and ion drag calculated on base of a presheath model, which are in a very good agreement with the experimental observations. The model accounts for ion-neutral collisions and provides the ion density and ion velocity distributions in the presheath of the probe for the calculation of the ion drag on the particles. The shape of the trapped dust cloud reveals the space charge layer around the floating probe, because the minimum of the formed confinement potential is located close to the sheath edge.

It is noted that the influence of charged particles on the presheath solution is not regarded and that both applied ion drag models [49, 50] suffer from the neglect of collisions [28, 29] and consider only the presence of a single dust particle. Nevertheless, enhanced ion drag theories have not been available at the time of writing.

Particle layering

The presented model also yields the confining strength of the particle trap, which allows to derive the number of particle layers corresponding to the stratifications observed in the experiment. This important feature allows, vice versa, to estimate immediately from experimentally observed formations of particle layers the force gradients of the effective confining potential generated by ion drag and field force.

Boundary induced layering effects are also known from 2D and 3D particle clusters [116, 117], where the outer particles arrange in distinct shells, and from complex plasmas confined in narrow channels [123] which is comparable to the present system. Other investigations evidence the existence of similar behavior

in colloidal suspensions [125] and on the nanometric scale in the ordering of molecules in thin liquid films [126, 206]. The study of confined complex plasmas may therefore have direct impact on, for example, the research of friction and lubrication at the atomic scale [127].

The observed layering mechanism cannot be effected by wake field attraction (e.g. [94]). Experiments have consistently shown that ion-flow-induced alignment leads to interparticle distances of the order of $a \approx \lambda_{De}$ (e.g. [93, 207]) which exceeds the present observations by a factor of $(3 \cdot \cdot 4)$. Furthermore, particle trapping wake fields have been observed only for $v_i \geq v_B$.

Results from different ion drag models

The obtained force equilibrium positions are only slightly dependent on the applied ion drag model. The Barnes formula [49] including a fixed cut-off radius on the order of the electron Debye length which is widely used (e.g. [16, 99, 100, 204]), yields the lower limit of the experimentally observed dust ring radii. The model of Khrapak *et al.* [50] results in the smallest magnitude of the ion friction force at the equilibrium position, which approximately reproduces the upper limit of the particle position observations. Nevertheless, both models suffer from the approximation of the ion scattering potential by a Coulomb potential with fixed cut-off radius (compare Section 2.3.5) which is questionable in the presence of the presheath, where the acceleration of ions strongly affects the shielding length [51]. As a first step towards this problem, the Barnes formula with an ion-velocity-dependent cut-off radius yields an equilibrium position in-between the results of the standard models. Qualifying is, that this model is not fully compatible to void experiments (refer to Section 2.4). Using this model for ion drifts below the average thermal ion velocity, the counteracting electric field force exceeds the ion drag. Thus, a completely dust-free region, generated by radially outflowing ions as observed in [9], cannot develop. Akdim and Goedheer [22] have pointed out this problem, when they initially used the Barnes formula with the linearized Debye length as cut-off radius in their complex plasma simulations.

Comparison with previous works

The phenomenological aspects of the interaction of a probe with a typical laboratory dusty plasma under gravity have first been investigated by Law *et al.* [51]. The authors already reported that a probe inserted into a dust cloud creates a sharply bounded void around the probe. To study the interaction of a floating rod-like object, similar to a probe shaft, with an extended complex plasma, Thompson *et al.* [203] immersed particles with $r_d < 0.5 \mu\text{m}$ in a DC discharge. The influence of gravity on these particles is negligible and probe generated voids under stationary and moving conditions have been observed. In contrast to our explanation, Thompson *et al.* [203] proposed an equilibrium of electric field force and dust kinetic pressure inside the cloud to determine the size of the void.

Samsonov *et al.* [204] pointed out the role of the ion drag as particle attracting force in the vicinity of a biased wire which was fixed close to a mono-layer

of particles being trapped in the lower sheath of an rf discharge. The authors observed an equilibrium particle position, but no stratifications in the mono-layer.

An independent study on the dependency of the size of an induced void on the probe bias has been published by Thomas *et al.* [99] after submission of [208]. The void, created by a cylindrical probe in a cloud of medium-sized particles trapped in an anode glow discharge, was found to increase with (negatively) increasing probe voltage. As theoretical approach to quantitatively describe the observations, the authors considered a one-dimensional sheath model as it is valid for plane probe. The model yields the potential distribution to calculate the interplay of electric field force and ion drag after the Barnes formula on a particle in the vicinity of the probe. The experiment [99] has similarities with the present work and the basic idea for explaining the phenomenon is similar to the one suggested here, except for the degree of approximations made on the probe geometry, the used ion drag model (Barnes formula with $b_{max} = \lambda_{De}$) and the assumption of a collisionless discharge. Moreover, an important difference must be pointed out. In [99], the dusty plasma itself is generally void-free. Therefore, a void of finite size can be already generated by the repulsive force of a negative probe and the counteracting inner kinetic and Coulomb pressure of the dust cloud as proposed in [203]. With increasing probe potential, the also increasing sheath surrounding the probe yields a larger void. Thus, an experimental indicator on the existence of the ion drag force has not been reported by the authors of [99]. Nevertheless, Thomas *et al.* [99] conclude that the ion drag force does play an attractive role in the probe-dust interaction – as it has been shown by the stability of the dust ring inside the particle-free void in this chapter.

With respect to the comparison of observed void size and results of the force model of Thomas *et al.* [99], it is noticeable that the theoretical dependence on the probe bias is nonlinear, while the experiment shows a strictly linear behavior. This may result from the plane sheath approximation for the cylindrical probe.

Closer inspection shows that the situation in [99] is even more different from the secondary voids described in this thesis. The total amount of particles in the vicinity of the probe is much larger than in the present case and leads to a different plasma environment in the presheath region of the probe, which is filled with dust in [99] but mostly empty of dust in the present case. As a result, the sheath edge around the probe is not generally identical with the force equilibrium point as it is assumed in [99]. This difference can be discussed with the aid of Fig. 6.10, which shows a potential well formed by electric field force and ion drag force calculated from the model presented in Section 6.3. A small amount of trapped dust fills the bottom of the well and thus reveals the shape of the sheath around the central object close to its edge. A large dust cloud also penetrates into the sheath. The force equilibrium of ion drag and field force is then visible only by an enhanced particle density at the potential well minimum, but not by the edge of the void. Figure 6.10 shows that, for example under the present conditions, a large particle cloud effects a reduction of the void radius by $\Delta r \approx 2$ mm. Therefore, we suggest to utilize as few particles as possible to visualize the force equilibrium point and thus the structure of the sheath around objects in a plasma.

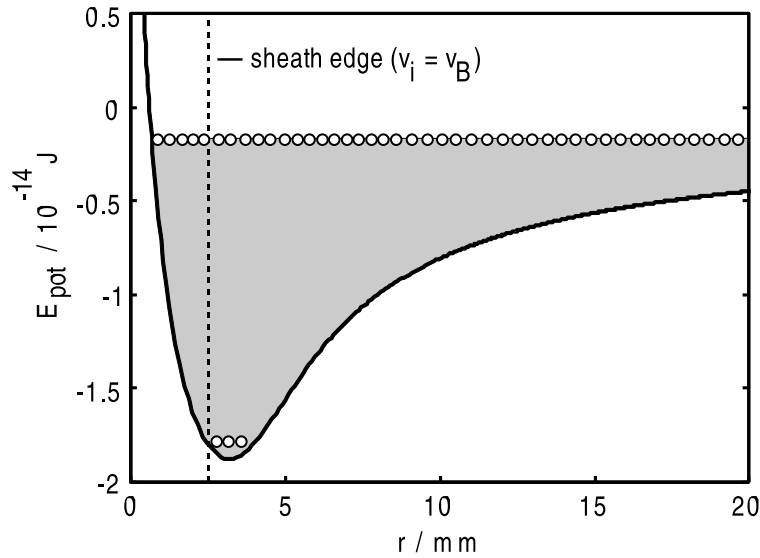


Figure 6.10: Particle confining potential well formed by electric field force and ion drag force in the presheath of a spherical probe as function of radial distance r . The curve has been calculated from the results presented in Fig. 6.8 using the Barnes formula (with $b_{max} = \lambda_{De}/\sqrt{2}$). The vertical line resembles the position of the sheath edge. The radial coverage of a small and a large population of particles in the potential well is indicated by the upper and lower group of white dots.

Impact on probe diagnostics

The experimental investigations on the dust-probe interaction have direct impact on the development of probe diagnostics for dusty plasmas. It has been shown, that the sheath remains dust-free as long as the probe is negatively biased with respect to the plasma potential. This ensures that the ion part and electron retardation part of the probe characteristic can be recorded while avoiding contamination of the probe by dust deposition. An advanced waveform as sweep function is sufficient to allow measurements above the plasma potential (see Section 3.4.2).

Important information on the effective geometry of a Langmuir probe which enters the design of a next probe generation or the theory applied in probe data analysis is obtained from the dust visualizing the space charge layer.

Generally, a Langmuir probe in a dusty plasma measures properties of the particle containing plasma, although it is surrounded by a self-generated dust-free region. This is apparent to assume, since the secondary void represents approximately the sheath around the probe – but the sheath still is, as in dust-free plasmas, determined by the ambient plasma.

Although an electrostatic probe remains an invasive diagnostic for complex plasmas, which is mostly a problem of the large probe support needed, the above results show, that it allows to investigate phenomena like ion drag and voids in more detail. And, the probe is capable to locally resolve parameters of a complex plasma as it is demonstrated in Chapter 8.

7 Force balance in complex plasmas under microgravity

Opposite to the dust-free region around a probe (“secondary void”), the phenomenon of a large central void, as it is observed in complex noble gas discharges like in PKE (see [9]) and IMPF, is understood to be driven by an inward directed electric field force and the counteracting ion drag force on the negatively charged particles, which is mediated by outward flowing positive ions. An introduction to the void phenomenon is given in Section 2.4.

To evaluate the dominance of F_E and F_i in the generation of the void, this section compares the size of a void under varying discharge conditions, as it has been observed in the IMPF experiment during parabolic flights, with results from modulation including only ion drag and electric field force. Two-dimensional plasma parameter profiles from simulations and probe measurements through the IMPF chamber are used to calculate the forces and obtain the equilibrium position injected dust grains. Since effects of the particles on the plasma, like depletion of the electrons or enhanced recombination on the dust surfaces, are not taken into account in the model, only a few particles have been immersed into the discharge during the experiments. Thus, the experimental conditions can be considered to be the same as during probe measurements in the dust-free discharge or in the dust-free SIGLO simulation code.

The investigations address the question if the general shape and size of a void is already predetermined in a particle-free plasma or if the void is an instability of a complex plasma effected by the presence of many particles. It also serves to evaluate if measured Langmuir probe data is suitable for further data processing and understanding of more sophisticated effects in complex plasmas.

7.1 Experiment and observations

The experiments have been performed in the IMPF experiment according to the setup, which is described in Section 3.1.1. To reduce the influence of gravity on the particles, the chamber was flown on the 5th DLR parabolic flight campaign in 2003. With injected monodisperse particles of radius $r_d = 1.74 \mu\text{m}$ it is obvious from Fig. 2.12 (A), that the thermophoretic force is negligible and the grains are subject to ion drag force F_i and electric field force only.

The IMPF chamber has the great advantage over PKE that the plasma profile

can be shaped by application of different rf voltages $U_{rf}^{d,r}$ to the disk and ring segments of the electrodes. In the presented experiment sequence the ring electrode voltages are increased in six steps from $U_{rf}^r = 27 V_{pp}$ to $U_{rf}^r = 69 V_{pp}$ at a fixed neutral gas pressure of 15 Pa. Although the applied power to the disk electrodes is kept constant, the disk rf voltage varies from $U_{rf}^d = 50 V_{pp}$ to $U_{rf}^d = 56 V_{pp}$ during the sequence due to capacitive coupling to the ring electrodes. The LFoV-camera (see Fig. 3.3) records the resulting positions of the particles, which are illuminated on a meridional cross section through the inter-electrode space by the laser fan.

The left column of Fig. 7.1 presents the initial particle distribution (a) and the positions after power step two (b), four (c) and six (d). Herein, the particles appear as a thin white line. The line is occasionally interrupted because of the small amount of dust, which has been injected in order to minimize its effects on the discharge conditions. Nevertheless, the dust clearly surrounds an oval shaped dust-free region in the central plasma which, in three dimensions, corresponds to an oblate spheroidal void. It is noticeable that even the movement of a single isolated particle is restricted to the invisible border line of the void.

With increasing rf voltage applied to the ring electrode, the shape of the dust arrangement expands radially from $r = 22.5$ mm to $r = 34$ mm, while the vertical extension is almost conserved. Columns two and three of Fig. 7.1 show the corresponding plasma densities in units of $1 \cdot 10^{14} \text{m}^{-3}$, which are obtained from Langmuir probe measurements and SIGLO simulations. The measured profiles comprise of (41×27) different probe positions for one half of the inter-electrode space and are, as well as the simulation results, mirrored at the chamber axis to obtain a full meridional profile of the discharge. In the probe profiles the maximum density region in the bulk plasma also elongates horizontally with increasing U_{rf}^r and splits into two density peaks, which are drifting radially away from each other. The simulated profiles show this feature only when $U_{rf}^r > U_{rf}^d$ (see Fig. 7.1 (d)). Comparing the oval particle formation with the density plots, the shape of the dust cloud resembles an equi-density line of the profiles.

Further reduction of the disk electrode voltage and increase of the ring electrode power yields an almost complete separation of the density peaks, which are then located directly in-between the ring electrodes. This is accompanied by a vertical constriction of the dust spheroid in the center of the plasma. The void changes from a convex to a hollow shape and finally transforms to a toroid as it is seen in Fig. 7.1 (e). The dust cloud is still comparable to an equi-density line.

7.2 2D-equilibrium model

It is obvious from the comparison of experimental particle observations and the corresponding plasma parameter profiles that the shape of the void is determined by the shape of the parameter profiles. Thus, the self-adjusting particle arrangement under given discharge conditions should be predictable from the profiles and the assumption that the particle motion is determined only by ion drag and

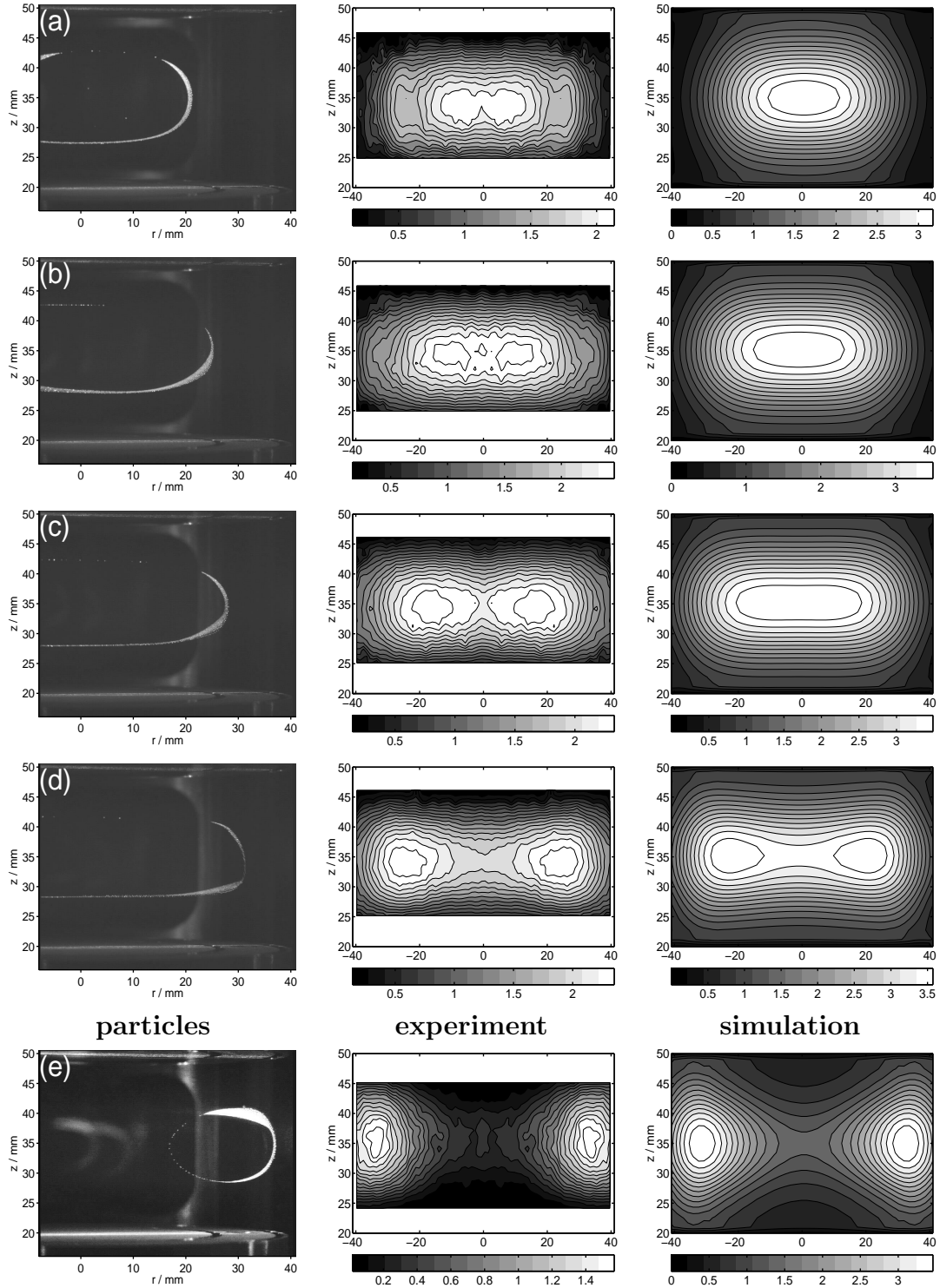


Figure 7.1: Modification of the density profile and dust arrangement by variation of the rf voltages applied to center/ring electrodes: (a) $50/27 V_{pp}$, (b) $54/40 V_{pp}$, (c) $55/54 V_{pp}$, (d) $56/69 V_{pp}$, (e) $41/88 V_{pp}$. The left column shows the resulting growth of the void by frames of the observation camera (compare with Fig. 3.3), the second column provides the corresponding density profiles from probe measurements (n^{icoll}) in a dust-free laboratory plasma, the right column contains the appropriate profiles from simulations (n_i) for the inter-electrode space of the IMPF-chamber. Plasma densities are normalized with a factor of $10^{14} m^{-3}$, argon pressure is 15 Pa. Video frame (e) shows one poloidal cross section of a dust torus, that is formed under the given conditions.

electric field force.

Langmuir probe measurements and SIGLO simulations have been performed for all steps of the U_{rf}^r -variation experiment and yield two-dimensional cross sections of the plasma potential ϕ_p , electron temperature T_e , electron and ion density $n^{esat,icoll}$ from measurements or $n_{e,i}$ from simulations, respectively. From both sets of parameters, simulated and measured, the resulting minimum energy particle positions can be calculated.

Figure 7.2 exemplarily provides the simulated plasma potential profile of the electrode voltage constellation $U_{rf}^d/U_{rf}^r = 51 V_{pp}/31 V_{pp}$ after the first power step. Considering the charge of a particle Q_d from Eq. (2.31) and estimating the grain's surface potential ϕ_f with Eq. (2.28), the electric field force on a dust grain can be easily deduced using ϕ_p , T_e , and n_e with

$$\vec{F}_E = Q_d \vec{E} = -Q_d \vec{\nabla} \phi_p \quad . \quad (7.1)$$

A resulting 2D vector field of \vec{F}_E is presented in Fig. 7.3. Note, that, for plotting reasons, a nonlinear scale for the vector length was chosen. As a result, a negatively charged particle that is injected into the plasma chamber would be pushed into the very center of the discharge if it were only subject to the electric field force. The highest electric fields are located in the rf sheaths near the electrodes (compare with Section 2.1.1). Here, the maximum force on a particle is found to be on the order of 10^{-11} N, while the radial confinement of particles to the inter-electrode space at $z = 35$ mm is on the order of 10^{-12} N. The field force is vanishing in the potential plateau of the central plasma.

The positive argon ions are accelerated by the electric fields in the direction opposite to \vec{F}_E . Their motion is restricted by ion-neutral collisions and, thus, the local ion velocity is derived with

$$\vec{v}_i = \mu \vec{E} \quad , \quad (7.2)$$

where $\mu = e(m_i v_{ti})^{-1} (n_n \sigma_t)^{-1}$. The total ion-neutral collision cross section is $\sigma_t = 85 \text{ \AA}^2$ [32], n_n is the neutral gas density. The modulus of \vec{v}_i up to Bohm velocity in the discharge is plotted in Fig. 7.4 in units of the average thermal ion velocity v_{ti} . In the center of the plasma the velocity of the outwards flowing ions is of the order of v_{ti} and strongly increases towards the electrodes. Radially, the ions reach a maximum velocity of $\approx 4v_{ti}$.

Again to calculate the magnitude of the ion drag force from the ion drift velocity, three models, which are listed in Section 6.3 are used: The Barnes model [49] with a cut-off radius at $b_{max} = 0.7 \cdot \lambda_{De}$ (see Section 2.3.5), the Barnes model with an ion velocity-dependent cut-off at $b_{max} = \lambda_D^v$ (see Eq. (2.17)) and Khrapak's model [50] (Section 2.3.5). The resulting forces derived from the different models are named F_{iB} , F_{iB}^v and F_{iK} . Khrapak *et al.* [50] confirmed their model to be valid for scattering parameters $\beta < 5$. With respect to the present discharge conditions this restriction is fulfilled for $v_i > v_{ti}$. Since particles have not been observed in the center of the plasma, where $v_i < v_{ti}$, the model [50] is used for the whole plasma volume.

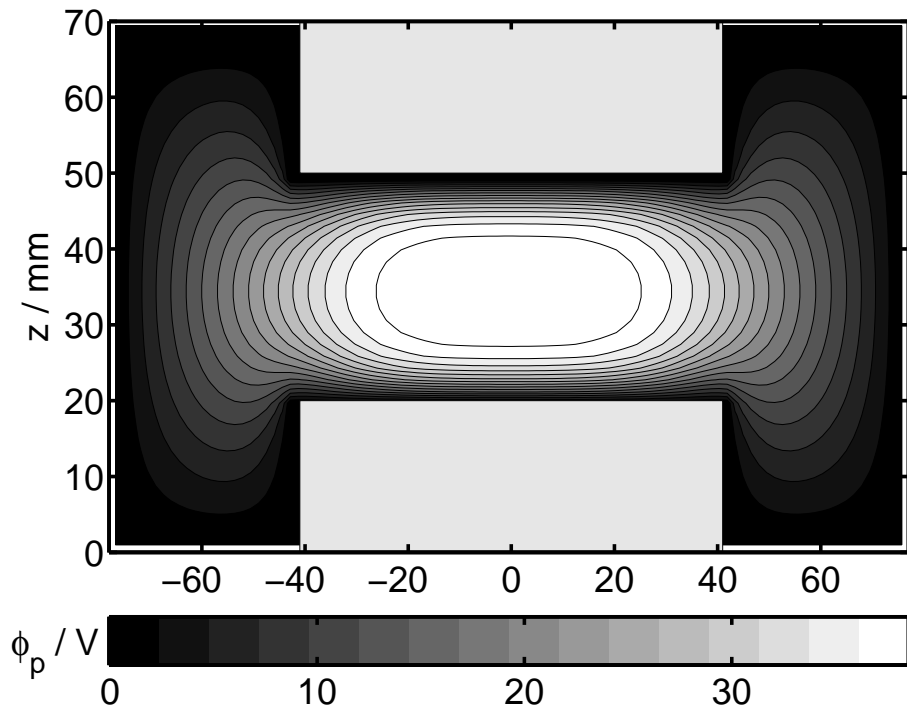


Figure 7.2: Simulated plasma potential profile of an IMPF discharge with $U_{rf}^d = 51 V_{pp}$ and $U_{rf}^r = 31 V_{pp}$ at an argon background gas pressure of 15 Pa.

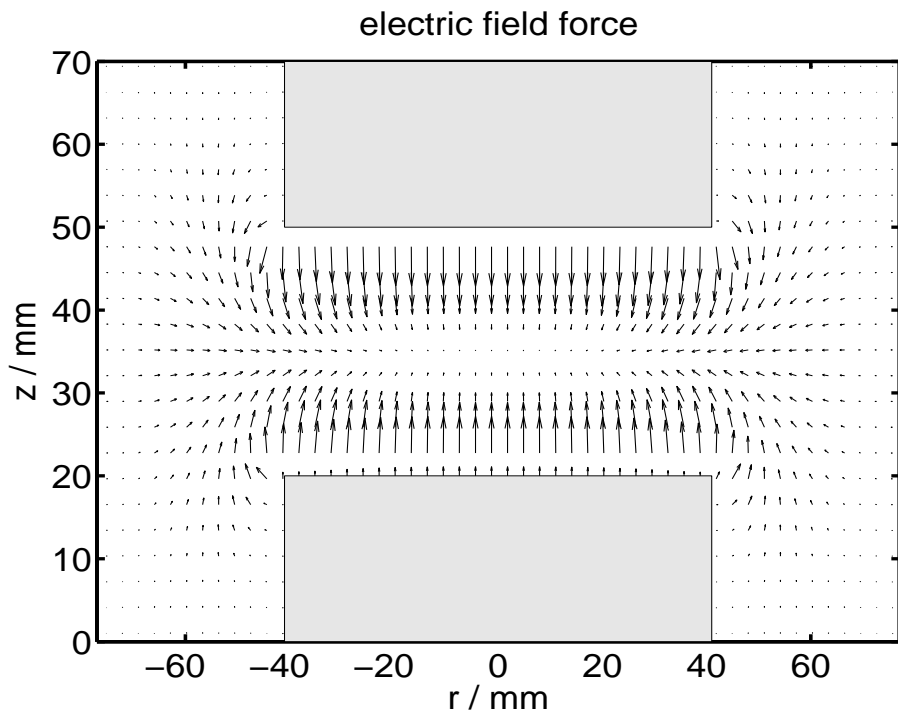


Figure 7.3: Vector field of the electric field force F_E on a negatively charged particle of $r_d = 1.74 \mu\text{m}$. The discharge conditions are the same as in Fig. 7.2. For presentation reasons the scale of the vector length is nonlinear and arbitrary.

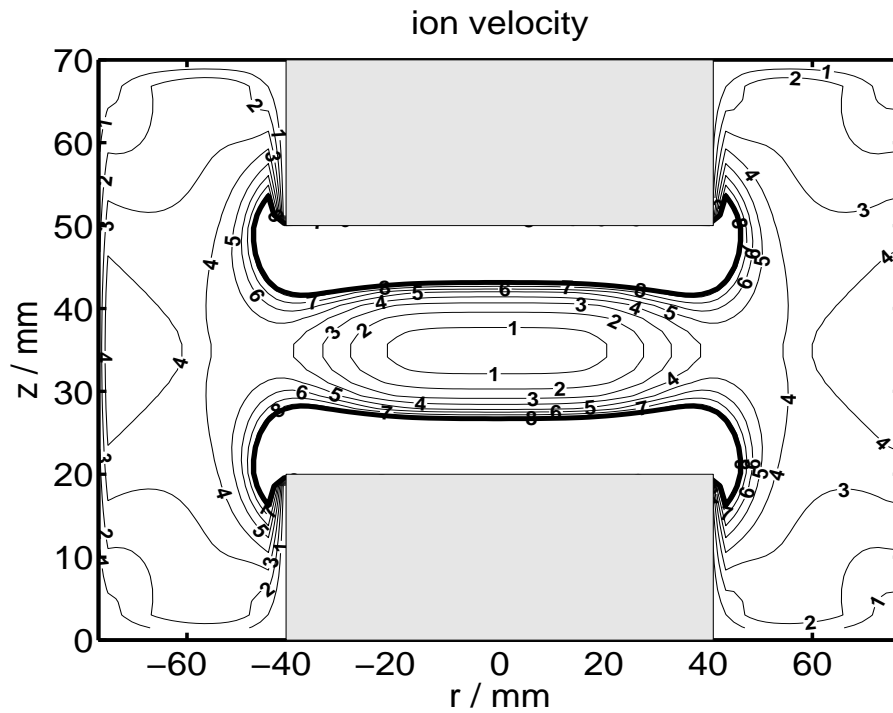


Figure 7.4: Drift velocity v_i of the outwards flowing ions corresponding to the potential distribution in Fig. 7.2. The velocity is normalized to the average thermal ion velocity $v_{ti} = 390 \text{ ms}^{-1}$. The thick contour line indicates the position where $v_i = v_B$.

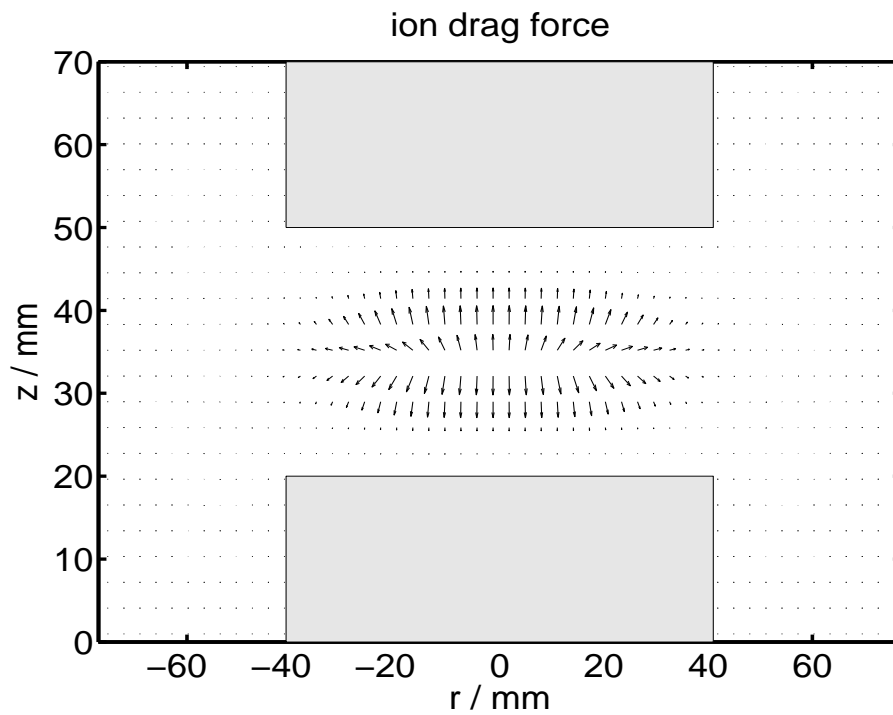


Figure 7.5: Ion drag force F_{iB} derived from the Barnes formula [49] with $b_{max} = 0.7\lambda_{De}$. An arbitrary and nonlinear scale is chosen for the vector length.

As an example that demonstrates the general features of all ion drag expressions, Fig. 7.5 shows the vector field of the ion drag force \vec{F}_{iB} after the Barnes formula with fixed cut-off radius. In most regions of the chamber the ion drag is negligible except for the central plasma, where the ion drift speed is of the order of the thermal velocity, as it is expected from Fig. 2.10 since the magnitude of the orbit force takes a maximum at $v_i \approx v_{ti}$.

The superposition of the forces $\vec{F}_{iB} + \vec{F}_E$ is shown in Fig. 7.6. According to the findings in Section 6.3, the ion drag forces, except for F_{iB}^v , exceed the counteracting electric field force in the region of low ion drift velocities and removes the dust particles from the plasma center. According to the findings in Section 6.4, the absolute value of F_{iB}^v is smaller than F_E for $v_i < v_{ti}$. Thus, only in this case, a stable equilibrium is found in the very center of the discharge. The direction of $\vec{F}_{iB}^v + \vec{F}_E$ changes sign for ion drift speeds larger than the thermal velocity. For all ion drag models the electric field force overcomes the ion drag at approximately $v_i = (3 \cdot \dots \cdot 5)v_{ti}$ and confines the particles to the bulk plasma. Thus, the two forces form a potential well with a minimum at $F_i = F_E$ which, in three dimensions, corresponds to the surface of an oblate spheroid. Particles can move along the minimum potential surface visualizing the region of dominant ion drag force – the void. The movement of particles in the trapping potential is limited only by small variations of the minimum potential energy, which is lowest at the radial boundaries of the void. Thus, the particles accumulate preferably in these areas. The maximum net force which drives the dust grains out of the void region is of the order of 10^{-12} N.

Figure 7.7 shows the region where the residual force on the particles $|\vec{F}_{iB} + \vec{F}_E| < 4.5 \cdot 10^{-13}$ N for the presented example together with the real dust distribution which is obtained from video observations. Experimental observations are compared with the model results in the following section.

7.3 Comparison of results

Comparing the observed dust distribution and the model force-equilibrium positions in Fig. 7.7, it is seen that the general shape and location of the dust cloud are quite well represented by this simple model. In more detail, the height of the void is only slightly underestimated, while the vertical extension of the observed void is found to be $(2 \cdot \dots \cdot 4)$ mm larger than the results which are derived from the simulated plasma profiles and $(1 \cdot \dots \cdot 3)$ mm larger than those from Langmuir probe measurements. Just as in the experiment, the modeled vertical void size also shows no variation within the ring electrode power sequence. The vertical equilibrium position of particles is determined by the steep force gradients, which are caused by the electric fields in the transition from bulk plasma to the edge. Recalling Eq. (5.1), a voltage difference of $(1 \cdot \dots \cdot 2) T_e$ is found in the discharge on a vertical distance of less than 1 cm. Therefore, the equilibrium is hardly influenced by slight variations of the discharge conditions.

The situation is quite different with respect to the horizontal extension of the

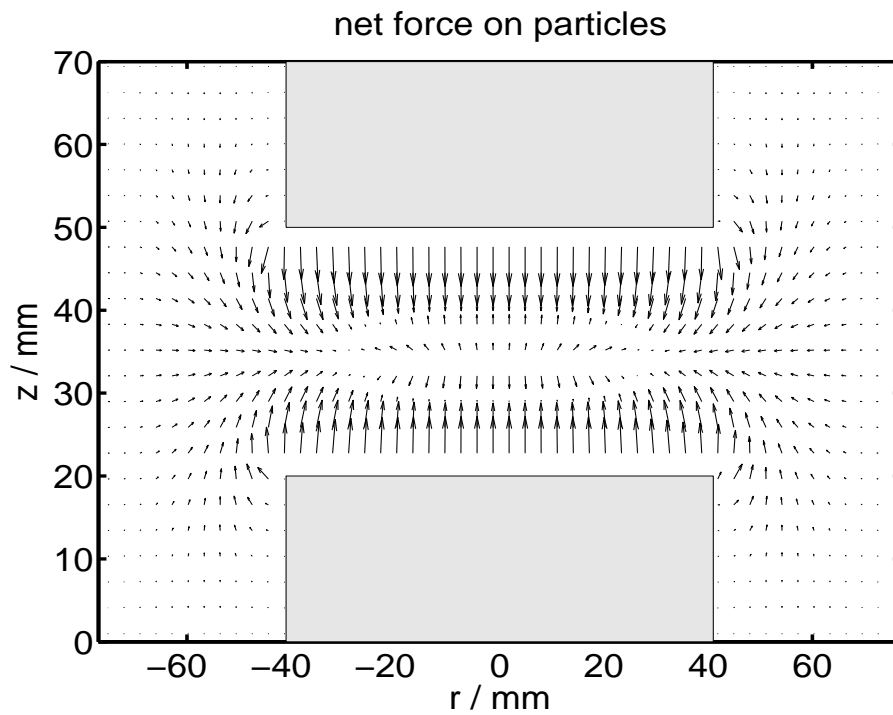


Figure 7.6: Net force $\vec{F}_{iB} + \vec{F}_E$ on the dust particles. (Same conditions as in Fig. 7.2)

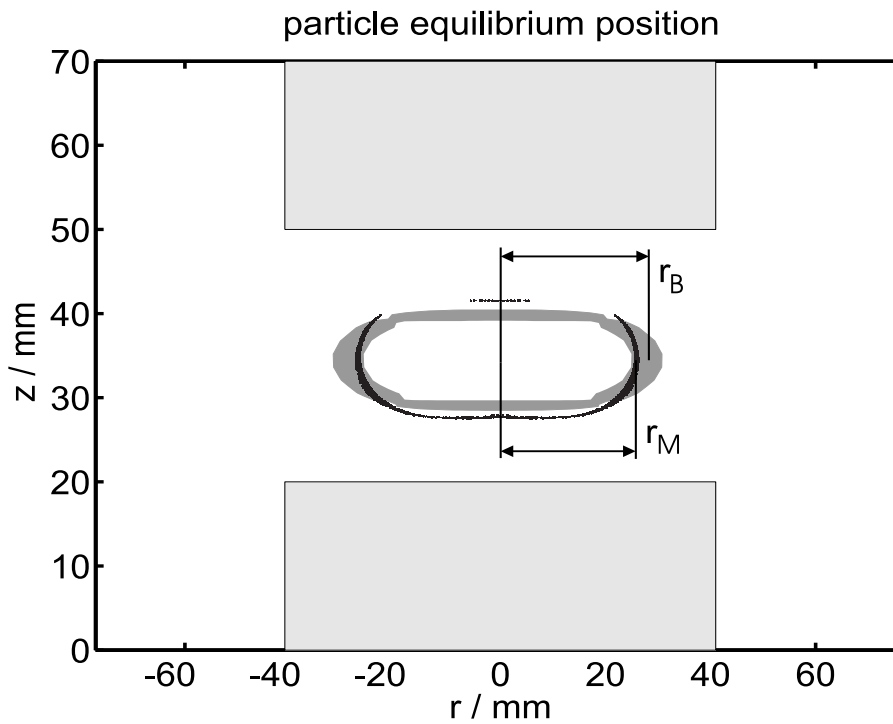


Figure 7.7: Location of the calculated force equilibrium. The grey shaded area indicates where the residual force $|\vec{F}_{iB} + \vec{F}_E|$ on the dust is smaller than $4.5 \cdot 10^{-13}$ N. The corresponding particle distribution from the video observations is overlaid in black.

void. In radial direction, the slope of the plasma potential towards the plasma boundaries is weak (see Fig. 7.2) and the particle confining potential well is wider. Thus, the dynamic response of the particle position on changed discharge conditions is more pronounced. For this reason, the horizontal extension of the observed voids are presented with the model results from probe measurements in Fig. 7.8 and from simulations in Fig. 7.9.

The results from both data sources reproduce the observed radial growth of the void with increasing U_{rf}^d . With respect to the different ion drag models, the predicted void size is largest for the calculations which use the Barnes ion drag model [49] with a fixed Coulomb cut-off radius of $b_{max} = 0.7\lambda_{De}$. These results always exceed the real observed void radius r_M in the experiments. Khrapak's model [50] yields the smallest radii r_K , while the results r_B^v which use F_{iB}^v lie in-between those of the two other models. The findings are in accordance with results of the secondary void investigations where the simple Barnes model which gives the highest force magnitude yielded the smallest anti-void, since in that case the ion drag was directed inwards. Note that for F_{iB}^v a stable equilibrium establishes also in the very center of the discharge, because $F_{iB}^v < F_E$ for $v_i < v_{ti}$. Such a feature is not observed in the experiments.

Focusing on the differences of Figs. 7.8 and Fig. 7.9, the void radii derived from measured plasma parameters match the observations within a maximum error of 3.5 mm, while the simulation results are widely spread with a maximum deviation of 5.5 mm from the real void radius. The best model on base of probe measurements includes F_{iK} , for the simulations it is F_{iB}^v . A quantitative measurement of the residual outward driving force on a particle inside a void of a PKE plasma at higher pressure is provided in [110]. The present modulation results exceed the reported maximum force by more than an order of magnitude.

7.4 Discussion

From the above findings it is obvious that at least the Barnes model [49] with a fixed Coulomb cut-off radius of the order of the electron Debye length yields ion drag forces which are systematically too high and that, therefore, a more sophisticated model should be used.

The qualitatively good agreement of the shape and size of the modeled voids in comparison with the observations also proves the dominant role of ion drag force and electric field force in the driving mechanism of the void phenomenon. Additionally, it becomes clear from the use of only a few particles that the main features of a void are already predetermined in the topology of a dust-free discharge, because even a single particle in the plasma can visualize the surface on which $F_E = F_i$. Nevertheless, in the presence of a large amount of particles, the profile of a discharge can be strongly modified compared to the particle-free plasma [23]. This is e.g. caused by a comparable enhancement of the ionization rate in the void region or lowered space potential inside a dust cloud due to electron collection on the particles [16]. The dust then forms its own confinement

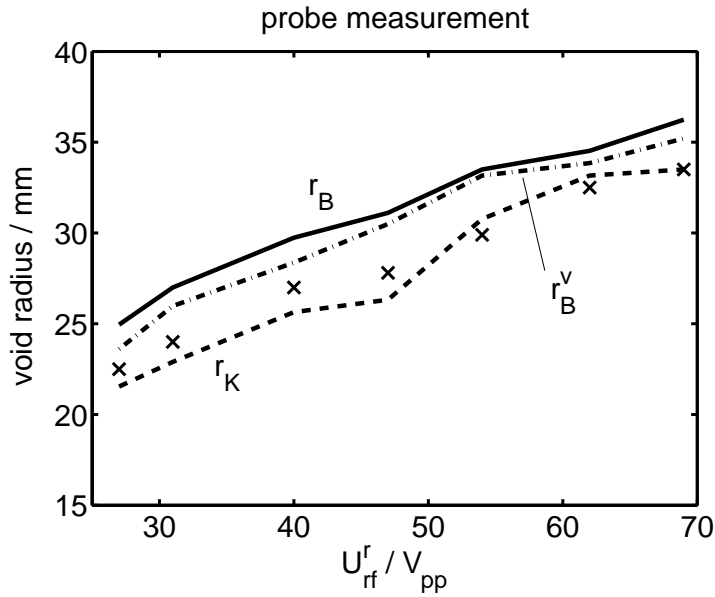


Figure 7.8: Radial size of a the modeled void region as function of the ring electrode voltage U_{rf}^r at 15 Pa argon pressure. r_B is calculated as equilibrium of electric field force and ion drag force on a particle from measured plasma parameter profiles using the Barnes formula [49] with $b_{max} = 0.7\lambda_{De}$, r_B^v uses $b_{max} = \lambda_D^v$ and the ion drag for r_K is derived with the force model of Khrapak et al. [50]. Crosses represent the experimental findings from video observations.

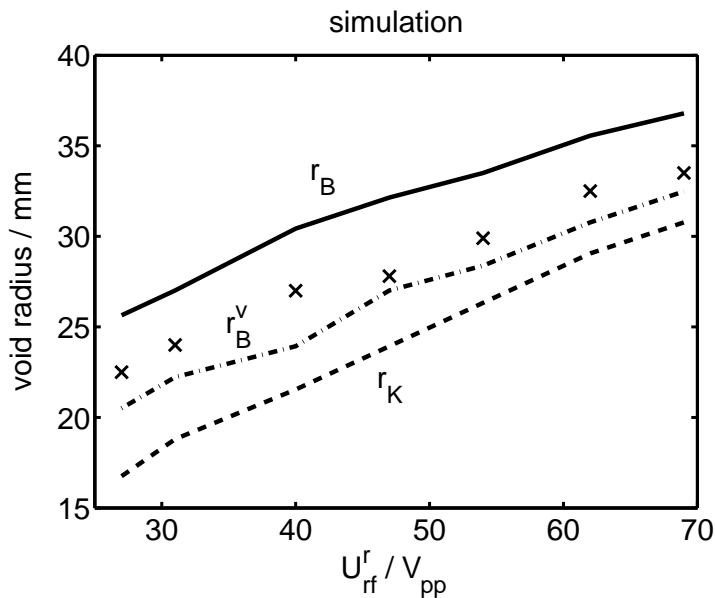


Figure 7.9: Radial size of a the modeled void region as function of the ring electrode voltage U_{rf}^r at 15 Pa argon pressure. r_B , r_B^v and r_K are calculated as equilibrium of electric field force and ion drag force on a particle from simulated plasma parameter profiles. Crosses represent the experimental findings from video observations.

potential well.

In order to close the void in a dusty rf discharge, it was suggested to primarily decrease the ionization rate [17]. This was experimentally realized in the PKE experiment onboard ISS at very low rf power close to the collapse of the plasma [18].

With respect to the Langmuir probe, it has been shown, that locally resolved probe measurements are a useful source of data to develop physical predictions on complex plasmas that are supported by experiments. Probe data can even refine discharge simulation results.

8 Discharges affected by dust

After studying the effects of a probe on small-volume low-ionized discharges, the interaction of dust particles with the probe and the probe measurement-based calculation of dust distributions in rf plasmas, this chapter will complete the present work on electrostatic probes in complex plasmas with a focus on measurable effects of dust on plasma properties, which are described in [71, 15]. Currently, only a few laboratory investigations on the changes in electron temperature, plasma density or space potential in the presence of dust exist, because invasive diagnostics (e.g. Langmuir probes) suffer from the contamination with dust, while the intensity of the glow of low-power discharges as they are used for dusty plasma experiments is often insufficient for optical diagnostic methods. Measurements on the electron temperature by the spectral line ratio method are reported in [30], sheath potentials affected by dust have been determined with LIF [209], electron density measurements with resonance cones are found in [210] and also Langmuir probes have been used [210, 211].

A technically more simpler approach represent complex plasma simulations [24, 23], which are especially related to the void-phenomenon. Additionally, a number of models (for example [18, 19]), which investigate voids, yield effects on plasma parameter profiles influenced by dust, like the depletion of free electrons or the local space charge.

An experimental setup for spatially resolved measurements in dust-free/dusty plasmas is a one-dimensional Langmuir probe scan through a particle cloud which is trapped above the lower electrode of a laboratory experiment. The results can then be extrapolated to cloud geometries, as they appear in microgravity experiments. This procedure is obvious, since the resolution of probe scans under microgravity conditions is still limited by a maximum measurement time of 20 s during parabolic flights. Nevertheless, in-flight measurements in a plasma with high dust density which have been performed during this project are reported in [212].

8.1 Experiment and results

The experiments have been performed in the PKE plasma chamber (see Section 3.1.1). At 40 Pa argon gas pressure and a fixed rf voltage of $U_{rf} = 80 V_{pp}$ a one dimensional probe scan from the lower to the upper electrode along the discharge axis has been measured as shown in Fig. 8.1. The position of the lower

electrode is $z = 0$ mm, the upper electrode is located at $z = 30$ mm. One scan comprises 54 different probe positions on the z -axis, alternating with reference probe sweeps in the discharge center to account for possible drifts in plasma properties during the measurements.

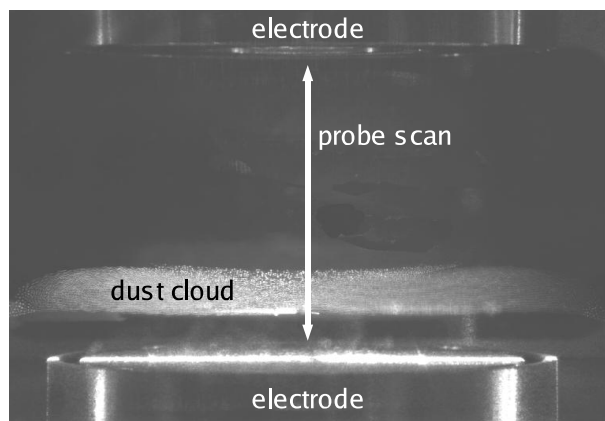


Figure 8.1: Scheme of the 1D probe scan path through a discharge with a thick cloud of trapped particles ($r_d = 1.74 \mu\text{m}$) in the PKE plasma chamber.

After a scan in a dust-free plasma, particles are injected without changing the external discharge conditions. The charged dust is vertically trapped by the strong electric fields in the plasma sheath above the lower electrode. A horizontal confinement is also given by the radial gradients of the plasma potential (compare with Fig. 5.7) which are strong enough to balance the inner Coulomb pressure of the dust cloud approximately at the edge of the electrodes. Thus, the plasma is filled up with particles of $r_d = 1.74 \mu\text{m}$ up to a level, which is, compared to the dust-free discharge, inside the bulk plasma. The subsequent probe scan then traverses a particle cloud on a length of approximately 4.5 mm. With the use of a random probe voltage sweep (see Section 3.4.2), the accumulated contamination of the probe with particles after the scan is weak and the probe can be easily refreshed by a cleaning procedure. The particle density in the center of the cloud is $n_d \approx 2 \cdot 10^{11} \text{m}^{-3}$.

Figure 8.2 shows the plasma potential distribution between the electrodes in a dust-free discharge. The profile is strictly symmetrical around the mid-plane of the discharge at $z = 15$ mm as it is expected from the chamber geometry. Close to the electrodes, steep potential drops reveal the beginnings of the time-averaged rf plasma sheaths. The almost field-free bulk plasma is recognizable as potential plateau. Still, a weakly pronounced maximum of $\phi_p = 41.6$ V can be identified in the center of the plasma.

In the presence of the dust cloud, this maximum is shifted towards the upper electrode, but its magnitude is left nearly unchanged at $\phi_p = 41.4$ V. The central plateau of the bulk plasma slightly slants towards the particle accumulation with only 0.8 V difference from the peak value to the dust-plasma interface. Inside the dust cloud, ϕ_p rapidly decreases and the transition region to the lower space charge sheath seems to be doubled in thickness, penetrating the cloud. Thus, for

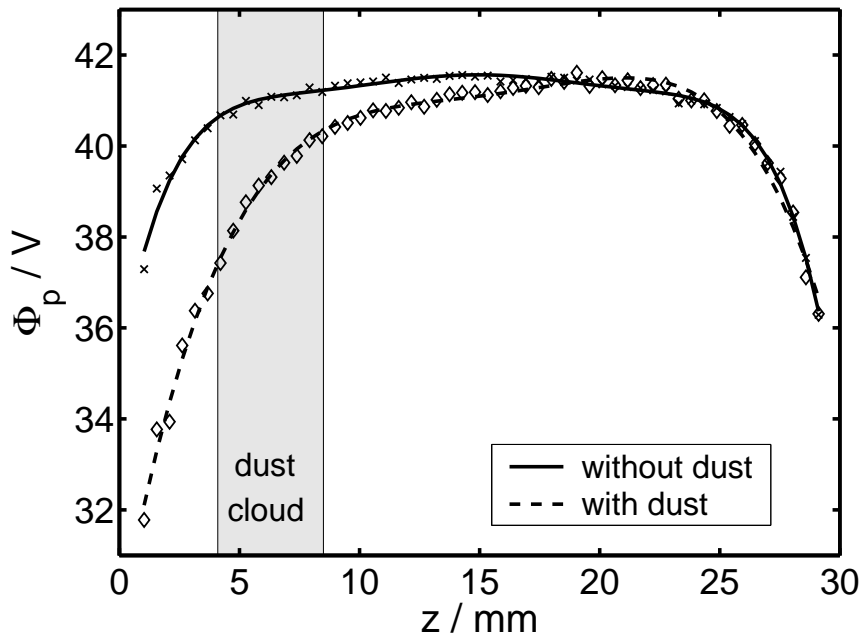


Figure 8.2: One dimensional profile of the plasma potential ϕ_p along the rotational (z -) axis of the PKE experiment at $p_{\text{argon}} = 40 \text{ Pa}$ and $U_{rf} = 80 V_{pp}$. Crosses represent measurements in a dust-free plasma, squares in a dusty plasma. The position of the particle cloud is indicated by the shaded area. The curves are the best fits of the two data sets. The lower electrode is located at $z = 0 \text{ mm}$, the upper at $z = 30 \text{ mm}$.

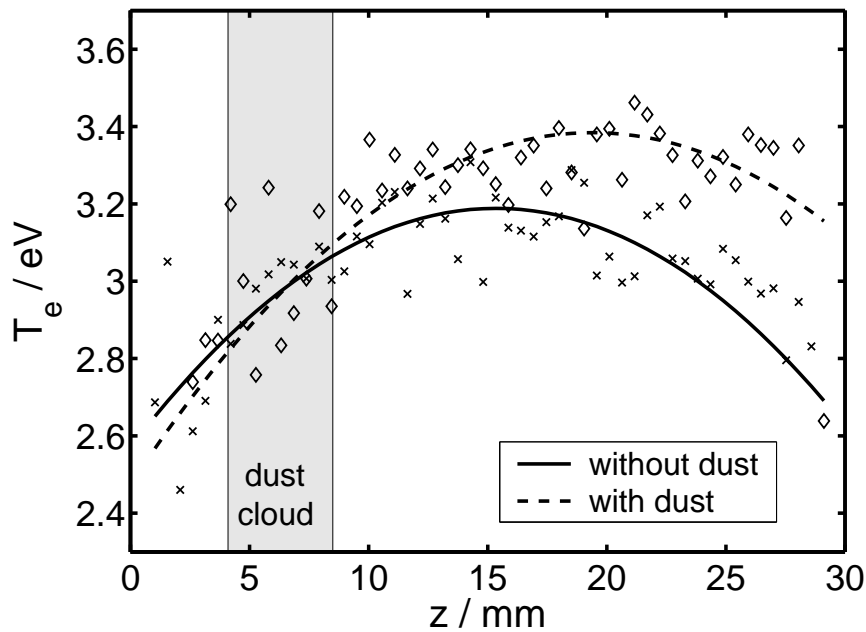


Figure 8.3: One dimensional profile of the electron temperature T_E along the rotational (z -) axis of the PKE experiment at $p_{\text{argon}} = 40 \text{ Pa}$ and $U_{rf} = 80 V_{pp}$. Crosses represent measurements in a dust-free plasma, squares in a dusty plasma. The curves are the best fits of the two data sets.

example, the space potential at $z = 3$ mm is approximately 5 V lower than in the particle-free case. The behavior of the potential close to the upper electrode is nearly unchanged by the particles.

Generally, the determination of the electron temperature includes the largest relative error of the derived plasma parameters (see Section 5.3.1). Nevertheless, with respect to the fitted curve (least-square fit), again a symmetrical inter-electrode profile is obtained for the dust-free discharge plotted in Fig. 8.3. The maximum electron temperature is found at approximately $T_e = 3.2$ eV, close to the electrodes it is still 2.7 eV. With injected particles, a distinct increase of $\Delta T_e \approx 0.2$ eV in the mid-plane of the plasma to $\Delta T_e \approx 0.5$ eV at the upper plasma boundary becomes visible in the particle-free part of the discharge. Towards the dust cloud, T_e significantly decreases and its characteristics in and below the cloud is similar to the dust-free case.

Figure 8.4 presents the distribution of the plasma density n^{icoll} along the discharge axis, which is derived from the ion saturation current of the probe characteristics with the model described in Section 4.5 using ABR theory and a correction for ion-neutral collisions. Figure 8.5 shows the plasma density n^{esat} , which is obtained from the probe's electron saturation current at $V_p = \phi_p$. Again, symmetrical distributions around $z = 15$ mm with (negatively) increasing gradients towards the electrodes are given for both density values without injected dust particles. The ratio n^{icoll}/n^{esat} of the fitted curves in the dust-free case is almost constant at 1.08, except for the sheath regions. This indicates that the average difference of the measured densities, derived from the two methods, is systematic and is probably caused by the collision correction of the probe analysis method as already mentioned in Section 5.2.

In the presence of the dust cloud, the peak plasma density is lowered by approximately 20 % and shifted from the center of the plasma upwards to $z = 20$ mm. From the maximum of the profile to the edge of the particle cloud at $z \approx 8.5$ mm the plasma density decreases almost linearly. Inside the cloud, the reduction rate is further enhanced in direction to the lower electrode. In comparison with the dust-free case the electron and ion density in the lower third of the plasma where the particles are confined is reduced by approximately 50 %, while, in the upper third, the reduction is only (10 ··· 15) %. The ratio n^{icoll}/n^{esat} with microparticles confined in the plasma is, even at the position of the dust cloud, nearly constant at 1.1. Thus, no distinct deviation from the equality of free electrons and ions can be detected in the complex plasma according to the accuracy of measurement.

8.2 Discussion

The influence of the presence of dust particles in a plasma has been shown by the comparison of plasma parameters obtained from highly resolved Langmuir probe measurements in a dust-free plasma and a plasma containing a large particle cloud under the same discharge conditions.

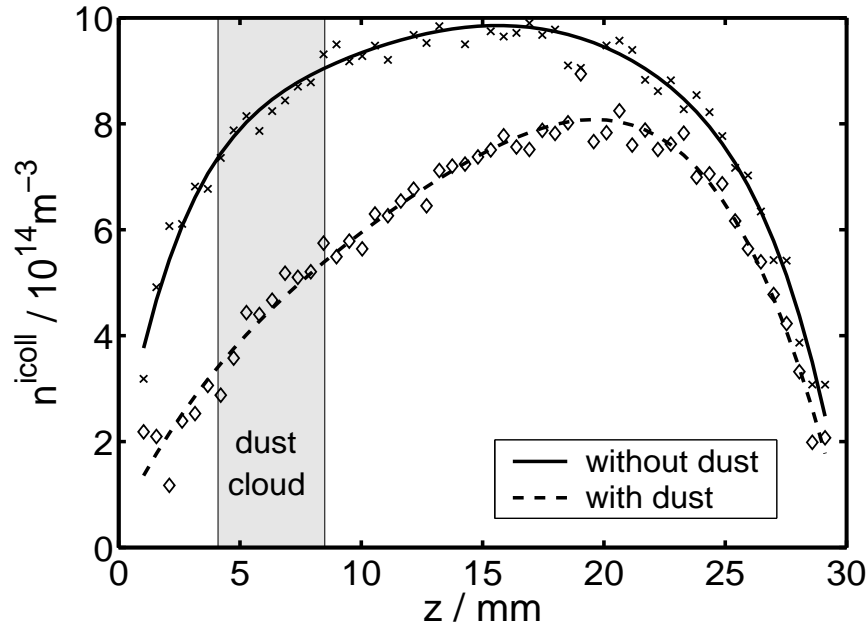


Figure 8.4: One dimensional profile of the plasma density n^{icoll} which is obtained from the ion saturation current of the probe characteristic according to the model described in Section 4.5. Experimental conditions are the same as in Fig. 8.2. Crosses represent measurements in a dust-free plasma, squares in a dusty plasma. The curves are the best fits of the two data sets.

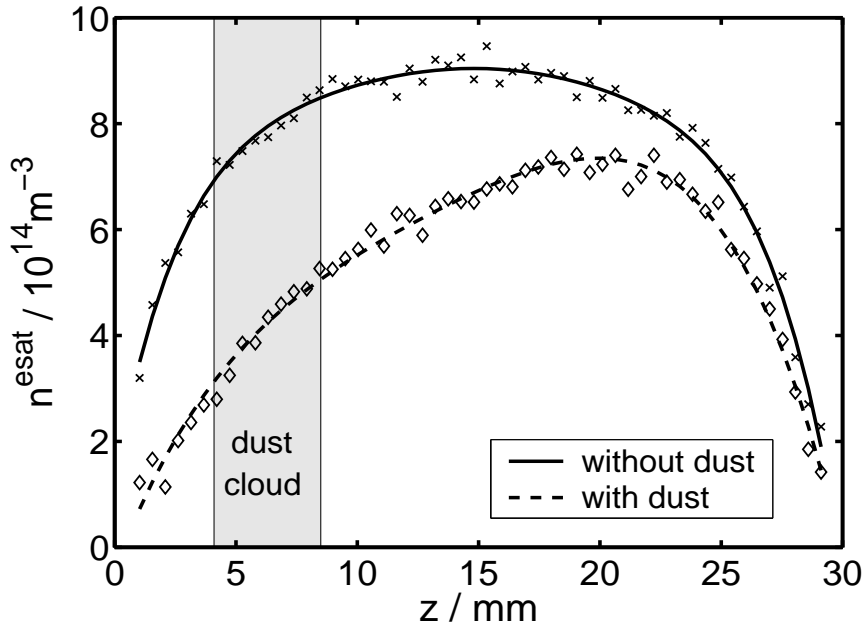


Figure 8.5: One dimensional profile of the plasma density n^{esat} which is obtained from the electron saturation current of the probe characteristic at ϕ_p according to Eq. (4.1). Experimental conditions are the same as in Fig. 8.2. Crosses represent measurements in a dust-free plasma, squares in a dusty plasma. The curves are the best fits of the two data sets.

Several significant differences in the resulting plasma parameter profiles are detected by the probe diagnostic. The measured reduction of the space potential close to and inside the dust cloud is in accordance with observation of Arnas *et al.* [209], who derived the potential distribution in a dust-free/dusty sheath from LIF-measurements. Our ϕ_p -profiles are also in a good agreement with numerical simulations of a dusty PKE plasma under microgravity conditions of Akdim and Goedheer [23]. There, a void structure establishes in the particle cloud, which corresponds, in a first approximation, to the present one-dimensional scan, if a second dust cloud were present near the upper electrode. Akdim and Goedheer [23] observed a lower central peak potential and the increase of electric fields near the plasma-dust interface and inside the cloud. The first feature is less pronounced in our experiment, which can be explained by the absence of a second (upper) dust cloud giving rise to an almost unchanged ionization rate and electron current to the electrode in the upper third of the discharge (see Fig. 8.2). This is also supported by the observed shift in the position of the maximum potential and plasma density which is only slightly decreased in the area close to the upper electrode. In the enhanced electric field of the slanted potential plateau ions are more effectively accelerated, which yields for super-thermal velocities to a stronger decreasing ion drag force on the first particle layers of the dust cloud as well as to a large gradient of the counteracting electric field force. This situation is similar to the confinement of particles in a shell around the probe as described in Section 6.2 and is, transferred to the void phenomenon, made responsible for the compression of the dust cloud close to the void-dust interface [24]. The possible generation of a thin electrostatic double layer localized at the dust-plasma interface (see [13]) is unlikely to be measurable with a Langmuir probe, since, even at the probe-tip, the effective probe diameter (sheath diameter) is approximately one millimeter (see Fig. 6.5). Therefore, the parameters obtained from the probe are spatially averaged over this length scale in vertical direction.

The reported significant plasma density reduction in the dust cloud and thus the concentration of the higher ionized region to the void in [23] is reproduced by the contraction of the measured density profile to the dust-free part of the plasma (see Figs. 8.4, 8.5). Obviously, the recombination of electrons and ions on the dust surface acts as an effective sink for plasma particles. As a result of the global decrease of the number of electrons and ions, the residual electrons can gain more energy from the discharge sustaining rf fields, yielding a higher electron temperature T_e (see Fig. 8.3). In a self-adjusting process the increase of T_e then increases the ionization rate which compensates the charge-carrier losses on the dust particles and maintains the discharge.

Besides the higher average electron temperature in a particle containing plasma, it is expected from numerical work [23, 213] that the highest magnitude of T_e should occur inside the dust region. The experiment of Samsonov and Goree [30] also suggests such an increased electron temperature. This is not seen in the present measurements and the observed reduction of electron temperature in the dust cloud which is here located close to the plasma edge requires comparison with future simulations for the present situation.

The determination of plasma densities from probe measurements obtained in the transition region from the bulk plasma to the sheath, where the dust cloud is levitated, is generally difficult, since the requirements for application of probe theories are no longer strictly fulfilled. The whole probe characteristic may be influenced, for example, by streaming ions and a larger methodical error must be assumed for the resulting density values than in the central equilibrium plasma. Therefore, the fact that even in the particle cloud $n^{icoll} \approx n^{esat}$ proves the reliability of the diagnostic method.

Under the current discharge conditions and the given particle density n_d , the Havnes parameter (see Eq. (2.44)) inside the dust cloud is estimated to be $P \approx 2$. Thus, a depletion of electrons manifesting in $n^{icoll} \gtrsim n^{esat}$ is expected in the cloud, since the simple quasi-neutrality condition Eq. (2.6) has to be substituted by Eq. (2.40), which takes into account the negative dust particle charge [15]. With respect to the restrictions of probe diagnostics arising from the cloud position at the plasma boundary this effect is unlikely to be measurable in the present case. In order to make spatially resolved measurements of the electron depletion effect, additional experiments in dust clouds located in the bulk plasma, which can be obtained under microgravity conditions have to be performed. In a completely different experimental setup, Barkan *et al.* [64] determined a depletion of electrons in the center of a plasma column applying a permanent flow of falling dust particles.

From the presented probe data, it becomes clear that, despite the limits of the diagnostic method, many effects of dust particles on the properties of a gas discharge can be already detected with a Langmuir probe. A main result is the importance of the consideration of the feedback of particle charge on the space potential as well as the dust-enhanced recombination rate when modeling complex plasmas.

9 Summary and outlook

In this thesis the fundamentals of Langmuir probe diagnostics in complex plasmas have been explored in a comprehensive experimental study in comparison with theoretical estimates and plasma simulations. The investigations have been focused on conditions which are found in experiments used on parabolic flights and are envisaged to be implemented, as internationally joined experimental infrastructure IMPACT-IMPF, aboard the ISS for studies on dusty plasmas under microgravity conditions.

The following topics have been addressed:

- the evaluation of suitable probe theories with respect to the influence of collisions and the verification of the chosen probe model
- the influence of the presence of a probe on small-volume discharges
- the quantitative plasma characterization of discharges for current and future experiments under microgravity
- the contamination of probes by particle attraction in a dusty plasma environment
- the effect of the probe on the distribution of surrounding dust particles
- the understanding of dust distribution mechanisms in rf-discharges by probe data
- the influence of dust on plasma parameter profiles

For this purpose the available probe theories have been critically evaluated under the given experimental conditions and an automated curve fitting algorithm has been implemented to process the huge amount of probe data that result from two-dimensional scans of plasma profiles in the PKE or IMPF prototype experiments. It could be shown, that, instead of the standard OML theory, the competing “radial motion theory” [27] with corrections for ion-neutral collisions [164, 185] is the appropriate model to describe the ion saturation part of the probe characteristic, which should be preferably used for data analysis in small-volume and especially dusty plasmas. As demonstrated, the presence of collisions is causal for the required radial motion of ions. Moreover the fitting

algorithm yields mutually agreeing density values n^{esat} and n^{icoll} from electron and ion currents up to high argon pressures of 60 Pa. Earlier probe data analysis, which was based on the OML theory with Laframboise's extensions [26], resulted in a measured discrepancy in ion and electron density by a full order of magnitude.

The perturbation of the small-volume and feeble plasma in the PKE device by the presence of a probe was investigated by introducing a second probe of same dimensions. In this way the systematic error of probe measurements could be quantified. It was demonstrated that reliable probe measurements can be performed even in discharges with extremely low plasma densities of the order of 10^{14}m^{-3} .

The reliability of the probe diagnostics has been proven by a comparison of measured two-dimensional profiles of plasma parameters from systematic laboratory studies in the PKE and IMPF devices with results of SIGLO simulations. The presently used radial motion probe theory with correction for collisions yields plasma profiles that match the simulations within better than a factor of two. For the remaining difference the simulation model can be made responsible since its results, using atomic parameters from different authors, differ by a factor of two. Within these limits, the measured profiles are supported by simulations even in their spatial distribution. The experimentally obtained scaling laws of plasma parameters with the discharge conditions are also in a very good agreement with theory and experimental finding of other authors. Thus, probe measurements are a source of information to evaluate the design of plasma device prototypes for orbit-based experiments and the refinement of corresponding simulation models.

The future application of Langmuir probes in the IMPF facility aboard the International Space Station requires long-term operation of the probe without contamination by the dust, which occurs when the probe bias $V_p > \phi_p$ and results in the attraction of negatively charged particles. Therefore, different waveforms for scanning the probe characteristic have been critically evaluated. It has been experimentally demonstrated that the deposition of particles on the probe-tip can be effectively avoided with a probe voltage sweep, which is, time-averaged, essentially negative with respect to the plasma potential. Scans with positive probe bias have to be performed alternating with negative biases at a frequency above the dust-plasma frequency ω_{pd} making use of the particle inertia to hold off the dust. It could further be shown that a residual long term contamination can be removed by electron heating of the probe.

The interaction of charged particles with the probe under microgravity conditions has been studied in a complex plasma during the 3rd DLR parabolic flight campaign in 2001. The experiments led to the discovery of unexpected dust distributions around the probe, which were named "secondary voids". This new phenomenon could be explained in terms of a force balance between

repulsive electric forces on dust grains from the negatively biased probe and ion drag forces from the ion attraction by the floating probe. The force orientation in the phenomenon of the large void-region in the central plasma is opposite to the probe induced void, which, therefore, have been shown to be driven by an “anti-void” mechanism. By application of a sophisticated model for the ion flow in the presheath, it became possible to predict the position of force equilibrium quantitatively in close agreement with the experimental observations. As an important result, the particles confined around the probe have been shown to closely reveal and thus to visualize the sheath structure around an object in the plasma. Moreover, it was observed that the particles in the dust sleeve around the probe arrange in distinct layers. This effect could also be quantitatively explained by the model in terms of the force gradients forming the dust confinement potential well.

During the 5th DLR parabolic flight campaign in 2003, experiments with the IMPF chamber yielded a wealth of data on the distribution of dust tracers in rf-discharges. From the observations it could be shown that the feature of a central void region is already predetermined in the characteristics of a dust-free plasma. Since a low amount of dust has little influence on the plasma parameters, it became possible to compare the observed dust distribution with corresponding profiles from two-dimensional probe scans of dust-free discharges and simulations. Based on a force balance between ion drag and electric field force, it could be shown that the observed particle distribution can be predicted with high accuracy. Thus, the dominance of the two forces, which are understood to be the driving mechanisms of the well-known void-phenomenon, has been proven experimentally. Applying different models for the ion drag force, it could also be demonstrated, as well as in the case of the secondary void investigation, that the standard Barnes formula [49] overestimates the magnitude of the ion drag on particles, while the more recent model of Khrapak [50] tends to underestimate the ion drag force. The finding contributes to the recent debate on ion drag models [28, 29] and claims a refinement of current theories with respect to the validity of the used scattering potential approximation with a fixed cut-off radius and the role of ion-neutral collisions. A particularly nice example for the agreement between observed particle distributions under microgravity and plasma profiles from measurements and simulation is the formation of a toroidal dust distribution in the IMPF device.

As a second advanced application of the developed probe diagnostic, the influence of large amounts of dust on rf discharges was studied in laboratory experiments with the PKE device. It could be demonstrated by direct probe measurements that the dust leads to a significant reduction of plasma density in the dust region, which also affects the global potential structure of the discharge. This can be attributed to charge-carriers losses by recombination on the dust particles. The trend represents an “internal wall” effect similar to the plasma losses to external surfaces and is in accordance with dusty plasma simulations of other authors [23]. Additionally, it was observed that the electron temper-

ature in the remaining volume rises as expected from the complex plasma models.

The present investigation has demonstrated the capabilities of Langmuir probe diagnostics in complex plasmas. Probe diagnostics represent an essential link between optical observation of dust distributions and dynamics and corresponding theoretical models and simulations of complex plasmas. The next step should be marked by long-term measurements in plasmas with high dust densities under microgravity conditions, as it will become possible with the IMPF facility aboard the ISS. Then, the properties of complex plasmas and the interaction of dusty and dust-free plasma regions like in the void phenomenon will be directly experimentally accessible and theoretical assumptions become verifiable.

Besides the specific diagnostical application of the Langmuir probe one could envisage further detailed studies of the ion drag force on tracer particles in future long-term experiments under microgravity.

From our observations of dust-free regions around probes we had suggested to use fine dust as a novel method to visualize the boundary region of the space charge layer around floating or biased objects in a plasma. This method will be of great help in the further refinement of minimum invasive probe techniques in general.

At last, the observation of particle layering in dust confinement regions is a very general finding in dusty plasmas that was observed for experiments with dust fluids in narrow channels [123], in simulations [122] and, very recently, in the structure of Coulomb balls [117]. This layering effect is an immediate hint at strong confining forces and can be used, as in the present case, to estimate the force gradients involved. In this way structure information from the dust arrangement can be utilized to deduce the acting force distribution on the dust. Moreover, induced particle stratifications by external forces are also known from other physical disciplines (for example [125, 126]), which emphasizes the role of complex plasmas as model systems for future fundamental studies.

Bibliography

- [1] P. Bliokh, V. Sinitsin, and V. Yaroshenko, *Dusty and self-gravitational plasma in space* (Kluwer Academic Publ., Dordrecht, 1995).
- [2] A. Bouchoule, *Dusty plasmas: physics, chemistry, and technological impacts in plasma processing* (John Wiley & Sons Ltd, New York, 1999).
- [3] H. Thomas, G. E. Morfill, and V. N. Tsytovich, *Plasma Physics Reports* **29**, 895 (2003).
- [4] A. Piel and A. Melzer, *Plasma Phys. Control. Fusion* **44**, 085004 (2002).
- [5] A. Piel *et al.*, *J. Phys. B* **36**, 533 (2003).
- [6] A. Melzer, *Der Plasmakristall: Phasenübergang und Stabilität*, Vol. 74 of *Reihe Physik* (Harri Deutsch Verlag GmbH, Frankfurt/ Main, 1997).
- [7] A. Piel and A. Melzer, *Adv. Space Res.* **29**, 1255 (2001).
- [8] D. J. Wineland *et al.*, *Phys. Rev. Lett.* **59**, 2935 (1987).
- [9] G. E. Morfill *et al.*, *Phys. Rev. Lett.* **83**, 1598 (1999).
- [10] H. Thomas *et al.*, *Physica Scripta* **89**, 16 (2001).
- [11] V. E. Fortov *et al.*, *JETP* **87**, 1087 (1998).
- [12] A. P. Nefedov *et al.*, *New J. Phys.* **5**, 33.1 (2003).
- [13] B. M. Annaratone *et al.*, *Phys. Rev. E* **66**, 056411 (2002).
- [14] G. E. Morfill *et al.*, in *Dusty Plasmas in the new Millennium: Third International Conference on the Physics of Dusty Plasmas, Durban, 2002*, edited by R. Bharuthram, M. A. Hellberg, P. K. Shukla, and F. Verheest (American Institute of Physics, Melville, NY, 2002), pp. 91–109.
- [15] O. Havnes *et al.*, *J. Geophys. Res.* **92 A3**, 2281 (1987).
- [16] J. Goree, G. E. Morfill, V. N. Tsytovich, and S. V. Vladimirov, *Phys. Rev. E* **59**, 7055 (1999).
- [17] G. Morfill and V. N. Tsytovich, *Phys. Plasmas* **9**, 4 (2002).

- [18] V. N. Tsytovich, G. E. Morfill, U. Konopka, and H. Thomas, *New J. Phys.* **5**, 66.1 (2003).
- [19] P. M. Bryant, *New J. Phys.* **6**, 60 (2004).
- [20] P. Belenguer *et al.*, *Phys. Rev. A* **46**, 7923 (1992).
- [21] J. P. Boeuf, P. Belenguer, and T. Hbid, *Plasma Sources Sci. Technol.* **3**, 407 (1994).
- [22] M. R. Akdim and W. J. Goedheer, *Phys. Rev. E* **65**, 015401 (2002).
- [23] M. R. Akdim and W. J. Goedheer, *Phys. Rev. E* **67**, 066407 (2003).
- [24] G. Gozadinos, A. V. Ivlev, and J. Boeuf, *New J. Phys.* **5**, 32.1 (2003).
- [25] SIGLO-2D, Version 1.1, Kinema Software.
- [26] J. G. Laframboise, University of Toronto Institute of Aerospace Studies, Report No. 100, (1966).
- [27] J. E. Allen, R. L. F. Boyd, and P. Reynolds, *Proc. Phys. Soc. B* **70**, 297 (1957).
- [28] S. A. Khrapak *et al.*, *Phys. Plasmas* **10**, 4579 (2003).
- [29] C. Zafiu, A. Melzer, and A. Piel, *Phys. Plasmas* **10**, 4582 (2003).
- [30] D. Samsonov and J. Goree, *Phys. Rev. E* **59**, 1047 (1999).
- [31] W. J. Goedheer, *Plasma Sources Science and Technology* **9**, 507 (2000).
- [32] M. A. Lieberman and A. J. Lichtenberg, *Principles of plasma discharges and material processing* (John Wiley and Sons Inc., New York, 1994).
- [33] T. Trottenberg, A. Melzer, and A. Piel, *Plasma Sources Sci. Technol.* **4**, 450 (1995).
- [34] C. Zafiu, A. Melzer, and A. Piel, *Phys. Rev. E* **63**, 066403 (2001).
- [35] K.-U. Riemann, *Phys. Fluids* **24**, 2163 (1981).
- [36] K.-U. Riemann, *Phys. Fluids B* **3**, 3331 (1991).
- [37] F. F. Chen, in *Plasma Diagnostic Techniques*, edited by R. H. Huddlestone and S. L. Leonard (Academic Press, New York, 1965), Chap. 4, pp. 113–200.
- [38] D. Bohm, in *The Characteristic of Electrical Discharges in Magnetic Fields*, edited by A. Guthrie and R. K. Wakerling (McGraw-Hill, New York, 1949), Chap. 3.

- [39] E. R. Harrison and W. B. Thompson, Proceedings of the Physical Society (London) **74**, 145 (1959).
- [40] K. U. Riemann, Phys. Plasmas **4**, 4158 (1997).
- [41] K.-U. Riemann, J. Phys. D: Appl. Phys. **24**, 493 (1991).
- [42] G. Gozadinos, Ph.D. thesis, Dublin City University, 2001.
- [43] R. Flohr, A. Melzer, and A. Piel, Plasma Sources Sci. Technol. **3**, 206 (1994).
- [44] V. A. Godyak, R. B. Piejak, and B. M. Alexandrovich, Phys. Rev. Lett. **68**, 40 (1992).
- [45] V. A. Godyak and R. B. P. ans B. M. Alexandrovich, Plasma Sources Sci. Technol. **1**, 36 (1992).
- [46] M. Lampe, V. Gavrishchaka, G. Ganguli, and G. Joyce, Phys. Rev. Lett. **86**, 5278 (2001).
- [47] M. Lampe, J. Plasma Phys. **65**, 171 (2001).
- [48] J. Goree, Phys. Rev. Lett. **69**, 277 (1992).
- [49] M. S. Barnes *et al.*, Phys. Rev. Lett. **68**, 313 (1992).
- [50] S. A. Khrapak, A. V. Ivlev, G. E. Morfill, and H. M. Thomas, Phys. Rev. E **66**, 046414 (2002).
- [51] D. A. Law, W. H. Steel, B. M. Annaratone, and J. E. Allen, Phys. Rev. Lett. **80**, 4189 (1998).
- [52] E. C. Whipple, Rep. Prog. Phys. **44**, 1197 (1981).
- [53] H. M. Mott-Smith and I. Langmuir, Phys. Rev. **28**, 727 (1926).
- [54] T. Matsoukas and M. Russell, J. Appl. Phys. **77**, 4285 (1995).
- [55] M. Hirt, Ph.D. thesis, Universität Kiel, 2003.
- [56] C. M. C. Nairn, B. M. Annaratone, and J. Allen, Plasma Sources Sci. Technol. **7**, 478 (1998).
- [57] P. Bryant, J. Phys. D: Appl. Phys. **36**, 2859 (2003).
- [58] J. E. Allen, B. M. Annaratone, and U. deAngelis, J. Plasma Phys. **63**, 299 (2000).
- [59] J. E. Daugherty, R. K. Porteous, M. D. Kilgore, and D. B. Graves, J. Appl. Phys. **72**, 3934 (1992).

- [60] A. Homann *et al.*, Phys. Rev. E **56**, 7138 (1997).
- [61] A. Homann *et al.*, Phys. Lett. A **242**, 173 (1998).
- [62] U. Konopka, L. Ratke, and H. M. Thomas, Phys. Rev. Lett. **79**, 1269 (1997).
- [63] B. Walch, M. Horanyi, and S. Robertson, IEEE Trans. Plasma Sci. **22**, 97 (1994).
- [64] A. Barkan, N. D'Angelo, and R. L. Merlino, Phys. Rev. Lett. **73**, 3093 (1994).
- [65] D. Winske and M. E. Jones, IEEE Trans. Plasma Sci. **23**, 188 (1995).
- [66] R. Kollath, *Sekundärelektronen-Emission fester Körper bei Bestrahlung mit Elektronen, Handbuch der Physik, XXI* (Springer Verlag, Berlin, Göttingen, Heidelberg, 1956).
- [67] O. Hachenberg and W. Brauer, Adv. Electron. Phys. **11**, 413 (1959).
- [68] D. J. Gibbons, *Handbook of Vacuum Physics*, Vol. 2 of 3 (A. H. Beck, Oxford: Pergamon, 1966).
- [69] W. C. Knudsen and K. K. Harris, J. Geophys. Res. **78**, 1145 (1973).
- [70] N. Meyer-Vernet, Astronom. Astrophys. **105**, 98 (1982).
- [71] C. K. Goertz, Rev. Geophys. **27**, 271 (1989).
- [72] C. K. Goertz, in *Plasmaphysik im Sonnensystem*, edited by K.-H. Glaßmeier and M. Scholer (BI-Wissenschaftsverlag, Mannheim, 1991), Chap. 14.
- [73] C. Cui and J. Goree, IEEE Trans. Plasma Sci. **22**, 151 (1994).
- [74] J. Goree, IEEE Trans. Plasma Sci. **22**, 89 (1994).
- [75] O. Havnes, T. K. Aanesen, and F. Melandsø, J. Geophys. Res. **95**, 6581 (1990).
- [76] J. H. Chu and L. I, Physica A **205**, 183 (1994).
- [77] H. Thomas *et al.*, Phys. Rev. Lett. **73**, 652 (1994).
- [78] A. Melzer, T. Trottenberg, and A. Piel, Phys. Lett. A **191**, 301 (1994).
- [79] S. G. Brush, H. L. Sahlin, and E. Teller, J. Chem. Phys. **45**, 2102 (1966).
- [80] W. L. Slattery, G. D. Doolen, and H. E. DeWitt, Phys. Rev. A **21**, 2087 (1980).

- [81] S. Hamaguchi, R. Farouki, and D. H. E. Dubin, *Phys. Rev. E* **56**, 4671 (1997).
- [82] T. Nitter, *Plasma Sources Sci. Technol.* **5**, 93 (1996).
- [83] P. S. Epstein, *Phys. Rev.* **23**, 710 (1924).
- [84] H. Schollmeyer, A. Melzer, A. Homann, and A. Piel, *Phys. Plasmas* **6**, 2693 (1999).
- [85] H. Vestner and L. Waldmann, *Physica* **86A**, 303 (1977).
- [86] L. Talbot, R. K. Cheng, R. W. Schefer, and D. R. Willis, *J. Fluid Mech.* **101**, 737 (1980).
- [87] H. Vestner and J. Halbritter, *Z. Naturforschung* **36a**, 559 (1981).
- [88] J. Perrin, P. Molinás-Mata, and P. Belenguer, *J. Phys. D: Appl. Phys.* **27**, 2499 (1994).
- [89] O. Havnes *et al.*, *Plasma Sources Sci. Technol.* **3**, 448 (1994).
- [90] H. Rothermel *et al.*, *Phys. Rev. Lett.* **89**, 175001 (2002).
- [91] J. E. Daugherty, R. K. Porteous, and D. B. Graves, *J. Appl. Phys.* **73**, 1617 (1993).
- [92] S. Hamaguchi and R. T. Farouki, *Phys. Plasmas* **1**, 2110 (1994).
- [93] A. Melzer *et al.*, *Phys. Rev. E* **54**, R46 (1996).
- [94] V. A. Schweigert *et al.*, *Phys. Rev. E* **54**, 4155 (1996).
- [95] M. D. Kilgore, J. E. Daugherty, R. K. Porteous, and D. B. Graves, *J. Appl. Phys.* **73**, 7195 (1993).
- [96] S. A. Khrapak, A. V. Ivlev, G. E. Morfill, and S. K. Zhdanov, *Phys. Rev. Lett.* **90**, 225002 (2003).
- [97] J. A. Bittencourt, *Fundamentals of Plasma Physics* (Pergamon, New York, 1986).
- [98] H.-S. Hahn, E. A. Mason, and F. J. Smith, *Phys. Fluids* **14**, 278 (1971).
- [99] E. Thomas Jr., K. Avinash, and R. L. Merlino, *Phys. Plasmas* **11**, 1770 (2004).
- [100] C. Zafiu, A. Melzer, and A. Piel, *Phys. Plasmas* **9**, 4794 (2002).
- [101] C. Zafiu, A. Melzer, and A. Piel, *Phys. Plasmas* **10**, 1278 (2003).

- [102] M. R. Akdim, W. J. Goedheer, and R. P. Dahiya, *New J. Phys.* **5**, 20.1 (2003).
- [103] I. V. Schweigert, A. L. Alexandrov, and F. M. Peeters, *Negative ion-drag force in a plasma of gas discharge* (30th EPS conference on Contr. Fusion and Plasma Phys., St. Petersburg, 2003), Vol. ECA 27A, pp. O-2.3Bpd.
- [104] R. L. Merlino, A. Barkan, C. Thompson, and N. D'Angelo, *Phys. Plasmas* **5**, 1607 (1998).
- [105] A. Melzer, V. A. Schweigert, and A. Piel, *Physica Scripta* **61**, 494 (2000).
- [106] G. Praburam and J. Goree, *Phys. Plasmas* **3**, 1212 (1996).
- [107] A. Melzer *et al.*, in *VII Workshop on The Physics of Dusty Plasmas* (AIP Conference Proceedings, Boulder, Colorado, 1998), No. 1, pp. 168–174.
- [108] V. N. Tsytovich, S. V. Vladimirov, G. E. Morfill, and J. Goree, *Phys. Rev. E* **63**, 056609 (2001).
- [109] D. Samsonov and J. Goree, *IEEE Trans. Plasma Sci.* **27**, 76 (1999).
- [110] E. Thomas Jr., B. M. Annaratone, G. E. Morfill, and H. Rothermel, *Phys. Rev. E* **66**, 016405 (2002).
- [111] J. J. Thomson, *Philos. Mag.* **7**, 237 (1904).
- [112] S. L. Gilbert, J. J. Bollinger, and D. J. Wineland, *Phys. Rev. Lett.* **60**, 2022 (1988).
- [113] W.-T. Juan *et al.*, *Phys. Rev. E* **58**, R6947 (1998).
- [114] M. Klindworth, A. Melzer, A. Piel, and V. A. Schweigert, *Phys. Rev. B* **61**, 8404 (2000).
- [115] S. Peters, A. Homann, A. Melzer, and A. Piel, *Phys. Lett. A* **223**, 389 (1996).
- [116] Y.-J. Lai and L. I, *Phys. Rev. E* **60**, 4743 (1999).
- [117] O. Arp, D. Block, A. Piel, and A. Melzer, *Phys. Rev. Lett.* **93**, 165004 (2004).
- [118] V. M. Bedanov and F. Peeters, *Phys. Rev. B* **49**, 2667 (1994).
- [119] H. Totsuji, C. Totsuji, and K. Tsuruta, *Phys. Rev. E* **64**, 066402 (2001).
- [120] W. J. Goedheer and M. R. Akdim, *Phys. Rev. E* **68**, 045401 (2003).
- [121] H. Totsuji *et al.*, *Phys. Lett. A* **221**, 215 (1996).
- [122] H. Totsuji, T. Kishimoto, and C. Totsuji, *Phys. Rev. Lett.* **78**, 3113 (1997).

- [123] L.-W. Teng, P.-S. Tu, and L. I, Phys. Rev. Lett. **90**, 245004 (2003).
- [124] D. Dubin, Phys. Rev. Lett. **71**, 2753 (1993).
- [125] D. T. Wasan, A. D. Nikolov, P. A. Kralchevski, and I. B. Ivanov, Colloid Surfaces **67**, 139 (1992).
- [126] J. N. Israelachvili, *Intermolecular and Surface Forces* (Acad. Press, London, 1985).
- [127] B. Bhushan, J. N. Israelachvili, and U. Landman, Nature **374**, 607 (1995).
- [128] M. Mikikian *et al.*, New J. Phys. **5**, 19.1 (2003).
- [129] A. Homann, Dissertation, Christian–Albrechts–Universität Kiel, 1998.
- [130] MICROPARTICLES GMBH, Rudower Chaussee 5, 12484 Berlin.
- [131] PRECISION EFORMING LLC, 839 Route 13, Cortland, NY 13045.
- [132] K. Hansen, T. Klinger, and A. Piel, Rev. Sci. Instrum. **65**, 2615 (1994).
- [133] V. A. Godyak and R. B. Piejak, J. Appl. Phys. **68**, 3157 (1990).
- [134] A. Garscadden and K. G. Emeleus, Proc. Phys. Soc. **79**, 535 (1961).
- [135] A. Boschi and F. Magistrelli, Il Nuovo Cimento **2**, 487 (1963).
- [136] J. D. Swift and M. J. R. Schwar, *Electric Probes for Plasma Diagnostics* (Ilfle Books, London, 1971).
- [137] V. A. Godyak and O. A. Popov, Sov. Phys. Tech. Phys. **22**, 461 (1977).
- [138] N. S. J. Braithwaite, N. M. P. Benjamin, and J. E. Allen, Journal of Physics E: Scientific Instruments **20**, 1046 (1987).
- [139] A. Dyson, P. Bryant, and J. E. Allen, Measurement Science and Technology **11**, 554 (2000).
- [140] R. R. J. Gagné and A. Cantin, J. Appl. Phys. **43**, 2639 (1972).
- [141] B. M. Annaratone and N. S. J. Braithwaite, Measurement Science and Technology **2**, 795 (1991).
- [142] A. P. Paranjpe, J. P. McVittie, and S. A. Self, J. Appl. Phys. **67**, 6718 (1990).
- [143] P. A. C. and J. A. Rees, W. L. Wu, and K. Al-Assadi, Vacuum **42**, 489 (1991).
- [144] I. D. Sudit and R. C. Woods, Rev. Sci. Instrum. **64**, 2440 (1993).

- [145] M. R. Akdim, Ph.D. thesis, Universiteit Utrecht, 2003.
- [146] C. K. Birdsall and A. B. Langdon, *Plasma physics via computer simulation, Plasma physics series* (Institute of Physics Publ., Bristol, 1995).
- [147] H. Totsuji, *Phys. Plasmas* **8**, 1856 (2001).
- [148] Z. Chen, M. Yu, and H. Luo, *Physica Scripta* **64**, 476 (2001).
- [149] D.-Z. Wang, J. Q. Dong, and S. M. Mahajan, *J. Phys. D: Appl. Phys.* **30**, 113 (1997).
- [150] G. Lapenta, *Phys. Plasmas* **6**, 1442 (1999).
- [151] J. P. Boeuf and L. C. Pitchford, *Phys. Rev. E* **51**, 1376 (1995).
- [152] J. P. Passchier and W. J. Goedheer, *J. Appl. Phys.* **74**, 3744 (1993).
- [153] G. J. Nienhuis *et al.*, *J. Appl. Phys.* **82**, 2060 (1997).
- [154] H. C. Kim and V. I. Manousiouthakis, *J. Appl. Phys.* **89**, 34 (2001).
- [155] S. J. Choi, P. L. G. Ventzek, R. J. Hoekstra, and M. J. Kushner, *Plasma Sources Sci. Technol.* **3**, 418 (1994).
- [156] V. Vyas, G. A. Hebner, and M. J. Kushner, *J. Appl. Phys.* **92**, 6451 (2002).
- [157] H. W. Ellis *et al.*, *Atomic Data & Nucl. Data Tables* **17**, 177 (1976).
- [158] A. Fiala, L. C. Pitchford, and J. P. Boeuf, *Phys. Rev. E* **49**, 5607 (1994).
- [159] A. V. Phelps and L. C. Pitchford, *Phys. Rev. A* **31**, 2932 (1985).
- [160] A. V. Phelps and R. J. V. Brunt, *J. Appl. Phys.* **64**, 4269 (1988).
- [161] A. V. Phelps, C. H. Greene, and J. P. Burke, *J. Phys. B* **33**, 2965 (2000).
- [162] F. F. Chen, *Introduction to Plasma Physics and Controlled Fusion*, 2nd ed. (Plenum Press, New York, 1984), Vol. 1.
- [163] N. Hershkowitz, in *Plasma Diagnostics: Discharge Parameters and Chemistry*, edited by O. Auciello and D. L. Flamm (Academic Press, New York, 1989), Vol. 1, Chap. 3, pp. 113–183.
- [164] P. Bryant, A. Dyson, and J. E. Allen, *Journal of Physics D: Applied Physics* **34**, 1491 (2001).
- [165] Chung, Talbot, and Touryan, *Electric probes in stationary and flowing plasmas* (Springer-Verlag, New York, 1975).
- [166] I. H. Hutchinson, *Principles of Plasma Diagnostics*, 2nd ed. (Cambridge University Press, Cambridge, 2002).

- [167] R. N. Franklin and J. Snell, *Phys. Plasmas* **7**, 3077 (2000).
- [168] R. N. Franklin and J. Snell, *Phys. Plasmas* **8**, 643 (2001).
- [169] R. N. Franklin, *J. Phys. D: Appl. Phys.* **34**, 1959 (2001).
- [170] I. B. Bernstein and I. N. Rabinowitz, *Phys. Fluids* **2**, 112 (1959).
- [171] L. S. Hall and R. R. Fries, *Proc. 7th Int. Conf. Phenomena Ionized Gases*, 1966.
- [172] R. E. Kiel, *AIAA Journal* **6**, 708 (1968).
- [173] R. E. Kiel, *AIAA Journal* **9**, 1380 (1971).
- [174] M. Mausbauch, *J. Vac. Sci. Technol. A* **15**, 2923 (1997).
- [175] C. Steinbrüchel, *J. Vac. Sci. Technol. A* **8**, 1663 (1990).
- [176] A. Karamcheti and C. Steinbrüchel, *J. Vac. Sci. Technol. A* **17**, 3051 (1999).
- [177] J. E. Allen, *Physica Scripta* **45**, 497 (1992).
- [178] F. F. Chen, *Plasma Phys.* **7**, 47 (1965).
- [179] A. A. Sonin, *AIAA J.* **4**, 1588 (1966).
- [180] I. D. Sudit and R. C. Woods, *J. Appl. Phys.* **76**, 4488 (1994).
- [181] M. Tuszewski and J. A. Tobin, *Plasma Sources Sci. Technol.* **5**, 640 (1996).
- [182] B. M. Annaratone, M. W. Allen, and J. E. Allen, *J. Phys. D: Appl. Phys.* **25**, 417 (1992).
- [183] G. J. Schulz and S. C. Brown, *Phys. Rev.* **98**, 1642 (1955).
- [184] S. D. Hester and A. A. Sonin, *Phys. Fluids* **13**, 1265 (1970).
- [185] C. H. Shih and E. Levi, *AIAA J.* **9**, 1673 (1971).
- [186] S. A. Self and C. H. Shih, *Phys. Fluids* **11**, 1532 (1968).
- [187] E. F. Jaeger, L. A. Berry, and D. B. Batchelor, *J. Appl. Phys.* **69**, 6918 (1991).
- [188] G. Narasimhan and C. Steinbrüchel, *J. Vac. Sci. Technol. A* **19**, 376 (2001).
- [189] W. J. Goedheer, *privat communications*.
- [190] K. Köhler *et al.*, *J. Appl. Phys.* **57**, 59 (1985).
- [191] V. A. Godyak and N. Sternberg, *Phys. Rev. A* **42**, 2299 (1990).

- [192] G. R. Misium, A. J. Lichtenberg, and M. A. Lieberman, *J. Vac. Sci. Technol. A* **7**, 1007 (1989).
- [193] C. Lai *et al.*, *J. Vac. Sci. Technol. A* **11**, 1199 (1993).
- [194] K. Wüst, *Rev. Sci. Instrum.* **63**, 2581 (1992).
- [195] T. I. Cox *et al.*, *J. Phys. D: Appl. Phys.* **20**, 820 (1987).
- [196] O. A. Popov and V. A. Godyak, *J. Appl. Phys.* **57**, 53 (1985).
- [197] L. J. Overzet and M. B. Hopkins, *J. Appl. Phys.* **74**, 4323 (1993).
- [198] T. H. Chung, H. S. Yoon, and J. K. Lee, *J. Appl. Phys.* **78**, 6441 (1995).
- [199] R. N. Franklin, *Plasma Sources Sci. Technol.* **11**, A31 (2002).
- [200] B. A. Klumov, A. V. Ivlev, and G. E. Morfill, *JETP Lett.* **78**, 300 (2003).
- [201] H. Amemiya, B. M. Annaratone, and J. E. Allen, *Plasma Sources Sci. Technol.* **8**, 179 (1999).
- [202] A. A. Mamun and P. K. Shukla, *Phys. Plasmas* **10**, 1518 (2003).
- [203] C. O. Thompson, N. D'Angelo, and R. L. Merlino, *Phys. Plasmas* **6**, 1421 (1999).
- [204] D. Samsonov, A. V. Ivlev, G. E. Morfill, and J. Goree, *Phys. Rev. E* **63**, 025401 (2001).
- [205] N. S. J. Braithwaite and J. E. Allen, *Phys. Fluids* **27**, 203 (1984).
- [206] R. Roth, R. Evans, and S. Dietrich, *Phys. Rev. E* **62**, 5360 (2000).
- [207] K. Takahashi *et al.*, *Phys. Rev. E* **58**, 7805 (1998).
- [208] M. Klindworth *et al.*, *Phys. Rev. Lett.* **93**, 195002 (2004).
- [209] C. Arnas, M. Mikikian, G. Bachet, and F. Doveil, *Phys. Plasmas* **7**, 4418 (2000).
- [210] T. Trottenberg, B. Brede, D. Block, and A. Piel, *Phys. Plasmas* **10**, 4627 (2003).
- [211] E. Thomas, Jr. and M. Watson, *Phys. Plasmas* **7**, 3194 (2000).
- [212] M. Klindworth *et al.*, in *Dusty Plasmas in the new Millennium: Third International Conference on the Physics of Dusty Plasmas, Durban, 2002*, edited by R. Bharuthram, M. A. Hellberg, P. K. Shukla, and F. Verheest (American Institute of Physics, Melville, NY, 2002), pp. 345–348.
- [213] J. P. Boeuf, *Phys. Rev. A* **46**, 7910 (1992).

Publikationsliste

Teile der vorliegenden Dissertation wurden aus Aktualitätsgründen bereits als wissenschaftliche Publikationen veröffentlicht.

Beiträge auf internationalen Konferenzen:

1. M. Klindworth, A. Melzer, A. Piel, U. Konopka, and G. E. Morfill,
“Langmuir Probe Measurements in a Complex Plasma under Microgravity Conditions”
in *Dusty Plasmas in the new Millennium: Third International Conference on the Physics of Dusty Plasmas, Durban, 2002*
edited by R. Bharuthram, M. A. Hellberg, P. K. Shukla, and F. Verheest
(American Institute of Physics, Melville, NY, 2002), pp. 345–348.
2. M. Klindworth, A. Melzer, and A. Piel,
“Langmuir Probe Measurements in a Complex Plasma under Microgravity Conditions”
in *Proceedings of the 29th EPS meeting on Controlled Fusion and Plasma Physics*,
edited by R. Behn and C. Varandas (European Physical Society, Montreux, 2002), Vol. ECA 26B, pp. O–4.33.
3. M. Klindworth, O. Arp, A. Melzer, and A. Piel,
“Particle Manipulation and Diagnostics of Complex Plasmas under Microgravity Conditions”
in *Proceedings of the 26th International Conference on Phenomena in Ionized Gases (XXVI ICPIG)*,
edited by J. Meichner, D. Loffhagen, and H. E. Wagner (XXVI ICPIG Committee, Greifswald, 2003), Vol. 1, pp. 243–244.
4. M. Klindworth, O. Arp, and A. Piel,
“Comparison of 2D Plasma Profiles and Particle Distributions in Complex Plasmas under Microgravity”
in *Proceedings of the 31th EPS meeting on Controlled Fusion and Plasma Physics*,
(European Physical Society, London, 2004), Vol. ECA 28G, pp. P1–017.

5. M. Klindworth, A. Piel, U. Konopka, and G. E. Morfill,
“Probe induced secondary Voids in Complex Plasmas under Microgravity”
in *Proceedings of the 31th EPS meeting on Controlled Fusion and Plasma Physics*,
(European Physical Society, London, 2004), Vol. ECA 28G, pp. P1–018 /
O5–08.

Beiträge in wissenschaftlichen Fachmagazinen:

1. M. Klindworth, A. Piel, A. Melzer, U. Konopka, H. Rothermel, K. Tarantik,
and G. E. Morfill,
“Dust-Free Regions around Langmuir Probes in Complex Plasmas under
Microgravity”,
Phys. Rev. Lett. **93**, 195002 (2004).

Danksagung

An erster Stelle möchte ich mich bei Herrn Prof. Dr. A. Piel bedanken, der mir die Gelegenheit zur Anfertigung dieser Dissertation in seiner Arbeitsgruppe gegeben hat. Er hat in zahlreichen Diskussionen Licht ins Dunkel von technischen und wissenschaftlichen Fragestellungen gebracht und auch durch moralische Unterstützung die Fertigstellung dieser Arbeit erst ermöglicht.

Dank gilt auch allen Mitgliedern der Arbeitsgruppe für die konstruktive Zusammenarbeit in allen Fragen der komplexen Plasmen. Insbesondere sei Oliver Arp für die Implementierung der Software der Parabelflugexperimente und die souveräne Mitarbeit im Projekt gedankt. Herrn Prof. Dr. André Melzer danke ich ebenfalls für seine Beiträge in der Frühphase dieses Projektes. Für die exzellente und rasante Umsetzung aller mechanischen Komponenten, insbesondere der Vielzahl von Sondenantriebsprototypen, gebührt der feinmechanischen Werkstatt des Physikzentrum mit allen Mitarbeitern außerordentlicher Dank. Für Beistand im Kampf gegen die Widrigkeiten der Bürokratie sei Frau Jahn und Frau Seeger gedankt.

Das DLR sei hier für die Finanzierung des Projektes und damit auch meiner Arbeitsstelle erwähnt.

Für das Korrekturlesen dieser Arbeit und die Freundschaft und Unterstützung in jeder Lebenslage bedanke ich mich bei Ciprian Zafiu. Letzteres gilt auch für Stefan Wichmann - besonders auch für die Ergänzung meines zuletzt mageren Speiseplans. Eine Entschuldigung für die zeitweise Vernachlässigung aller anderen Freunde in der vergangenen Zeit darf hier nicht fehlen.

Und Dank von ganzem Herzen an Sonja.

Eidesstattliche Erklärung

Hiermit versichere ich an Eides Statt, daß die vorliegende Dissertation - abgesehen von der Beratung durch meinen wissenschaftlichen Lehrer und der Verwendung der angegebenen Hilfsmittel - nach Inhalt und Form meine eigene ist. Sie hat weder ganz noch teilweise an einer anderen Stelle im Rahmen eines Prüfungsverfahrens vorgelegen.

Kiel, den

Lebenslauf

Name: Klindworth, Markus
geboren: 01.01.1973 in Buxtehude
Familienstand: ledig
Staatsangehörigkeit: deutsch

Schulbildung: 1979 - 1983 Grundschule in Wiegersen
1983 - 1985 Orientierungsstufe, Schulzentrum Süd in Buxtehude
1985 - 1989 Gymnasium, Schulzentrum Süd in Buxtehude
1989 - 1992 Gymnasium, Halepaghen-Schule in Buxtehude
1992 Abitur mit den Prüfungsfächern:
Physik, Mathematik, Englisch und Geschichte

Wehrdienst: 1992 - 1993 in Hamburg und Husum

Studium: WS 1993/94 Immatrikulation im Fach Physik
an der Christian-Albrechts-Universität zu Kiel

WS 1995/96 Diplom-Vorprüfung mit Nebenfach Chemie

WS 1998/99 Diplom-Hauptprüfung mit Nebenfach Ozeanogra-
phie

WS 1998/99 - Anfertigung der Diplomarbeit "Struktur und Sta-
WS 1999/2000 bilität finiter Coulomb-Cluster in staubigen Plas-
men" in der Arbeitsgruppe "Plasmadynamik" am
Institut für Experimentelle und Angewandte Physik
der Christian-Albrechts-Universität zu Kiel

SS 2000 - Promotion in der Arbeitsgruppe "Plasmadynamik"
WS 2004/05 am Institut für Experimentelle und Angewandte
Physik der Christian-Albrechts-Universität zu Kiel

